

Two-Phase Detailed Numerical Analysis of Falling Film Absorption Phenomena

by

Robabeh Abbasi Havestini

A Thesis submitted to the Faculty of Graduate Studies of
The University of Manitoba
in partial fulfilment of the requirements for the degree of

Doctor of Philosophy

Department of Mechanical Engineering
University of Manitoba

Winnipeg, Manitoba, Canada

Copyright © August 2021 by Robabeh Abbasi Havestini

Abstract

Absorption refrigeration systems have the potential to provide cooling at relatively low cost by using waste heat in industrial sectors or geothermal or solar energy. The performance of an absorption system is highly affected by the design and operating conditions of the absorber. Falling film type of absorbers are commonly used to enhance the heat and mass transfer rate during the absorption process. This process is complex due to the concurrent mass and heat transfer occurring in absorbent-absorbate two-phase flow and the equilibrium condition at the vapour-liquid interface. A deeper understanding of the coupled heat, mass, and momentum transfer in the absorption process using a numerical model would permit refinements needed to optimize refrigeration system performance.

Previous theoretical studies were mainly focused on a single-phase numerical analysis of the absorption phenomena and neglected the effect of the gas flow at the interface. In this research, however, detailed two-phase two-dimensional numerical models are developed to study the absorption of pure water vapour into an aqueous LiBr solution flowing inside a vertical channel or over a horizontal tube. The falling film in a vertical channel is studied using a parabolic and an elliptic numerical model, then the elliptic model is applied to a horizontal tube.

The numerical model results are carefully compared to available numerical or experimental data. A wide range of parameters are studied to investigate the development of co-current flows of liquid and gas in absorption phenomena. The velocity, pressure, and temperature distributions in both phases and the mass fraction distribution in the liquid phase are presented. The parabolic model predictions for the interfacial parameters are in a good agreement with the results of the elliptic model in the case of the vertical channel up to the axial point where insufficient vapour mass in the gas phase ceases the advancement of the parabolic model. The elliptic model is computationally more expensive, but has the capability of predicting recirculating flows. The elliptic model predicted the details of flow over a horizontal tube that were in good agreement with previous work.

Acknowledgements

I would like to express my gratitude to my adviser, Dr. Scott Ormiston for his help and supervision during my Ph.D. research. I would like to thank my Ph.D. committee members, Dr. Kuhn and Dr. Jeffrey for their time and inputs in this thesis. The financial assistance provided by the Natural Sciences and Engineering Research Council of Canada (NSERC) and the University of Manitoba is gratefully acknowledged. I would like to show my greatest appreciation to my mother and father, Nazli and Jamshid, for their endless love, support, and sacrifices. I would also like to gratefully thank my husband and best friend, Mohsen, for his patience, encouragement, and for our many invaluable discussions over the course of this research. I would like to thank my sisters, Masoumeh, Fatemeh, and Atefeh who have encouraged and supported me during my academic pursuits. Last but not least, I thank my incredible teacher and friend, Mrs. Miranzadeh, who inspired me and many other young women to pursue higher education and build a brighter future.

Dedication

To my loving family

Contents

Abstract	ii
Acknowledgements	iii
Dedication	iv
List of Tables	xiii
List of Figures	xv
Nomenclature	xxiii
1 Introduction	1
1.1 Overview	1
1.1.1 Absorption Refrigeration Cycles	2
1.1.2 Vapour-Liquid Interface Equilibrium	4
1.2 Problem Statement	5
1.2.1 Vertical Plate Geometry	5
1.2.2 Horizontal Tube Geometry	7
1.3 Literature Review	8
1.3.1 Analytical Solutions	8
1.3.1.1 Vertical Channel Geometry	8
1.3.1.2 Horizontal Tube Geometry	9
1.3.1.3 Summary of Analytical Model Literature	11

1.3.2	Numerical Approaches	13
1.3.2.1	Vertical Channel Geometry	13
1.3.2.2	Horizontal Tube Geometry	17
1.3.2.3	Summary of Numerical Model Literature	24
1.3.3	Experimental Studies	25
1.3.3.1	Horizontal Tubes	25
1.3.4	Contribution of the Present Work	34
1.3.5	Layout of the Thesis	36
2	Mathematical Model	37
2.1	Introduction	37
2.2	Problem Statement	37
2.3	Parabolic Model Governing Equations	39
2.3.1	Liquid Phase	39
2.3.2	Gas Phase	40
2.3.3	Interface Conditions	42
2.3.4	Domain and Boundary Condition Definitions	43
2.4	Elliptic Model Governing Equations	45
2.4.1	Liquid Phase	45
2.4.2	Gas Phase	45
2.4.3	Interface Conditions	46
2.4.4	Domain and Boundary Condition Definitions	48
2.4.5	Interface Moving Strategy	49

3	Discretisation of the Domain	52
3.1	Parabolic Model	52
3.1.1	Introduction	52
3.1.2	Coordinate Transformation	52
3.1.3	Transformed Governing Equations	53
3.1.4	Grid system	54
3.2	Elliptic Model	57
3.2.1	Introduction	57
3.2.2	Grid Nomenclature	59
3.2.3	Grid Expansion Factor	64
3.2.4	Grid Assembly	65
4	Numerical Solution Method	67
4.1	Introduction	67
4.2	Discretisation of the Governing Equations in Parabolic Model	67
4.2.1	Face values for Variables	67
4.2.2	Face Values for Properties	68
4.2.3	Newton-Raphson Linearisation	69
4.2.4	Discretisation Steps	69
4.2.5	Algebraic Equations	74
4.2.6	Solution Method	76
4.2.6.1	Construction of the Matrix	76

4.2.6.2	Matrix Solver	77
4.2.6.3	Solution Procedure and Convergence	79
4.3	Discretisation of the Governing Equations in Elliptic Model	80
4.3.1	Algebraic Transport Equations	81
4.3.1.1	Liquid Phase Continuity Equation	81
4.3.1.2	Liquid Phase x -momentum Equation	87
4.3.1.3	Liquid Phase y -momentum Equation	90
4.3.1.4	Liquid Phase Energy Equation	91
4.3.1.5	Liquid Phase Mass Fraction Equation	93
4.3.2	Algebraic Interface Equations	93
4.3.2.1	Normal Force Balance	93
4.3.2.2	Zero Pressure Gradient	97
4.3.2.3	Tangential Force Balance	97
4.3.2.4	Tangential Velocity Equality	98
4.3.2.5	Continuity of Mass at the Interface	99
4.3.2.6	Continuity of Energy at the Interface	99
4.3.2.7	Equilibrium Condition at the Interface	100
4.3.2.8	Temperature Equality at the Interface	100
4.3.2.9	Impermeability of LiBr	100
4.3.3	Boundary Condition Equations Implementation	101
4.3.3.1	Dirichlet	102
4.3.3.2	Neumann	102

4.3.3.3	Algebraic Absorption of the Boundary Conditions	104
4.3.3.4	Face Velocity Boundary Conditions	106
4.3.4	E-factor	108
4.3.5	Interface Movement Procedure	109
4.3.6	Solution Method	111
4.3.6.1	Convergence Criteria	111
5	Parallel-Plate Channels: Parabolic Model	113
5.1	Introduction	113
5.2	Grid Independence Study	113
5.3	Comparisons with Previous Work	114
5.3.1	Comparison Case C1: Andberg and Vliet (1983)	114
5.3.2	Comparison Case C2: Kawae et al. (1989)	118
5.3.3	Comparison Case C3: Mittermaier and Ziegler (2015)	120
5.3.4	Summary of Comparison Cases	122
5.4	New Results for the Parabolic Two-Phase Absorption Model	124
5.4.1	Effect of Changing the Operating Parameters	124
5.4.2	Effect of the Gas Phase	130
6	Parallel-Plate Channels: Elliptic Model	140
6.1	Introduction	140
6.2	Grid Independence Study	140
6.3	Comparisons with Previous Work	141

6.3.1	Definition of Comparison Cases	141
6.3.2	Axial Variations	142
6.3.3	Transverse Profiles	147
6.3.4	Summary of Comparison Cases	156
6.4	New Results for the Elliptic Two-phase Absorption Model	156
7	Horizontal Tubes: Elliptic Model	164
7.1	Introduction	164
7.2	Grid Independence Study	164
7.3	Comparisons with Previous Work	165
7.3.1	Definition of Comparison Cases	165
7.3.2	Comparison Case HT1: Min and Choi (1999)	166
7.3.3	Comparison Cases HT2 and HT3: Papaefthimiou et al. (2006)	173
7.3.4	Comparison Case HT4: Kyung et al.(2007)	175
7.3.5	Comparison Case HT5: Seol and Lee (2005)	181
7.3.6	Summary of Comparison Cases	184
7.4	New Results for the Elliptic Two-phase Absorption Over a Horizontal Tube	184
7.4.1	Effect of changing ΔT and $Re_{L,in}$	186
7.4.2	Effect of changing d	203
7.4.3	Effect of changing S_T/d	209
7.4.3.1	Over-Tube Variations	209
7.4.3.2	Transverse Profiles	213
7.4.4	Computational Time	226

8	Summary, Conclusions, and Recommendations for Future Work	229
8.1	Summary	229
8.2	Conclusion	234
8.3	Recommendation for Future Works	235
	References	238
A	Equilibrium Conditions	245
A.1	Equilibrium Condition by McNeely (1977)	245
A.2	Equilibrium Condition by Uemura and Hasaba (1964)	246
A.3	Equilibrium Condition by Siebe (1986)	247
A.4	Equilibrium Condition by Mittermaier et al. (2014)	248
B	Mixture Energy Equation	249
C	Parabolic Model Coefficients in Algebraic Equations	255
C.1	Coefficients of Liquid Mass Fraction Equation	255
C.2	Coefficients of Interfacial Boundary Condition Equations	256
C.2.1	Velocity Continuity	256
C.2.2	Mass Continuity	256
C.2.3	Temperature Continuity	256
C.2.4	LiBr Impermeability	257
C.2.5	Energy Continuity	257
C.2.6	Overall Mass Balance	258

D Bordered Block Matrix Entries in Parabolic Model	259
E Elliptic Model Coefficients in Interface Algebraic Equations	263
E.1 Normal Force Balance	263
E.2 Zero Pressure Gradient	264
E.3 Tangential Force Balance	265
E.4 Tangential Velocity Equality	266
E.5 Continuity of Mass at the Interface	266
E.6 Continuity of Energy at the Interface	267
E.7 Equilibrium Condition at the Interface	267
E.8 Temperature Equality at the Interface	268
E.9 Impermeability of LiBr	268
F Equilibrium Condition by Mittermaier et al. (2014)	269
F.1 LiBr-Water Solution Density ρ_L	269
F.2 LiBr-Water Solution Kinematic viscosity ν_L	270
F.3 LiBr-Water Solution specific Heat $C_{p,L}$	270
F.4 LiBr-Water Solution Thermal Conductivity k_L	271
F.5 LiBr-Water Solution Binary Diffusion Coefficient D_L^{AB}	272
G Heat of Absorption by Papaefthimiou et al. (2006)	273
H The Effect of Changing S_T/d on the Falling Liquid Film with $Re_{L,in} = 80$ Over a Horizontal Tube	274
I The Liquid and Gas Pressure Profiles for $S_T/d = 3$ and 9 Over a Horizontal Tube	278

List of Tables

1.1	Summary of single phase analytical studies of laminar LiBr-water falling film on a flat plate.	10
1.2	Summary of single phase analytical study of laminar NH ₃ -water falling film on a horizontal tube by Conlisk and Mao (1996)	12
1.3	Summary of numerical studies of laminar LiBr-water solution over a vertical plate.	18
1.4	Operating parameters and physical properties in numerical studies of laminar LiBr-water solution over a vertical plate.	19
1.5	Summary of numerical studies of laminar LiBr-water falling film over horizontal tubes.	26
1.6	Operating parameters and physical properties in numerical studies of laminar LiBr-water solution over horizontal tubes.	27
1.7	Summary of experimental studies of LiBr laminar falling film over horizontal tubes.	31
1.8	Summary of experimental studies of NH ₃ -water laminar falling film over horizontal tubes.	32
5.1	Operating parameters and physical properties in comparison cases.	115
5.2	Comparison case parameters.	115
5.3	Operating parameters for two-phase model test cases.	125
6.1	Definition of comparison cases.	142
6.2	Operating parameters for cases E4 to E7.	157
7.1	Geometric parameters in comparison cases.	167

List of Tables

7.2	Operating parameters in comparison cases.	167
7.3	Tube wall and liquid film inlet temperatures in Case HT5.	182
7.4	Number of nodes in the x and y direction in parametric study cases*.	186
7.5	Froude number for the parametric study cases.	187
7.6	Total amount of the mass absorbed over the tube $\left(\frac{\dot{m}_{\text{inf,tot}}}{\dot{m}_{L,\text{in}}}\right)_{5 \leq \theta \leq 175} \times 100\%$ for the parametric study cases.	227
7.7	Elliptic model compute times in horizontal tube cases.	228

List of Figures

1.1	Absorption refrigeration cycle.	3
1.2	Duhring diagram for LiBr-water solution.	5
1.3	Schematic diagram of LiBr-water absorption over a cold wall.	6
1.4	Schematic diagram of LiBr-water absorption over horizontal tubes.	7
2.1	Domain definition and boundary conditions for two-phase absorption in a vertical channel; the outlet boundary conditions apply to the elliptic model only.	38
2.2	Domain definition and boundary conditions for two-phase absorption over a horizontal tube.	41
2.3	Grid information of the phases and a typical liquid region used in ILMB method; the interface nodes are shown separated for illustration purposes.	50
3.1	Grid nomenclature in transformed coordinates.	55
3.2	Grid nomenclature in Cartesian coordinates.	56
3.3	Grid information in the liquid and gas regions; the spacing between the nodes at the interface is exaggerated for illustration purposes.	58
3.4	Computational molecule: indexing and notation.	59
3.5	Coordinates of control volume points and quadrant notation.	60
3.6	Distances, areas and volumes of a control volume.	60
3.7	Grid directional unit vectors.	61
3.8	Location of distance variables.	63
3.9	Example of grid assembly for falling film absorption over a horizontal tube.	66
4.1	Co-located variable storage scheme.	80

List of Figures

4.2	Indexing notation for interface and neighbouring control volumes; the spacing between the nodes at the interface is exaggerated for illustration purposes.	94
4.3	South boundary computational molecule.	101
4.4	Nomenclature used in the ILMB method. The interface node spacing is exaggerated for illustration purposes.	110
5.1	Axial variation of (a) interface mass fraction, (b) interface temperature, (c) interface and wall heat flux, and (d) interface mass flux for Comparison Case C1.	117
5.2	Comparison Case C2: axial variation of (a) interface mass fraction and (b) interface and wall heat flux; transverse-direction profiles at selected axial locations of (c) LiBr mass fraction and (d) liquid temperature.	119
5.3	Comparison Case C3: axial variation of (a) interface mass flux and (b) liquid film thickness with a fully developed inlet velocity profile; axial variation of (c) interface mass flux and (d) liquid film thickness with a uniform inlet velocity profile.	121
5.4	Comparison Case C3: (a) liquid velocity profile at x values of 0 m and 0.1 m with a fully developed inlet velocity profile and (b) water mass fraction profile at $x = 0.1$ m with a uniform inlet velocity profile.	123
5.5	Comparison of (a) total absorbed mass ratio to the inlet vapour mass and (b) liquid film thickness.	126
5.6	Comparison of interfacial (a) mass flux, (b) mass fraction, and (c) temperature in cases with $\xi_{W,in} = 0.5$; comparison of interfacial (d) mass flux, (e) mass fraction, and (f) temperature in cases with $\xi_{W,in} = 0.45$	127
5.7	(a) mass fraction variation across the film in Case 1 and (b) liquid film and vapour velocity profiles at different axial locations in Case 4.	129

List of Figures

5.8	Effect of $Re_{G,in}$ change on (a) interface velocity, (b) film thickness , and (c) mass absorption rate in Case 4.	131
5.9	Effect of $Re_{G,in}$ change on mass and heat fluxes in Case 4.	133
5.10	Vapour inlet temperature effect on (a) interface and wall heat fluxes and (b) interface mass flux in Case 4.	134
5.11	Vapour inlet temperature effect on total absorbed mass ratio to the inlet vapour mass in Case 4.	135
5.12	Vapour inlet temperature effect on liquid film thickness in Case 4.	136
5.13	Vapour inlet temperature effect on vapour temperature distribution across the channel in Case 4.	137
5.14	Vapour inlet temperature effect on adiabatic wall temperature variation in Case 4.	137
5.15	Vapour inlet temperature effect on axial variation of pressure in Case 4.	138
5.16	Vapour inlet temperature effect on axial variation of pressure gradient in Case 4.	139
6.1	Comparison of axial variation of interface temperature and mass fraction for Cases E1, E2, P1, and P2 with Habib and Wood (1990)	143
6.2	Comparison of axial variation of interface mass flux, interface and wall heat flux for Cases E1, E2, P1, and P2 with Habib and Wood (1990)	145
6.3	Comparison of LiBr mass fraction distribution for Cases E1 and E2 with Habib and Wood (1990)	147
6.4	Comparison of temperature distribution in the liquid film for Cases E1 and E2 with Habib and Wood (1990)	149
6.5	Comparison of temperature distribution in the gas phase for Cases E1 and E2 with Habib and Wood (1990)	150

List of Figures

6.6	Axial variation of interface temperature and mass fraction for Cases E1 and E3.	151
6.7	Axial variation of interface mass flux, interface and wall heat flux for Cases E1 and E3.	152
6.8	Total absorbed mass ratio to the inlet vapour mass and film thickness for Cases E1 and E3.	153
6.9	LiBr mass fraction distribution for Case E3.	154
6.10	Temperature distribution in the liquid and gas phases for Case E3.	155
6.11	Axial variation of interface temperature and mass fraction for Cases E4 to E7.	158
6.12	Axial variation of interface and wall heat flux for Cases E4 to E7.	159
6.13	Total absorbed mass ratio to the inlet vapour mass and film thickness for Cases E4 to E7.	160
6.14	Temperature distribution in the liquid and gas phases for Case E6.	162
6.15	Axial variation of Sh number for Case E6.	163
7.1	Geometric parameters definition for horizontal tubes studied using the elliptic model.	166
7.2	Liquid falling film shape around the tube for Case HT1 and Min and Choi (1999)	169
7.3	Comparison of LiBr mass fraction distribution in the liquid film for Case HT1 with Min and Choi (1999)	170
7.4	Comparison of local Sherwood number along the interface for Case HT1 with Min and Choi (1999)	171
7.5	Comparison of local Nusselt number along the tube surface for Case HT1 with Min and Choi (1999)	172
7.6	Comparison of the interface and the bulk (a) water mass fraction and (b) temperature along the flow direction for Case HT2 with Papaefthimiou et al. (2006) .	174

List of Figures

7.7	Comparison of the interface and the bulk (a) water mass fraction and (b) temperature along the flow direction for Case HT3 with Papaefthimiou et al. (2006)	176
7.8	Comparison of the interface and bulk temperatures along the flow direction for Case HT4 with Kyung et al. (2006)	178
7.9	Comparison of the liquid interface and bulk mass fraction along the flow direction for Case HT4 with Kyung et al. (2007)	179
7.10	Comparison of interface mass flux along the flow direction for Case HT4 with Kyung et al. (2007)	180
7.11	Comparison of temperature distribution in the liquid film for Case HT4 with Kyung et al. (2007)	181
7.12	Comparison of the liquid film inlet and outlet temperature for Case HT5 with Seol and Lee (2005)	183
7.13	Variation of the liquid film thickness around the tube with ΔT for $Re_{L,in} = [20, 40, 80]$, $S_T/d = 6$, and $d = 12.7$ mm.	188
7.14	Change of the liquid film shape at the top and bottom of the tube with ΔT for $Re_{L,in} = [20, 40, 80]$, $S_T/d = 6$, and $d = 12.7$ mm.	189
7.15	Variation around the tube of (a) interface mass fraction and (b) interface dimensionless temperature for $\Delta T = [5 \text{ K}, 10 \text{ K}]$ and $Re_{L,in} = [20, 40, 80]$ with $S_T/d = 6$ and $d = 12.7$ mm.	191
7.16	Variation around the tube of (a) local Nusselt number and (b) interface dimensionless mass flux for $\Delta T = [5 \text{ K}, 10 \text{ K}]$ and $Re_{L,in} = [20, 40, 80]$ with $S_T/d = 6$ and $d = 12.7$ mm.	193
7.17	Variation of the liquid film thickness around the tube with ΔT for $Re_{L,in} = [20, 40, 80]$, $S_T/d = 6$, and $d = 19.05$ mm.	194

List of Figures

7.18	Change of the liquid film shape at the top and bottom of the tube with ΔT for $Re_{L,in} = [20, 40, 80]$, $S_T/d = 6$, and $d = 19.05$ mm.	195
7.19	Variation around the tube of (a) interface mass fraction and (b) interface dimensionless temperature for $\Delta T = [5 \text{ K}, 10 \text{ K}]$ and $Re_{L,in} = [20, 40, 80]$ with $S_T/d = 6$ and $d = 19.05$ mm.	196
7.20	Variation around the tube of (a) local Nusselt number and (b) interface dimensionless mass flux for $\Delta T = [5 \text{ K}, 10 \text{ K}]$ and $Re_{L,in} = [20, 40, 80]$ with $S_T/d = 6$ and $d = 19.05$ mm.	198
7.21	Variation of the liquid film thickness around the tube with ΔT for $Re_{L,in} = [20, 40, 80]$, $S_T/d = 6$, and $d = 28.575$ mm.	199
7.22	Change of the liquid film shape at the top and bottom of the tube with ΔT for $Re_{L,in} = [20, 40, 80]$, $S_T/d = 6$, and $d = 28.575$ mm.	200
7.23	Variation around the tube of (a) interface mass fraction and (b) interface dimensionless temperature for $\Delta T = [5 \text{ K}, 10 \text{ K}]$ and $Re_{L,in} = [20, 40, 80]$ with $S_T/d = 6$ and $d = 28.575$ mm.	201
7.24	Variation around the tube of (a) local Nusselt number and (b) interface dimensionless mass flux for $\Delta T = [5 \text{ K}, 10 \text{ K}]$ and $Re_{L,in} = [20, 40, 80]$ with $S_T/d = 6$ and $d = 28.575$ mm.	202
7.25	Variation of the liquid film thickness around the tube with d for $S_T/d = 6$ and $\Delta T = 10 \text{ K}$	204
7.26	Change of the liquid film shape at the top and bottom of the tube with d for $S_T/d = 6$ and $\Delta T = 10 \text{ K}$	205
7.27	Variation around the tube of (a) interface mass fraction and (b) interface dimensionless temperature for $d = [12.7 \text{ mm}, 19.05 \text{ mm}, 28.575 \text{ mm}]$ and $Re_{L,in} = [20, 80]$ with $S_T/d = 6$ and $\Delta T = 10 \text{ K}$	206

7.28	Variation around the tube of (a) local Nusselt number and (b) interface dimensionless mass flux for $d = [12.7 \text{ mm}, 19.05 \text{ mm}, 28.575 \text{ mm}]$ and $\text{Re}_{L,\text{in}} = [20, 80]$ with $S_T/d = 6$ and $\Delta T = 10 \text{ K}$	208
7.29	Film thickness at the top and bottom of the tube and over the tube for $\text{Re}_{L,\text{in}} = [40, 80]$ and $\Delta T = [5 \text{ K}, 10 \text{ K}]$ with $S_T/d = 6$ (a) $d = 12.7 \text{ mm}$ and (b) $d = 28.575 \text{ mm}$	209
7.30	Variation of the liquid film thickness around the tube with S_T/d for $\text{Re}_{L,\text{in}} = 20$ and $\Delta T = [5 \text{ K}, 10 \text{ K}]$	210
7.31	Change of the liquid film shape at the top and bottom of the tube with S_T/d for $\text{Re}_{L,\text{in}} = 20$ and $\Delta T = [5 \text{ K}, 10 \text{ K}]$	211
7.32	Variation around the tube of (a) interface mass fraction and (b) interface dimensionless temperature for $S_T/d = [3, 9]$ and $\Delta T = [5 \text{ K}, 10 \text{ K}]$ with $d = [12.7 \text{ mm}, 19.05 \text{ mm}, 28.575 \text{ mm}]$ and $\text{Re}_{L,\text{in}} = 20$	212
7.33	Variation around the tube of (a) local Nusselt number and (b) interface dimensionless mass flux for $S_T/d = [3, 9]$ and $\Delta T = [5 \text{ K}, 10 \text{ K}]$ with $d = [12.7 \text{ mm}, 19.05 \text{ mm}, 28.575 \text{ mm}]$ and $\text{Re}_{L,\text{in}} = 20$	214
7.34	x/d locations in the domain ($S_T/d = 3$).	215
7.35	U velocity profiles in the liquid film at different axial locations for $S_T/d = [3, 9]$, $d = 19.05 \text{ mm}$, $\text{Re}_{L,\text{in}} = 40$ and $\Delta T = 10 \text{ K}$ ($U_{L,\text{in}} = 0.23 \text{ m s}^{-1}$).	216
7.36	V velocity profiles in the liquid film at different axial locations for $S_T/d = [3, 9]$, $d = 19.05 \text{ mm}$, $\text{Re}_{L,\text{in}} = 40$ and $\Delta T = 10 \text{ K}$ ($U_{L,\text{in}} = 0.23 \text{ m s}^{-1}$).	217
7.37	Temperature profiles in the liquid film at different axial locations for $S_T/d = [3, 9]$, $d = 19.05 \text{ mm}$, $\text{Re}_{L,\text{in}} = 40$ and $\Delta T = 10 \text{ K}$	218
7.38	Mass fraction profiles in the liquid film at different axial locations for $S_T/d = [3, 9]$, $d = 19.05 \text{ mm}$, $\text{Re}_{L,\text{in}} = 40$ and $\Delta T = 10 \text{ K}$	219

List of Figures

7.39	Flow streamlines and temperature contours for $d = 19.05$ mm, $\Delta T = 10$ K, and $Re_{L,in} = 40$ (a) $S_T/d = 3$, (b) $S_T/d = 6$, and (c) $S_T/d = 9$	220
7.40	Flow streamlines and temperature contours in $S_T/d = 6$ for various combinations of $Re_{L,in}$, ΔT , and d , as indicated in the figure labels.	222
7.41	U velocity profiles in the gas at different axial locations for $d = 19.05$ mm, $Re_{L,in} = 40$ and $\Delta T = 10$ K (a) $S_T/d = 9$ and (b) $S_T/d = 3$ ($U_{G,in} = 1.35$ m s ⁻¹).	223
7.42	V velocity profiles in the gas at different axial locations for $d = 19.05$ mm, $Re_{L,in} = 40$ and $\Delta T = 10$ K (a) $S_T/d = 9$ and (b) $S_T/d = 3$ ($U_{G,in} = 1.35$ m s ⁻¹).	224
7.43	Temperature profiles in the gas at different axial locations for $d = 19.05$ mm, $Re_{L,in} = 40$ and $\Delta T = 10$ K (a) $S_T/d = 9$ and (b) $S_T/d = 3$	225
H.1	Variation of the liquid film thickness around the tube with S_T/d for $Re_{L,in} = 80$ and $\Delta T = [5$ K, 10 K].	274
H.2	Change of the liquid film shape at the top and bottom of the tube with S_T/d for $Re_{L,in} = 80$ and $\Delta T = [5$ K, 10 K].	275
H.3	Variation around the tube of (a) interface mass fraction and (b) interface dimensionless temperature for $S_T/d = [3, 9]$ and $\Delta T = [5$ K, 10 K] with $d = [12.7$ mm, 19.05 mm, 28.575 mm] and $Re_{L,in} = 80$	276
H.4	Variation around the tube of (a) local Nusselt number and (b) interface dimensionless mass flux for $S_T/d = [3, 9]$ and $\Delta T = [5$ K, 10 K] with $d = [12.7$ mm, 19.05 mm, 28.575 mm] and $Re_{L,in} = 80$	277
I.1	Pressure profiles in the liquid at different axial locations for $d = 19.05$ mm, $Re_{L,in} = 40$ and $\Delta T = 10$ K (a) $S_T/d = 9$ and (b) $S_T/d = 3$	278
I.2	Pressure profiles in the gas at different axial locations for $d = 19.05$ mm, $Re_{L,in} = 40$ and $\Delta T = 10$ K (a) $S_T/d = 9$ and (b) $S_T/d = 3$	279

Nomenclature

A	area, [m ²]
A, a, B, b	coefficients in the algebraic equations
A_x, A_y, B_x, B_y	geometric parameters
A, B, E, F, X	block matrices
\tilde{b}	source term in PWIM equations
C	coefficient for interpolations of corner values
C_h	heat transfer coefficient, [W m ⁻² K ⁻¹]
C_m	mass transfer coefficient, [m s ⁻¹]
C_p	specific heat, [J kg ⁻¹ K ⁻¹]
D	diffusion coefficient of a transport equation
D^{AB}	binary diffusion coefficient, [m ² s ⁻¹]
\tilde{D}	diffusion coefficient of mass fraction terms in liquid energy equation, [W]
d	tube diameter, [m]
\tilde{d}	weight function in PWIM equations
ds	distance along \hat{s} vector for a single control volume, [m]
dt	distance along \hat{t} vector for a single control volume, [m]
$\frac{dP^*}{dx^*}$	pressure gradient ($2(\frac{dP}{dx})H / (\rho_G \bar{U}_{G,in}^2)$)
E	E-factor
f	interpolation coefficient
Fr_L	liquid Froude number ($\bar{U}_{L,in}^2 / (g_x \delta_{in})$)
g_x, g_y	gravitational acceleration in the x, y direction, [m s ⁻²]
H	channel or domain width, [m]
H_a	heat of absorption, [J kg ⁻¹]
h	overall heat transfer coefficient, [W m ⁻² K ⁻¹]
\bar{h}	partial mass enthalpy, [J kg ⁻¹]
h_L	interface height, [m]
h_v	water vapour enthalpy, [J kg ⁻¹]

Nomenclature

i	index in the x or χ direction
\hat{i}	normal unit vector in the x direction
i_B, i_E	first, last control volume indices in the x or χ direction
J	mass flow rate through a control volume north face, [kg s^{-1}]
J''	mass flux through a control volume north face, [$\text{kg m}^{-2} \text{s}^{-1}$]
Ja	liquid Jacob number ($C_{p,L}(T_{L,\text{in}} - T_{\text{wall}})/[H_a(\xi_{W,\text{in}} - \xi_{W(P,T_{\text{wall}})})]$)
j	index in the y or η direction
\hat{j}	normal unit vector in the y direction
j_B, j_E	first, last control volume indices in the y or η direction
j_{BL}, j_{EL}	first, last control volume indices in the liquid in the y direction
j_{BG}, j_{EG}	first, last control volume indices in the gas in the y direction
jL, jG	index in the y or η direction in the liquid, gas
K	curvature of the interface, [m^{-1}]
k	thermal conductivity, [$\text{W m}^{-1} \text{K}^{-1}$]
L	channel length, [m]
L_1	inlet to tube wall length, [m]
L_2	tube wall to outlet length, [m]
L_t	tube length, [m]
\dot{m}	mass flow rate, [kg s^{-1}]
\dot{m}'	mass flow rate per unit depth, [$\text{kg m}^{-1} \text{s}^{-1}$]
\dot{m}''	mass flux, [$\text{kg m}^{-2} \text{s}^{-1}$]
Nu	Nusselt number ($\dot{q}''_{\text{wall}} d/(k_L(T_{L,\text{in}} - T_{\text{wall}}))$)
N_x	number of nodes in the x direction
N_y	number of nodes in the y direction
n	normal direction
\hat{n}	normal unit vector: $n_x \hat{i} + n_y \hat{j}$
P	pressure, [N m^{-2}]

Nomenclature

P^*	non-dimensional pressure ($2(P - P_{in}) / (\rho_G \bar{U}_{G,in}^2)$)
Pr	liquid Prandtl number ($\nu_L \rho_L C_{p,L} / k_L$)
Q_{abs}	absorber heat flux, [$W m^{-2}$]
q''	heat flux, [$W m^{-2}$]
q''_{ref}	reference heat flux, [$W m^{-2}$] ($k_L(T_{L,in} - T_{wall}) / \delta_{in}$)
R	tube radius [m]
\mathcal{R}	algebraic equation residual
Re_G	gas Reynolds number ($\rho_G \bar{U}_{G,in} 2(H - \delta_{in}) / \mu_G$)
$Re_{G,d}$	gas Reynolds number for tube ($\rho_G \bar{U}_{G,in} d / \mu_G$)
$Re_{G,HW}$	gas Reynolds number ($\rho_G \bar{U}_{G,in} H / \mu_G$), Habib and Wood (1990)
Re_L	liquid Reynolds number ($4\rho_L \bar{U}_{L,in} \delta_{in} / \mu_L$)
$Re_{L,MC}$	liquid Reynolds number ($\rho_L \bar{U}_{L,in} \delta_{in} / \mu_L$), Min and Choi (1999)
r	distance from the tube centre, [m]
S	grid geometric expansion factor
s	west to east node-to-node and node-to-face direction
\hat{s}	west to east geometric grid unit vector: $s_x \hat{i} + s_y \hat{j}$
Sh	liquid Sherwood number ($C_m \delta / D_{intf}^{AB}$) or ($C_m R / D_{intf}^{AB}$)
Sc	liquid Schmidt number (ν_L / D_L^{AB})
S_L	tube centre-to-centre spacing in the x direction (longitudinal pitch), [m]
S_T	tube centre-to-centre spacing in the y direction (transverse pitch), [m]
T	temperature, [K]
t	time, [s]
t	south to north node-to-node and node-to-face direction
\hat{t}	south to north geometric grid unit vector: $t_x \hat{i} + t_y \hat{j}$
ΔT_{sub}	inlet temperature subcooling, [K]
U	velocity in the x direction, [$m s^{-1}$]
V	velocity in the y direction, [$m s^{-1}$]

Nomenclature

\vec{V}	velocity vector, [m s^{-1}], $U\hat{i} + V\hat{j}$
\vec{V}_t	tangential velocity, [m s^{-1}]
\forall	volume of a control volume, [m^3]
\mathcal{W}	geometric linear interpolation factor
x, y	Cartesian coordinate directions, [m]
\mathcal{X}, \mathcal{Y}	geometric parameter for calculation of gradient

Greek Letters

α	convective weighting coefficient
β	diffusive weighting coefficient
Γ	gradient value at the boundary
γ	geometric parameter
δ	film thickness, [m]
ϵ	steady state convergence criterion
η	transformed transverse coordinate
θ	tube central angle [rad]
Θ	dimensionless temperature $((T - T_{\text{wall}})/(T_{\text{in}} - T_{\text{wall}}))$
ξ	mass fraction in the liquid phase
ξ^*	non-dimensional mass fraction in the liquid phase
μ	dynamic viscosity, [$\text{kg m}^{-1} \text{s}^{-1}$]
ρ	density, [kg m^{-3}]
σ	surface tension, [N m^{-1}]
τ	stress tensor, [N m^{-2}]
Φ	general variable (referring to U, V, J, P, T , or ξ_w)
χ	transformed axial coordinate

Ψ a function of dependent variables

Subscripts

b referring to bulk value

air referring to air in the gas phase

bnd referring to domain boundary

BTDM referring to block-tridiagonal matrix

cw referring to cooling water

ea end of absorption

Eq referring to equilibrium

e, w, n, s referring to quantities at the east, west, north, south face of a control volume

E, W, N, S referring to quantities at the east, west, north, south nodal points

G referring to the gas

i west to east control volume index

iG referring to quantities at the gas interface

iL referring to quantities at the liquid interface

in at the inlet

intf at the interface

j south to north control volume index

L referring to the liquid

LiBr referring to lithium bromide in the solution

NB4 referring to E, W, N, S

NB8 referring to NB4 and NE, NW, SE, SW

ne, nw, se, sw referring to quantities at the northeast, northwest, southeast, southwest of a control volume

Nomenclature

NE, NW, SE, SW	referring to quantities at the northeast, northwest, southeast, southwest nodal points
NH_3	referring to ammonia
out	at the outlet
P	referring to the node
spec	referring to a specified value
W	referring to water in the solution
wall	at the wall
x_e	referring to the x component of a vector on the east face
x_n	referring to the x component of a vector on the north face
x_P	referring to the x component of a vector on the node
y_e	referring to the y component of a vector on the east face
y_n	referring to the y component of a vector on the north face
y_P	referring to the y component of a vector on the node
tot	total amount

Superscripts

c, u, v, t, ξ_W	referring to continuity, U , V , energy, and mass fraction equations
n	referring to the current iteration or time step
o	referring to the previous iteration or time step
ϕ	referring to a general transport parameter
\oplus	referring to the modifications
-	referring to an average value

Miscellaneous

BTDMA	block-tridiagonal matrix algorithm
ILMB	Integral Liquid Mass Balance
ip	integration point
PETSc	The Portable, Extensible Toolkit for Scientific Computation
PWIM	Pressure-Weighted Interpolation Method

Chapter 1

Introduction

1.1 Overview

Absorbers have a critical role in cost and performance of the absorption refrigeration cycles and the absorption heat pump systems. The absorption of water vapour by an absorbent, commonly a lithium bromide (LiBr) plus water solution, is found in many applications in different sectors of industry. Air conditioning and food preservation systems, water purification, and desalination are some of the areas where absorption phenomena play an important role. Due to the growing demand in many parts of the world for energy, absorption is getting greater attention to recover waste heat through use of solar energy. Intensive research has been done to improve the efficiency of the absorbers. Simultaneous heat and mass transfer in and between the vapour and liquid phases makes the two-phase phenomena such as condensation and absorption modelling a great challenge. The absorption process is complex due to the concurrent mass and heat transfer happening in absorbent-absorbate two-phase flow and the equilibrium relation at the vapour-liquid interface. Absorption is more complex than film condensation because the liquid phase is a binary mixture and the heat of absorption is a combination of the heat released because of the phase change and also the heat of dilution of absorbate into the absorbent. Also there is no analytical solution for absorption whereas the classic Nusselt solution has been developed for condensation. Numerical simulations provide the possibility of investigating the liquid and vapour interaction in the absorption.

In the open literature, most of the numerical models ignore the vapour phase and only simulate the liquid phase using simplified governing equations with assumptions. Developing a two-dimensional steady two-phase numerical model to compute the film hydrodynamics and precise interface heat, mass and momentum transfers along with tracking the phase interface are the goals of this research.

1.1.1 Absorption Refrigeration Cycles

In an absorption refrigeration cycle, heat is used as the driving energy to transfer heat from a low to a high pressure. In absorption refrigeration cycles much less energy is needed than the traditional vapour-compression refrigeration cycle. Heat sources like solar energy, geothermal heat, or any unused and waste heat could be used to produce heating and cooling when needed using an absorption cycle technology. The working fluids (absorbent/refrigerant) are commonly lithium bromide/water and water/ammonia.

Figure 1.1 shows a schematic of a single-effect absorption refrigeration cycle. In this cycle, the compressor of an equivalent vapour-compression cycle is replaced with the components surrounded by the blue dashed line in Figure 1.1.

In a single-effect absorption cycle the absorbent and the refrigerant are generated in a single step and this cycle is the simplest absorption cycle configuration. The solution, LiBr (aq), circulates between the low pressure absorber and the higher pressure generator. In the absorber, a strong solution (poor in refrigerant) absorbs the refrigerant vapour and becomes concentrated in refrigerant (Point 1). This solution leaving the absorber passes through the heat exchanger where it exchanges energy with the hot solution coming from the generator. At point 3, the solution enters the generator and, by receiving heat, some of the refrigerant leaves the generator as vapour (Point 6). This process makes the solution flowing back to the absorber stronger in absorbent (Point 4). In the refrigerant loop, the vapour refrigerant (water vapour) leaves the generator at a high temperature and rejects heat passing through the condenser (Points 6 to 7). The subcooled liquid refrigerant is directed to the evaporator after throttling through a valve and experiencing a pressure drop (Point 8). In the evaporator, refrigerant receives heat and transforms to vapour before entering the absorber (Point 9). In the absorber, the vapour is absorbed by the strong solution coming from the generator (Point 5).

The absorber has a critical impact on the performance, cost, and system size of an absorption refrigeration cycle. The hydrodynamics of the flow in an absorber could affect its performance to

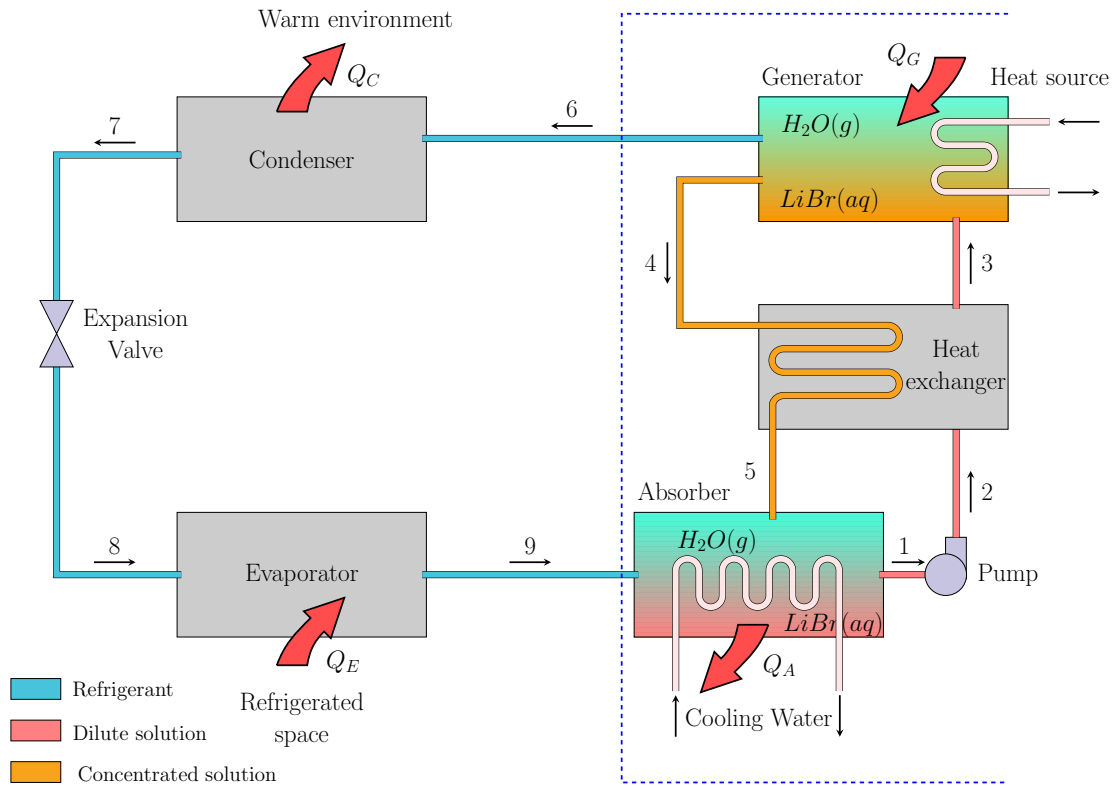


Figure 1.1: Absorption refrigeration cycle.

a great degree. In addition, the complex heat and mass transfer phenomena during absorption of vapour into the solution demands a full understanding of multi-component two-phase flow. Falling film absorbers received greater attention among other types of absorbers because of higher mass and heat transfer rates. The absorber performance could be improved if the liquid film is mixed and interfacial surface areas are increased.

Different geometries have been numerically modelled or experimentally investigated for absorbers. The common geometries are flow in a vertical channel, inside or outside a vertical tube or over horizontal tubes. Although, to the best knowledge of the author, the absorption in a vertical channel has not been measured experimentally, a number of analytical and numerical models of vertical falling film absorption inside a vertical channel have appeared in the literature. On the

other hand, absorption over horizontal tubes has been studied utilizing a variety of apparatuses and with a range of operating conditions. The difficulty of numerical modelling of two-phase flow over a tube geometry adds to the challenge of numerical modelling of the absorption phenomena.

1.1.2 Vapour-Liquid Interface Equilibrium

One of the major differences between vapour absorption and condensation is the equilibrium relation at the phase interface. In condensation, the equilibrium relation is between the vapour temperature and pressure, whereas in absorption, in addition to temperature and pressure, the mass fraction of the solution is also one of the factors contributing to the equilibrium condition. When vapour is absorbed into the liquid solution, the heat of absorption is released because of the vapour-liquid phase change and also dilution of water vapour into the liquid solution. The absorption heat is dependent on the interfacial absorbed mass and the mass fraction of solution components are related to the interface temperature. Both mass and heat transfer at the interface control the liquid-vapour interface temperature and mass fraction.

Based on experimental data, correlation equilibrium relations for aqueous LiBr solution are presented by McNeely [1], Uemura and Hasaba [2], and Siebe [3]. These equilibrium functions are given in the Appendix A.

Applying a different equilibrium relation at the liquid-gas interface has a great impact on the numerical model results, because the temperature, mass fraction, and pressure are closely connected through this relation. Figure 1.2 shows the diagrams for the equilibrium relations presented by McNeely [1] and Uemura and Hasaba [2]. These type of plots originally presented by Duhring are called a Duhring diagram [4].

Each line in the diagram represents a constant pressure starting from $P = 1$ kPa to $P = 196$ kPa from bottom to the top, respectively. At lower pressures, there is a slight difference between the equilibrium temperatures. This small difference could have a noticeable effect on the numerical results due to the fact that temperature and mass fraction changes at the interface are usually small.

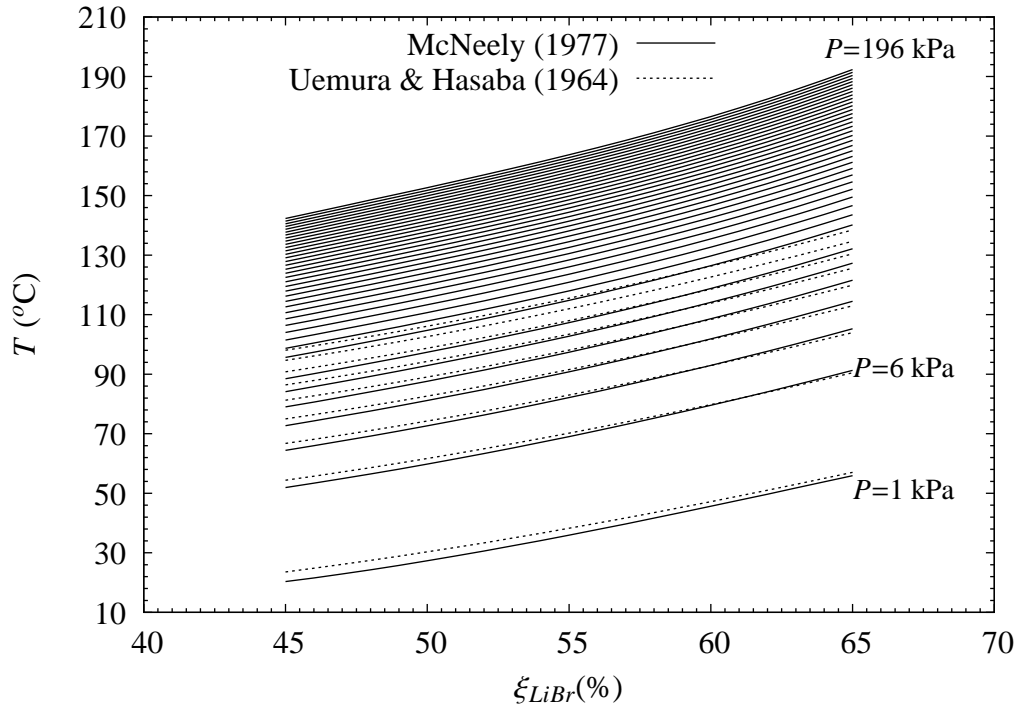


Figure 1.2: Dühring diagram for LiBr-water solution.

1.2 Problem Statement

The objective of this research is to develop detailed numerical models, parabolic and elliptic, to study the absorption of pure water vapour into an aqueous LiBr solution flowing inside a vertical channel or over a horizontal tube.

1.2.1 Vertical Plate Geometry

In absorption over vertical plates or inside vertical channels, a thin solution film consisting of two components flows down on a cold wall. When the refrigerant vapour comes in contact with the liquid film, as shown in Figure 1.3, the mass fraction difference of the refrigerant in the vapour and

in the liquid film causes the absorption of the refrigerant at the liquid-gas interface. The vapour refrigerant may be at lower temperature than the liquid film and the wall and also at a superheated state. The temperature differences between the cold wall, the liquid film and the vapour plus the release of the heat of absorption at the interface combine to cause temperature gradients between the liquid and gas phases and between the wall and the interface.

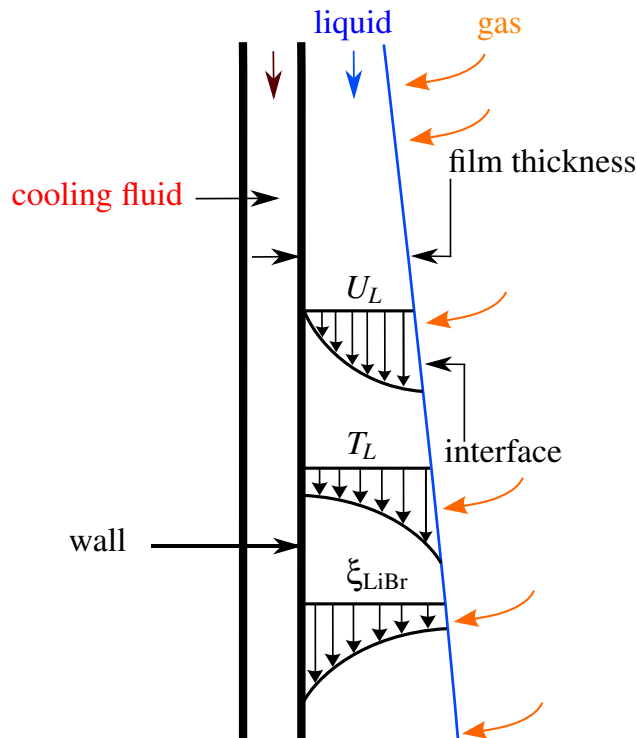


Figure 1.3: Schematic diagram of LiBr-water absorption over a cold wall.

While the energy is being transferred to the cold wall, the temperature changes in the liquid film and the gas phase. The mass fraction of species in the liquid film also changes. The addition of mass of refrigerant to the liquid causes the liquid film to grow along the plate. A solution that is richer in refrigerant leaves the cold plate at the end of the absorption process.

1.2.2 Horizontal Tube Geometry

Absorption over internally cooled horizontal pipes is widely used in absorption heat pumps and chillers. Figure 1.4 shows a schematic diagram of a LiBr-water liquid film around a tube. In practice, the tubes are usually located on top of each other in an aligned tube bank arrangement.

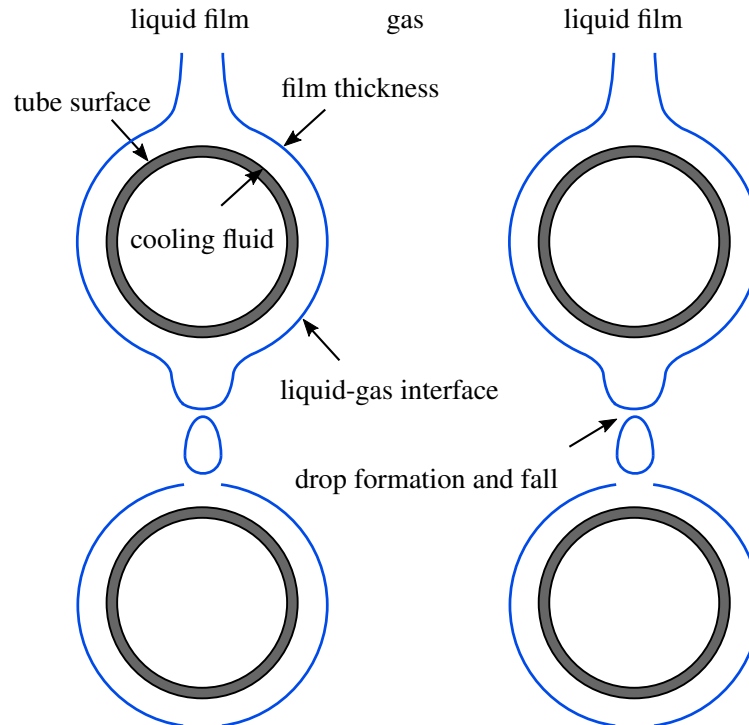


Figure 1.4: Schematic diagram of LiBr-water absorption over horizontal tubes.

Although falling film absorption over horizontal tubes has been used for decades in many applications, the detailed features of these systems that may be used for design purposes have not been fully understood. In horizontal tube absorbers, the solution is sprayed over the tubes from the top of the absorber and the refrigerant vapour flows into the absorber. The liquid film with an initial thickness, flows over the tube under the effect of the gravity while the cooling fluid flows inside the tube. The absorption principles are similar to the case of vertical plate. In the case of horizontal tube, however, the liquid film thickness experiences thinning and thickening due the curvature of the geometry, the gravity effect, and the refrigerant vapour flow effect. Film thickness

tracking of the mesh generated around the tube is one of the challenges in numerical modelling of this phenomena around the tube. The geometry of the tube, the shape of the liquid film around the tube especially on the top and bottom of the tube, the tube surface wetting, and droplet formation between the tubes all add to the complexity of absorption phenomena over tubes.

1.3 Literature Review

The complex nature of absorption phenomena has been studied analytically, numerically, and experimentally by researchers. Absorption is a physical process in which a substance is absorbed and distributed into another substance. The substance being absorbed is referred to as the absorbate. The substance with the ability of absorbing the absorbate is known as the absorbent. Water-lithium bromide (nonvolatile) and ammonia-water (volatile) are the most widely used absorbate-absorbent pairs in industrial absorbers. Significant efforts have been made to model the coupled heat and mass transfer in laminar ($Re_L < 20$), wavy ($20 < Re_L < 200$), and turbulent ($Re_L > 200$) film flows [5]. The most common geometries of interest in the absorbers are falling liquid films in a vertical channel or tube and over the outside of horizontal tubes. In this review, the previous studies of falling film absorption are categorized into the three main groups of analytical, numerical, and experimental studies. Following that the literature focused on numerical modelling of absorption over vertical plates, inside vertical channels, and over horizontal tubes is summarized. Additionally, some experimental works in the area of absorption over horizontal tubes are presented.

1.3.1 Analytical Solutions

1.3.1.1 Vertical Channel Geometry

Laminar falling film absorption on an isothermal vertical plate was modelled analytically by Nakoryakov and Grigor'eva [6]. The streamwise film velocity and film thickness were assumed to be

constant. Diffusion and advection terms in the streamwise direction were neglected and a linear temperature profile was obtained for the film. A linear equilibrium relation between the temperature and mass fraction was applied at the interface. They concluded that the solution to absorption problem was dependent on the boundary and inlet conditions as well as Lewis, Prandtl, and Reynolds numbers and a non-dimensional number which related the specific heat of solution and the heat of absorption. In a similar paper published in the same year, Grigor'eva and Nakoryakov solved the governing equations with the same simplification as their previous paper using Fourier series [7].

In 1983, Grossman [8] used a series expansion (near the inlet of the channel) and similarity solution method to simulate falling film absorption over an isothermal or adiabatic wall. Grossman solved simplified governing equations for the liquid phase only with a constant absorption heat. In his model, linear mass fraction and temperature relations were applied at the interface. In a similar conclusion to Nakoryakov and Grigor'eva [6], Grossman stated that the variation of temperature and mass fractions of components depended on Lewis number and non-dimensional heat of absorption. Table 1.1 presents a summary of analytical solutions of falling film absorption on a wall. In these studies, constant film thickness and a linear equilibrium condition were used and the interfacial shear and the y -direction convection and mass diffusion in the energy equations were neglected. No values were provided for $Re_{L,in}$, $T_{L,in}$, and $\xi_{LiBr,in}$.

1.3.1.2 Horizontal Tube Geometry

Conlisk and Mao [9] presented an analytical solution for absorption of a two-component gas to a liquid film of NH_3 -water on a horizontal tube. The authors emphasized the dependence of the absorption on the characteristics of the vapour phase. The tube was assumed to be fully wetted by the film. The liquid film was studied before droplet formation and separation from the bulk liquid film because of gravity. Due to the small thickness of the film in comparison to the tube radius, the curvature terms were neglected in the Navier-Stokes equations and the momentum equation was

Table 1.1: Summary of single phase analytical studies of laminar LiBr-water falling film on a flat plate.

Author(s)	Year	Geometry	Phase(s) Modelled	Solution Method	Ha	$U_{L,in}$	Quantities Studied
Nakoryakov and Grigor'eva [6]	1977	Vertical plate	Liquid	Similarity solution	Constant	Uniform	$T_L(y), \xi_{LiBr}(y)$
Grigor'eva and Nakoryakov [7]	1977	Vertical plate	Liquid	Expansion series	Constant	Uniform	$T_{intf}, \xi_{LiBr,intf},$ $\dot{m}''_{intf}, q''_{intf}$
Grossman [8]	1983	Inclined plane	Liquid	Fourier series	Calculated	Nusselt	Dimensionless $T_{intf}, \xi_{LiBr,intf},$ $T_{wall}, T_L(y),$ $\xi_{LiBr}(y), \dot{m}''_{intf},$ Sh, Nu

simplified to the Nusselt velocity profile. They obtained an equation for the film thickness variation as a function of film position at circumference of the tube. A linear temperature distribution was assumed on the top of the tube and the continuity of the flux of species was applied at the interface. The mass fraction and temperature equations were solved analytically employing a Fourier cosine transform. The heat and mass coefficients as functions of position and temperature were derived and evaluated. The analytical results suggested that the absorption is more rapid on the top of the tube where the film is thinning compared to the bottom of the tube. The operating conditions and the quantities studied by Conlisk and Mao [9] are summarized in Table 1.2. In this study, properties were assumed to be constant. The shear stress at the interface was neglected and a linear equilibrium condition was applied at the interface.

1.3.1.3 Summary of Analytical Model Literature

Although the analytical solutions are less expensive than numerical methods in modelling of absorption phenomena because of the simplifications applied to the governing equations, they do not couple the hydrodynamics of the film and the co-current heat and mass transfer in the absorption. The analytical solutions of absorption over a vertical wall or horizontal tube summarized in this section are based on many simplifications such as: applying Nusselt liquid film velocity profile instead of solving the continuity and momentum equations, neglecting the energy transfer due to the mass diffusion and dilution heat of solution species (mixture nature of the film) and neglecting the spanwise convection term in mass fraction equation. The impermeability of LiBr at the interface was not satisfied at the interface and the equilibrium condition was simplified to a linear equation in some cases. The dependences of the heat of absorption and the solution properties on the temperature and mass fraction of the solution mixture were ignored. Finally, these analytical solutions were associated with modelling the liquid film only and the vapour phase effects were neglected.

Table 1.2: Summary of single phase analytical study of laminar NH_3 -water falling film on a horizontal tube by Conlisk and Mao [9].

Author	Year	Geometry	Phase(s) Modelled	Solution Method	$\text{Re}_{L,\text{in}}$ –	$T_{L,\text{in}}$ [°C]	$\xi_{\text{NH}_3,\text{L},\text{in}}$ –	$T_{G,\text{in}}$ [°C]	$\xi_{\text{NH}_3,\text{G},\text{in}}$ –	P [kPa]	Quantities Studied
Conlisk and Mao [9]	1996	Horizontal tube	Liquid	Fourier cosine transform	7.599	66.85	0.065	181.85	0.998	475.7	\dot{m}''_{intf} , $\xi_{\text{NH}_3,\text{intf}}$, \bar{T}_L , $\bar{\xi}_{\text{NH}_3,\text{L}}$, $\bar{T}_{L,\text{out}}$, C_m

1.3.2 Numerical Approaches

Generally, numerical approaches in absorption simulation fall into two major categories: single-phase flow and two-phase flow modelling. In the former, only the liquid film is modelled and an unlimited supply of vapour mass is available to migrate toward the liquid film. In the latter category, momentum and heat transfer in the vapour are also included in the simulation. Some of the previous works in this category also investigated non-absorbable gas effects on the heat and mass transfer rates in the absorption.

Due to the complicated physics of absorption and strong coupling of transport equations there have been a number of simplifying assumptions in most of the numerical studies to create workable mathematical models. The first part of this section is a review of numerical methods presented in the literature for falling film absorption over vertical plates and inside vertical channels. In the second part, the numerical studies of solution flow over horizontal tube absorbers are described.

1.3.2.1 Vertical Channel Geometry

Grossman [8] developed a numerical model to solve the simplified energy and mass fraction equations (streamwise advection and spanwise diffusion terms only) for a LiBr-water falling film over a constant-temperature or adiabatic inclined wall. A fully developed parabolic velocity profile was used throughout the liquid film. He assumed a linear equilibrium condition and a constant heat of absorption at the vapour-liquid interface. Using a method of lines or semi-discretization method in a finite difference form, results of interfacial and cross-sectional non-dimensional temperature and concentration were produced.

Applying the same numerical method as Grossman [8], Andberg and Vliet [10] investigated a LiBr-water solution flowing downward on a vertical surface. Although they used Grossman's assumption to replace continuity and momentum equations with a fully developed velocity profile in the flow direction, the interdiffusion term was not neglected in the energy equation. To maintain

a structured grid domain while film thickness grows, a coordinate transformation was done and the model results were transferred to the real geometry. Downstream and cross-stream concentration and temperature variations plus local heat and mass fluxes were plotted and compared with experimental data.

The article by Kawae et al. [11] has been a validation reference for several numerical researches in the area of LiBr liquid film absorption. A great similarity can be observed between this article and that of Andberg and Vliet [10] in terms of the case study, numerical method, and assumptions. Some of the similarities are: a fully developed axial velocity profile, a non-linear equilibrium condition and no shear at the interface, and effect of the change in energy due to mass diffusion. The main difference between Kawae et al. [11] and Andberg and Vliet [10] is that Kawae et al. [11] applied both constant and variable thermophysical properties and investigated the operating parameters effects on heat and mass fluxes. The effect of the change in the absorber pressure, the wall temperature, and the inlet LiBr film thickness and LiBr concentration were also discussed in [11]. The authors pointed out the optimal absorption rate occurs at a certain distance from the inlet for a specific film thickness.

Recently, Mittermaier and colleagues [12–15] published a series of articles on simulation of absorption and desorption processes on a vertical isothermal plate. Mittermaier et al. [12] used constant uniform streamwise velocity to simplify the model and facilitate the investigation of hydrodynamic and thermodynamic effects and a comparison with analytical solutions. The differential heat of solution has been included in the energy equation to account for the mixture nature of the liquid solution and the enthalpy change due to diffusion of species. Therefore, the partial mass enthalpies of components were expressed in terms of the mixture enthalpy and the gradient of the components' concentrations. An iterative parabolic solution approach was used to update the variable properties and to obtain temperature and concentration profiles within the LiBr solution. It was concluded that under similar conditions, the mass transfer during absorption is noticeably higher than desorption and non-constant properties and differential heat of solution change the results slightly.

Mittermaier and Ziegler [13] presented a subsequent extension paper to the previous research [12] to perform a more comprehensive simulation of simultaneous heat and mass transfer. In this work, the continuity and longitudinal momentum equation were solved along with the mass fraction and energy equations (with advection terms of partial enthalpies for both coordinates). The film thickness and physical properties were allowed to change as water was absorbed or desorbed. The film thickness, mass flux, velocity, and mass fraction profiles for absorption and desorption were plotted and compared.

Mittermaier and Ziegler [14] investigated the impact of inlet velocity profiles on mass fraction and temperature profile across the liquid film as well as the absorbed mass flux. They noted when the solution flows in with a uniform velocity instead of a fully developed profile, absorption starts in a shorter distance from the inlet.

Mittermaier and Ziegler [15] used their previous single-phase model to investigate the interactive influence of hydrodynamics of an aqueous LiBr laminar film and mass transfer during absorption phenomena. They considered cases of fully developed or uniform velocity at the inlet with constant or variable thermophysical properties. Their results showed an increase of 9.3% in the absorbed mass over a length of 0.03 m in the uniform inlet velocity case compared to the fully developed inlet velocity case. It was also reported that the absorbed mass in the case of uniform inlet velocity was increased by 50% due to 3 K subcooling at the inlet. Mittermaier and Ziegler [15] increased the viscosity to a value five times larger than that of the LiBr solution and observed a decrease in the overall mass and heat transfer rates.

The commercial code Fluent was used by Zhang et al. [16] to simulate the absorption of water vapour into a LiBr solution. The density and specific heat of the solution were assumed to be constant whereas the thermal conductivity and viscosity were allowed to change with the temperature and concentration of the liquid. A finite control volume technique and the PISO method were used to discretise and solve the fully elliptic governing equations in the film only. At the entrance, the film velocity profile was assumed to be fully developed and at the outlet, an outflow boundary

condition was applied. The liquid film Reynolds number in the range of 10.6 to 150 was studied. They found that as the Reynolds number of the film increases, the maximum mass transfer flux along the plate decreases. They also observed that the heat transfer coefficient reduces along the falling film while the mass transfer coefficient shows the opposite behaviour.

Armou et al. [17] solved the parabolic governing equations of absorption using an in-house code of finite volume approach. They modelled the LiBr-water liquid film only by solving continuity, momentum, energy, and mass fraction governing equations and drew the same conclusion as presented in [16] about the Reynolds number and the mass flux relation. They also noted that an increase in the inlet pressure raises the the interfacial temperature and mass flux.

All the previous research, reviewed in this section focused on numerical simulation of absorption as a single phase phenomenon and neglected the gas phase interaction with the absorbent. To the best knowledge of the author, only three articles were concerned with modelling absorption as a two-phase process in a vertical plate geometry. Habib and Wood [18] presented an elliptic numerical solution for modelling the laminar LiBr-water film and vapour flowing co-currently inside a vertical channel. Comprehensive governing equations for both phases were used except that energy transfer due to mass diffusion in the solution was neglected and the film thickness was assumed to be constant. They enforced continuity of energy and absorbate mass and shear force at the interface. Distribution of the temperature in both phases and the concentration profile in the liquid film were plotted at various locations down the channel. The authors noted that the absorption rate increases with increasing the vapour pressure and inlet mass concentration of the solution but decreases with increasing the absorber wall temperature. It was emphasized that the vapour temperature cannot be neglected as other researchers had assumed. There was, however, no evidence provided on vapour temperature influence on the absorption rate.

In another two-phase analysis by Habib and Wood [19], the effect of a non-absorbable gas on the heat and mass transfer in absorption of vapour into LiBr-water solution was investigated. All of the assumptions were identical to their earlier research [18]. Because of the presence of air along

with water vapour in the gas phase, a diffusion equation was added to the governing equations and an air impermeability condition was imposed at the interface. The effect of non-absorbable gas on temperature and concentration in the liquid film was discussed. They identified a significant reduction in the local mass flux at the interface when air concentration increases.

The inert gas impact on absorption was the subject of a study by Chen and Vliet [20]. The numerical model developed includes more simplifications than those of Habib and Wood [19]. For instance, fully developed velocity profiles were used for the LiBr-water liquid film and gas phase. In addition to dependent variable profiles in the solution film, they presented temperature, velocity, and non-absorbable gas concentration in the gas phase. The interactions between the pressure, the wall temperature, the inlet solution concentration, and the inlet air concentration were studied.

Relevant numerical studies of absorption in a vertical channel and their assumptions are summarized in Table 1.3. The operating conditions and the quantities studied in the numerical methods reviewed here are presented in Table 1.4.

1.3.2.2 Horizontal Tube Geometry

In 1986 Andberg [21] extended their previous numerical model [10] to LiBr-water falling film absorption over horizontal tube bundles. Boundary layer approximations were used to simplify continuity, momentum, energy, and mass fraction equations to solve the problem for top and interior tubes in an absorber. Due to the complex geometry, body fitted coordinates were used. The author pointed out that dilution of water into the liquid film is not infinite and a proper boundary condition must be used for the diffusion of water through the liquid interface. The heat of absorption was given as a function of the solution temperature and concentration. Numerical results for liquid velocity, temperature, and concentration profiles, as well as heat and mass fluxes were presented. The results were in acceptable agreement with experimental results.

One of the first numerical models for LiBr-water absorption over a single cooled horizontal tube was developed by Andberg and Vliet [22]. The liquid film came in contact with the tube surface

Table 1.3: Summary of numerical studies of laminar LiBr-water solution over a vertical plate.

Author(s)	Year	Phase(s) ^a Modelled	Equations ^b Solution Method	Film ^c Velocity Equation	Film ^d Energy Equation	Film ^e Thickness	Properties	Equilibrium ^f Condition	Interfacial ^g Shear
Grossman [8]	1983	L	P	N	ST	C	C	L	N
Andberg and Vliet [10]	1983	L	P	N	IT	V	C	NL	N
Kawae et al. [11]	1989	L	P	N	IT	C	V	NL	N
Habib and Wood [18]	1990	L+G	E	S	ST	C	V	NL	A
Chen and Vliet [20]	1997	L+G	P	N	ST	C	–	NL	N
Habib and Wood [19]	2000	L+G	E	S	ST	C	V	NL	A
Mittermaier et al. [12]	2014	L	P	C	ID+PE	C	V	NL	N
Mittermaier and Ziegler [13]	2015	L	P	S	ID+PE	V	V	NL	N
Zhang et al. [16]	2015	L	E	S	IT	C	–	NL	N
Mittermaier and Ziegler [14]	2016	L	P	S	ST	V	C	NL	N
Armou et al. [17]	2016	L	P	S	IT	V	C	NL	N

^a L: Liquid; G: Gas ^b P: Parabolic; E: Elliptic ^c N: Nusselt; S: Solved numerically; C: Constant across the film

^d ST: Simplified terms; IT: Interdiffusion terms; PE: Partial enthalpies ^e C: Constant; V: variable ^f L: Linear; NL: Non-linear

^g N: Neglected; A: Applied

Table 1.4: Operating parameters and physical properties in numerical studies of laminar LiBr-water solution over a vertical plate.

Author(s)	Year	$Re_{L,in}$	T_{wall} [°C]	$T_{L,in}$ [°C]	$\xi_{LiBr,in}$	P [kPa]	δ_{in} [mm]	H_a [J kg ⁻¹]	Quantities Studied
Grossman [8]	1983	–	–	–	–	–	–	$(h_v - \bar{h}_W)_{intf}$	$T_{intf}, \xi_{LiBr,intf}, T_{wall}, T_L(y), \xi_{LiBr}(y), \dot{m}''_{intf}, Sh, Nu$
Andberg and Vliet [10]	1983	10	35	44.44	0.6	0.9348	0.1719	2.6605×10^6	$T_{intf}, \xi_{LiBr,intf}, T_L(y), \xi_{LiBr}(y), \dot{m}''_{intf}, q''_{intf}$
Kawae et al. [11]	1989	10.6	35	46.50	0.6	1.0	0.2	2.7727×10^6	$T_{intf}, \xi_{LiBr,intf}, T_L(y), \xi_{LiBr}(y), \dot{m}''_{intf}, q''_{intf}$
Habib and Wood [18]	1990	30	35	44	0.6	0.9359	–	–	$T_{intf}, \xi_{LiBr,intf}, T_L(y), \xi_{LiBr}(y), \dot{m}''_{intf}, q''_{intf}$
Chen and Vliet [20]	1997	–	35	45	0.6	0.9332	0.25	–	$T_{intf}, \xi_{W,intf}, T_G(y), U_G(y), \dot{m}''_{intf}, \xi_{air}(y)$
Habib and Wood [19]	2000	30	35	44	0.6	0.9359	–	–	$T_L(y), \xi_{LiBr}(y), \dot{m}''_{intf}, \xi_{air}(y)$
Mittermaier et al. [12]	2014	36	27	39.25	0.53	1.5	–	$(h_v - \bar{h}_W)_{intf}$	$T_{intf}, \xi_{W,intf}, H_a, \dot{m}''_{intf}$
Mittermaier and Ziegler [13]	2015	52.174	29.09	35.08	0.5	1.5	0.2359	$(h_v - \bar{h}_W)_{intf}$	$\delta, \xi_W(y), U_L(y), \dot{m}''_{intf}$
Zhang et al. [16]	2015	10.6 to 150	35	46.5	0.6012	1.0	0.2 to 0.48	–	$T_{intf}, \xi_{W,intf}, \dot{m}''_{intf}, q''_{intf}$
Mittermaier and Ziegler [14]	2016	40.57	30.09	39.09	0.5	1.50	0.216	2.5570×10^6	$T_L(y), \xi_W(y), U_{intf}, \dot{m}''_{intf}$
Armou et al. [17]	2016	10 to 100	32 to 36	45	0.58 to 0.62	0.5 to 1.0	–	–	$T_{intf}, \xi_{LiBr,intf}, T_L(y), \xi_{LiBr}(y), \dot{m}''_{intf}$

as a planar jet with entrance conditions of uniform velocity, temperature and mass concentration. They simplified the streamwise momentum equation to use a Nusselt solution with change of gravity angle as the calculation progresses along the tube surface and used a continuity equation to obtain an equation for the spanwise velocity. It was pointed out that the spanwise velocity equation does not fulfill the continuity equation for larger film thickness. The parabolic energy equation was solved numerically using a finite difference method with upwinding in a Crank-Nicholson method and mass fraction was obtained by a similarity solution. For the similarity solution, the problem of a double root was reported by the authors. The model presented in [22] is a simplified version of a more complete model presented in the Ph.D. thesis of Andberg [21] and the assumptions are made based on the observation of the more complete model results. The outlet temperature and mass fraction at the bottom of the tube were compared to the results of [21]. It was reported that this simplified model is in a reasonable agreement with the Ph.D. thesis. In [21] it was concluded that the numerical results of the simplified model were in quite good agreement with experimental data, with an average error of 7.5%.

Choudhury et al. [23] used boundary layer assumptions to obtain parabolic governing equations for the absorption of water vapour into LiBr-water liquid film. Velocity equations are similar to those used by Andberg and Vliet [22] except that the rate of the film thickness change was considered in the spanwise velocity equation. The liquid film flow over the tube with uniform inlet temperature and mass fraction and parabolic form of energy and mass conservation equations was used to obtain the film temperature and LiBr mass fraction over the tube. A coordinate transformation was performed to map the film thickness variation to the domain mesh. A finite difference marching scheme was applied to each section of the nodes at a particular angle starting from the flow entrance. Once the film thickness, velocities, temperature and mass fraction were calculated for a given section, the numerical solution was moved to the next section. It was concluded that when the flow rate is higher, using larger tube diameters results in an improvement in the heat transfer coefficient.

Min and Choi [24] applied the SIMPLER algorithm to fully elliptic equations of momentum,

temperature, and concentration to model the free-falling film of LiBr solution over a single isothermal tube. The liquid film properties were assumed to be constant. Surface-tension effects were taken into account and a linear equilibrium condition was applied at the free surface (liquid-gas interface). The numerical solution was accomplished in two steps: First, continuity and momentum equations were solved on an orthogonal grid over both phases to determine the free surface location using the MAC method. Second, the energy and concentration equations were solved in the liquid phase only by using a non-orthogonal grid matching the free surface obtained in the first step. Examination of the surface tension effects for Reynolds number of 16.7 and 166.7 showed that at lower Reynolds number, the numerical model without surface tension was unable to predict the recirculation region close to upper stagnation point of the tube and resulted in a very thin film whereas it had negligible effect at a higher Reynolds number. It was noted that considering surface tension alters the mass transfer characteristics and mass absorption rate, especially at lower flow rates.

Francés and Ojer [25] used a mathematical approach to model the LiBr-water falling film absorption in an absorber consisting 14 horizontal tubes. They applied their experimental test factor values to the mathematical method. In the mathematical model, the fully developed Nusselt velocity solution was assumed and the vapour effect on the liquid film was neglected. Based on the assumption of complete mixing between the tubes, the inlet solution temperature and concentration of each tube were considered to be uniform. The wetting of the tubes was taken into account in the mathematical model. The model predicted the heat load and heat transfer coefficient accurately, but it did not perform well in the prediction of mass transfer. It was noted that the resistance at the vapour phase produced by non-absorbable gases and coupling terms at the interface should be considered in numerical simulations to make the mass transfer more accurate.

Killion and Garimella [26] presented a numerical method to investigate droplet formation and impact over horizontal tubes. The CFD package, Fluent, was used to model a LiBr film in contact with air. A Volume of Fluid (VOF) method was used to track the free surface between the liquid film and air. The “continuum surface force” (CSF) approach was used to model the surface ten-

sion. A modified continuity equation (including the volume fraction of gas phase) and momentum equations for the liquid film were solved using the PISO method in a segregated manner. They presented flow visualization results to illustrate the flow pattern and droplet formation.

Babadi and Farhanieh [27] performed a numerical study of the heat and mass transfer phenomenon in the lithium bromide-water absorption process over a horizontal tube. Their methodology followed the same assumptions as in Choudhury et al. [23] and used the same set of governing equations and grid mapping. They performed the numerical solution for a realistic operating condition of an absorber. They assumed the pressure of the absorber to be 1 kPa which is the pressure of a steam-heated single effect absorber chiller. The Reynolds, Prandtl, and Schmidt numbers were used to obtain the heat and mass transfer coefficients. The numerical results were compared to the experimental results provided in Andberg and Vliet [22]. Using the numerical data of their research, they proposed two correlations for estimating the average heat and mass transfer coefficients of the transport phenomena over the tube based on the Schmidt and Reynolds numbers.

The heat and mass transfer in a LiBr liquid film over a single cooled horizontal tube was analyzed by Papaefthimiou et al. [28] using a simplified description of the absorption phenomena. Nusselt's equations were used for determining the film thickness and stream-wise velocity. A coordinate transformation was applied to solve the two-dimensional simplified parabolic temperature and mass conservation equations using a finite element collocation method. In their single-phase model, the heat transfer to the gas phase and the interfacial shear force were neglected. Special attention was paid to calculation of superheated vapour enthalpy and variable heat of absorption. Solution outlet and inlet temperatures were compared to experimental results of Seol and Lee [29]. The effects of the solution mass flow rate, the coolant temperature, and the tube geometry on the heat and mass transfer during absorption were also investigated.

Kyung et al. [30] employed an absorption model for a horizontal tube with a liquid film divided into three regimes: falling film, drop formation, and falling drops. They stated that when a drop is forming beneath the tube, an adiabatic process causes a temperature increase and a mass fraction

decrease in the LiBr solution. The transformed mass fraction and energy equations were solved using a finite difference method in a marching scheme for the falling film regime. Streamwise and transverse velocities were obtained by a Nusselt solution and a continuity equation, respectively. The authors adapted the model developed by Kirby and Perez-Blanco [31] for drop formation and drop falling regimes. They concluded that when the film is flowing on top of the tube, where the temperature of the wall has not affected the film, the temperature profile is very nonlinear. The authors also highlighted that the interface temperature and mass fraction of LiBr decrease as the liquid film passes over the tube. The liquid film inlet subcooling with respect to equilibrium temperature at the inlet mass fraction was also studied as an important factor of mass absorption in absorbers consisting of a bundle of tubes.

Kyung et al. [32] verified the results of their previous numerical method [30] with the experimental data of Kyung and Herold [33] on a bundle of tubes. The shear stress at the vapour-solution interface and heat transfer to the gas phase were neglected and horizontal tubes were assumed to be completely wetted. Their two-dimensional numerical analysis showed that the absorber performance is highly dependent on the mass diffusivity coefficient. Due to lack of experimental data on mass diffusivity of LiBr solution, they estimated the value of $10^{-10} \text{ m}^2/\text{s}$ for a solution of 57-60% LiBr and observed a result closer to the experimental measurements. Increasing the number of tubes in their numerical study, increased the absorber heat rate while decreasing the heat transfer coefficient.

Papaefthimiou et al. [34] applied their previous numerical approach, presented in Papaefthimiou et al. [28], on a bundle of tubes. They described the thermophysical properties of superheated water vapour in detail. The absorption cooling load was compared to experimental measurements by Nomura et al. [35] for an array of 13 horizontal pipes. Their study showed that decreases in the LiBr concentration and the solution temperature were more significant at lower mass flow rates of the solution, when the number of the tubes was increased. They also concluded that at higher values of solution mass flow rates per tube length, the average solution mass flux was not affected by the number of tubes if it was higher than the average mass flux of one third of the total number

of tubes.

Neglecting the temperature and mass fraction in a LiBr-water liquid film, Ji et al. [36] studied the solution sprinkle density (mass flow rate) and tube surface wettability effects on the film distribution over a hydrophilic horizontal tube. They solved continuity and momentum equations along with an interface transport equation (using the level set method) to capture the vapour-liquid interface. It was stated that dry spots on the tube were produced because of shrinkage and breakage of the liquid film if the mass flow rate was small. They also suggested a modified Nusselt film thickness equation considering the asymmetric distribution of the film thickness over the tubes.

A summary of the numerical studies of laminar falling film for LiBr solution on horizontal tubes is presented in Table 1.5. Table 1.6 presents the corresponding operating conditions.

1.3.2.3 Summary of Numerical Model Literature

To the best knowledge of the author, only three articles in vertical parallel plate channel, [18–20], and one article in horizontal tube case, [24], were concerned with the two phase modelling of the absorption phenomena. All the other researchers limited their numerical models to the liquid film only and neglected the gas and the liquid interactions. Between the two-phase numerical models in vertical channel case, the models in [18] and [19] may be considered to be the most complete because of solving the elliptic governing equations. However, in the model proposed by Habib and Wood [18, 19] the non-ideal mixture nature of the LiBr-water solution was not taken into account, the film thickness growth was neglected, and the impermeability of LiBr at the interface was not satisfied correctly. The authors also did not study the gas phase impact on the absorption. In the horizontal tube case, although Min and Choi [24] introduced their numerical model as a two-phase model, the energy and mass fraction equations were considered for the liquid film only and the mass transfer relation with the film thickness was ignored. The majority of the single-phase models used parabolic form of temperature and mass fraction equations ignoring the energy transfer because of mass diffusion and also the heat of dilution. A Nusselt velocity profile was

used by many of the studies to decouple the numerical solution of velocity from other field variables. These models were more simplified assuming a constant film thickness, constant heat of absorption, a linear equilibrium condition between the mass fraction and temperature (neglecting the pressure effect), and also neglecting the shear stress at the liquid-gas interface.

1.3.3 Experimental Studies

1.3.3.1 Horizontal Tubes

The characteristics of LiBr-water or NH₃-water falling film on a horizontal single tube or a column of horizontal tubes were measured under a variety of different operating conditions and arrangements. The experimental studies using the nonvolatile LiBr-water solution and volatile NH₃-water solution are summarized in Tables 1.7 and 1.8, respectively.

Consenza and Vliet [37] experimentally investigated LiBr-water falling film absorption over smooth horizontal tubes. A single column of tubes being cooled internally was used as the absorber assembly. The absorption heat transfer was correlated in terms of Nusselt and Reynolds numbers. Additionally, the effect of tube diameter on Nusselt number was investigated and a linear relation between the absorption rate and the heat of absorption was presented.

Nomura et al. [35] measured the solution temperature over and between the tubes and the absorber cooling capacity at different mass flow rates of LiBr solution using an absorber device having the same construction as that of existing absorption refrigerators. The absorber glass windows facilitated the observation of solution's behaviour and wetting condition of the tubes. Their experiment revealed that 1°C increase in temperature of water vapour causes about 5 to 8% increase in refrigerating capacity. Nomura et al. [35] noticed a significant solution temperature increase (2°C) between the tubes. They concluded that because no external heat existed, the temperature increase is the result of water vapour absorption into the solution while dropping from one tube to the next tube.

Table 1.5: Summary of numerical studies of laminar LiBr-water falling film over horizontal tubes.

Authors	Year	Geom. ^a	Phase(s) ^b Modelled	Solution Method	Film ^c Velocity Equation	Film ^d Energy Equation	Properties ^e	Equilibrium ^f Condition
Andberg and Vliet [22]	1987	HT	L	Marching Scheme (FDM)	N	NMD	C	NL
Choudhury et al. [23]	1993	HT	L	Marching Scheme (FDM)	N	NMD	C	NL
Min and Choi [24]	1999	HT	L+G/G	Staggered SIMPLER	S	NMD	C	L
Francés and Ojer [25]	2003	TB	L	–	N	NMD	C	NL
Babadi and Farhanieh [27]	2005	HT	L	Marching Scheme (FDM)	N	NMD	–	NL
Papaefthimiou et al. [28]	2006	HT	L	Collocated (FEM)	N	NMD	V	NL
Kyung et al. [30]	2007	HT	L 3 Regimes	Marching Scheme (FDM)	N	NMD	C	NL
Kyung et al. [32]	2007	TB	L 3 Regimes	Marching Scheme (FDM)	N	NMD	C	NL
Papaefthimiou et al. [34]	2012	TB	L	Collocated (FEM)	N	NMD	V	NL
Ji et al. [36]	2017	HT	L	Level set method	S	None	C	None

^a HT: Horizontal tube; TB: Tube bundle ^b L: Liquid; G: Gas ^c N: Nusselt; S: Solved numerically ^d NMD: No mass diffusion

^e C: Constant; V: Variable ^f NL: Non-linear; L: Linear

Table 1.6: Operating parameters and physical properties in numerical studies of laminar LiBr-water solution over horizontal tubes.

Author(s)	Year	$Re_{L,in}$	T_{wall} [°C]	$T_{L,in}$ [°C]	$\xi_{LiBr,in}$	P [kPa]	d [mm]	H_a [J kg ⁻¹]	Quantities Studied
Andberg and Vliet [22]	1987	10 to 40	25 to 35	32 to 42	0.58 to 0.62	0.8 to 1.4	14, 20, 30	–	$\xi_{LiBr,intf}$, $\xi_{LiBr}(y)$, $\xi_{LiBr,out}$, $T_{L,out}$
Choudhury et al. [23]	1993	0.80 to 80.1	30	50.05	0.60	1 to 1.8	4 to 20	2.721×10^6	T_{intf} , $\xi_{LiBr,intf}$, $U_{L,intf}$, $V_{L,intf}$
Min and Choi [24]	1999	16.7	30	40	0.612	1.0	19.05	–	$\xi_{LiBr}(y)$, \dot{m}'_{tot} , Nu, Sh
Francés and Ojer [25]	2003	–	30 to 35	40 to 46	0.52 to 0.61	–	15.9	–	C_m , C_h
Babadi and Farhanieh [27]	2005	5 to 100	32	40	0.612	1	20	–	$U_L(y)$, $T_{L,out}$, Sh, Nu, C_h
Papaefthimiou et al. [28]	2006	10, 20	25-32	50	0.6	1.227	8	$(h_v - \bar{h}_W)_{intf}$	T_{intf} , $\xi_{LiBr,intf}$, $T_{L,out}$, q''_{wall} , \dot{m}''_{intf} , Q_{abs}
Kyung et al. [30]	2007	15.8	30	40	0.6	1.079	19.05	$(h_v - \bar{h}_W)_{intf}$	$T_L(y)$, $\xi_{LiBr}(y)$, T_{intf} , $\xi_{LiBr,intf}$, \dot{m}''_{intf} , q''_{wall}
Kyung et al. [32]	2007	10 to 43	30	–	0.57, 0.6	1.06, 1.09	19.05	$(h_v - \bar{h}_W)_{intf}$	$T_{L,out}$, q''_{wall} , C_h , Q_{abs}
Papaefthimiou et al. [34]	2012	1 to 80	32	54	0.612	1 to 1.4	16, 22	$(h_v - \bar{h}_W)_{intf}$	ξ_{LiBr} , T_L , q''_{wall} , Nu, Q_{abs}
Ji et al. [36]	2017	42 to 264	–	–	0.60	–	16	Neglected	δ , V_{intf} ,

Hoffmann et al. [38] correlated heat transfer coefficient with changes in kinematic viscosity and surface tension for an aqueous LiBr solution flowing over a horizontal tube absorber. A single column of 24 tubes with a plain or structured surface were examined in their experiment setup, a geometry similar to commercial absorbers. The overall heat transfer coefficient of 200-1900 $\text{W/m}^2\cdot\text{K}$ and 1400 $\text{W/m}^2\cdot\text{K}$ was reported for the solutions of 40-61% LiBr and 57% LiBr with additives, respectively. Error analysis of the measured data yielded a total error of about 19% for the resulting heat transfer coefficient. The solution and cooling water temperature evolution over each individual tube was presented. The experimental data revealed that the heat transfer coefficient increases with increasing solution mass flow rate at a specific concentration and also with decreasing viscosity due to concentration change at a specific flow rate. It was observed that the heat transfer coefficient reached an asymptotic value for mass flow rates larger than 0.03 $\text{kg/m}\cdot\text{s}$, independent of the solution concentration. The heat transfer coefficient was increased by using structured surface tubes and adding surfactants to the solution. The structured surface improved the wetting area on the tube and made the flow turbulent. The surfactant reduced the surface tension.

Francés and Ojer [39] also studied experimentally LiBr-water falling film with a corrosion inhibitor over a bundle of smooth tubes. The experiment was conducted for two sets of operating conditions. The solution inlet temperature, mass fraction, and mass flow rate were varied in the experiments. The solution mass fraction and temperature were measured only at the inlet and outlet of the experimental setup. The cooling water temperature was measured at the inlet and outlet of each tube. Based on the cooling water evolution data, the authors concluded that neglecting the effect of the wetting area in numerical models would lead to overestimation of the absorber thermal load.

The performance of a horizontal smooth tube absorber with and without adding a surfactant to the solution of LiBr-water was experimentally studied by Kyung and Herold [33]. Their experiment was conducted in a single effect chiller. The absorber consisted of a set of 19.1 mm OD smooth horizontal copper tubes arranged in a vertical column. The flow rate of cooling water and

temperature difference of cooling water across the tube bundle were used to calculate the absorber heat transfer rate. The solution inlet subcooling had a significant effect on the absorber heat transfer rate and the heat transfer coefficient. An increase in the solution inlet subcooling caused a decrease in heat transfer coefficient. Heat transfer coefficient increased by higher film flow rate, whereas the inlet mass fraction of the solution did not affect the heat transfer coefficient. The authors explained the physics of absorption enhancement due to 2-ethyl-Hexanol surfactant. Kyung and Herold [33] also pointed out that the increase in absorption heat transfer coefficient by the absorption flux is the opposite of the condensation phenomena behaviour. In condensation normally the increase in the absorption flux leads to a thicker film and lower heat transfer coefficient whereas in absorption, mass diffusivity controls the absorption flux and film thickness is not a factor.

A medium size horizontal tube absorber installation with LiBr-water solution was experimentally tested by Francés and Ojer [25]. Parameters such as the solution concentration, temperature and mass flow rate, the cooling water inlet temperature, and the solution volumetric flow rate were given a low and high value to run the experiments. The heat transfer and mass transfer coefficients were correlated to a polynomial which indicated 72% dependency of both coefficients on the studied factors.

Seol and Lee [29] investigated the characteristics of heat and mass transfer and flow pattern of the liquid film flowing over a single horizontal tube. In a test chamber, a LiBr-water solution strong in LiBr discharged from a nozzle array over a cooled horizontal tube. The outer and inner diameters of the tube were reported as 19.05 mm and 16.6 mm, respectively. During the experiment, the inlet and outlet temperature of the solution and coolant and the pressure of the chamber (absorber) were measured. The outlet temperature of the solution was calculated by averaging the temperature of three points along the bottom line of the tube. Their study showed that increasing the absorber pressure caused wave formation on the liquid film which resulted in partial film ruptures and dry spots on the tube. Seol and Lee's [29] experimental data showed a linear increase in the solution outlet temperature when the solution inlet temperature was increased except at small solution flow rates with high absorber pressures. The effects of jet-flow and sheet-flow drainage patterns were

also investigated in this study. The absorption rate was higher for a sheet-flow drainage at lower solution flow rates. This drainage pattern was intentionally induced by installing a thin vertical plate beneath the tube. This plate helped stabilizing the liquid film and produced less resistance by formation of a thinner liquid film. It was observed that at higher flow rates, the mixing effect is enhanced and mass absorption becomes higher than for the sheet-flow drainage case.

The effect of the vapour flow direction on the heat and mass transfer during the absorption of NH_3 vapour into the NH_3 -water falling film in a helical coil absorber was investigated by Kwon and Jeong [40]. In this study, the average heat transfer coefficient was calculated from the inlet and outlet temperature of the solution because the sensors used to measure the temperature were not able to measure the thin liquid film local temperatures needed for calculation of local heat transfer coefficients. The absorber outlet mass fraction was calculated iteratively using the mass, concentration and energy balance in the absorber because of some difficulties associated with measurement of the outlet mass fraction. The interface shear stress was considered to be a function of the friction coefficient and vapour density and velocity. It was emphasized that the shear stress effect is significant on the heat transfer coefficient at high vapour velocity. The experimental results showed that the total heat transfer rate was increased with solution flow rate. Using a counter-current vapour flow decreased the heat transfer rate slightly compared with the co-current vapour flow direction. This decrease became more noticeable when the solution concentration was decreased. A similar behaviour was observed for the film Nusselt number with respect to the solution flow rate and concentration and the vapour flow direction. It was also concluded that, because of the effect of the shear stress in counter-current vapour flow case, the Nusselt number should be correlated to the shear stress as well as the Reynolds number.

Ammonia-water falling film around microchannel tube banks in contact with counter-current vapour flow was investigated experimentally by Nagavarapu and Garimella [42]. Microchannel tube arrays were installed in a test facility consisting of all the components of a functional single effect absorption chiller including a desorber, rectifier, condenser, and evaporator. The temperatures and pressures were measured at various locations of the the absorption cycle. A mass fraction

Table 1.7: Summary of experimental studies of LiBr laminar falling film over horizontal tubes.

Authors	Year	No. of Tubes	d^a [mm]	S_L/d^b –	L_t [mm]	$\dot{m}'_{L,in}$ [kg/m·s]	$T_{L,in}$ [°C]	$\xi_{LiBr,in}$ [%]	P [kPa]	Quantities Measured
Consenza and Vliet [37]	1990	5,3	19.5,42.2	2	150	0.02 to 0.06	30	50 to 58	0.8 to 1.33	$Q_{abs}, \dot{m}''_{intf}$
Nomura et al. [35]	1993	13	15.88	1.32	200	0.012 to 0.052	55	62	–	T_L, Q_{abs}
Hoffmann et al. [38]	1996	24	–	–	–	0.075 to 0.045	40 to 43	40 to 61	–	T_L, T_{wall}, C_h
Francés and Ojer [39]	2000	14	15.9	2.94	–	0.01 to 0.045	35.42, 42.7750 to 601.0225	1.9822	–	$T_{L,in}, \xi_{LiBr,in}, T_{L,out}, \xi_{LiBr,out}, T_{wall}$
Kyung and Herold [33]	2001	4,8	19.1	2.33	360,460	0.014 to 0.05	37.7 to 52.6	57,60	1.23,1.09	C_h, Q_{abs}
Francés and Ojer [25]	2003	14	15.99	2.93	330	0.01 to 0.045	40 to 46	52 to 61	–	C_m, C_h
Seol and Lee [29]	2005	1	19.05	–	100	–	32 to 50	60, 62	0.53, 1.33	$T_{L,in}, T_{L,out}, P, T_{wall}, \dot{m}''_{intf}$

^a d : diameter of the tube ^b S_L : centre to centre distance of the tubes

All multi-tube absorbers are arranged in a vertical single column.

Table 1.8: Summary of experimental studies of NH₃-water laminar falling film over horizontal tubes.

Authors	Year	No. of Tubes	d^a [mm]	L_t [mm]	$\dot{m}'_{L,in}$ [kg/m·s]	$T_{L,in}$ [°C]	$\xi_{NH_3,L,in}$ [%]	$\xi_{NH_3,G,in}$ [%]	P [kPa]	Quantities Measured
Kwon and Jeong [40]	2004	30 ^b	12.7	600.6	0.00443 to 0.0909	45,50, 55,60	3.13,14, 30	45.6,84.4, 96.5	17 to 193	\dot{m}''_{intf} , Nu, Q_{abs}
Lee et al. [41]	2012	24 ^c	9.5	292	0.0081, 0.0113, 0.0146	–	5, 15, 25, 40	97.81	150, 345, 500	Q_{abs} , C_m , C_h
Nagavarapu and Garimella [42]	2013	33 ^d	1.575	137	0.011 to 0.023	–	40,48,55	15 to 40	–	\dot{m}''_{intf} , C_h

^a d : outer diameter of the tube ^b Number of coil winding ^c Four columns of six tubes ^d Thirty three tubes per row, two row per pass, ten passes

balance was conducted to obtain mass fraction of the solution needed for defining the state of the solution. The enthalpy and specific volume of the solution were estimated based on the solution state. The Nusselt velocity profile was assumed in the liquid film and used to calculate the mean temperature assuming a linear temperature profile between the tube wall and the interface. The total heat of absorption was calculated using an energy balance between the liquid film and the vapour. Nagavarapu and Garimella [42] observed a higher heat transfer coefficient for higher solution concentration and higher vapour flow rate.

An absorption heat and mass experiment was conducted by Lee et al. [41] on a test facility replicating a single stage absorption heat pump. A NH_3 -water solution falling film absorber consisted of an outer shell and a horizontal tube array. The tube array consisted of four columns of six horizontal tubes. Lee et al. [41] followed the same procedure as Nagavarapu and Garimella [42] to measure the solution temperature and pressure and calculate the film mass concentration to define the solution states at different positions. The absorber heat transfer rate, the solution heat transfer coefficient, and the vapour and liquid mass transfer coefficients were studied at three different pressures (150, 345, and 500 kPa), four different solution inlet mass fractions (5, 15, 25, and 40%) and three different solution flow rates (0.0081, 0.0113, 0.0146 kg/m·s). The experimental results revealed that at any pressure and solution concentration, the absorber heat transfer rate and the solution heat transfer coefficient increases with the solution mass flow rate. The solution heat transfer coefficient was found to decrease with increasing pressure and solution concentration at a specific mass flow rate. The mass transfer coefficients were only slightly affected by a change in the solution mass flow rate.

Among the experimental measurements conducted in horizontal tube absorbers, only the experiment by Seol and Lee [29] was done over a single horizontal tube. The operating conditions of the absorber were provided by the authors. For validation purpose of a numerical model, the experimental data presented for two different volumetric flow rates could be used. Seol and Lee [29] measured the inlet and outlet temperature of the liquid film at different pressure values and the variation of absorption rate over a range of liquid inlet temperature and absorber pressure values.

The interfacial variation of the temperature and mass fraction of the liquid film over the tubes were not presented by any of the articles reviewed in this section.

1.3.4 Contribution of the Present Work

In numerical modelling of absorption, all of the governing equations are coupled: continuity, momentum, energy, and mass fraction. Two-phase, multi-component flow on a complex geometry makes the falling film absorption a challenging problem to model. As a result, most numerical models consider only the film phase and neglect the shear stress impact at the liquid-vapour interface. These models also simplify the film hydrodynamics and do not take into account the effect of heat and mass transfer and interaction with the vapour on the liquid flow. The liquid film thickness growth is one of the parameters that could be affected by operating conditions but usually is neglected for the purpose of simplification or is simply related to the absorbed mass at the interface. One of the common numerical approaches is simulation of boundary layer (parabolic) equations in the liquid which is not capable of capturing recirculation zones in the flow. The thermophysical properties of a binary mixture and also the heat of absorption are functions of temperature and mass fractions of the components. In most of the previous numerical work this dependency is neglected in the falling film regime.

Because the interfacial interaction between the vapour and solution film is related to the equilibrium condition and the heat of absorption at the interface, a full understanding of absorption physics is required. The present study, applies a finite volume method using two different approaches to develop detailed numerical models of two-phase laminar absorption of vapour to an aqueous LiBr solution.

The first numerical model uses a parabolic approach to investigate absorption of water vapour into a liquid film of LiBr-water solution flowing inside a vertical parallel plate channel. Compared to previous single-phase models, the present two-phase model provides the opportunity of exploring the effect of gas flow on the transfer of heat, mass, and momentum at the interface. This

approach is potentially a more accurate overall model that includes the gas phase flow completely. Compared to previous two-phase models, the present model has a variable film thickness. A mesh adaption to changing film thickness is facilitated by a coordinate transformation. The liquid-gas interface location is matched exactly with the mesh at every axial location in the solution. The appropriate interaction between the flows of the liquid and gas is assured by fundamental balances of energy, mass and shear force at the interface. In addition, the physical properties, heat of absorption, and equilibrium condition are applied based on temperature, mass fraction and pressure in the liquid film. A complete set of two-dimensional parabolic governing equations is solved using a marching scheme and a robust fully coupled solution approach.

The second numerical model uses an elliptic approach to study absorption phenomena inside a vertical channel and over a horizontal tube. This model applies an Eulerian approach to solve an implicitly coupled co-located elliptic two-dimensional set of governing equations on a structured non-orthogonal grid. Mass, momentum, and energy conservation equations are solved for both liquid and gas phases. The comprehensive form of the energy conservation equation including the partial massive enthalpies and mass diffusion terms, and water mass fraction conservation equation are solved in the liquid phase. The pressure field is calculated implicitly for the entire domain. An adaptive-grid Eulerian method is used to track the interface precisely so that a grid line always coincides with the liquid-vapour interface. When the solution variables are obtained on a fixed mesh, the grid is regenerated based on the new interface location at the end of each time step. The fundamental balances of energy, mass, shear and normal forces are applied at the interface and the variation of thermophysical and transport properties is included. The elliptic model is capable of capturing the liquid film shape over the whole range of tube angle ($0 \leq \theta \leq \pi/2$) and recirculation zones. To the best of the author's knowledge, the elliptic model developed in this work is a more complete, detailed model than any previous numerical studies in falling film absorption.

1.3.5 Layout of the Thesis

The chapters of this thesis are arranged as follows:

Chapter 2 presents the parabolic and elliptic mathematical models including the governing equations in both liquid and gas phases along with all the equations at the interface. The interface moving strategy is explained. The boundary conditions are described in detail in this chapter.

Chapter 3 presents the discretisation of the domain and grid generation for both parabolic and elliptic models. The transformed governing equations are given for the parabolic model. The basic nomenclature of the grid system is also illustrated. The details of the grid assembly are provided.

Chapter 4 explains the numerical solution method in parabolic and elliptic models. In this chapter, discretisation of the governing equations is described. There is a detailed discussion of the each term in the set of equations, as well as the boundary conditions implementation.

Chapter 5 presents the results of the parabolic model for the falling film absorption inside a parallel plate vertical channel. This chapter includes the comparison of the results with previous studies and new results that investigate different parameters' effect on absorption.

Chapter 6 presents detailed results for the elliptic model solution of absorption inside a vertical parallel plate channel. The results include comparison with the parabolic model and a previous two-phase study of absorption process.

Chapter 7 presents the elliptic model results investigating liquid film flow around the tube in contact with water vapour. This chapter includes the validation results and also new results for the cases with different film Reynolds numbers, inlet-to-wall temperature differences, tube diameters, and tube spacing.

Chapter 8 provides a summary of the main results in this work and presents the significant conclusions.

Chapter 2

Mathematical Model

2.1 Introduction

In this work, the simultaneous heat and mass transfer phenomena in absorption of water vapour into the LiBr solution is numerically studied by applying conservation laws on a domain of control volumes. Assuming steady-state and laminar flow in both the liquid and gas phases, the governing equations for describing two-dimensional, incompressible, Newtonian fluid flows of the LiBr-water solution and the water vapour are formulated based on conservation of mass, momentum, and energy. The governing equations are written in Cartesian coordinates, x and y , which denote the stream-wise and transverse (wall-normal) directions, respectively. The liquid and vapour interface is assumed to be smooth, non-wavy and impermeable to the LiBr in the solution. The phase equations are connected through interface conditions enforced at the liquid-gas interface.

2.2 Problem Statement

In the present work, parabolic and elliptical methods are used to study absorption inside a vertical channel and over a horizontal tube. Both models are applied to the vertical channel geometry and only the elliptic model is applied to the horizontal tube geometry. In the following sections, the governing equations of the numerical models and the domain definition and boundary conditions of both geometries are presented.

A fully developed two-phase flow of an aqueous LiBr solution and water vapour flowing down inside a vertical parallel plate channel with a plate spacing of H and length L is shown in Figure 2.1. The thin liquid film (solution) with initial thickness of δ_{in} enters the channel at a uniform

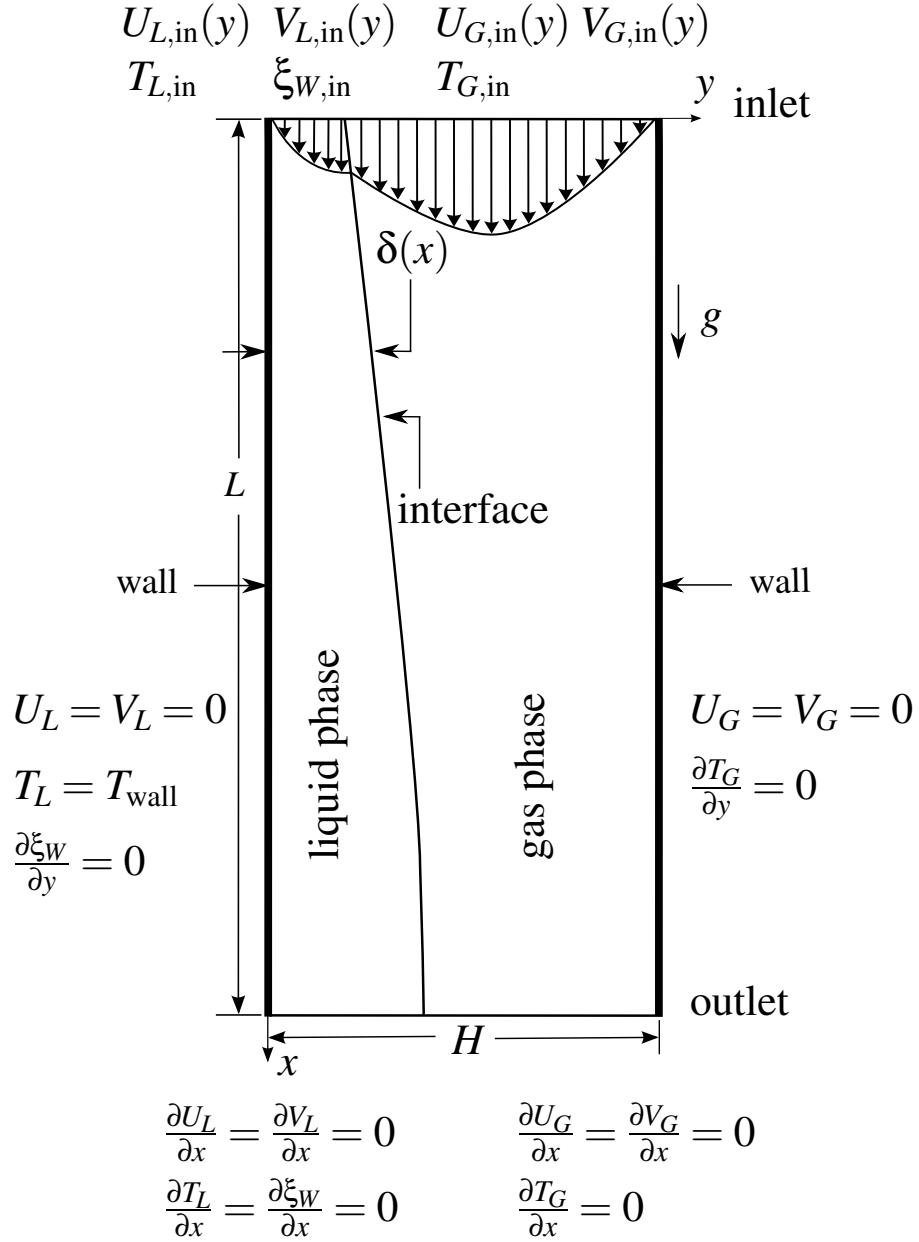


Figure 2.1: Domain definition and boundary conditions for two-phase absorption in a vertical channel; the outlet boundary conditions apply to the elliptic model only.

temperature and water mass fraction with a fully developed axial velocity profile and zero transverse velocity. The pure water vapour has a uniform inlet temperature with a fully developed

axial velocity profile and zero transverse velocity. The liquid-side wall is maintained at a constant temperature. The vapour-side wall is adiabatic. The stream-wise and transverse (wall-normal) directions are denoted by x and y , respectively. Heat and mass transfer occur at the phase interface. Due to the absorption of vapour into the liquid film, the film thickness changes along the channel.

In the case of horizontal tube shown in Figure 2.2, the liquid film and the water vapour come in contact with uniform inlet velocities and temperatures at the inlet of the domain. The liquid film with a specified mass fraction at the domain inlet falls over the tube while absorbing vapour from the gas phase. The liquid film falling distances above the tube and below the tube are L_1 and L_2 , respectively. Because of symmetry, half of the physical problem may be solved. The tube with the diameter d is maintained at a constant temperature. The solution domain width $H = S_T/2$ is determined based on the distance between tubes in a multiple tube arrangement.

2.3 Parabolic Model Governing Equations

In the parabolic approach, the stream-wise diffusion is assumed to be negligible for the momentum, energy and mass fraction equations. The pressure is considered to be uniform in the y direction.

2.3.1 Liquid Phase

The liquid phase mass, momentum, and energy conservation equations are:

- Liquid continuity equation

$$\frac{\partial(\rho_L U_L)}{\partial x} + \frac{\partial(\rho_L V_L)}{\partial y} = 0 \quad (2.1)$$

- Liquid momentum equation in the x direction

$$\frac{\partial(\rho_L U_L U_L)}{\partial x} + \frac{\partial(\rho_L V_L U_L)}{\partial y} = -\frac{dP}{dx} + \frac{\partial}{\partial y} \left(\mu_L \frac{\partial U_L}{\partial y} \right) + \rho_L g_x \quad (2.2)$$

- Liquid energy equation

$$\begin{aligned} \frac{\partial}{\partial x} [\rho_L U_L (C_{p,L} T_L + \xi_W (\bar{h}_W - \bar{h}_{LiBr}))] + \frac{\partial}{\partial y} [\rho_L V_L (C_{p,L} T_L + \xi_W (\bar{h}_W - \bar{h}_{LiBr}))] = \\ \frac{\partial}{\partial y} \left(k_L \frac{\partial T_L}{\partial y} \right) + \frac{\partial}{\partial y} \left(\rho_L D_L^{AB} \frac{\partial \xi_W}{\partial y} (\bar{h}_W - \bar{h}_{LiBr}) \right) \end{aligned} \quad (2.3)$$

Equation (2.3) is consistent with the energy equation presented in Mittermaier and Ziegler [13] (Appendix B).

The conservation of mass equation for water is:

- Liquid mass fraction equation

$$\frac{\partial(\rho_L U_L \xi_W)}{\partial x} + \frac{\partial(\rho_L V_L \xi_W)}{\partial y} = \frac{\partial}{\partial y} \left(\rho_L D_L^{AB} \frac{\partial \xi_W}{\partial y} \right) \quad (2.4)$$

2.3.2 Gas Phase

The gas phase mass, momentum, and energy conservation equations are:

- Gas continuity equation

$$\frac{\partial(\rho_G U_G)}{\partial x} + \frac{\partial(\rho_G V_G)}{\partial y} = 0 \quad (2.5)$$

- Gas momentum equation in the x direction

$$\frac{\partial(\rho_G U_G U_G)}{\partial x} + \frac{\partial(\rho_G V_G U_G)}{\partial y} = -\frac{dP}{dx} + \frac{\partial}{\partial y} \left(\mu_G \frac{\partial U_G}{\partial y} \right) + \rho_G g_x \quad (2.6)$$

- Gas energy equation

$$\frac{\partial}{\partial x} (\rho_G U_G C_{p,G} T_G) + \frac{\partial}{\partial y} (\rho_G V_G C_{p,G} T_G) = \frac{\partial}{\partial y} \left(k_G \frac{\partial T_G}{\partial y} \right) \quad (2.7)$$

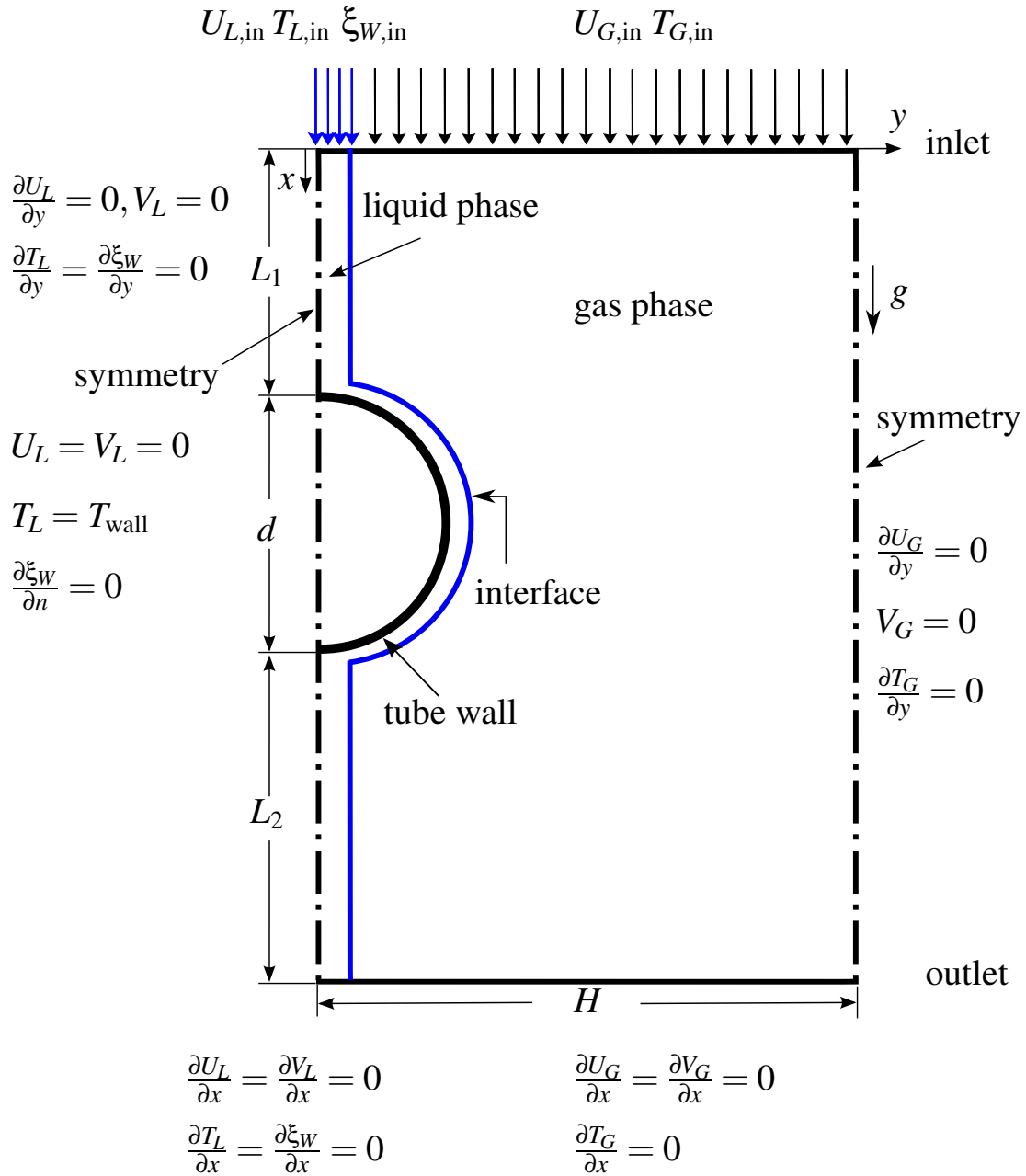


Figure 2.2: Domain definition and boundary conditions for two-phase absorption over a horizontal tube.

2.3.3 Interface Conditions

The following conditions are applied at the phase interface:

- Continuity of velocity and shear stress

$$U_L = U_G, \quad \mu_L \frac{\partial U_L}{\partial y} = \mu_G \frac{\partial U_G}{\partial y} \quad (2.8)$$

- Continuity of the absorbed mass

$$\rho_L V_L - \rho_L U_L \frac{d\delta}{dx} = \rho_G V_G - \rho_G U_G \frac{d\delta}{dx} = \dot{m}''_{\text{intf}} \quad (2.9)$$

- Continuity of the temperature

$$T_L = T_G = T_{\text{intf}}, \quad T_{\text{intf}} = T(\xi_{W,\text{intf}}, P_{\text{intf}}) \quad (2.10)$$

The T_{intf} function of P_{intf} and $\xi_{W,\text{intf}}$ represents the assumption that the LiBr solution is in thermodynamic equilibrium with the water vapour at the interface. The interface temperature is related to the interfacial pressure and mass fraction through an equilibrium condition. The equilibrium relation presented by McNeely [1] or Mittermaier and et al. [12] is used in the parabolic model, depending on the case studied. One part of the SI version of McNeely's equilibrium equation is not given in the 1977 article. That part appears in ASHRAE [43]; a correction to one coefficient in the ASHRAE version was required, as given in Appendix A.1. The details of the correction made in Mittermaier and et al. [12] equilibrium condition are also presented in Appendix A.4.

- Impermeability of LiBr at the interface

$$-\rho_L D_L^{AB} \frac{\partial \xi_W}{\partial y} = \dot{m}''_{\text{intf}} (1 - \xi_W) \quad (2.11)$$

- Continuity of energy

$$k_L \frac{\partial T_L}{\partial y} = k_G \frac{\partial T_G}{\partial y} - \dot{m}''_{\text{intf}} H_a \quad (2.12)$$

where H_a is the heat of absorption and defined as:

$$H_a = (h_v - \bar{h}_W)_{\text{intf}} \quad (2.13)$$

where h_v and \bar{h}_W are the enthalpy of water vapour and the partial enthalpy of water in the solution at the interface temperature, respectively.

The global mass balance is applied as an additional constraint equation to determine the pressure gradient, dP/dx .

$$\int_0^\delta \rho_L U_L dy + \int_\delta^H \rho_G U_G dy = \dot{m}'_{L,\text{in}} + \dot{m}'_{G,\text{in}} \quad (2.14)$$

2.3.4 Domain and Boundary Condition Definitions

The boundary conditions shown in Figure 2.1 are prescribed as follows:

- at the inlet ($x = 0$): uniform temperature and mass fraction and fully developed velocity profiles

$$T_L = T_{L,\text{in}}, \quad \xi_W = \xi_{W,\text{in}}, \quad U_L = U_{L,\text{in}}(y), \quad V_{L,\text{in}} = 0 \quad \text{for} \quad 0 \leq y \leq \delta_{\text{in}} \quad (2.15)$$

$$T_G = T_{G,\text{in}}, \quad U_G = U_{G,\text{in}}(y), \quad V_{G,\text{in}} = 0 \quad \text{for} \quad \delta_{\text{in}} \leq y \leq H \quad (2.16)$$

$$P_{L,\text{in}} = P_{G,\text{in}} = P_{\text{in}} \quad (2.17)$$

The analytical equations presented by Saleh and Ormiston [44] are used to determine the liquid and gas phase fully developed velocities and the consistent film thickness and pressure gradient at the inlet of the channel. In theory, the temperature of the entering solution is consistent with the equilibrium pressure and mass fraction. In practice, if the solution is superheated relative to the equilibrium condition, evaporation of vapour from the solution will cause a temperature drop in the solution before contacting the cooled wall (Andberg [45]). If this solution comes in contact with the cold wall, absorption will begin at the inlet of the

channel. When the solution is nearly at the equilibrium temperature, some heat must be removed by the cold wall at the channel entrance to reduce the interface temperature and make the absorption possible (Killion and Garimella [46]). In this study, it was observed that, just after the inlet, the interface temperature decreases relative to the liquid bulk temperature while absorbing water at the interface. This condition results in a negative temperature gradient at the interface and consequently, heat transfer to the gas phase. It is apparent that the liquid film subcooling at the inlet is essential and also more practical in the modelling of the absorption phenomena. Therefore, the liquid inlet temperature is specified as:

$$T_{L,\text{in}} = T_L(\xi_{W,\text{in}}, P_{L,\text{in}}) - \Delta T_{\text{sub}} \quad (2.18)$$

where $T_L(\xi_{W,\text{in}}, P_{L,\text{in}})$ refers to the equilibrium temperature corresponding to $\xi_{W,\text{in}}$ and $P_{L,\text{in}}$ and ΔT_{sub} is the subcooling.

- at the wall beside the liquid phase ($y = 0$): constant temperature, no mass transfer, and no slip and no penetration conditions at the wall

$$T_L = T_{\text{wall}}, \quad \frac{\partial \xi_W}{\partial y} = 0, \quad U_L = 0, \quad V_L = 0 \quad (2.19)$$

- at the wall beside the gas phase ($y = H$): adiabatic wall, no slip and no penetration conditions for the gas

$$\frac{\partial T_G}{\partial y} = 0, \quad U_G = 0, \quad V_G = 0 \quad (2.20)$$

This mathematical model, consisting of governing equations and boundary and interface conditions, may be used to determine the velocity and temperature in both phases, the water mass fraction in the liquid phase, the film thickness, and the pressure gradient. In this scheme, the interface energy balance, Equation (2.12), is used as an equation for δ .

2.4 Elliptic Model Governing Equations

2.4.1 Liquid Phase

- Liquid continuity equation

$$\frac{\partial(\rho_L)}{\partial t} + \frac{\partial(\rho_L U_L)}{\partial x} + \frac{\partial(\rho_L V_L)}{\partial y} = 0 \quad (2.21)$$

- Liquid momentum equation in the x direction

$$\frac{\partial(\rho_L U_L)}{\partial t} + \frac{\partial(\rho_L U_L U_L)}{\partial x} + \frac{\partial(\rho_L V_L U_L)}{\partial y} = -\frac{\partial P_L}{\partial x} + \frac{\partial}{\partial x} \left(\mu_L \frac{\partial U_L}{\partial x} \right) + \frac{\partial}{\partial y} \left(\mu_L \frac{\partial U_L}{\partial y} \right) + \rho_L g_x \quad (2.22)$$

- Liquid momentum equation in the y direction

$$\frac{\partial(\rho_L V_L)}{\partial t} + \frac{\partial(\rho_L U_L V_L)}{\partial x} + \frac{\partial(\rho_L V_L V_L)}{\partial y} = -\frac{\partial P_L}{\partial y} + \frac{\partial}{\partial x} \left(\mu_L \frac{\partial V_L}{\partial x} \right) + \frac{\partial}{\partial y} \left(\mu_L \frac{\partial V_L}{\partial y} \right) + \rho_L g_y \quad (2.23)$$

- Liquid energy equation

$$\begin{aligned} \frac{\partial(\rho_L C_{p,L} T_L)}{\partial t} + \frac{\partial}{\partial x} \left[\rho_L U_L (C_{p,L} T_L + \xi_W (\bar{h}_W - \bar{h}_{LiBr})) \right] + \frac{\partial}{\partial y} \left[\rho_L V_L (C_{p,L} T_L + \xi_W (\bar{h}_W - \bar{h}_{LiBr})) \right] = \\ \frac{\partial}{\partial x} \left(k_L \frac{\partial T_L}{\partial x} \right) + \frac{\partial}{\partial y} \left(k_L \frac{\partial T_L}{\partial y} \right) + \frac{\partial}{\partial x} \left(\rho_L D_L^{AB} \frac{\partial \xi_W}{\partial x} (\bar{h}_W - \bar{h}_{LiBr}) \right) + \frac{\partial}{\partial y} \left(\rho_L D_L^{AB} \frac{\partial \xi_W}{\partial y} (\bar{h}_W - \bar{h}_{LiBr}) \right) \end{aligned} \quad (2.24)$$

- Liquid mass fraction equation

$$\frac{\partial(\rho_L \xi_W)}{\partial t} + \frac{\partial(\rho_L U_L \xi_W)}{\partial x} + \frac{\partial(\rho_L V_L \xi_W)}{\partial y} = \frac{\partial}{\partial x} \left(\rho_L D_L^{AB} \frac{\partial \xi_W}{\partial x} \right) + \frac{\partial}{\partial y} \left(\rho_L D_L^{AB} \frac{\partial \xi_W}{\partial y} \right) \quad (2.25)$$

2.4.2 Gas Phase

- Gas continuity equation

$$\frac{\partial(\rho_G)}{\partial t} + \frac{\partial(\rho_G U_G)}{\partial x} + \frac{\partial(\rho_G V_G)}{\partial y} = 0 \quad (2.26)$$

- Gas momentum equation in the x direction

$$\frac{\partial(\rho_G U_G)}{\partial t} + \frac{\partial(\rho_G U_G U_G)}{\partial x} + \frac{\partial(\rho_G V_G U_G)}{\partial y} = -\frac{\partial P_G}{\partial x} + \frac{\partial}{\partial x} \left(\mu_G \frac{\partial U_G}{\partial x} \right) + \frac{\partial}{\partial y} \left(\mu_G \frac{\partial U_G}{\partial y} \right) + \rho_G g_x \quad (2.27)$$

- Gas momentum equation in the y direction

$$\frac{\partial(\rho_G V_G)}{\partial t} + \frac{\partial(\rho_G U_G V_G)}{\partial x} + \frac{\partial(\rho_G V_G V_G)}{\partial y} = -\frac{\partial P_G}{\partial y} + \frac{\partial}{\partial x} \left(\mu_G \frac{\partial V_G}{\partial x} \right) + \frac{\partial}{\partial y} \left(\mu_G \frac{\partial V_G}{\partial y} \right) + \rho_G g_y \quad (2.28)$$

- Gas energy equation

$$\frac{\partial(\rho_G C_{p,G} T_G)}{\partial t} + \frac{\partial}{\partial x} (\rho_G U_G C_{p,G} T_G) + \frac{\partial}{\partial y} (\rho_G V_G C_{p,G} T_G) = \frac{\partial}{\partial x} \left(k_G \frac{\partial T_G}{\partial x} \right) + \frac{\partial}{\partial y} \left(k_G \frac{\partial T_G}{\partial y} \right) \quad (2.29)$$

The pressure, P , in the governing equations is the local static pressure. To calculate the flow properties in the liquid and gas phases and the interface, a reference pressure of $P = P_{L,\text{in}}$ is added to the solution static pressure. The LiBr solution thermodynamic properties and partial massive enthalpies are calculated based on the local temperature, mass fraction, and pressure.

2.4.3 Interface Conditions

At the liquid-gas interface ($y = \delta$) the following conditions are applied to couple the fields in the liquid and gas phases:

- Normal force balance

$$(\hat{n} \cdot \boldsymbol{\tau})_{L,\text{intf}} \cdot \hat{n} + \sigma K = (\hat{n} \cdot \boldsymbol{\tau})_{G,\text{intf}} \cdot \hat{n} \quad (2.30)$$

where \hat{n} and $\boldsymbol{\tau}$ are the local normal unit vector to the interface and the stress tensor, respectively. σ is the surface tension and K is the curvature of the interface. In the vertical channel geometry, the curvature of the interface is assumed to be negligible.

- Tangential force balance

$$(\hat{n} \cdot \boldsymbol{\tau})_{L,\text{intf}} \cdot \hat{s} - \frac{\partial \sigma}{\partial s} \Big|_{L,\text{intf}} = (\hat{n} \cdot \boldsymbol{\tau})_{G,\text{intf}} \cdot \hat{s} \quad (2.31)$$

where \hat{s} is the local tangential unit vector to the interface.

- Continuity of tangential velocity

$$(\vec{V}_t)_{L,\text{intf}} = (\vec{V}_t)_{G,\text{intf}} \quad (2.32)$$

- Continuity of temperature

$$T_L = T_G = T_{\text{intf}}, \quad T_{\text{intf}} = T(\xi_{W,\text{intf}}, P_{\text{intf}}) \quad (2.33)$$

It is assumed that the LiBr solution and the water vapour are in thermodynamic equilibrium at the interface. This condition is described by an equilibrium equation that relates the interface temperature, T_{intf} , to its pressure, P_{intf} , and mass fraction, $\xi_{W,\text{intf}}$. The equilibrium condition of either Siebe [3], given in Appendix A.3, or Mittermaier and et al. [12] (corrected version as given in Appendix A.4) is used, depending on the case studied.

- Continuity of absorbed mass

$$\dot{m}''_{L,\text{intf}} = \dot{m}''_{G,\text{intf}} \quad (2.34)$$

- Continuity of energy

$$k_L \frac{\partial T_L}{\partial n} \Big|_{L,\text{intf}} = k_G \frac{\partial T_G}{\partial n} \Big|_{G,\text{intf}} - \dot{m}''_{\text{intf}} H_a \quad (2.35)$$

where H_a is the heat of absorption and defined as a function of the enthalpy of water vapour, h_v , and the partial enthalpy of water in the solution, \bar{h}_W , at the interface temperature:

$$H_a = (h_v - \bar{h}_W)_{\text{intf}} \quad (2.36)$$

- Impermeability of LiBr at the interface

$$-\rho_L D_L^{AB} \frac{\partial \xi_W}{\partial n} \Big|_{L,\text{intf}} = \dot{m}''_{\text{intf}} (1 - \xi_{W,\text{intf}}) \quad (2.37)$$

- Zero pressure gradient in the normal direction at the interface

$$\left. \frac{\partial P_G}{\partial n} \right|_{G,\text{intf}} = 0 \quad (2.38)$$

2.4.4 Domain and Boundary Condition Definitions

The following boundary conditions, as shown in Figure 2.1 for a vertical channel and in Figure 2.2 for a horizontal tube, are prescribed:

- at the inlet ($x = 0$)

Vertical channel: uniform temperature and mass fraction and fully developed velocity profiles (Equations (2.15) and (2.16))

Horizontal Tube: uniform temperature, mass fraction, and velocity

$$T_L = T_{L,\text{in}}, \quad \xi_W = \xi_{W,\text{in}}, \quad U_L = U_{L,\text{in}}, \quad V_{L,\text{in}} = 0 \quad \text{for } 0 \leq y \leq \delta_{\text{in}} \quad (2.39)$$

$$T_G = T_{G,\text{in}}, \quad U_G = U_{G,\text{in}}, \quad V_{G,\text{in}} = 0 \quad \text{for } \delta_{\text{in}} \leq y \leq H \quad (2.40)$$

- at the boundary beside the liquid phase:

Vertical Channel: constant temperature, no mass transfer, and no slip and no penetration conditions at the wall (Equation (2.19))

Horizontal tube: constant temperature, no mass transfer, and no slip and no penetration conditions at the tube wall

$$T_L = T_{\text{wall}}, \quad \frac{\partial \xi_W}{\partial n} = 0, \quad U_L = 0, \quad V_L = 0 \quad (2.41)$$

Zero temperature gradient, no mass transfer, zero U velocity gradient, and no penetration conditions at symmetry lines L_1 and L_2

$$\frac{\partial T_L}{\partial y} = 0, \quad \frac{\partial \xi_W}{\partial y} = 0, \quad \frac{\partial U_L}{\partial y} = 0, \quad V_L = 0 \quad (2.42)$$

- at the boundary beside the gas phase ($y = H$):

Vertical channel: adiabatic wall, no slip and no penetration conditions for the gas (Equation (2.20))

Horizontal tube: zero temperature and U velocity gradients and no penetration condition for the gas

$$\frac{\partial T_G}{\partial y} = 0, \quad \frac{\partial U_G}{\partial y} = 0, \quad V_G = 0 \quad (2.43)$$

- at the outlet ($x = L$)

Vertical channel: fully developed conditions in both phases

$$\frac{\partial T_L}{\partial x} = 0, \quad \frac{\partial \xi_W}{\partial x} = 0, \quad \frac{\partial U_L}{\partial x} = 0, \quad \frac{\partial V_L}{\partial x} = 0 \quad \text{for } 0 \leq y \leq \delta \quad (2.44)$$

$$\frac{\partial T_G}{\partial x} = 0 \quad \text{or} \quad T_G = T_{\text{wall}} \quad (\text{if } U_G < 0), \quad \frac{\partial U_G}{\partial x} = 0, \quad \frac{\partial V_G}{\partial x} = 0 \quad \text{for } \delta \leq y \leq H \quad (2.45)$$

Horizontal tube: fully developed conditions in both phases (Equations (2.44) and (2.45))

In the elliptic model, the relative pressure at the outlet is specified as a reference pressure and the inlet pressure is determined from the solution.

Once the geometry, the properties, and the interface and boundary conditions are prescribed, the elliptic model may be used to determine the U and V velocities, pressure, and temperature in both phases and the water mass fraction in the liquid phase. The location of the phase interface is determined by an adaptive-grid Eulerian method that is described in the following section.

2.4.5 Interface Moving Strategy

Absorption phenomena is a moving boundary problem and the location of the interface that is separating the two phases must be part of a detailed solution. A significant contribution of this work is the development of a precise phase interface tracking scheme.

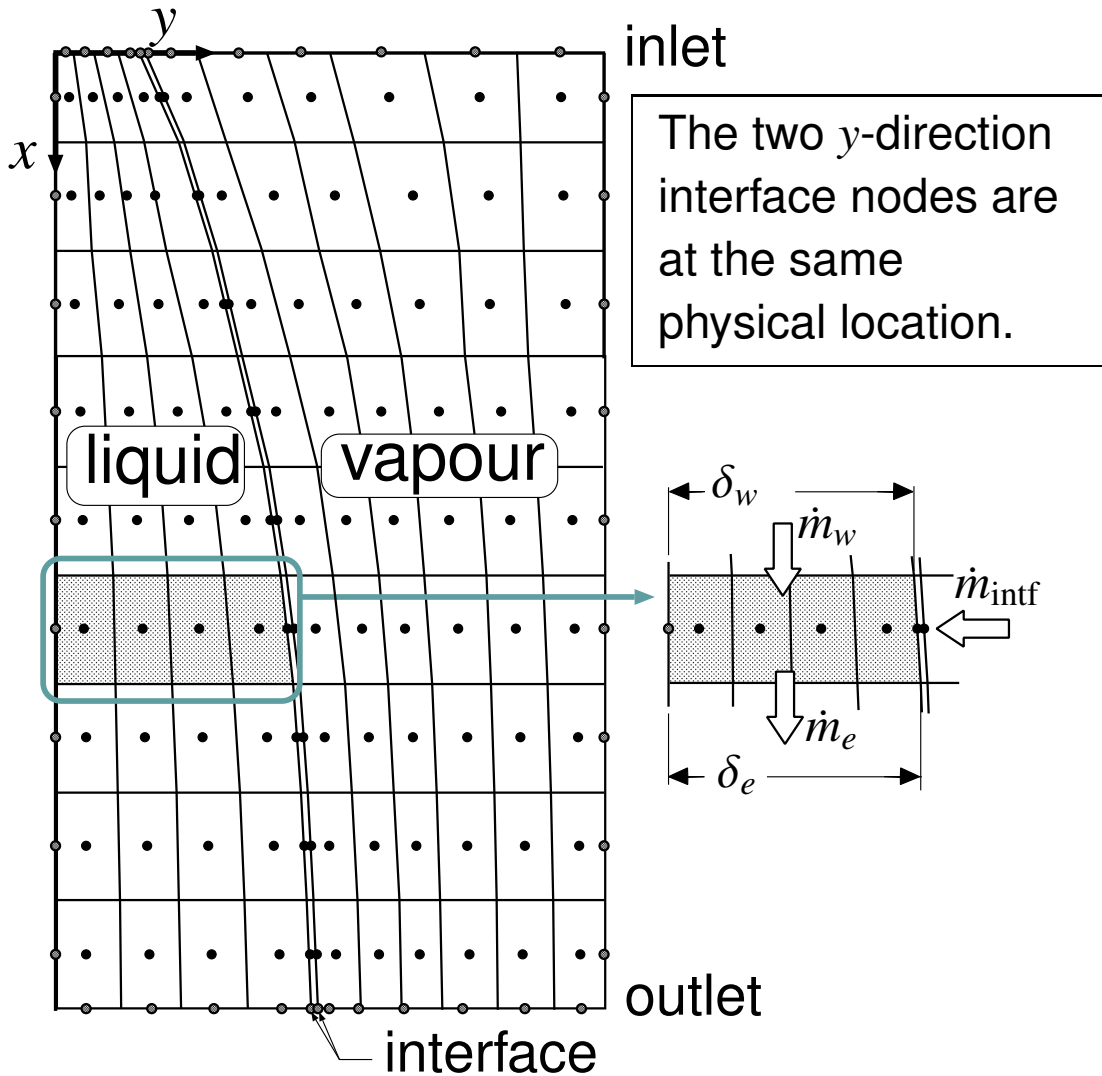


Figure 2.3: Grid information of the phases and a typical liquid region used in ILMB method; the interface nodes are shown separated for illustration purposes.

Once the solution field is obtained on a fixed grid, the interface location is determined by applying an integral liquid mass balance (ILMB) on all the axial columns of liquid at the end of each time step using the following:

$$\int_0^{\delta_e} \rho_{L,e} U_{L,e} dy = \int_0^{\delta_w} \rho_{L,w} U_{L,w} dy + \dot{m}'_{\text{intf}} \quad (2.46)$$

This equation is defined over the grid of a vertical channel where the east and west faces of the

control volumes are normal to the x axis. The ILMB equation is presented in a general form in Section 4.3.5. In Equation (2.46), δ_w and δ_e are the film thicknesses at the axial locations of the west and east faces, respectively, of a typical column of control volumes in the liquid. The mass balance is shown schematically in Figure 2.3. Equation (2.46) states that the total mass flow rate that crosses the control volumes through the west faces and the absorbed mass flow rate crossing the interface must be equal to the total mass flow rate that leaves the column from the east faces. Starting from the inlet of the domain, the downstream side film thickness, δ_e , is obtained using the upstream side film thickness, δ_w , and the absorbed mass at the interface, \dot{m}'_{inf} , by applying a forward marching scheme. The application of the ILMB is enabled by not solving the continuity equations in the row of the control volumes adjacent to the interface in the liquid. The details of the grid are described in Chapter 3 and further details about discretised form of the ILMB equation are presented in Section 4.3.5.

Chapter 3

Discretisation of the Domain

3.1 Parabolic Model

3.1.1 Introduction

To keep a structured grid system while the film thickness changes along the x direction, a coordinate transformation is performed in the parabolic model. An index in the x direction denotes a station, which consists of a column of control volumes. Based on the inlet conditions described in Figure 2.1, a set of parabolic governing equations is solved at the first station. A finite volume method is applied as the discretisation technique in this numerical approach. Because the inlet conditions are known, the solution is progressed station by station along the channel. This method is called marching scheme. In the following sections the coordinate transformation details will be described.

3.1.2 Coordinate Transformation

The Cartesian coordinates x and y are transformed into χ and η following the work by Siow [47]:

$$\chi = x \quad \text{for } x \geq 0, \quad (3.1)$$

$$\eta = \frac{y}{\delta} \quad \text{for } 0 \leq y \leq \delta, \quad (3.2)$$

$$\eta = \frac{y - \delta}{H - \delta} + 1 \quad \text{for } \delta \leq y \leq H. \quad (3.3)$$

This transformation allows the grid boundary to adapt to δ variation along the channel and maintains a structured grid in both phases. With the new coordinate system, the liquid region is now clearly defined as $0 \leq \eta \leq 1$ and the gas region is defined as $1 \leq \eta \leq 2$. Although the film thickness

is increasing in the x direction, the interface is always located at $\eta = 1$. All the governing equations and boundary conditions for both phases must be rewritten according to the new coordinates. In the following section only the final versions of the transformed equations are presented. Details of the derivations can be found in Appendix B of Siow [47].

3.1.3 Transformed Governing Equations

The liquid phase governing equations, Equations (2.1) to (2.4), become:

$$\frac{\partial(\delta\rho_L U_L)}{\partial\chi} + \frac{\partial(J_L'')}{\partial\eta} = 0 \quad (3.4)$$

$$\frac{\partial(\delta\rho_L U_L U_L)}{\partial\chi} + \frac{\partial(J_L'' U_L)}{\partial\eta} = -\delta \frac{dP}{d\chi} + \frac{\partial}{\partial\eta} \left(\frac{\mu_L}{\delta} \frac{\partial U_L}{\partial\eta} \right) + \delta\rho_L g_x \quad (3.5)$$

$$\begin{aligned} \frac{\partial}{\partial\chi} \left[\delta\rho_L U_L (C_{p,L} T_L + \xi_W (\bar{h}_W - \bar{h}_{LiBr})) \right] + \frac{\partial}{\partial\eta} \left[J_L'' (C_{p,L} T_L + \xi_W (\bar{h}_W - \bar{h}_{LiBr})) \right] = \\ \frac{\partial}{\partial\eta} \left(\frac{k_L}{\delta} \frac{\partial T_L}{\partial\eta} \right) + \frac{\partial}{\partial\eta} \left(\frac{\rho_L D_L^{AB}}{\delta} \frac{\partial \xi_W}{\partial\eta} (\bar{h}_W - \bar{h}_{LiBr}) \right) \end{aligned} \quad (3.6)$$

$$\frac{\partial(\delta\rho_L U_L \xi_W)}{\partial\chi} + \frac{\partial(J_L'' \xi_W)}{\partial\eta} = \frac{\partial}{\partial\eta} \left(\frac{\rho_L D_L^{AB}}{\delta} \frac{\partial \xi_W}{\partial\eta} \right) \quad (3.7)$$

The gas phase governing equations, Equations (2.5) to (2.7), become:

$$\frac{\partial((H-\delta)\rho_G U_G)}{\partial\chi} + \frac{\partial(J_G'')}{\partial\eta} = 0 \quad (3.8)$$

$$\frac{\partial((H-\delta)\rho_G U_G U_G)}{\partial\chi} + \frac{\partial(J_G'' U_G)}{\partial\eta} = -(H-\delta) \frac{dP}{d\chi} + \frac{\partial}{\partial\eta} \left(\frac{\mu_G}{(H-\delta)} \frac{\partial U_G}{\partial\eta} \right) + (H-\delta)\rho_G g_x \quad (3.9)$$

$$\frac{\partial}{\partial\chi} \left((H-\delta)\rho_G U_G C_{p,G} T_G \right) + \frac{\partial}{\partial\eta} \left(J_G'' C_{p,G} T_G \right) = \frac{\partial}{\partial\chi} \left(k_G \frac{\partial T_G}{\partial\chi} \right) \quad (3.10)$$

The continuity of velocity and shear, Equation (2.8), and mass, Equation (2.9), at the interface become:

$$U_L = U_G, \quad \frac{\mu_L}{\delta} \frac{\partial U_L}{\partial\eta} = \frac{\mu_G}{(H-\delta)} \frac{\partial U_G}{\partial\eta} \quad (3.11)$$

$$J''_{L,\text{intf}} = J''_{G,\text{intf}} \quad (3.12)$$

The impermeability of LiBr, Equation (2.11), and continuity of energy, Equation (2.12), at the interface become:

$$-\frac{\rho_L D_L^{AB}}{\delta} \frac{\partial \xi_W}{\partial \eta} = J''_{\text{intf}}(1 - \xi_W) \quad (3.13)$$

$$\frac{k_L}{\delta} \frac{\partial T_L}{\partial \eta} = \frac{k_G}{(H - \delta)} \frac{\partial T_G}{\partial \eta} - J''_{\text{intf}} H_a \quad (3.14)$$

Overall mass balance, Equation (2.14), becomes:

$$\int_0^1 \delta \rho_L U_L d\eta + \int_1^2 (H - \delta) \rho_G U_G d\eta = \dot{m}'_{L,\text{in}} + \dot{m}'_{G,\text{in}} \quad (3.15)$$

The transformed governing equations are solved for U_L , J_L , T_L , ξ_W , U_G , J_G , T_G , and scalar unknowns δ and $dP/d\chi$ using a marching scheme. It should be noted that V is replaced by J , the mass flow rate in the η direction (e.g., $J_{\text{intf}} = \dot{m}_{\text{intf}}$).

3.1.4 Grid system

The coordinate transformation facilitates dividing the liquid and gas regions to two equal logically rectangular domains. The Figure 3.1 shows a simplified grid with $N_x \times N_{y,L}$ and $N_x \times N_{y,G}$ control volumes in the liquid and gas regions, respectively. The same number of control volumes is used in the χ direction for both phases. Each rectangle represents a control volume with a node at the centre, where indexing is applied. The index i is used to label the station number in the χ direction, jL is used to label the nodes in the η direction in the liquid (starting at the isothermal wall), and jG is used to label the nodes in the η direction in the gas region (starting at the interface).

The grid spacings in the χ direction are uniform and very fine at the beginning of the channel to capture the sharp gradients at the entrance. The grid then expands exponentially and becomes coarser at the end of the channel. In the η direction the grid spacing is different in the liquid and the gas regions. A sufficient number of nodes is used in the solution film in order to capture the changes in temperature and mass fraction of the film at the interface. The gas phase also has a fine grid

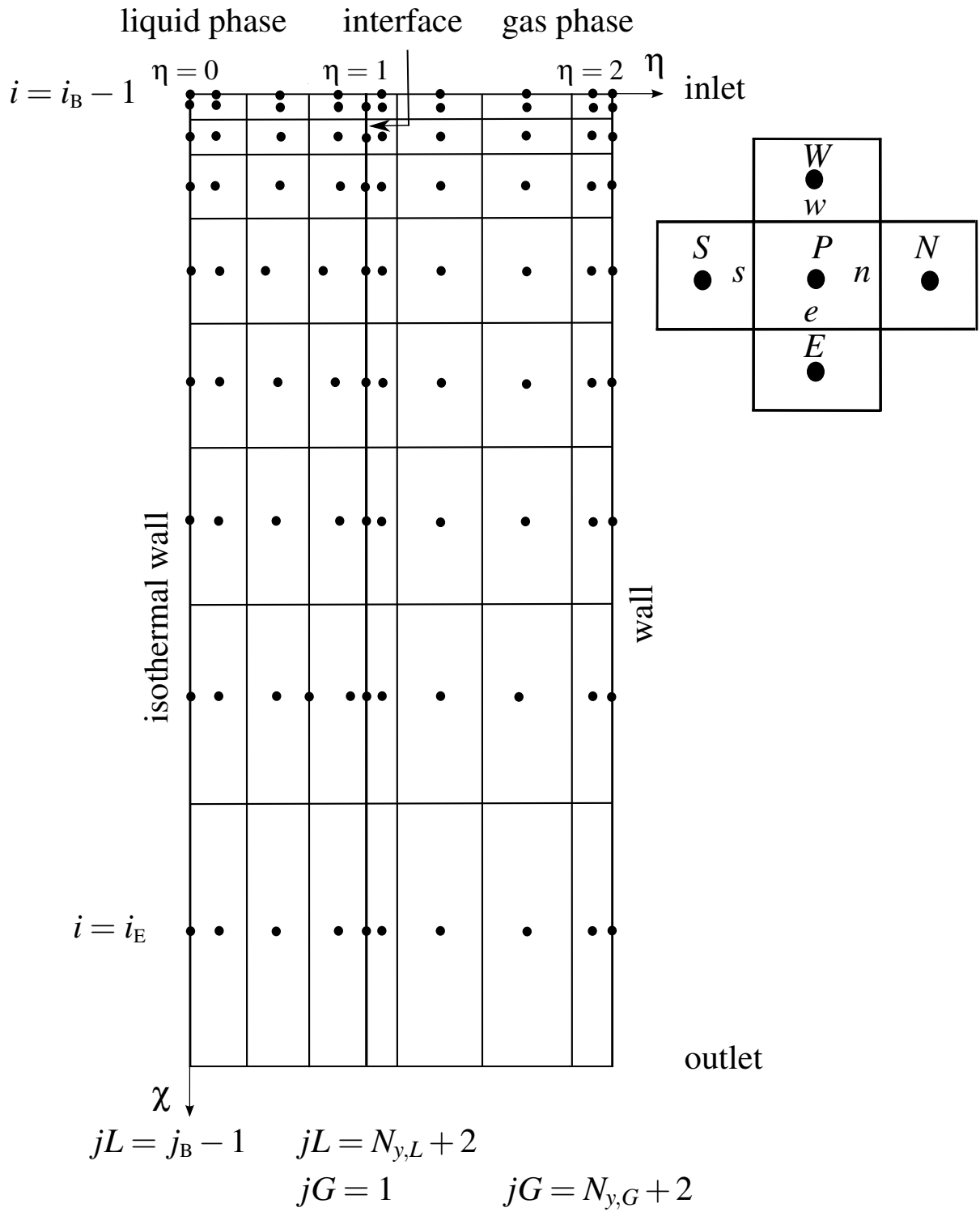


Figure 3.1: Grid nomenclature in transformed coordinates.

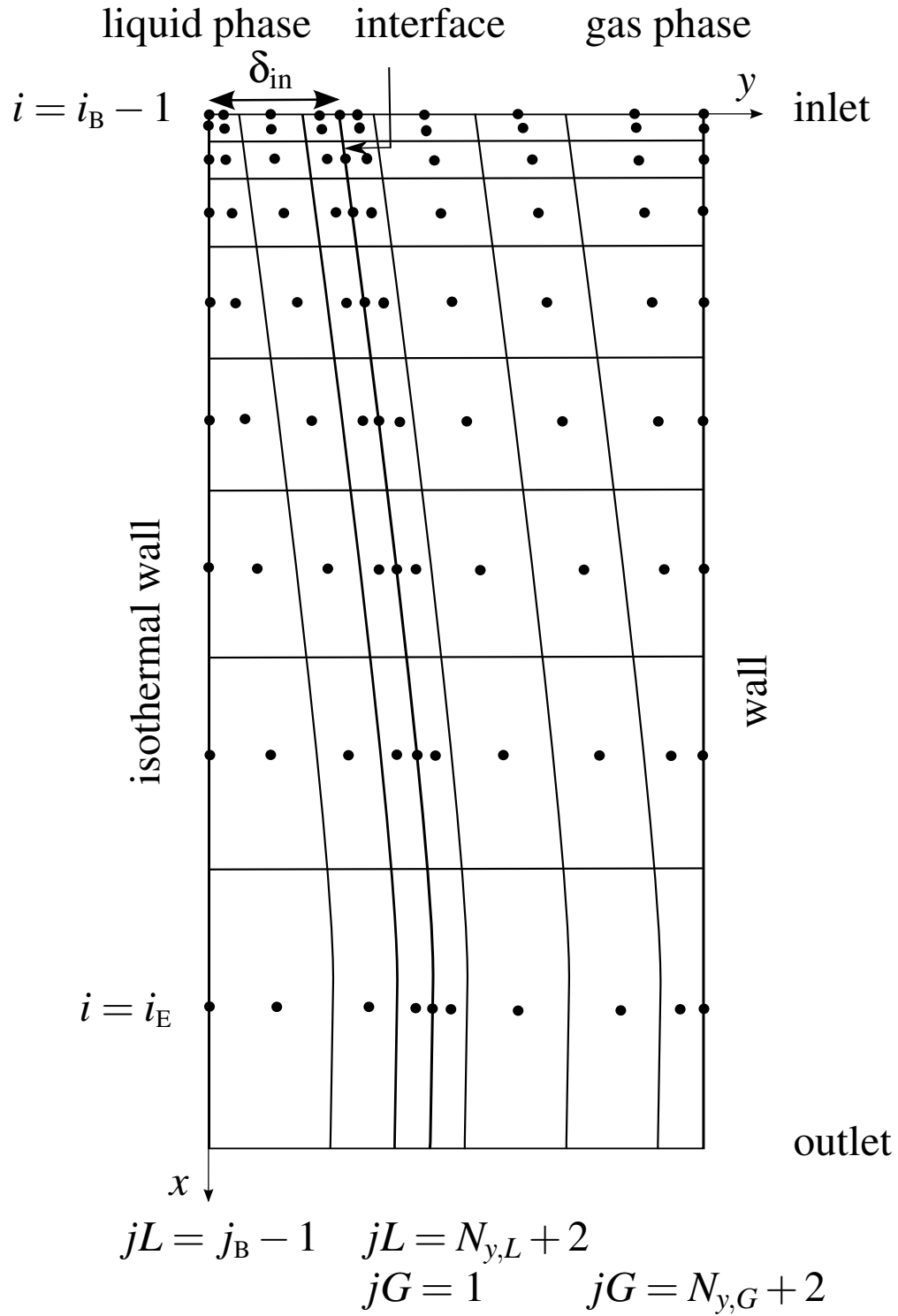


Figure 3.2: Grid nomenclature in Cartesian coordinates.

adjacent to the interface to ensure implementing the continuity of the shear at the interface. Control volumes at the inlet ($i = i_B - 1$), control volumes at the liquid–gas interface ($jL = N_{y,L} + 2$, $jG = 1$), and control volumes located at the lower and upper boundaries ($jL = j_B - 1$ and $jG = N_{y,G} + 2$) all have zero thickness. Field variables such as U , T , and ξ_W are stored at the nodal point, whereas J is stored at the north face of a control volume. J is always normal to the north face of the control volume. Because the film thickness δ and pressure gradient $\frac{dP}{d\chi}$ are constant at each χ , they have a single value at each station.

Figure 3.2 represents the actual domain in the x – y coordinate system, showing the film thickness starting at $x = 0$ and growing along the channel.

3.2 Elliptic Model

3.2.1 Introduction

A non-orthogonal structured mesh is used to discretise the solution domain in the elliptic model. The use of transfinite interpolation in mesh generation as described in Wang et al. [48] provides the capability of dividing the domain to more than one panel in each coordinate direction. In each panel, nodes are distributed independently to control mesh refinement in desired areas (e.g., near a wall or interface). In this work, separate panels are used for the liquid and gas regions. These two regions are separated by a smooth interface. The non-orthogonal mesh enables the precise grid adaption to the interface changing shape along a channel or over a tube. The gas region bottom boundary is spatially coincident with the liquid region top boundary. The liquid–gas interface consists of two rows of zero-width control volumes as shown in Figure 3.3. Each row represents the interface of one of the phases. Figure 3.3 shows a sample complete computational grid for liquid–gas flow in a channel. In the y direction, the liquid region has $N_{y,L}$ uniform control volumes in one panel and the gas region has total number of $N_{y,G}$ control volumes that could be divided into more than one panel if necessary. In the x direction, N_x interior control volumes are used.

As shown in Figure 3.3, j_{BL} to $j_{EL} + 1$ and $j_{BG} - 1$ to $j_{EG} + 1$ belong to the liquid region and gas

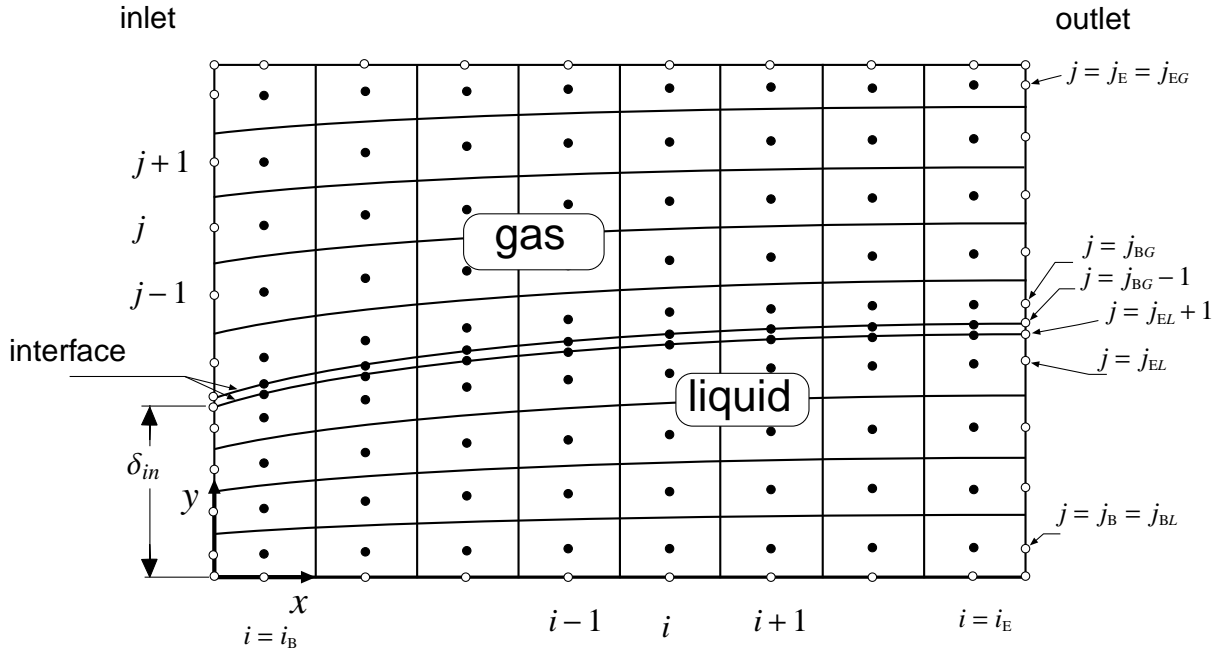


Figure 3.3: Grid information in the liquid and gas regions; the spacing between the nodes at the interface is exaggerated for illustration purposes.

region, respectively. Each control volume is identified by a pair of indices (i, j) that is changing in an organized fashion. The i index proceeds from $i_B = 2$ for the first interior control volume on the west side of the domain to $i_E = N_x + 1$ for the last interior control volume on the east. Along the y direction, the j index proceeds from $j_B = 2$ to $j_{EL} + 1 = N_{y,L} + 2$ in the liquid region and from $j_{BG} - 1 = N_{y,L} + 3$ to $j_{EG} = N_{y,L} + N_{y,G} + 3$ in the gas region.

The zero-width control volumes of the interface are located at $j = j_{EL} + 1$ and $j = j_{BG} - 1$ which are at the same physical location. In Figure 3.3, however, the spacing between these two rows are exaggerated to emphasize that they are two separate sets of nodes. The domain boundary nodes are also zero-width control volumes that are used to implement the boundary conditions. These nodes are referenced by $i_B - 1$ on the west, $i_E + 1$ on the east, $j_B - 1$ on the south, and $j_E + 1$ on the north.

3.2.2 Grid Nomenclature

A typical control volume P and its eight neighbours are presented in Figure 3.4. The neighbouring control volumes are referred by compass notation relative to the centre node P . The faces of the central control volume, P , are distinguished by lower case letters according to their relative location to the centre. Each control volume consists of four quadrants as shown in Figure 3.5. These

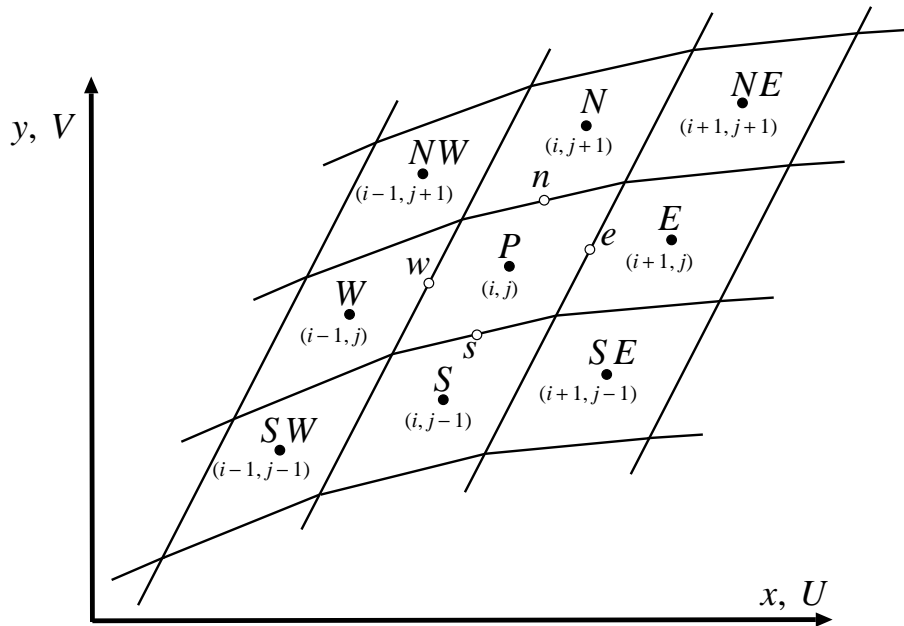


Figure 3.4: Computational molecule: indexing and notation.

quadrants are referred to by geographical directions, northeast (NE), southeast (SE), northwest (NW), and southwest (SW). The points on the faces of the control volume P are located at the centre of each face. The location of centre node P is indicated by $(X_{SW}(i, j), Y_{SW}(i, j))$. The coordinates of points P , e , n , and ne (the solid points in Figure 3.5) are calculated and stored for each control volume. The location of other points are derived from the locations stored for neighbouring control volumes.

The nomenclature for control volume distances, areas, and volumes is shown in Figure 3.6. The distances are calculated based on the coordinates of the first and second endpoints. Each quadrant

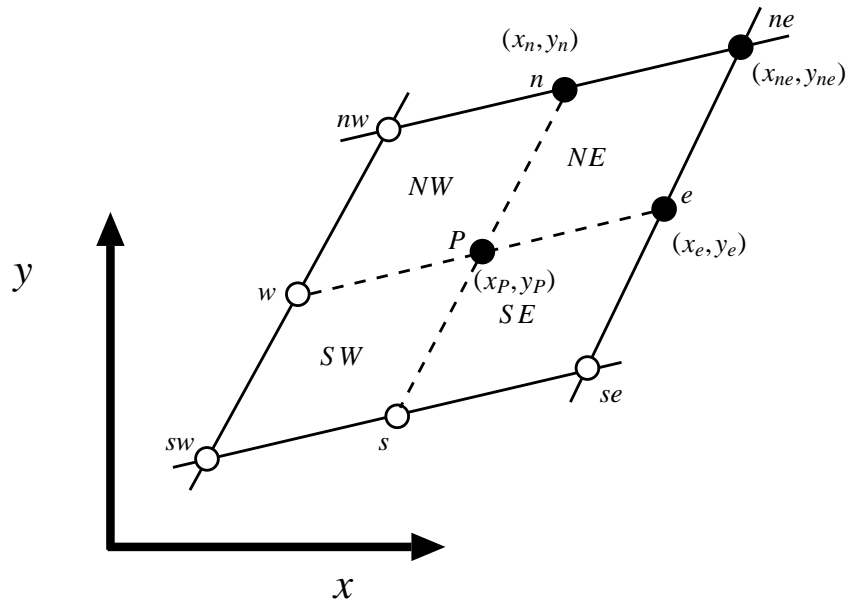


Figure 3.5: Coordinates of control volume points and quadrant notation.

in a control volume is divided into two triangles. The areas of these two triangles are calculated and then added to calculate the area of each quadrant. Unit depth is used to compute the areas and volumes.

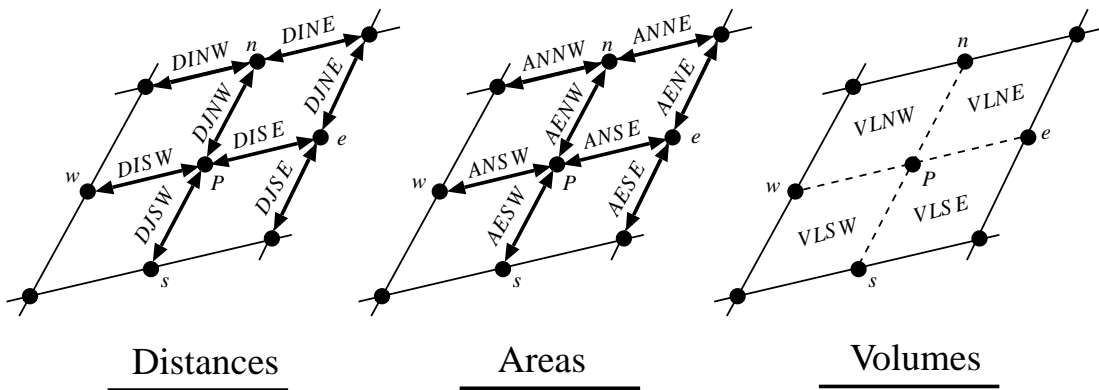


Figure 3.6: Distances, areas and volumes of a control volume.

The accurate evaluation of different quantities in non-orthogonal grid needs introduction of some local directional unit vectors, because the non-orthogonal grid will not be necessarily aligned

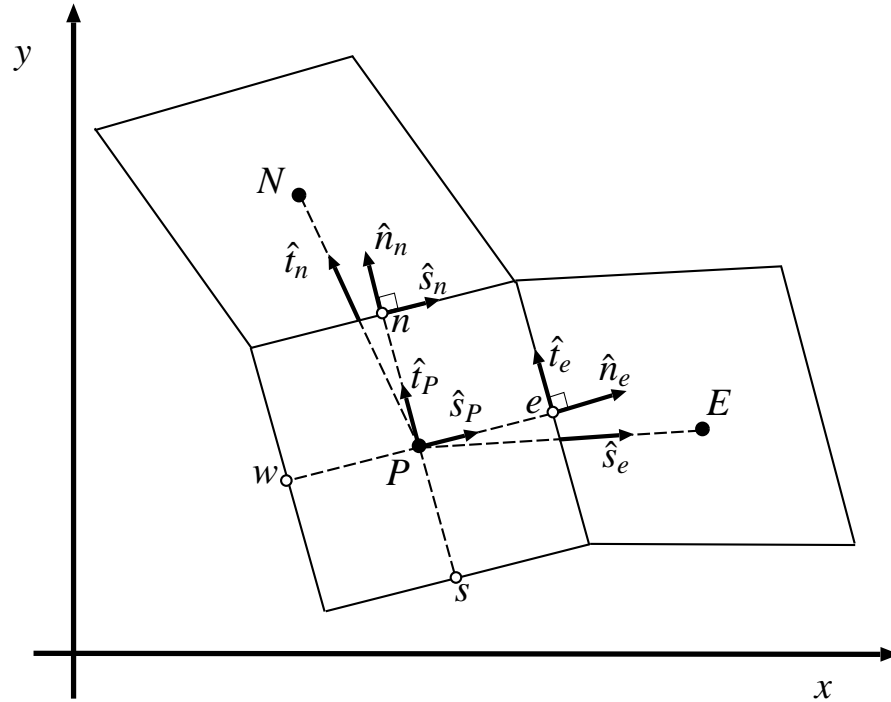


Figure 3.7: Grid directional unit vectors.

with the Cartesian coordinate directions. Figure 3.7 shows directions of unit vectors at the east and north faces and the central node of the main control volume. In general, the \hat{s} vectors denote moving along the i index and the \hat{t} vectors denote moving along the j index and they are not necessarily aligned with the Cartesian unit vectors \hat{i} and \hat{j} . The unit vector \hat{n} is normal to the faces of the P control volume. The unit vectors on the east face, north face, and centre of the control volume are referred by subscripts e , n , and P , respectively. The unit vectors \hat{t}_e and \hat{s}_n are tangent to the east and north face, respectively. \hat{s}_e gives the direction of the line that connects nodal point P and its first neighbouring node on the east. \hat{t}_n gives the direction of the line that connects nodal point P and its first neighbouring node on the north. \hat{t}_p and \hat{s}_p determine the directions of the imaginary lines between the nodal point P and the central points of its faces. The unit vectors at the west and south faces of the control volume P, (i, j) , are identical to those at east and north of the control volumes $(i - 1, j)$ and $(i, j - 1)$, respectively. The unit vectors shown in Figure 3.7 are

defined in terms of their component in the x and y directions as following:

$$\left. \begin{aligned}
 \hat{n}_n &= \left. \frac{\partial x}{\partial n} \right|_n \hat{i} + \left. \frac{\partial y}{\partial n} \right|_n \hat{j} = n_{xn} \hat{i} + n_{yn} \hat{j} \\
 \hat{n}_e &= \left. \frac{\partial x}{\partial n} \right|_e \hat{i} + \left. \frac{\partial y}{\partial n} \right|_e \hat{j} = n_{xe} \hat{i} + n_{ye} \hat{j} \\
 \hat{s}_n &= \left. \frac{\partial x}{\partial s} \right|_n \hat{i} + \left. \frac{\partial y}{\partial s} \right|_n \hat{j} = s_{xn} \hat{i} + s_{yn} \hat{j} \\
 \hat{s}_e &= \left. \frac{\partial x}{\partial s} \right|_e \hat{i} + \left. \frac{\partial y}{\partial s} \right|_e \hat{j} = s_{xe} \hat{i} + s_{ye} \hat{j} \\
 \hat{s}_p &= \left. \frac{\partial x}{\partial s} \right|_p \hat{i} + \left. \frac{\partial y}{\partial s} \right|_p \hat{j} = s_{xp} \hat{i} + s_{yp} \hat{j} \\
 \hat{t}_n &= \left. \frac{\partial x}{\partial t} \right|_n \hat{i} + \left. \frac{\partial y}{\partial t} \right|_n \hat{j} = t_{xn} \hat{i} + t_{yn} \hat{j} \\
 \hat{t}_e &= \left. \frac{\partial x}{\partial t} \right|_e \hat{i} + \left. \frac{\partial y}{\partial t} \right|_e \hat{j} = t_{xe} \hat{i} + t_{ye} \hat{j} \\
 \hat{t}_p &= \left. \frac{\partial x}{\partial t} \right|_p \hat{i} + \left. \frac{\partial y}{\partial t} \right|_p \hat{j} = t_{xp} \hat{i} + t_{yp} \hat{j}
 \end{aligned} \right\} \quad (3.16)$$

The variables assigned to distances used in the computations for a non-orthogonal grid are shown in Figure 3.8. These distances could be calculated using the definitions presented in Figure 3.6. For nodal point P, $(ds)_P$ and $(dt)_P$ are:

$$(ds)_{P(i,j)} = DISW_{(i,j)} + DISE_{(i,j)} \quad (3.17)$$

$$(dt)_{P(i,j)} = DJSW_{(i,j)} + DJNW_{(i,j)} \quad (3.18)$$

The distances $(dt)_e$ and $(ds)_n$ along the east and north faces are defined as:

$$(dt)_{e(i,j)} = DJSE_{(i,j)} + DJNE_{(i,j)} \quad (3.19)$$

$$(ds)_{n(i,j)} = DINW_{(i,j)} + DINE_{(i,j)} \quad (3.20)$$

Equations (3.21) and (3.22) calculate the distance between node P and node E along the \hat{s}_e vector and the distance between node P and node N along the \hat{t}_n vector:

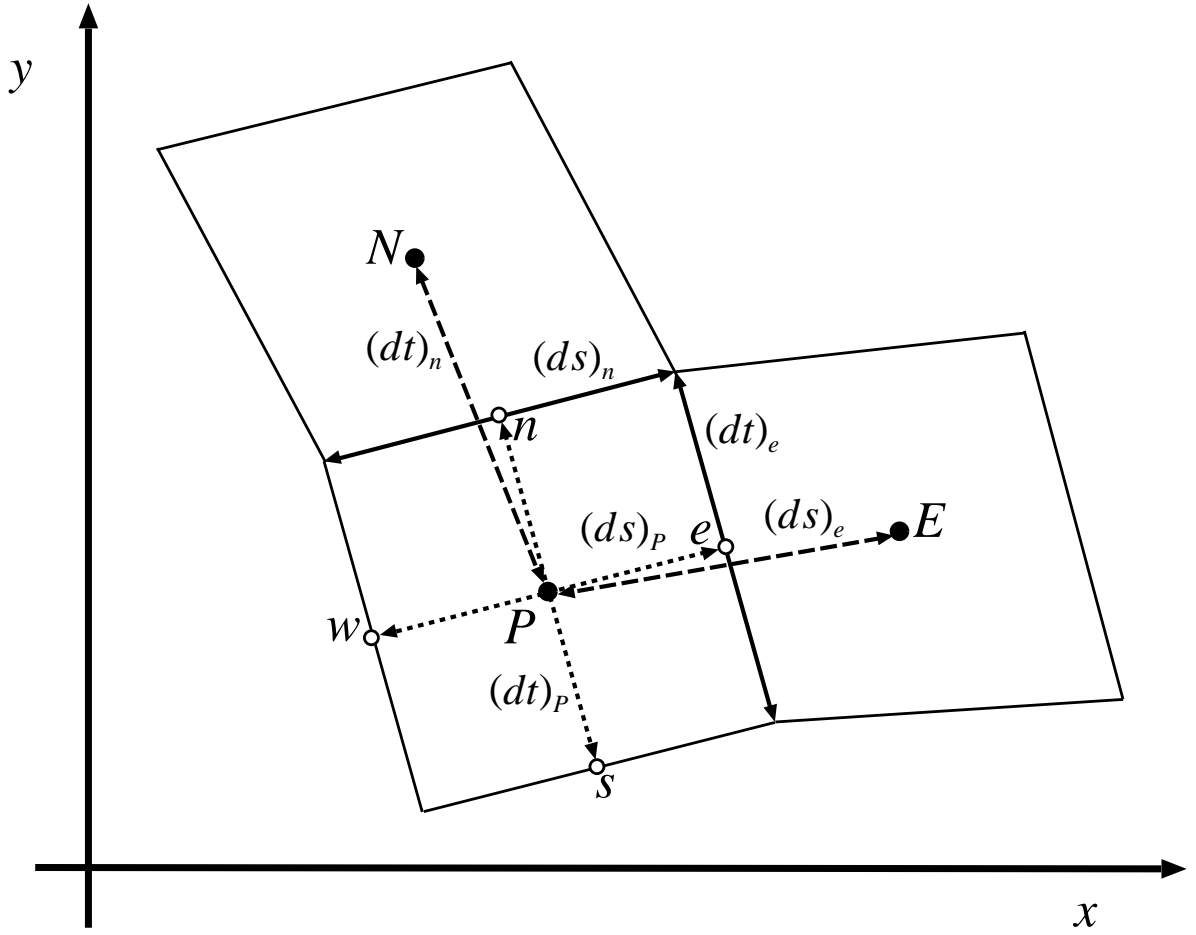


Figure 3.8: Location of distance variables.

$$(ds)_{e(i,j)} = \sqrt{(XS W_{(i+1,j)} - XS W_{(i,j)})^2 + (YS W_{(i+1,j)} - YS W_{(i,j)})^2} \quad (3.21)$$

$$(dt)_{n(i,j)} = \sqrt{(XS W_{(i,j+1)} - XS W_{(i,j)})^2 + (YS W_{(i,j+1)} - YS W_{(i,j)})^2} \quad (3.22)$$

Using the definitions for distances in a non-orthogonal grid, the components of the unit vectors

are defined as follows:

$$\left. \begin{aligned}
 \hat{n}_{n(i,j)} &= \frac{-(YNE_{(i,j)}-YNE_{(i-1,j)})}{(ds)_{n(i,j)}} \hat{i} + \frac{(XNE_{(i,j)}-XNE_{(i-1,j)})}{(ds)_{n(i,j)}} \hat{j} \\
 \hat{n}_{e(i,j)} &= \frac{(YNE_{(i,j)}-YNE_{(i,j-1)})}{(dt)_{e(i,j)}} \hat{i} + \frac{-(XNE_{(i,j)}-XNE_{(i,j-1)})}{(dt)_{e(i,j)}} \hat{j} \\
 \hat{s}_{n(i,j)} &= \frac{(XNE_{(i,j)}-XNE_{(i-1,j)})}{(ds)_{n(i,j)}} \hat{i} + \frac{(YNE_{(i,j)}-YNE_{(i-1,j)})}{(ds)_{n(i,j)}} \hat{j} \\
 \hat{s}_{e(i,j)} &= \frac{(XSW_{(i+1,j)}-XSW_{(i,j)})}{(ds)_{e(i,j)}} \hat{i} + \frac{(YSW_{(i+1,j)}-YSW_{(i,j)})}{(ds)_{e(i,j)}} \hat{j} \\
 \hat{s}_{p(i,j)} &= \frac{(XSE_{(i,j)}-XSE_{(i-1,j)})}{(ds)_{p(i,j)}} \hat{i} + \frac{(YSE_{(i,j)}-YSE_{(i-1,j)})}{(ds)_{p(i,j)}} \hat{j} \\
 \hat{t}_{n(i,j)} &= \frac{(XSW_{(i,j+1)}-XSW_{(i,j)})}{(dt)_{n(i,j)}} \hat{i} + \frac{(YSW_{(i,j+1)}-YSW_{(i,j)})}{(dt)_{n(i,j)}} \hat{j} \\
 \hat{t}_{e(i,j)} &= \frac{(XNE_{(i,j)}-XNE_{(i,j-1)})}{(dt)_{e(i,j)}} \hat{i} + \frac{(YNE_{(i,j)}-YNE_{(i,j-1)})}{(dt)_{e(i,j)}} \hat{j} \\
 \hat{t}_{p(i,j)} &= \frac{(XNW_{(i,j)}-XNW_{(i,j-1)})}{(dt)_{p(i,j)}} \hat{i} + \frac{(YNW_{(i,j)}-YNW_{(i,j-1)})}{(dt)_{p(i,j)}} \hat{j}
 \end{aligned} \right\} \quad (3.23)$$

3.2.3 Grid Expansion Factor

To refine the grid in the desired regions where rapid changes in solution field variables occur, an expansion factor could be applied to the boundaries of each panel in the grid domain. An expansion factor is defined such that the ratio of the length of the neighbouring control volume edges along a grid boundary is fixed. This geometric expansion factor can be used independently at each side of a grid segment. Equation (3.24) shows the expansion factor along the south boundary of a grid:

$$S = \frac{(ds)_{i+1,j_B-1}}{(ds)_{i,j_B-1}} \quad (3.24)$$

The grid cells are expanding if $S > 1$, contracting if $S < 1$, and uniform if $S = 1$. When the control volumes are non-uniformly spaced between the vertices of the grid in one panel, it is crucial to ensure smooth transition between grid panels.

3.2.4 Grid Assembly

Applying a panelling technique provides the advantage of producing grids that matches the shape of a complicated solution domain and controlling mesh refinement where it is required. In the case of a parallel plate channel, two separate panels are used for the liquid and the gas regions. In the y direction, the liquid region has $N_{y,L}$ uniform control volumes in one panel and the gas region has total number of $N_{y,G}$ control volumes divided into two panels. In the gas region, the mesh is refined adjacent to the interface and the upper wall. In the x direction only one panel with an expanding grid is used in each phase. There is a total of three panels in the configuration.

In the case of a horizontal tube, more panels and some with an arc along their edges are required. Figure 3.9 shows an illustrative example of grid assembly around a tube. In this example, twenty-one panels are used to construct the overall computational domain. In Figure 3.9, the film thickness is magnified and the boundaries of the panel are shown thicker for the purpose of the illustration. In the y direction, one panel in the liquid region and two panels in the gas region are used. In the x direction, the liquid and gas regions are divided to seven panels, e.g. panels 1 and 2 cover the falling film before the tube top stagnation point, panels 3, 4, and 5 cover the film around the tube, and panels 6 and 7 cover the liquid film after the bottom stagnation point. The control volumes are uniformly spaced in the y direction in the liquid and are refined in the gas region toward the interface. To resolve the flow near the top and bottom of the tube accurately, a sufficient number of nodes are required in the panels 2, 3, 5, and 6.

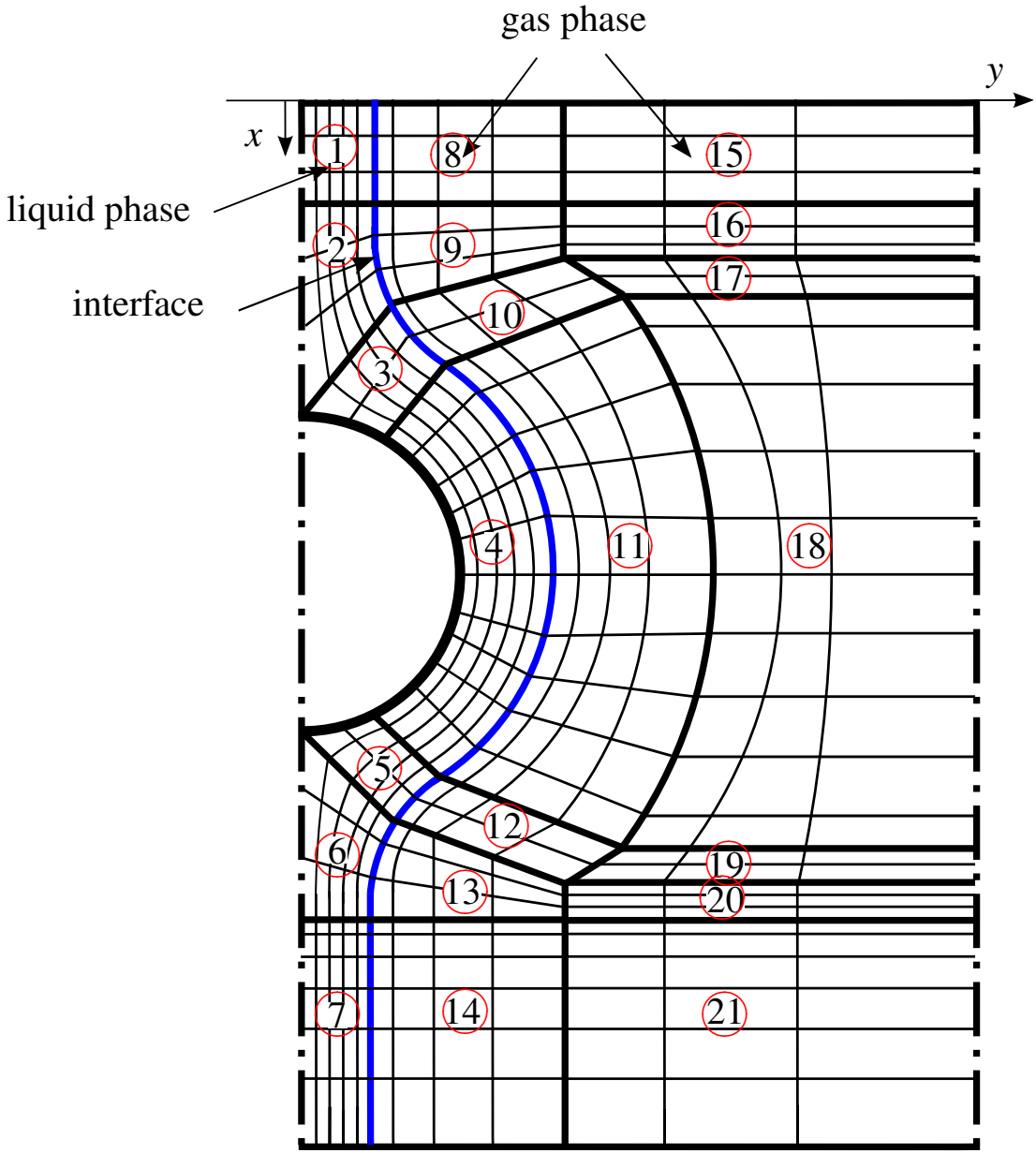


Figure 3.9: Example of grid assembly for falling film absorption over a horizontal tube.

Chapter 4

Numerical Solution Method

4.1 Introduction

In this chapter, the partial differential equations in the liquid and gas phases are discretised using a finite volume method [49] to obtain a set of algebraic equations for solution variables. The details of the discretisation approaches in the parabolic and elliptic models are presented in the following sections.

4.2 Discretisation of the Governing Equations in Parabolic Model

The transformed governing equations are integrated over a typical interior control volume of thickness $d\eta$ and length $d\chi$ using a finite volume method. The resulting algebraic equations require north, south, east, and west face values for all the variables and properties. Plus variable gradients are needed at north and south faces of a control volume. All the properties and the field variables are stored at the centre of a control volume. In addition, a Newton-Raphson Linearisation is used for all the non-linear terms. The details of the methods followed in discretising the governing equations will be discussed in the following sections.

4.2.1 Face values for Variables

The east and west values for $\Phi = \{U_L, T_L, \xi_W, U_G, T_G\}$, is calculated using the upwind scheme:

$$\Phi_e = \Phi_P, \quad \Phi_w = \Phi_W \quad (4.1)$$

At the north and south faces, an exponential differencing scheme (EDS) is applied:

$$\Phi_n = (0.5 + \alpha_n) \Phi_P + (0.5 - \alpha_n) \Phi_N, \quad \Phi_s = (0.5 + \alpha_s) \Phi_S + (0.5 - \alpha_s) \Phi_P \quad (4.2)$$

The exponential differencing scheme is also used to determine the derivatives at the north and south faces:

$$\left. \frac{\partial \Phi}{\partial \eta} \right|_n = \beta_n \frac{\Phi_N - \Phi_P}{\eta_N - \eta_P}, \quad \left. \frac{\partial \Phi}{\partial \eta} \right|_s = \beta_s \frac{\Phi_P - \Phi_S}{\eta_P - \eta_S} \quad (4.3)$$

where,

$$\alpha_n = \frac{0.5\text{Pe}_n^2}{5 + \text{Pe}_n^2}, \quad \alpha_s = \frac{0.5\text{Pe}_s^2}{5 + \text{Pe}_s^2} \quad (4.4)$$

$$\beta_n = \frac{1 + 0.005\text{Pe}_n^2}{1 + 0.05\text{Pe}_n^2}, \quad \beta_s = \frac{1 + 0.005\text{Pe}_s^2}{1 + 0.05\text{Pe}_s^2} \quad (4.5)$$

For the liquid region ($0 \leq \eta \leq 1$):

$$\text{Pe}_n = \frac{\delta J_n'' (\eta_N - \eta_P)}{D_n}, \quad \text{Pe}_s = \frac{\delta J_s'' (\eta_P - \eta_S)}{D_s} \quad (4.6)$$

For the gas region ($1 \leq \eta \leq 2$):

$$\text{Pe}_n = \frac{(H - \delta) J_n'' (\eta_N - \eta_P)}{D_n}, \quad \text{Pe}_s = \frac{(H - \delta) J_s'' (\eta_P - \eta_S)}{D_s} \quad (4.7)$$

The diffusion coefficient D for U , T , and ξ_w equations is μ , $\frac{k}{C_p}$, and ρD^{AB} , respectively. The normal mass flow rate, J , is stored at the north face of each control volume:

$$J_n = J_P, \quad J_s = J_S \quad (4.8)$$

The film thickness is assumed to vary linearly across a station:

$$\delta_e = 2\delta_p - \delta_w \quad (4.9)$$

4.2.2 Face Values for Properties

The east and west face values for the thermodynamic properties (ρ, μ, k, C_p , and D^{AB}) are determined using the upwind scheme. For example, the value of density at the east and west faces are calculated as:

$$\rho_e = \rho_P, \quad \rho_w = \rho_W \quad (4.10)$$

The north and south face values are evaluated using a harmonic mean:

$$\rho_n = \frac{\rho_P \rho_N}{\mathcal{W}_n \rho_P + (1 - \mathcal{W}_n) \rho_N}, \quad \rho_s = \frac{\rho_S \rho_P}{\mathcal{W}_s \rho_S + (1 - \mathcal{W}_s) \rho_P} \quad (4.11)$$

where,

$$\mathcal{W}_n = \frac{\eta_N - \eta_n}{\eta_N - \eta_P}, \quad \mathcal{W}_s = \frac{\eta_P - \eta_s}{\eta_P - \eta_S} \quad (4.12)$$

4.2.3 Newton-Raphson Linearisation

If $\Psi = f(\Phi_1, \Phi_2, \Phi_3)$ and $\Phi_1, \Phi_2,$ and Φ_3 are one of the field variables $\{U_L, T_L, J_L, \xi_W, U_G, T_G, J_G, \delta, \frac{dP}{dX}\}$, the general Newton-Raphson Linearisation would give the following:

$$\Psi^n = \Psi^o + \frac{\partial \Psi^o}{\partial \Phi_1} (\Phi_1^n - \Phi_1^o) + \frac{\partial \Psi^o}{\partial \Phi_2} (\Phi_2^n - \Phi_2^o) + \frac{\partial \Psi^o}{\partial \Phi_3} (\Phi_3^n - \Phi_3^o) \quad (4.13)$$

The superscript ‘ n ’ refers to the current iteration and ‘ o ’ refers to the previous iteration.

4.2.4 Discretisation Steps

In this section, discretisation of the liquid energy equation is presented to illustrate the discretisation process. For the other governing equations the same process is used. For brevity, only the coefficients of the liquid energy equation are shown in this section.

Step 1: Integrate Equation (3.6) over a control volume.

$$\begin{aligned} & \int_w^e \int_s^n \frac{\partial}{\partial \chi} [\delta \rho_L U_L (C_{p,L} T_L + \xi_W (\bar{h}_W - \bar{h}_{LiBr}))] d\eta d\chi + \\ & \int_w^e \int_s^n \frac{\partial}{\partial \eta} [J_L'' (C_{p,L} T_L + \xi_W (\bar{h}_W - \bar{h}_{LiBr}))] d\eta d\chi = \\ & \int_w^e \int_s^n \frac{\partial}{\partial \eta} \left(\frac{k_L}{\delta} \frac{\partial T_L}{\partial \eta} \right) d\eta d\chi + \int_w^e \int_s^n \frac{\partial}{\partial \eta} \left(\frac{\rho_L D_L^{AB}}{\delta} \frac{\partial \xi_W}{\partial \eta} (\bar{h}_W - \bar{h}_{LiBr}) \right) d\eta d\chi \end{aligned} \quad (4.14)$$

$$\begin{aligned}
 & \int_w^e \frac{\partial}{\partial \chi} \left[\delta \rho_L U_L (C_{p,L} T_L + \xi_W (\bar{h}_W - \bar{h}_{LiBr})) \right] \Delta \eta d\chi + \\
 & \int_w^e \left[J''_{Ln} (C_{p,Ln} T_{Ln} + \xi_{Wn} (\bar{h}_{Wn} - \bar{h}_{LiBrn})) \right] d\chi - \int_w^e \left[J''_{Ls} (C_{p,Ls} T_{Ls} + \xi_{Ws} (\bar{h}_{Ws} - \bar{h}_{LiBr_s})) \right] d\chi \\
 & = \int_w^e \left(\frac{k_{Ln}}{\delta_P} \frac{\partial T_L}{\partial \eta} \Big|_n - \frac{k_{Ls}}{\delta_P} \frac{\partial T_L}{\partial \eta} \Big|_s \right) d\chi + \\
 & \int_w^e \left(\frac{\rho_{Ln} D_{Ln}^{AB}}{\delta_P} (\bar{h}_{Wn} - \bar{h}_{LiBrn}) \frac{\partial \xi_W}{\partial \eta} \Big|_n - \frac{\rho_{Ls} D_{Ls}^{AB}}{\delta_P} (\bar{h}_{Ws} - \bar{h}_{LiBr_s}) \frac{\partial \xi_W}{\partial \eta} \Big|_s \right) d\chi
 \end{aligned} \tag{4.15}$$

And we know $J = J'' \Delta \chi$:

$$\begin{aligned}
 & \delta_e \rho_{Le} U_{Le} C_{p,Le} T_{Le} \Delta \eta - \delta_w \rho_{Lw} U_{Lw} C_{p,Lw} T_{Lw} \Delta \eta \\
 & + \delta_e \rho_{Le} U_{Le} (\bar{h}_{We} - \bar{h}_{LiBr_e}) \xi_{We} \Delta \eta - \delta_w \rho_{Lw} U_{Lw} (\bar{h}_{Ww} - \bar{h}_{LiBr_w}) \xi_{Ww} \Delta \eta \\
 & + J_{Ln} C_{p,Ln} T_{Ln} + J_{Ln} \xi_{Wn} (\bar{h}_{Wn} - \bar{h}_{LiBrn}) - J_{Ls} C_{p,Ls} T_{Ls} - J_{Ls} \xi_{Ws} (\bar{h}_{Ws} - \bar{h}_{LiBr_s}) \\
 & = \frac{k_{Ln}}{\delta_P} \frac{\partial T_L}{\partial \eta} \Big|_n \Delta \chi - \frac{k_{Ls}}{\delta_P} \frac{\partial T_L}{\partial \eta} \Big|_s \Delta \chi \\
 & + \frac{\rho_{Ln} D_{Ln}^{AB}}{\delta_P} (\bar{h}_{Wn} - \bar{h}_{LiBrn}) \frac{\partial \xi_W}{\partial \eta} \Big|_n \Delta \chi - \frac{\rho_{Ls} D_{Ls}^{AB}}{\delta_P} (\bar{h}_{Ws} - \bar{h}_{LiBr_s}) \frac{\partial \xi_W}{\partial \eta} \Big|_s \Delta \chi
 \end{aligned} \tag{4.16}$$

Step 2: Use the upwind differencing scheme to obtain the east face and west face values in terms of nodal values, Equation (4.8) for the north and south face mass fluxes, Equation (4.9) for the east film thickness, and apply Newton-Raphson linearisation to non-linear terms.

$$\begin{aligned}
& (2\rho_{Le}C_{p,Le}\Delta\eta)\left[\delta_P U_{LP}^o T_{LP}^o + \delta_P^o U_{LP} T_{LP}^o + \delta_P^o U_{LP}^o T_{LP} - 2\delta_P^o U_{LP}^o T_{LP}^o\right] \\
& \quad - (\delta_w \rho_{Le} C_{p,Le} \Delta\eta) \left[U_{LP} T_{LP}^o + U_{LP}^o T_{LP} - U_{LP}^o T_{LP}^o \right] - (\delta_w \rho_{Lw} U_{Lw} C_{p,Lw} T_{Lw} \Delta\eta) \\
& \quad + (2\rho_{Le}(\bar{h}_{W_e} - \bar{h}_{LiBr_e})\Delta\eta)\left[\delta_P U_{LP}^o \xi_{WP}^o + \delta_P^o U_{LP} \xi_{WP}^o + \delta_P^o U_{LP}^o \xi_{WP} - 2\delta_P^o U_{LP}^o \xi_{WP}^o\right] \\
& \quad - (\delta_w \rho_{Le}(\bar{h}_{W_e} - \bar{h}_{LiBr_e})\Delta\eta)\left[U_{LP} \xi_{WP}^o + U_{LP}^o \xi_{WP} - U_{LP}^o \xi_{WP}^o \right] - (\delta_w \rho_{Lw} U_{Lw}(\bar{h}_{W_w} - \bar{h}_{LiBr_w})\xi_{Ww} \Delta\eta) \\
& \quad + C_{p,L_n} [J_{L_n} T_{L_n}^o + J_{L_n}^o T_{L_n} - J_{L_n}^o T_{L_n}^o] + (\bar{h}_{W_n} - \bar{h}_{LiBr_n}) [J_{L_n} \xi_{W_n}^o + J_{L_n}^o \xi_{W_n} - J_{L_n}^o \xi_{W_n}^o] \\
& \quad - C_{p,L_s} [J_{L_s} T_{L_s}^o + J_{L_s}^o T_{L_s} - J_{L_s}^o T_{L_s}^o] - (\bar{h}_{W_s} - \bar{h}_{LiBr_s}) [J_{L_s} \xi_{W_s}^o + J_{L_s}^o \xi_{W_s} - J_{L_s}^o \xi_{W_s}^o] \\
& \quad = \frac{k_{L_n} \Delta\chi}{\delta_P^o} \left[\left. \frac{\partial T_L}{\partial \eta} \right|_n - \frac{1}{\delta_P^o} \left. \frac{\partial T_L}{\partial \eta} \right|_n^o \delta_P + \left. \frac{\partial T_L}{\partial \eta} \right|_n^o \right] \\
& \quad - \frac{k_{L_s} \Delta\chi}{\delta_P^o} \left[\left. \frac{\partial T_L}{\partial \eta} \right|_s - \frac{1}{\delta_P^o} \left. \frac{\partial T_L}{\partial \eta} \right|_s^o \delta_P + \left. \frac{\partial T_L}{\partial \eta} \right|_s^o \right] \\
& \quad + \frac{\rho_{L_n} D_{L_n}^{AB} (\bar{h}_{W_n} - \bar{h}_{LiBr_n}) \Delta\chi}{\delta_P^o} \left[\left. \frac{\partial \xi_W}{\partial \eta} \right|_n - \frac{1}{\delta_P^o} \left. \frac{\partial \xi_W}{\partial \eta} \right|_n^o \delta_P + \left. \frac{\partial \xi_W}{\partial \eta} \right|_n^o \right] \\
& \quad - \frac{\rho_{L_s} D_{L_s}^{AB} (\bar{h}_{W_s} - \bar{h}_{LiBr_s}) \Delta\chi}{\delta_P^o} \left[\left. \frac{\partial \xi_W}{\partial \eta} \right|_s - \frac{1}{\delta_P^o} \left. \frac{\partial \xi_W}{\partial \eta} \right|_s^o \delta_P + \left. \frac{\partial \xi_W}{\partial \eta} \right|_s^o \right]
\end{aligned} \tag{4.17}$$

where superscript “ o ” refers to the previous iteration.

Step 3: Approximate η -direction derivatives and use a diffusion weight

$$\begin{aligned}
 & (2\rho_{Le}C_{p,Le}\Delta\eta)\left[\delta_P U_{LP}^o T_{LP}^o + \delta_P^o U_{LP} T_{LP}^o + \delta_P^o U_{LP}^o T_{LP} - 2\delta_P^o U_{LP}^o T_{LP}^o\right] \\
 & \quad - \left(\delta_w \rho_{Lw} C_{p,Lw} \Delta\eta\right)\left[U_{LP} T_{LP}^o + U_{LP}^o T_{LP} - U_{LP}^o T_{LP}^o\right] - \left(\delta_w \rho_{Lw} U_{Lw} C_{p,Lw} T_{Lw} \Delta\eta\right) \\
 & \quad + \left(2\rho_{Le}\left(\bar{h}_{W_e} - \bar{h}_{LiBr_e}\right)\Delta\eta\right)\left[\delta_P U_{LP}^o \xi_{WP}^o + \delta_P^o U_{LP} \xi_{WP}^o + \delta_P^o U_{LP}^o \xi_{WP} - 2\delta_P^o U_{LP}^o \xi_{WP}^o\right] \\
 & \quad - \left(\delta_w \rho_{Lw}\left(\bar{h}_{W_w} - \bar{h}_{LiBr_w}\right)\Delta\eta\right)\left[U_{LP} \xi_{WP}^o + U_{LP}^o \xi_{WP} - U_{LP}^o \xi_{WP}^o\right] - \left(\delta_w \rho_{Lw} U_{Lw}\left(\bar{h}_{W_w} - \bar{h}_{LiBr_w}\right)\xi_{W_w} \Delta\eta\right) \\
 & \quad + C_{p,L_n}\left[J_{L_n} T_{L_n}^o + J_{L_n}^o T_{L_n} - J_{L_n}^o T_{L_n}^o\right] + \left(\bar{h}_{W_n} - \bar{h}_{LiBr_n}\right)\left[J_{L_n} \xi_{W_n}^o + J_{L_n}^o \xi_{W_n} - J_{L_n}^o \xi_{W_n}^o\right] \\
 & \quad - C_{p,L_s}\left[J_{L_s} T_{L_s}^o + J_{L_s}^o T_{L_s} - J_{L_s}^o T_{L_s}^o\right] - \left(\bar{h}_{W_s} - \bar{h}_{LiBr_s}\right)\left[J_{L_s} \xi_{W_s}^o + J_{L_s}^o \xi_{W_s} - J_{L_s}^o \xi_{W_s}^o\right] \\
 & \quad = \frac{k_{L_n} \Delta\chi}{\delta_P^o} \left[\beta_{L_n}^T \frac{T_{L_n} - T_{LP}}{\eta_N - \eta_P} - \frac{1}{\delta_P^o} \frac{\partial T_L}{\partial \eta} \Big|_n^o \delta_P + \frac{\partial T_L}{\partial \eta} \Big|_n^o \right] \\
 & \quad - \frac{k_{L_s} \Delta\chi}{\delta_P^o} \left[\beta_{L_s}^T \frac{T_{LP} - T_{L_s}}{\eta_P - \eta_S} - \frac{1}{\delta_P^o} \frac{\partial T_L}{\partial \eta} \Big|_s^o \delta_P + \frac{\partial T_L}{\partial \eta} \Big|_s^o \right] \\
 & \quad + \frac{\rho_{L_n} D_{L_n}^{AB} \left(\bar{h}_{W_n} - \bar{h}_{LiBr_n}\right) \Delta\chi}{\delta_P^o} \left[\beta_{L_n}^\xi \frac{\xi_{W_n} - \xi_{WP}}{\eta_N - \eta_P} - \frac{1}{\delta_P^o} \frac{\partial \xi_W}{\partial \eta} \Big|_n^o \delta_P + \frac{\partial \xi_W}{\partial \eta} \Big|_n^o \right] \\
 & \quad - \frac{\rho_{L_s} D_{L_s}^{AB} \left(\bar{h}_{W_s} - \bar{h}_{LiBr_s}\right) \Delta\chi}{\delta_P^o} \left[\beta_{L_s}^\xi \frac{\xi_{WP} - \xi_{W_s}}{\eta_P - \eta_S} - \frac{1}{\delta_P^o} \frac{\partial \xi_W}{\partial \eta} \Big|_s^o \delta_P + \frac{\partial \xi_W}{\partial \eta} \Big|_s^o \right]
 \end{aligned} \tag{4.18}$$

Step 4: Apply a generalized advection scheme for north and south face values, factor out the dependent variables, and group terms to determine the coefficients of the liquid energy equation:

$$\begin{aligned}
 & A_{L,S}^{T,J} J_{L,S} + A_{L,S}^{T,T} T_{L,S} + A_{L,S}^{T,\xi} \xi_{L,S} + A_{L,P}^{T,U} U_{L,P} + A_{L,P}^{T,J} J_{L,P} + A_{L,P}^{T,T} T_{L,P} + A_{L,P}^{T,\xi} \xi_{L,P} + \\
 & \quad A_{L,N}^{T,T} T_{L,N} + A_{L,N}^{T,\xi} \xi_{L,N} + A_{L,P}^{T,\delta} \delta_P = B_{L,P}^T
 \end{aligned} \tag{4.19}$$

where,

$$A_{L,S}^{T,J} = -C_{p,L_s} T_{L_s}^o - \left(\bar{h}_{W_s} - \bar{h}_{LiBr_s}\right) \xi_{W_s}^o \tag{4.20}$$

$$A_{L,S}^{T,T} = -C_{p,L_s} J_{L_s}^o \left(0.5 + \alpha_{L_s}^T\right) - \frac{k_{L_s} \beta_{L_s}^T \Delta\chi}{\delta_P^o (\eta_P - \eta_S)} \tag{4.21}$$

$$A_{L,S}^{T,\xi} = -\left(\bar{h}_{W_s} - \bar{h}_{LiBr_s}\right) J_{L_s}^o \left(0.5 + \alpha_{L_s}^\xi\right) - \frac{\rho_{L_s} D_{L_s}^{AB} \beta_{L_s}^\xi \left(\bar{h}_{W_s} - \bar{h}_{LiBr_s}\right) \Delta\chi}{\delta_P^o (\eta_P - \eta_S)} \tag{4.22}$$

$$A_{L,P}^{T,U} = 2\rho_{L_e}C_{p,L_e}\Delta\eta T_{LP}^o\delta_p^o - \delta_w\rho_{L_e}C_{p,L_e}\Delta\eta T_{LP}^o + 2\rho_{L_e}(\bar{h}_{W_e} - \bar{h}_{LiBr_e})\Delta\eta\delta_p^o\xi W_p^o - \delta_w\rho_{L_e}(\bar{h}_{W_e} - \bar{h}_{LiBr_e})\Delta\eta\xi W_p^o \quad (4.23)$$

$$A_{L,P}^{T,J} = C_{p,L_n}T_{L_n}^o + (\bar{h}_{W_n} - \bar{h}_{LiBr_n})\xi W_n^o \quad (4.24)$$

$$A_{L,P}^{T,T} = 2\rho_{L_e}C_{p,L_e}\Delta\eta U_{LP}^o\delta_p^o - \delta_w\rho_{L_e}C_{p,L_e}\Delta\eta U_{LP}^o + C_{p,L_n}J_{LP}^o(0.5 + \alpha_{L_n}^T) - C_{p,L_s}J_{L_s}^o(0.5 - \alpha_{L_s}^T) + \frac{k_{L_n}\beta_{L_n}^T\Delta\chi}{\delta_p^o(\eta_N - \eta_P)} + \frac{k_{L_s}\beta_{L_s}^T\Delta\chi}{\delta_p^o(\eta_P - \eta_S)} \quad (4.25)$$

$$A_{L,P}^{T,\xi} = 2\rho_{L_e}(\bar{h}_{W_e} - \bar{h}_{LiBr_e})\Delta\eta\delta_p^o U_{LP}^o - \delta_w\rho_{L_e}(\bar{h}_{W_e} - \bar{h}_{LiBr_e})\Delta\eta U_{LP}^o + (\bar{h}_{W_n} - \bar{h}_{LiBr_n})J_{LP}^o(0.5 + \alpha_{L_n}^{\xi}) - (\bar{h}_{W_s} - \bar{h}_{LiBr_s})J_{L_s}^o(0.5 - \alpha_{L_s}^{\xi}) + \frac{\rho_{L_n}D_{L_n}^{AB}\beta_{L_n}^{\xi}(\bar{h}_{W_n} - \bar{h}_{LiBr_n})\Delta\chi}{\delta_p^o(\eta_N - \eta_P)} + \frac{\rho_{L_s}D_{L_s}^{AB}\beta_{L_s}^{\xi}(\bar{h}_{W_s} - \bar{h}_{LiBr_s})\Delta\chi}{\delta_p^o(\eta_P - \eta_S)} \quad (4.26)$$

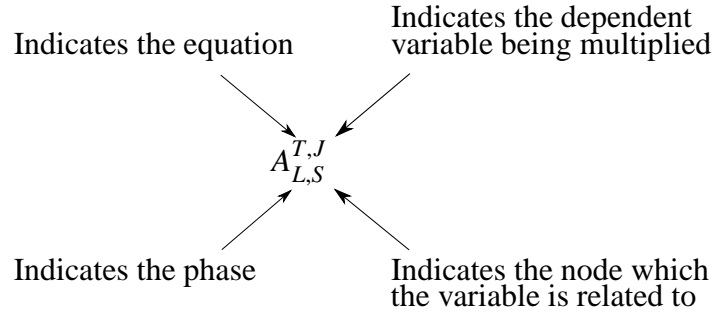
$$A_{L,N}^{T,T} = C_{p,L_n}J_{LP}^o(0.5 - \alpha_{L_n}^T) - \frac{k_{L_n}\beta_{L_n}^T\Delta\chi}{\delta_p^o(\eta_N - \eta_P)} \quad (4.27)$$

$$A_{L,N}^{T,\xi} = -(\bar{h}_{W_n} - \bar{h}_{LiBr_n})J_{LP}^o(0.5 - \alpha_{L_n}^{\xi}) - \frac{\rho_{L_n}D_{L_n}^{AB}\beta_{L_n}^{\xi}(\bar{h}_{W_n} - \bar{h}_{LiBr_n})\Delta\chi}{\delta_p^o(\eta_N - \eta_P)} \quad (4.28)$$

$$A_{L,P}^{T,\delta} = 2\rho_{L_e}C_{p,L_e}\Delta\eta T_{LP}^o U_{LP}^o + 2\rho_{L_e}(\bar{h}_{W_e} - \bar{h}_{LiBr_e})\Delta\eta U_{LP}^o\xi W_p^o + \frac{k_{L_n}\Delta\chi}{(\delta_p^o)^2} \frac{\partial T_L}{\partial \eta} \Big|_n - \frac{k_{L_s}\Delta\chi}{(\delta_p^o)^2} \frac{\partial T_L}{\partial \eta} \Big|_s + \frac{\rho_{L_n}D_{L_n}^{AB}(\bar{h}_{W_n} - \bar{h}_{LiBr_n})\Delta\chi}{(\delta_p^o)^2} \frac{\partial \xi W}{\partial \eta} \Big|_n - \frac{\rho_{L_s}D_{L_s}^{AB}(\bar{h}_{W_s} - \bar{h}_{LiBr_s})\Delta\chi}{(\delta_p^o)^2} \frac{\partial \xi W}{\partial \eta} \Big|_s \quad (4.29)$$

$$B_{L,P}^T = 4\rho_{L_e}C_{p,L_e}\Delta\eta\delta_p^o T_{LP}^o U_{LP}^o - \delta_w\rho_{L_e}C_{p,L_e}\Delta\eta T_{LP}^o U_{LP}^o + 4\rho_{L_e}\Delta\eta(\bar{h}_{W_e} - \bar{h}_{LiBr_e})\delta_p^o U_{LP}^o\xi W_p^o - \delta_w\rho_{L_e}\Delta\eta(\bar{h}_{W_e} - \bar{h}_{LiBr_e})U_{LP}^o\xi W_p^o + \delta_w\rho_{L_w}U_{LW}C_{p,L_w}T_{LW}\Delta\eta + \delta_w\rho_{L_w}\Delta\eta(\bar{h}_{W_w} - \bar{h}_{LiBr_w})U_{LW}\xi W_w + C_{p,L_n}J_{LP}^o T_{L_n}^o + (\bar{h}_{W_n} - \bar{h}_{LiBr_n})J_{LP}^o\xi W_n^o - C_{p,L_s}J_{L_s}^o T_{L_s}^o - (\bar{h}_{W_s} - \bar{h}_{LiBr_s})J_{L_s}^o\xi W_s^o + \frac{k_{L_n}\Delta\chi}{\delta_p^o} \frac{\partial T_L}{\partial \eta} \Big|_n - \frac{k_{L_s}\Delta\chi}{\delta_p^o} \frac{\partial T_L}{\partial \eta} \Big|_s + \frac{\rho_{L_n}D_{L_n}^{AB}(\bar{h}_{W_n} - \bar{h}_{LiBr_n})\Delta\chi}{\delta_p^o} \frac{\partial \xi W}{\partial \eta} \Big|_n - \frac{\rho_{L_s}D_{L_s}^{AB}(\bar{h}_{W_s} - \bar{h}_{LiBr_s})\Delta\chi}{\delta_p^o} \frac{\partial \xi W}{\partial \eta} \Big|_s \quad (4.30)$$

The coefficients of the algebraic equation are represented as follows:



4.2.5 Algebraic Equations

Algebraic equations of all the other governing equations after discretisation are as follows:

- The liquid phase continuity equation, Equation (3.4), becomes:

$$A_{L,S}^{J,J} J_{L,S} + A_{L,P}^{J,U} U_{L,P} + A_{L,P}^{J,J} J_{L,P} + A_{L,P}^{J,\delta} \delta_P = B_{L,P}^J \quad (4.31)$$

- The liquid phase momentum equation, Equation (3.5), becomes:

$$A_{L,S}^{U,U} U_{L,S} + A_{L,S}^{U,J} J_{L,S} + A_{L,P}^{U,U} U_{L,P} + A_{L,P}^{U,J} J_{L,P} + A_{L,N}^{U,U} U_{L,N} + A_{L,P}^{U,\delta} \delta_P + A_{L,P}^{U,P} \left(\frac{dP}{d\chi} \right)_P = B_{L,P}^U \quad (4.32)$$

- The liquid phase mass fraction equation, Equation (3.7), becomes:

$$A_{L,S}^{\xi,J} J_{L,S} + A_{L,S}^{\xi,\xi} \xi_{L,S} + A_{L,P}^{\xi,U} U_{L,P} + A_{L,P}^{\xi,J} J_{L,P} + A_{L,P}^{\xi,\xi} \xi_{L,P} + A_{L,N}^{\xi,\xi} \xi_{L,N} + A_{L,P}^{\xi,\delta} \delta_P = B_{L,P}^\xi \quad (4.33)$$

- The gas phase continuity equation, Equation (3.8), becomes:

$$A_{G,S}^{J,J} J_{G,S} + A_{G,P}^{J,U} U_{G,P} + A_{G,P}^{J,J} J_{G,P} + A_{G,P}^{J,\delta} \delta_P = B_{G,P}^J \quad (4.34)$$

- The gas phase momentum equation, Equation (3.9), becomes:

$$A_{G,S}^{U,U} U_{G,S} + A_{G,S}^{U,J} J_{G,S} + A_{G,P}^{U,U} U_{G,P} + A_{G,P}^{U,J} J_{G,P} + A_{G,N}^{U,U} U_{G,N} + A_{G,P}^{U,\delta} \delta_P + A_{G,P}^{U,P} \left(\frac{dP}{d\chi} \right)_P = B_{G,P}^U \quad (4.35)$$

- The gas phase energy equation, Equation (3.10), becomes:

$$A_{G,S}^{T,J} J_{G,S} + A_{G,S}^{T,T} T_{G,S} + A_{G,P}^{T,U} U_{G,P} + A_{G,P}^{T,J} J_{G,P} + A_{G,P}^{T,T} T_{G,P} + A_{G,N}^{T,T} T_{G,N} + A_{G,P}^{T,\delta} \delta_P = B_{G,P}^T \quad (4.36)$$

The coefficients of the liquid mass fraction algebraic equation, Equation (4.33), are presented in Appendix C.1. The coefficients of the discretised continuity and momentum equations in the liquid region and the coefficients of discretised continuity, momentum, and energy equations in the gas region are given in Appendix D of Siow [47].

Algebraic equations of the interface conditions are as follows:

- Discretisation and combination of velocity and shear continuity at the interface, Equation (3.11), leads to the following equation:

$$A_{\text{intf},S}^{U,U} U_{L,S} + A_{\text{intf},P}^{U,U} U_{G,P} + A_{\text{intf},N}^{U,U} U_{G,N} + A_{\text{intf},P}^{U,\delta} \delta_P = B_{\text{intf},P}^U \quad (4.37)$$

- The absorbed mass continuity equation, Equation (3.12), becomes:

$$A_{\text{intf},S}^{J,J} J_{L,S} + A_{\text{intf},P}^{J,J} J_{G,P} = B_{\text{intf},P}^J \quad (4.38)$$

- The temperature continuity equation, Equation (2.10), becomes:

$$A_{\text{intf},P}^{T,T} T_{G,P} + A_{\text{intf},P}^{T,\xi} \xi_{G,P} + A_{\text{intf},P}^{T,P} \left(\frac{dP}{d\chi} \right)_P = B_{\text{intf},P}^T \quad (4.39)$$

- The LiBr impermeability equation, Equation (3.13), becomes:

$$A_{\text{intf},S}^{\xi,\xi} \xi_{L,S} + A_{\text{intf},P}^{\xi,J} J_{G,P} + A_{\text{intf},P}^{\xi,\xi} \xi_{L,P} + A_{\text{intf},P}^{\xi,\delta} \delta_P = B_{\text{intf},P}^{\xi} \quad (4.40)$$

- The energy continuity equation, Equation (3.14) becomes:

$$A_{\text{intf},S}^{\delta,T} T_{L,S} + A_{\text{intf},P}^{\delta,J} J_{G,P} + A_{\text{intf},P}^{\delta,T} T_{G,P} + A_{\text{intf},N}^{\delta,T} T_{G,N} + A_{\text{intf},P}^{\delta,\delta} \delta_P = B_{\text{intf},P}^{\delta} \quad (4.41)$$

The overall mass conservation, Equation (3.15) is approximated as the summation of the mass flows at east faces of each column of control volumes:

$$\sum_{jL=1}^{N_{y,L}-1} A_{L,jL}^{P,U} U_{L,jL} + \sum_{jG=1}^{N_{y,G}} A_{G,jG}^{P,U} U_{G,jG} + A_P^{P,\delta} \delta_P = B_P^P \quad (4.42)$$

The coefficients of Equations (4.37) to (4.42) are given in Appendix C.2.

4.2.6 Solution Method

An in-house computer code was developed using Fortran 95 to compute the equation coefficients and solve the above set of linear algebraic equations.

4.2.6.1 Construction of the Matrix

Starting at the first station, a full matrix is constructed using the discretised governing Equations (4.19) and (4.31) to 4.33 for the liquid region, Equations (4.34) to (4.36) for the gas region, and Equations (4.37) to (4.41) for the interface boundary conditions and the overall mass balance, Equation (4.42). The unknowns in the matrix are the variables U , J , T , ξ_w , and scalars δ and $dP/d\chi$. The U -momentum equations is solved for U , the continuity equation for J , the energy equation for T , the liquid mass fraction equation for ξ_w , the interface energy continuity equation for δ and the global mass balance equation for $dP/d\chi$. The coefficients of four variables U , J , T , and ξ_w make up a 4×4 block matrix for each control volume which is an element in the full matrix. Equation (4.43) shows how the bordered block matrix is set up:

Equation (4.43) can be written as

$$\begin{bmatrix} \mathbf{A}_{BTDM} & \mathbf{E}_2 \\ \mathbf{E}_1 & \mathbf{E}_3 \end{bmatrix} \begin{bmatrix} \mathbf{X}_1 \\ \mathbf{X}_2 \end{bmatrix} = \begin{bmatrix} \mathbf{B}_1 \\ \mathbf{B}_2 \end{bmatrix} \quad (4.44)$$

where, \mathbf{A}_{BTDM} is a block-tridiagonal matrix of size $(N \times N)$, \mathbf{E}_1 , \mathbf{E}_2 and \mathbf{E}_3 are $(2 \times N)$, $(N \times 2)$, (2×2) block matrices, respectively, \mathbf{B}_1 and \mathbf{X}_1 are $(N \times 1)$ vectors, \mathbf{B}_2 and \mathbf{X}_2 are (2×1) vectors, and $N = 4(N_{y,L} + N_{y,G} - 1)$.

Equation (4.44) can be transformed into following equations:

$$\begin{bmatrix} \mathbf{A}_{BTDM} & \mathbf{O} \\ \mathbf{E}_1 & \mathbf{I} \end{bmatrix} \begin{bmatrix} \mathbf{I} & \mathbf{A}_{BTDM}^{-1} \mathbf{E}_2 \\ \mathbf{O} & \mathbf{E}_3 - \mathbf{E}_1 \mathbf{A}_{BTDM}^{-1} \mathbf{E}_2 \end{bmatrix} \begin{bmatrix} \mathbf{X}_1 \\ \mathbf{X}_2 \end{bmatrix} = \begin{bmatrix} \mathbf{B}_1 \\ \mathbf{B}_2 \end{bmatrix} \quad (4.45)$$

$$\begin{bmatrix} \mathbf{A}_{BTDM} & \mathbf{O} \\ \mathbf{E}_1 & \mathbf{I} \end{bmatrix} \begin{bmatrix} \mathbf{F}_1 \\ \mathbf{F}_2 \end{bmatrix} = \begin{bmatrix} \mathbf{B}_1 \\ \mathbf{B}_2 \end{bmatrix} \quad (4.46)$$

where,

$$\begin{bmatrix} \mathbf{F}_1 \\ \mathbf{F}_2 \end{bmatrix} = \begin{bmatrix} \mathbf{I} & \mathbf{A}_{BTDM}^{-1} \mathbf{E}_2 \\ \mathbf{O} & \mathbf{E}_3 - \mathbf{E}_1 \mathbf{A}_{BTDM}^{-1} \mathbf{E}_2 \end{bmatrix} \begin{bmatrix} \mathbf{X}_1 \\ \mathbf{X}_2 \end{bmatrix} \quad (4.47)$$

Equation (4.46) can be written as the combination of two matrix equations:

$$\mathbf{A}_{BTDM} \mathbf{F}_1 = \mathbf{B}_1 \quad (4.48)$$

$$\mathbf{E}_1 \mathbf{F}_1 + \mathbf{F}_2 = \mathbf{B}_2 \quad (4.49)$$

\mathbf{F}_1 in Equation (4.48) is determined using the BTDMA method. Since \mathbf{A}_{BTDM} is an $(N \times N)$ matrix and \mathbf{B}_1 is an $(N \times 1)$ vector, the result \mathbf{F}_1 is also an $(N \times 1)$ vector. Next, \mathbf{F}_2 , a (2×1) vector, is calculated from Equation (4.49).

If \mathbf{F}_3 is defined as follows:

$$\mathbf{F}_3 = \mathbf{A}_{BTDM}^{-1} \mathbf{E}_2 \quad (4.50)$$

$$\mathbf{A}_{BTDM} \mathbf{F}_3 = \mathbf{E}_2 \quad (4.51)$$

Equation (4.51) can be solved using BTDMA. Since \mathbf{E}_2 is an $(N \times 2)$ matrix, BTDMA has to be applied twice to get \mathbf{F}_3 , an $(N \times 2)$ matrix.

Substitution of Equation (4.50) into Equation (4.47) results in:

$$\mathbf{X}_1 + \mathbf{F}_3 \mathbf{X}_2 = \mathbf{F}_1 \quad (4.52)$$

$$(\mathbf{E}_3 - \mathbf{E}_1 \mathbf{F}_3) \mathbf{X}_2 = \mathbf{F}_2 \quad (4.53)$$

$(\mathbf{E}_3 - \mathbf{E}_1 \mathbf{F}_3)$ is a (2×2) matrix and thus Equation (4.53) can be easily solved using Cramer's rule to obtain \mathbf{X}_2 . Finally, \mathbf{X}_1 is calculated from Equation (4.52).

4.2.6.3 Solution Procedure and Convergence

Because of non-linearities, an iterative approach is needed to arrive at a solution. The coefficients of the matrix are calculated based on an initial guess for velocity, mass flux, temperature, water mass fraction, film thickness and the pressure gradient. When the matrix is solved directly at one station, the new solution obtained is compared with the values from the previous iteration. If the convergence criterion is not met, the coefficients are re-calculated with the new results and the matrix is re-solved. Convergence of the solution is declared at each station when the maximum relative change, Equation (4.54), of all unknowns is less than 10^{-7} .

$$\epsilon^\phi = \left| \frac{\Phi^n - \Phi^{n-1}}{\Phi^n} \right| \quad (4.54)$$

In addition to maximum relative change in solution variables, the residual of the linearised governing equations were checked at each station but not used as a convergence test. The average residual values were found to be typically less than 1×10^{-7} . After the converged solution is obtained for one station, the computation proceeds along the channel until the flow solution is terminated. The flow solution could be terminated by one of the following conditions: (1) the marching reaches the end of the channel, (2) the absorption process ends (discussed later), or (3) there is a negative axial velocity. The last condition typically corresponds to the situation where all of the inlet vapour mass has been absorbed.

4.3 Discretisation of the Governing Equations in Elliptic Model

In the elliptic model, a co-located variable storage scheme is applied, so that all the unknowns are located at the centre, P, of a typical non-orthogonal control volume as shown in Figure 4.1. The mass flow rate at each face of the control volume is determined by the face velocities. These velocities are determined at the integration point (ip) located at the centre of the face of the control volume (e, w, n, or s). Other fluxes are determined using the face value and gradient of the independent variables evaluated at the integration points. These fluxes are assumed constant along the face. Using the non-orthogonal grid results in a nine-point computational molecule, consisting of

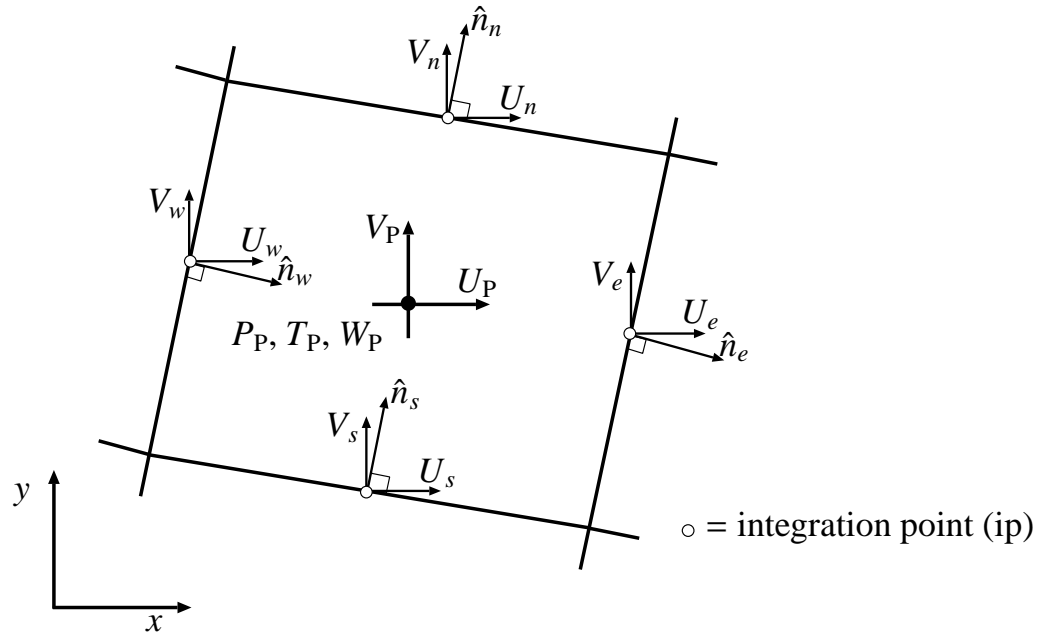


Figure 4.1: Co-located variable storage scheme.

the central node and its eight neighbouring nodes shown in Figure 3.4, for each field variable (U , V , P , and T in both phases, and ξ_w in the liquid phase). The values at the corners of the control volume (ne, nw, se, and sw) are estimated by linear interpolation, Figure 3.5. The discretisation procedure used in the elliptic model is applicable to both the liquid and gas phases. The liquid phase is chosen to show the discretisation details because the temperature equation of this phase

has extra terms compared to the gas phase and in this study the mass fraction equation is applied to the liquid phase only.

4.3.1 Algebraic Transport Equations

In this section, the details of the liquid phase governing equations discretisation are presented. The same methodology is applied to discretise the gas phase governing equations.

4.3.1.1 Liquid Phase Continuity Equation

The discretisation of Equation (2.21) yields to the following equation:

$$\begin{aligned} & \rho A_e (U_e n_{xe} + V_e n_{ye}) - \rho A_w (U_w n_{xw} + V_w n_{yw}) \\ & + \rho A_n (U_n n_{xn} + V_n n_{yn}) - \rho A_s (U_s n_{xs} + V_s n_{ys}) + \frac{\nabla_P (\rho_P - \rho_P^o)}{\Delta t} = 0 \end{aligned} \quad (4.55)$$

where U_e and V_e are face velocity components and n_{xe} and n_{ye} are the components of the normal unit vector on the east face. Note that the normal unit vector is outward on the east and north faces and inward on the west and south faces. In the development of the coupled algebraic equations, unsuperscripted variable represent values at the new time step; variables with “ o ” indicate the previous time step values. Equation (4.55) can be written as the balance of the mass flow rates as follows:

$$\dot{m}_e - \dot{m}_w + \dot{m}_n - \dot{m}_s + \frac{\nabla_P (\rho_P - \rho_P^o)}{\Delta t} = 0 \quad (4.56)$$

A pressure-weighted interpolation method (PWIM) based on the work of Rhie and Chow [51] is applied to estimate the face velocities. The PWIM estimations for the east and west face velocities are as follows. The estimation of the north and south face velocities follows the same procedure.

$$U_e = \mathcal{W}_e U_P + (1 - \mathcal{W}_e) U_E - \hat{d}_e^u \frac{\partial P}{\partial x} \Big|_e + \tilde{b}_e^u \quad (4.57)$$

$$U_w = \mathcal{W}_w U_W + (1 - \mathcal{W}_w) U_P - \hat{d}_w^u \frac{\partial P}{\partial x} \Big|_w + \tilde{b}_w^u \quad (4.58)$$

$$V_e = \mathcal{W}_e V_P + (1 - \mathcal{W}_e) V_E - \hat{d}_e^v \left. \frac{\partial P}{\partial y} \right|_e + \tilde{b}_e^v \quad (4.59)$$

$$V_w = \mathcal{W}_w V_W + (1 - \mathcal{W}_w) V_P - \hat{d}_w^v \left. \frac{\partial P}{\partial y} \right|_w + \tilde{b}_w^v \quad (4.60)$$

where \mathcal{W} is a geometric linear interpolation at the face of the control volume and is defined as follows for the east and west faces:

$$\mathcal{W}_{e(i,j)} = \frac{\text{DISW}_{(i+1,j)}}{\text{DISE}_{(i,j)} + \text{DISW}_{(i+1,j)}} \quad (4.61)$$

$$\mathcal{W}_{w(i,j)} = \mathcal{W}_{e(i-1,j)} = \frac{\text{DISW}_{(i,j)}}{\text{DISE}_{(i-1,j)} + \text{DISW}_{(i,j)}} \quad (4.62)$$

and

$$\tilde{b}_e^u = \hat{d}_e^u \left\{ \mathcal{W}_e \left. \frac{\partial P}{\partial x} \right|_P^o + (1 - \mathcal{W}_e) \left. \frac{\partial P}{\partial x} \right|_E^o \right\} + \frac{\rho}{\Delta t} \hat{d}_e^u \left\{ U_e^o - [\mathcal{W}_e U_P^o + (1 - \mathcal{W}_e) U_E^o] \right\} \quad (4.63)$$

$$\tilde{b}_w^u = \hat{d}_w^u \left\{ \mathcal{W}_w \left. \frac{\partial P}{\partial x} \right|_W^o + (1 - \mathcal{W}_w) \left. \frac{\partial P}{\partial x} \right|_P^o \right\} + \frac{\rho}{\Delta t} \hat{d}_w^u \left\{ U_w^o - [\mathcal{W}_w U_W^o + (1 - \mathcal{W}_w) U_P^o] \right\} \quad (4.64)$$

$$\tilde{b}_e^v = \hat{d}_e^v \left\{ \mathcal{W}_e \left. \frac{\partial P}{\partial y} \right|_P^o + (1 - \mathcal{W}_e) \left. \frac{\partial P}{\partial y} \right|_E^o \right\} + \frac{\rho}{\Delta t} \hat{d}_e^v \left\{ V_e^o - [\mathcal{W}_e V_P^o + (1 - \mathcal{W}_e) V_E^o] \right\} \quad (4.65)$$

$$\tilde{b}_w^v = \hat{d}_w^v \left\{ \mathcal{W}_w \left. \frac{\partial P}{\partial y} \right|_W^o + (1 - \mathcal{W}_w) \left. \frac{\partial P}{\partial y} \right|_P^o \right\} + \frac{\rho}{\Delta t} \hat{d}_w^v \left\{ V_w^o - [\mathcal{W}_w V_W^o + (1 - \mathcal{W}_w) V_P^o] \right\} \quad (4.66)$$

$$\hat{d}_e^\phi = \nabla_w \left\{ \frac{\mathcal{W}_e}{(a_P^{\phi,\phi})_P} + \frac{(1 - \mathcal{W}_e)}{(a_P^{\phi,\phi})_E} \right\} \quad (4.67)$$

$$\hat{d}_w^\phi = \nabla_e \left\{ \frac{\mathcal{W}_w}{(a_P^{\phi,\phi})_W} + \frac{(1 - \mathcal{W}_w)}{(a_P^{\phi,\phi})_P} \right\} \quad (4.68)$$

In Equations (4.67) and (4.68), ϕ is u or v and $a_P^{\phi,\phi}$ is the nodal points coefficients in the U or V momentum equations. In order to compute the face volumes (∇_e and ∇_w), each control volume is divided into quadrants by lines connecting the integration points e to w and n to s in Figure 3.7. The volume at an integration point is the summation of the volumes of the quadrants adjacent to the face. The pressure gradients at faces in Equations (4.57) to (4.60) are evaluated using the

appropriate combination of co-ordinate derivatives $(\frac{\partial x}{\partial s}, \frac{\partial x}{\partial t}, \frac{\partial y}{\partial s}, \frac{\partial y}{\partial t})$ and derivatives of pressure in the \hat{s} and \hat{t} directions on a non-orthogonal grid. Using the chain rule and Cramer's rule, the derivatives in the x and y directions on face f are defined as follows:

$$\frac{\partial \Phi}{\partial x} \Big|_f = \mathcal{Y}_{t,f} \frac{\partial \Phi}{\partial s} \Big|_f - \mathcal{Y}_{s,f} \frac{\partial \Phi}{\partial t} \Big|_f \quad (4.69)$$

$$\frac{\partial \Phi}{\partial y} \Big|_f = \mathcal{X}_{s,f} \frac{\partial \Phi}{\partial t} \Big|_f - \mathcal{X}_{t,f} \frac{\partial \Phi}{\partial s} \Big|_f \quad (4.70)$$

where,

$$\mathcal{X}_{s,f} = \frac{\frac{\partial x}{\partial s} \Big|_f}{\left(\frac{\partial x}{\partial s} \Big|_f \frac{\partial y}{\partial t} \Big|_f - \frac{\partial x}{\partial t} \Big|_f \frac{\partial y}{\partial s} \Big|_f \right)} \quad (4.71)$$

$$\mathcal{X}_{t,f} = \frac{\frac{\partial x}{\partial t} \Big|_f}{\left(\frac{\partial x}{\partial s} \Big|_f \frac{\partial y}{\partial t} \Big|_f - \frac{\partial x}{\partial t} \Big|_f \frac{\partial y}{\partial s} \Big|_f \right)} \quad (4.72)$$

$$\mathcal{Y}_{s,f} = \frac{\frac{\partial y}{\partial s} \Big|_f}{\left(\frac{\partial x}{\partial s} \Big|_f \frac{\partial y}{\partial t} \Big|_f - \frac{\partial x}{\partial t} \Big|_f \frac{\partial y}{\partial s} \Big|_f \right)} \quad (4.73)$$

$$\mathcal{Y}_{t,f} = \frac{\frac{\partial y}{\partial t} \Big|_f}{\left(\frac{\partial x}{\partial s} \Big|_f \frac{\partial y}{\partial t} \Big|_f - \frac{\partial x}{\partial t} \Big|_f \frac{\partial y}{\partial s} \Big|_f \right)} \quad (4.74)$$

As shown in Figure 3.7, there are two direction vectors, \hat{s} and \hat{t} , for each face and central node of the main control volume. The x and y derivatives for each face in Equations (4.69) and (4.70) should be approximated using the nodal and corner values indicated as ne , nw , se , and sw in Figure 3.5:

$$\frac{\partial \Phi}{\partial x} \Big|_e = \frac{\mathcal{Y}_{t,e}}{(ds)_e} (\Phi_E - \Phi_P) - \frac{\mathcal{Y}_{s,e}}{(dt)_e} (\Phi_{ne} - \Phi_{se}) \quad (4.75)$$

$$\frac{\partial \Phi}{\partial y} \Big|_e = \frac{\mathcal{X}_{s,e}}{(dt)_e} (\Phi_{ne} - \Phi_{se}) - \frac{\mathcal{X}_{t,e}}{(ds)_e} (\Phi_E - \Phi_P) \quad (4.76)$$

$$\left. \frac{\partial \Phi}{\partial x} \right|_w = \frac{\mathcal{Y}_{t,w}}{(ds)_w} (\Phi_P - \Phi_W) - \frac{\mathcal{Y}_{s,w}}{(dt)_w} (\Phi_{nw} - \Phi_{sw}) \quad (4.77)$$

$$\left. \frac{\partial \Phi}{\partial y} \right|_w = \frac{\mathcal{X}_{s,w}}{(dt)_w} (\Phi_{nw} - \Phi_{sw}) - \frac{\mathcal{X}_{t,w}}{(ds)_w} (\Phi_P - \Phi_W) \quad (4.78)$$

$$\left. \frac{\partial \Phi}{\partial x} \right|_n = \frac{\mathcal{Y}_{t,n}}{(ds)_n} (\Phi_{ne} - \Phi_{nw}) - \frac{\mathcal{Y}_{s,n}}{(dt)_n} (\Phi_N - \Phi_P) \quad (4.79)$$

$$\left. \frac{\partial \Phi}{\partial y} \right|_n = \frac{\mathcal{X}_{s,n}}{(dt)_n} (\Phi_N - \Phi_P) - \frac{\mathcal{X}_{t,n}}{(ds)_n} (\Phi_{ne} - \Phi_{nw}) \quad (4.80)$$

$$\left. \frac{\partial \Phi}{\partial x} \right|_s = \frac{\mathcal{Y}_{t,s}}{(ds)_s} (\Phi_{se} - \Phi_{sw}) - \frac{\mathcal{Y}_{s,s}}{(dt)_s} (\Phi_P - \Phi_S) \quad (4.81)$$

$$\left. \frac{\partial \Phi}{\partial y} \right|_s = \frac{\mathcal{X}_{s,s}}{(dt)_s} (\Phi_P - \Phi_S) - \frac{\mathcal{X}_{t,s}}{(ds)_s} (\Phi_{se} - \Phi_{sw}) \quad (4.82)$$

The values at the control volume corners are calculated using a geometric interpolation in a non-uniform grid:

$$\Phi_{ne} = C_{ne1} \Phi_P + C_{ne2} \Phi_E + C_{ne3} \Phi_{NE} + C_{ne4} \Phi_N \quad (4.83)$$

$$\Phi_{nw} = C_{nw1} \Phi_W + C_{nw2} \Phi_P + C_{nw3} \Phi_N + C_{nw4} \Phi_{NW} \quad (4.84)$$

$$\Phi_{se} = C_{se1} \Phi_S + C_{se2} \Phi_{SE} + C_{se3} \Phi_E + C_{se4} \Phi_P \quad (4.85)$$

$$\Phi_{sw} = C_{sw1} \Phi_{SW} + C_{sw2} \Phi_S + C_{sw3} \Phi_P + C_{sw4} \Phi_W \quad (4.86)$$

where the numbering of C coefficients starts from 1 at the left bottom corner node and goes counter-clockwise around the control volume.

The nodal gradients of pressure in Equations (4.63) to (4.66) are calculated using the following equations:

$$\left. \frac{\partial \Phi}{\partial x} \right|_P = \frac{\mathcal{Y}_{t,P}}{(ds)_P} (\Phi_e - \Phi_w) - \frac{\mathcal{Y}_{s,P}}{(dt)_P} (\Phi_n - \Phi_s) \quad (4.87)$$

$$\left. \frac{\partial \Phi}{\partial y} \right|_P = \frac{\mathcal{X}_{s,P}}{(dt)_P} (\Phi_n - \Phi_s) - \frac{\mathcal{X}_{t,P}}{(ds)_P} (\Phi_e - \Phi_w) \quad (4.88)$$

The face values are computed by geometric interpolation using surrounding nodal values.

After substitution of Equations (4.83) to (4.86) into Equations (4.75) to (4.82) for variable P , the pressure gradients on the faces are approximated in terms of nodal pressure values. Now, the liquid continuity algebraic equation can be written in terms of nodal velocity and pressure values:

$$a_P^{c,p} P_P + \sum a_{NB8}^{c,p} P_{NB8} + a_P^{c,u} U_P + \sum a_{NB4}^{c,u} U_{NB4} + a_P^{c,v} V_P + \sum a_{NB4}^{c,v} V_{NB4} = b_P^c \quad (4.89)$$

The first and second superscripts of the a coefficients refer to the equation label and the multiplied variable, respectively. In summations, $NB4=\{E,W,N,S\}$ and $NB8=\{NB4,NE,NW,SE,SW\}$. The details of the summations are:

$$\sum a_{NB4}^{c,\phi} \Phi_{NB4} = a_E^{c,\phi} \Phi_E + a_W^{c,\phi} \Phi_W + a_N^{c,\phi} \Phi_N + a_S^{c,\phi} \Phi_S \quad (4.90)$$

and,

$$\sum a_{NB8}^{c,\phi} \Phi_{NB8} = \sum a_{NB4}^{c,\phi} \Phi_{NB4} + a_{NE}^{c,\phi} \Phi_{NE} + a_{NW}^{c,\phi} \Phi_{NW} + a_{SE}^{c,\phi} \Phi_{SE} + a_{SW}^{c,\phi} \Phi_{SW} \quad (4.91)$$

Therefore, discretisation of the continuity equation produces implicit connections between five U nodes, five V nodes, and nine P nodes. The coefficients of the liquid continuity equation are given in the following equations:

$$a_P^{c,u} = \rho_e A_e n_{xe} \mathcal{W}_e - \rho_w A_w n_{xw} (1 - \mathcal{W}_w) + \rho_n A_n n_{xn} \mathcal{W}_n - \rho_s A_s n_{xs} (1 - \mathcal{W}_s) \quad (4.92)$$

$$a_E^{c,u} = \rho_e A_e n_{xe} (1 - \mathcal{W}_e) \quad (4.93)$$

$$a_W^{c,u} = -\rho_w A_w n_{xw} \mathcal{W}_w \quad (4.94)$$

$$a_N^{c,u} = \rho_n A_n n_{xn} (1 - \mathcal{W}_n) \quad (4.95)$$

$$a_S^{c,u} = -\rho_s A_s n_{xs} \mathcal{W}_s \quad (4.96)$$

$$a_P^{c,v} = \rho_e A_e n_{ye} \mathcal{W}_e - \rho_w A_w n_{yw} (1 - \mathcal{W}_w) + \rho_n A_n n_{yn} \mathcal{W}_n - \rho_s A_s n_{ys} (1 - \mathcal{W}_s) \quad (4.97)$$

$$a_E^{c,v} = \rho_e A_e n_{ye} (1 - \mathcal{W}_e) \quad (4.98)$$

$$a_W^{c,v} = -\rho_w A_w n_{yw} \mathcal{W}_w \quad (4.99)$$

$$a_N^{c,v} = \rho_n A_n n_{yn} (1 - \mathcal{W}_n) \quad (4.100)$$

$$a_S^{c,v} = -\rho_s A_s n_{ys} \mathcal{W}_s \quad (4.101)$$

$$\begin{aligned} a_P^{c,p} = & \rho_e A_e \hat{d}_e^u n_{xe} \left[\frac{\mathcal{Y}_{t,e}}{(ds)_e} + \frac{\mathcal{Y}_{s,e}}{(dt)_e} (C_{ne1} - C_{se4}) \right] + \rho_w A_w \hat{d}_w^u n_{xw} \left[\frac{\mathcal{Y}_{t,w}}{(ds)_w} - \frac{\mathcal{Y}_{s,w}}{(dt)_w} (C_{nw2} - C_{sw3}) \right] \\ & - \rho_n A_n \hat{d}_n^u n_{xn} \left[\frac{\mathcal{Y}_{s,n}}{(dt)_n} + \frac{\mathcal{Y}_{t,n}}{(ds)_n} (C_{ne1} - C_{nw2}) \right] - \rho_s A_s \hat{d}_s^u n_{xs} \left[\frac{\mathcal{Y}_{s,s}}{(dt)_s} - \frac{\mathcal{Y}_{t,s}}{(ds)_s} (C_{se4} - C_{sw3}) \right] \\ & - \rho_e A_e \hat{d}_e^v n_{ye} \left[\frac{\mathcal{X}_{t,e}}{(ds)_e} + \frac{\mathcal{X}_{s,e}}{(dt)_e} (C_{ne1} - C_{se4}) \right] - \rho_w A_w \hat{d}_w^v n_{yw} \left[\frac{\mathcal{X}_{t,w}}{(ds)_w} - \frac{\mathcal{X}_{s,w}}{(dt)_w} (C_{nw2} - C_{sw3}) \right] \\ & + \rho_n A_n \hat{d}_n^v n_{yn} \left[\frac{\mathcal{X}_{s,n}}{(dt)_n} + \frac{\mathcal{X}_{t,n}}{(ds)_n} (C_{ne1} - C_{nw2}) \right] + \rho_s A_s \hat{d}_s^v n_{ys} \left[\frac{\mathcal{X}_{s,s}}{(dt)_s} - \frac{\mathcal{X}_{t,s}}{(ds)_s} (C_{se4} - C_{sw3}) \right] \end{aligned} \quad (4.102)$$

$$\begin{aligned} a_E^{c,p} = & -\rho_e A_e \left(\hat{d}_e^u n_{xe} \frac{\mathcal{Y}_{t,e}}{(ds)_e} - \hat{d}_e^v n_{ye} \frac{\mathcal{X}_{t,e}}{(ds)_e} \right) - \rho_n A_n \left(\hat{d}_n^u n_{xn} \frac{\mathcal{Y}_{t,n}}{(ds)_n} - \hat{d}_n^v n_{yn} \frac{\mathcal{X}_{t,n}}{(ds)_n} \right) C_{ne2} \\ & + \rho_s A_s \left(\hat{d}_s^u n_{xs} \frac{\mathcal{Y}_{t,s}}{(ds)_s} - \hat{d}_s^v n_{ys} \frac{\mathcal{X}_{t,s}}{(ds)_s} \right) C_{se3} + \rho_e A_e \left(\hat{d}_e^u n_{xe} \frac{\mathcal{Y}_{s,e}}{(dt)_e} - \hat{d}_e^v n_{ye} \frac{\mathcal{X}_{s,e}}{(dt)_e} \right) (C_{ne2} - C_{se3}) \end{aligned} \quad (4.103)$$

$$\begin{aligned} a_W^{c,p} = & -\rho_w A_w \left(\hat{d}_w^u n_{xw} \frac{\mathcal{Y}_{t,w}}{(ds)_w} - \hat{d}_w^v n_{yw} \frac{\mathcal{X}_{t,w}}{(ds)_w} \right) + \rho_n A_n \left(\hat{d}_n^u n_{xn} \frac{\mathcal{Y}_{t,n}}{(ds)_n} - \hat{d}_n^v n_{yn} \frac{\mathcal{X}_{t,n}}{(ds)_n} \right) C_{nw1} \\ & - \rho_s A_s \left(\hat{d}_s^u n_{xs} \frac{\mathcal{Y}_{t,s}}{(ds)_s} - \hat{d}_s^v n_{ys} \frac{\mathcal{X}_{t,s}}{(ds)_s} \right) C_{sw4} + \rho_w A_w \left(\hat{d}_w^u n_{xw} \frac{\mathcal{Y}_{s,w}}{(dt)_w} - \hat{d}_w^v n_{yw} \frac{\mathcal{X}_{s,w}}{(dt)_w} \right) (C_{sw4} - C_{nw1}) \end{aligned} \quad (4.104)$$

$$\begin{aligned} a_N^{c,p} = & \rho_n A_n \left(\hat{d}_n^u n_{xn} \frac{\mathcal{Y}_{s,n}}{(dt)_n} - \hat{d}_n^v n_{yn} \frac{\mathcal{X}_{s,n}}{(dt)_n} \right) + \rho_e A_e \left(\hat{d}_e^u n_{xe} \frac{\mathcal{Y}_{s,e}}{(dt)_e} - \hat{d}_e^v n_{ye} \frac{\mathcal{X}_{s,e}}{(dt)_e} \right) C_{ne4} \\ & - \rho_w A_w \left(\hat{d}_w^u n_{xw} \frac{\mathcal{Y}_{s,w}}{(dt)_w} - \hat{d}_w^v n_{yw} \frac{\mathcal{X}_{s,w}}{(dt)_w} \right) C_{nw3} - \rho_n A_n \left(\hat{d}_n^u n_{xn} \frac{\mathcal{Y}_{t,n}}{(ds)_n} - \hat{d}_n^v n_{yn} \frac{\mathcal{X}_{t,n}}{(ds)_n} \right) (C_{ne4} - C_{nw3}) \end{aligned} \quad (4.105)$$

$$\begin{aligned} a_S^{c,p} = & \rho_s A_s \left(\hat{d}_s^u n_{xs} \frac{\mathcal{Y}_{s,s}}{(dt)_s} - \hat{d}_s^v n_{ys} \frac{\mathcal{X}_{s,s}}{(dt)_s} \right) - \rho_e A_e \left(\hat{d}_e^u n_{xe} \frac{\mathcal{Y}_{s,e}}{(dt)_e} - \hat{d}_e^v n_{ye} \frac{\mathcal{X}_{s,e}}{(dt)_e} \right) C_{se1} \\ & + \rho_w A_w \left(\hat{d}_w^u n_{xw} \frac{\mathcal{Y}_{s,w}}{(dt)_w} - \hat{d}_w^v n_{yw} \frac{\mathcal{X}_{s,w}}{(dt)_w} \right) C_{sw2} + \rho_s A_s \left(\hat{d}_s^u n_{xs} \frac{\mathcal{Y}_{t,s}}{(ds)_s} - \hat{d}_s^v n_{ys} \frac{\mathcal{X}_{t,s}}{(ds)_s} \right) (C_{se1} - C_{sw2}) \end{aligned} \quad (4.106)$$

$$a_{NE}^{c,p} = \left(\rho_e A_e \hat{d}_e^u n_{xe} \frac{\mathcal{Y}_{s,e}}{(dt)_e} - \rho_e A_e \hat{d}_e^v n_{ye} \frac{\mathcal{X}_{s,e}}{(dt)_e} - \rho_n A_n \hat{d}_n^u n_{xn} \frac{\mathcal{Y}_{t,n}}{(ds)_n} + \rho_n A_n \hat{d}_n^v n_{yn} \frac{\mathcal{X}_{t,n}}{(ds)_n} \right) C_{ne3} \quad (4.107)$$

$$a_{NW}^{c,p} = - \left(\rho_w A_w \hat{d}_w^u n_{xw} \frac{\mathcal{Y}_{s,w}}{(dt)_w} - \rho_w A_w \hat{d}_w^v n_{yw} \frac{\mathcal{X}_{s,w}}{(dt)_w} - \rho_n A_n \hat{d}_n^u n_{xn} \frac{\mathcal{Y}_{t,n}}{(ds)_n} + \rho_n A_n \hat{d}_n^v n_{yn} \frac{\mathcal{X}_{t,n}}{(ds)_n} \right) C_{nw4} \quad (4.108)$$

$$a_{SE}^{c,p} = - \left(\rho_e A_e \hat{d}_e^u n_{xe} \frac{\mathcal{Y}_{s,e}}{(dt)_e} - \rho_e A_e \hat{d}_e^v n_{ye} \frac{\mathcal{X}_{s,e}}{(dt)_e} - \rho_s A_s \hat{d}_s^u n_{xs} \frac{\mathcal{Y}_{t,s}}{(ds)_s} + \rho_s A_s \hat{d}_s^v n_{ys} \frac{\mathcal{X}_{t,s}}{(ds)_s} \right) C_{se2} \quad (4.109)$$

$$a_{SW}^{c,p} = \left(\rho_w A_w \hat{d}_w^u n_{xw} \frac{\mathcal{Y}_{s,w}}{(dt)_w} - \rho_w A_w \hat{d}_w^v n_{yw} \frac{\mathcal{X}_{s,w}}{(dt)_w} - \rho_s A_s \hat{d}_s^u n_{xs} \frac{\mathcal{Y}_{t,s}}{(ds)_s} + \rho_s A_s \hat{d}_s^v n_{ys} \frac{\mathcal{X}_{t,s}}{(ds)_s} \right) C_{sw1} \quad (4.110)$$

$$b_P^c = -\rho_e A_e (n_{xe} \tilde{b}_e^u + n_{ye} \tilde{b}_e^v) + \rho_w A_w (n_{xw} \tilde{b}_w^u + n_{yw} \tilde{b}_w^v) - \rho_n A_n (n_{xn} \tilde{b}_n^u + n_{yn} \tilde{b}_n^v) + \rho_s A_s (n_{xs} \tilde{b}_s^u + n_{ys} \tilde{b}_s^v) \quad (4.111)$$

4.3.1.2 Liquid Phase x -momentum Equation

Equation (2.22) yields to the following algebraic equation for x -momentum:

$$\frac{(\rho_P \overline{\mathcal{V}}_P)}{\Delta t} (U_P - U_P^o) + \dot{m}_e U_e - \dot{m}_w U_w + \dot{m}_n U_n - \dot{m}_s U_s = - \frac{\partial P}{\partial x} \Big|_P \overline{\mathcal{V}}_P + \rho_{PGx} \overline{\mathcal{V}}_P + D_e^u \frac{\partial U}{\partial n} \Big|_e - D_w^u \frac{\partial U}{\partial n} \Big|_w + D_n^u \frac{\partial U}{\partial n} \Big|_n - D_s^u \frac{\partial U}{\partial n} \Big|_s \quad (4.112)$$

In Equation (4.112), $D_f^u = \mu_f A_f$ and mass flow rates from the previous time step (\dot{m}_f^o) are used for \dot{m} values in the advection terms. The faces U velocities are approximated in terms of nodal values using the convective weight coefficient α_f at each face and an algebraic approximation to the exponential differencing scheme by Raithby and Schneider [52]:

$$\Phi_e = (0.5 + \alpha_e) \Phi_P + (0.5 - \alpha_e) \Phi_E \quad (4.113)$$

$$\Phi_w = (0.5 + \alpha_w) \Phi_P + (0.5 - \alpha_w) \Phi_W \quad (4.114)$$

$$\Phi_n = (0.5 + \alpha_n) \Phi_P + (0.5 - \alpha_n) \Phi_N \quad (4.115)$$

$$\Phi_s = (0.5 + \alpha_s) \Phi_P + (0.5 - \alpha_s) \Phi_S \quad (4.116)$$

α_f values are computed as a function of the local ratio of advective to diffusive transport rates:

$$\alpha_f = \text{sign}(\dot{m}_f) \frac{0.5 \text{Pe}_f^2}{5 + \text{Pe}_f^2} \quad (4.117)$$

$$\text{Pe}_f = \frac{\dot{m}_f}{D_f} \quad (4.118)$$

The normal derivative of U velocity at the east and north faces is defined as:

$$\left. \frac{\partial U}{\partial n} \right|_e = \beta_e \frac{\left. \frac{\partial U}{\partial s} \right|_e - (\hat{s}_e \cdot \hat{t}_e) \left. \frac{\partial U}{\partial t} \right|_e}{\hat{n}_e \cdot \hat{s}_e} \quad (4.119)$$

$$\left. \frac{\partial U}{\partial n} \right|_n = \beta_n \frac{- (\hat{s}_n \cdot \hat{t}_n) \left. \frac{\partial U}{\partial s} \right|_n + \left. \frac{\partial U}{\partial t} \right|_n}{\hat{t}_n \cdot \hat{n}_n} \quad (4.120)$$

where β_f is the diffusion weighting coefficient and defined as follows:

$$\beta_f = \frac{1 + 0.005\text{Pe}_f^2}{1 + 0.05\text{Pe}_f^2} \quad (4.121)$$

The gradients at the east and north faces are:

$$\left. \frac{\partial U}{\partial s} \right|_e = \frac{U_E - U_P}{(ds)_e}, \quad \left. \frac{\partial U}{\partial t} \right|_e = \frac{U_{ne} - U_{se}}{(dt)_e} \quad (4.122)$$

$$\left. \frac{\partial U}{\partial s} \right|_n = \frac{U_{ne} - U_{nw}}{(ds)_n}, \quad \left. \frac{\partial U}{\partial t} \right|_n = \frac{U_N - U_P}{(dt)_n} \quad (4.123)$$

U_{ne} , U_{nw} , and U_{se} are approximated using Equations (4.83) to (4.85), respectively.

Following the discretisation procedure explained above, the final form of the linearised U -momentum equation is:

$$a_P^{u,u} U_P + \sum a_{\text{NB8}}^{u,u} U_{\text{NB8}} + a_P^{u,p} P_P + \sum a_{\text{NB4}}^{u,p} P_{\text{NB4}} = b_P^u \quad (4.124)$$

The coefficients of the U -momentum equation are given in the following equations:

$$\begin{aligned} a_P^{u,u} = & \left(\frac{\rho_P \bar{V}_P}{\Delta t} \right) + (0.5 + \alpha_e) \dot{m}_e - (0.5 - \alpha_w) \dot{m}_w + (0.5 + \alpha_n) \dot{m}_n - (0.5 - \alpha_s) \dot{m}_s \\ & + \frac{D_e^u \beta_e}{\hat{n}_e \cdot \hat{s}_e} + \frac{D_w^u \beta_w}{\hat{n}_w \cdot \hat{s}_w} + \frac{D_n^u \beta_n}{\hat{n}_n \cdot \hat{t}_n} + \frac{D_s^u \beta_s}{\hat{n}_s \cdot \hat{t}_s} + D_e^u \beta_e \gamma_{x,e} (C_{ne1} - C_{se4}) \\ & - D_w^u \beta_w \gamma_{x,w} (C_{nw2} - C_{sw3}) + D_n^u \beta_n \gamma_{y,n} (C_{ne1} - C_{nw2}) - D_s^u \beta_s \gamma_{y,s} (C_{se4} - C_{sw3}) \end{aligned} \quad (4.125)$$

$$\begin{aligned} a_E^{u,u} = & (0.5 - \alpha_e) \dot{m}_e - \frac{D_e^u \beta_e}{\hat{n}_e \cdot \hat{s}_e} + D_n^u \beta_n \gamma_{y,n} C_{ne2} - D_s^u \beta_s \gamma_{y,s} C_{se3} \\ & + D_e^u \beta_e \gamma_{x,e} (C_{ne2} - C_{se3}) \end{aligned} \quad (4.126)$$

$$a_W^{u,u} = -(0.5 + \alpha_w) \dot{m}_w - \frac{D_w^u \beta_w}{\hat{n}_w \cdot \hat{s}_w} - D_n^u \beta_n \gamma_{y,n} C_{nw1} + D_s^u \beta_s \gamma_{y,s} C_{sw4} - D_w^u \beta_w \gamma_{x,w} (C_{nw1} - C_{sw4}) \quad (4.127)$$

$$a_N^{u,u} = (0.5 - \alpha_n) \dot{m}_n - \frac{D_n^u \beta_n}{\hat{n}_n \cdot \hat{t}_n} + D_e^u \beta_e \gamma_{x,e} C_{ne4} - D_w^u \beta_w \gamma_{x,w} C_{nw3} + D_n^u \beta_n \gamma_{y,n} (C_{ne4} - C_{nw3}) \quad (4.128)$$

$$a_S^{u,u} = -(0.5 + \alpha_s) \dot{m}_s - \frac{D_s^u \beta_s}{\hat{n}_s \cdot \hat{t}_s} - D_e^u \beta_e \gamma_{x,e} C_{se1} + D_w^u \beta_w \gamma_{x,w} C_{sw2} - D_s^u \beta_s \gamma_{y,s} (C_{se1} - C_{sw2}) \quad (4.129)$$

$$a_{NE}^{u,u} = (D_e^u \beta_e \gamma_{x,e} + D_n^u \beta_n \gamma_{y,n}) C_{ne3} \quad (4.130)$$

$$a_{NW}^{u,u} = -(D_w^u \beta_w \gamma_{x,w} + D_n^u \beta_n \gamma_{y,n}) C_{nw4} \quad (4.131)$$

$$a_{SE}^{u,u} = -(D_e^u \beta_e \gamma_{x,e} + D_s^u \beta_s \gamma_{y,s}) C_{se2} \quad (4.132)$$

$$a_{SW}^{u,u} = (D_w^u \beta_w \gamma_{x,w} + D_s^u \beta_s \gamma_{y,s}) C_{sw1} \quad (4.133)$$

where,

$$D_e^u = \frac{\mu_e A_e}{(ds)_e} \quad D_w^u = \frac{\mu_w A_w}{(ds)_w} \quad D_n^u = \frac{\mu_n A_n}{(dt)_n} \quad D_s^u = \frac{\mu_s A_s}{(dt)_s} \quad (4.134)$$

$$\gamma_{x,f} = \frac{(ds)_f \hat{t}_f \cdot \hat{s}_f}{(dt)_f \hat{n}_f \cdot \hat{s}_f} \quad \gamma_{y,f} = \frac{(dt)_f \hat{t}_f \cdot \hat{s}_f}{(ds)_f \hat{n}_f \cdot \hat{t}_f} \quad (4.135)$$

The pressure coefficients of main node ($a_P^{u,p}$) and its four neighbours ($a_{NB4}^{u,p}$) are derived as follows:

$$a_P^{u,p} = \forall_P \frac{\mathcal{Y}_{t,P}}{(ds)_P} (\mathcal{W}_e - 1 + \mathcal{W}_w) - \forall_P \frac{\mathcal{Y}_{s,P}}{(dt)_P} (\mathcal{W}_n - 1 + \mathcal{W}_s) \quad (4.136)$$

$$a_E^{u,p} = \forall_P \frac{\mathcal{Y}_{t,P}}{(ds)_P} (1 - \mathcal{W}_e) \quad (4.137)$$

$$a_W^{u,p} = -\forall_P \frac{\mathcal{Y}_{t,P}}{(ds)_P} \mathcal{W}_w \quad (4.138)$$

$$a_N^{u,p} = -\bar{V}_P \frac{\mathcal{Y}_{s,P}}{(dt)_P} (1 - \mathcal{W}_n) \quad (4.139)$$

$$a_S^{u,p} = \bar{V}_P \frac{\mathcal{Y}_{s,P}}{(dt)_P} \mathcal{W}_s \quad (4.140)$$

The right hand side of Equation (4.124) is:

$$b_P^u = \left(\frac{\rho_P \bar{V}_P}{\Delta t} \right) U_P^o + \rho_P g_x \bar{V}_P \quad (4.141)$$

4.3.1.3 Liquid Phase y-momentum Equation

The discretisation of Equation (2.23) yields to the following equation:

$$\begin{aligned} \frac{(\rho_P \bar{V}_P)}{\Delta t} (V_P - V_P^o) + \dot{m}_e V_e - \dot{m}_w V_w + \dot{m}_n V_n - \dot{m}_s V_s = \\ - \left. \frac{\partial P}{\partial y} \right|_P \bar{V}_P + D_e^v \left. \frac{\partial V}{\partial n} \right|_e - D_w^v \left. \frac{\partial V}{\partial n} \right|_w + D_n^v \left. \frac{\partial V}{\partial n} \right|_n - D_s^v \left. \frac{\partial V}{\partial n} \right|_s \end{aligned} \quad (4.142)$$

where $D_f^u = \mu_f A_f$. Equation (4.142) is discretised in the same manner as was used for the x -momentum equation:

$$a_P^{v,v} V_P + \sum a_{NB8}^{v,v} V_{NB8} + a_P^{v,p} P_P + \sum a_{NB4}^{v,p} P_{NB4} = b_P^v \quad (4.143)$$

The coefficients of V -velocity of the main node and its neighbours are analogous to those of the U -momentum equation:

$$a_P^{v,v} = a_P^{u,u} \quad a_{NB}^{v,v} = a_{NB}^{u,u} \quad (4.144)$$

Note that D_f^u changes to D_f^v and $D_f^v = D_f^u$ (Equation (4.134)). The other coefficients are as follows:

$$a_P^{v,p} = \bar{V}_P \frac{\mathcal{X}_{s,P}}{(dt)_P} (\mathcal{W}_n - 1 + \mathcal{W}_s) - \bar{V}_P \frac{\mathcal{X}_{t,P}}{(ds)_P} (\mathcal{W}_e - 1 + \mathcal{W}_w) \quad (4.145)$$

$$a_E^{v,p} = -\bar{V}_P \frac{\mathcal{X}_{t,P}}{(ds)_P} (1 - \mathcal{W}_e) \quad (4.146)$$

$$a_W^{v,p} = \bar{V}_P \frac{\mathcal{X}_{t,P}}{(ds)_P} \mathcal{W}_w \quad (4.147)$$

$$a_N^{v,p} = \nabla_P \frac{X_{s,P}}{(dt)_P} (1 - \mathcal{W}_n) \quad (4.148)$$

$$a_S^{v,p} = -\nabla_P \frac{X_{s,P}}{(dt)_P} \mathcal{W}_s \quad (4.149)$$

$$b_P^v = \left(\frac{\rho_P \nabla_P}{\Delta t} \right) V_P^o \quad (4.150)$$

4.3.1.4 Liquid Phase Energy Equation

Equation (2.24) yields to the following equation for conservation of energy in the liquid phase:

$$\begin{aligned} & \frac{(\rho_P C_{pP} \nabla_P)}{\Delta t} (T_P - T_P^o) + \dot{m}_e [C_{pe} T_e + \xi_{W_e} (\bar{h}_W - \bar{h}_{\text{LiBr}})_e] - \dot{m}_w [C_{pw} T_w + \xi_{W_w} (\bar{h}_W - \bar{h}_{\text{LiBr}})_w] \\ & + \dot{m}_n [C_{pn} T_n + \xi_{W_n} (\bar{h}_W - \bar{h}_{\text{LiBr}})_n] - \dot{m}_s [C_{ps} T_s + \xi_{W_s} (\bar{h}_W - \bar{h}_{\text{LiBr}})_s] = \\ & D_e^t \frac{\partial T}{\partial n} \Big|_e - D_w^t \frac{\partial T}{\partial n} \Big|_w + D_n^t \frac{\partial T}{\partial n} \Big|_n - D_s^t \frac{\partial T}{\partial n} \Big|_s + \tilde{D}_e^t \frac{\partial \xi_W}{\partial n} \Big|_e - \tilde{D}_w^t \frac{\partial \xi_W}{\partial n} \Big|_w + \tilde{D}_n^t \frac{\partial \xi_W}{\partial n} \Big|_n - \tilde{D}_s^t \frac{\partial \xi_W}{\partial n} \Big|_s \end{aligned} \quad (4.151)$$

where $D_f^t = k_f A_f$ and $\tilde{D}_f^t = \rho_f D_f^{AB} A_f (\bar{h}_W - \bar{h}_{\text{LiBr}})_f$. Discretisation of Equation (4.151) yields to:

$$a_P^{t,t} T_P + \sum a_{\text{NB8}}^{t,t} T_{\text{NB8}} + a_P^{t,\xi} \xi_{WP} + \sum a_{\text{NB8}}^{t,\xi} \xi_{W\text{NB8}} = b_P^t \quad (4.152)$$

The derivation of $a_P^{t,t}$ and $a_{\text{NB}}^{t,t}$ is analogous to those for the U velocity coefficient in the x -momentum equation using k instead of μ in D_f coefficients and $\dot{m} C_p$ instead of \dot{m} .

$$D_e^t = \frac{k_e A_e}{(ds)_e} \quad D_w^t = \frac{k_w A_w}{(ds)_w} \quad D_n^t = \frac{k_n A_n}{(dt)_n} \quad D_s^t = \frac{k_s A_s}{(dt)_s} \quad (4.153)$$

The mass fraction coefficients and the right hand side of Equation (4.152) are as follows:

$$\begin{aligned} a_P^{t,\xi} &= (0.5 + \alpha_e) (\bar{h}_W - \bar{h}_{\text{LiBr}})_e \dot{m}_e - (0.5 - \alpha_w) (\bar{h}_W - \bar{h}_{\text{LiBr}})_w \dot{m}_w \\ &+ (0.5 + \alpha_n) (\bar{h}_W - \bar{h}_{\text{LiBr}})_n \dot{m}_n - (0.5 - \alpha_s) (\bar{h}_W - \bar{h}_{\text{LiBr}})_s \dot{m}_s \\ &+ \frac{\tilde{D}_e^t \beta_e}{\hat{n}_e \cdot \hat{s}_e} + \frac{\tilde{D}_w^t \beta_w}{\hat{n}_w \cdot \hat{s}_w} + \frac{\tilde{D}_n^t \beta_n}{\hat{n}_n \cdot \hat{t}_n} + \frac{\tilde{D}_s^t \beta_s}{\hat{n}_s \cdot \hat{t}_s} + \tilde{D}_e^t \beta_e \gamma_{x,e} (C_{ne1} - C_{se4}) \\ &- \tilde{D}_w^t \beta_w \gamma_{x,w} (C_{nw2} - C_{sw3}) + \tilde{D}_n^t \beta_n \gamma_{y,n} (C_{ne1} - C_{nw2}) - \tilde{D}_s^t \beta_s \gamma_{y,s} (C_{se4} - C_{sw3}) \end{aligned} \quad (4.154)$$

$$a_E^{t,\xi} = (0.5 - \alpha_e)(\bar{h}_W - \bar{h}_{\text{LiBr}})_e \dot{m}_e - \frac{\tilde{D}_e^t \beta_e}{\hat{n}_e \cdot \hat{s}_e} + \tilde{D}_n^t \beta_n \gamma_{y,n} C_{ne2} - \tilde{D}_s^t \beta_s \gamma_{y,s} C_{se3} + \tilde{D}_e^t \beta_e \gamma_{x,e} (C_{ne2} - C_{se3}) \quad (4.155)$$

$$a_W^{t,\xi} = -(0.5 + \alpha_w)(\bar{h}_W - \bar{h}_{\text{LiBr}})_w \dot{m}_w - \frac{\tilde{D}_w^t \beta_w}{\hat{n}_w \cdot \hat{s}_w} - \tilde{D}_n^t \beta_n \gamma_{y,n} C_{nw1} + \tilde{D}_s^t \beta_s \gamma_{y,s} C_{sw4} - \tilde{D}_w^t \beta_w \gamma_{x,w} (C_{nw1} - C_{sw4}) \quad (4.156)$$

$$a_N^{t,\xi} = (0.5 - \alpha_n)(\bar{h}_W - \bar{h}_{\text{LiBr}})_n \dot{m}_n - \frac{\tilde{D}_n^t \beta_n}{\hat{n}_n \cdot \hat{t}_n} + \tilde{D}_e^t \beta_e \gamma_{x,e} C_{ne4} - \tilde{D}_w^t \beta_w \gamma_{x,w} C_{nw3} + \tilde{D}_n^t \beta_n \gamma_{y,n} (C_{ne4} - C_{nw3}) \quad (4.157)$$

$$a_S^{t,\xi} = -(0.5 + \alpha_s)(\bar{h}_W - \bar{h}_{\text{LiBr}})_s \dot{m}_s - \frac{\tilde{D}_s^t \beta_s}{\hat{n}_s \cdot \hat{t}_s} - \tilde{D}_e^t \beta_e \gamma_{x,e} C_{se1} + \tilde{D}_w^t \beta_w \gamma_{x,w} C_{sw2} - \tilde{D}_s^t \beta_s \gamma_{y,s} (C_{se1} - C_{sw2}) \quad (4.158)$$

$$a_{NE}^{t,\xi} = (\tilde{D}_e^t \beta_e \gamma_{x,e} + \tilde{D}_n^t \beta_n \gamma_{y,n}) C_{ne3} \quad (4.159)$$

$$a_{SE}^{t,\xi} = -(\tilde{D}_e^t \beta_e \gamma_{x,e} + \tilde{D}_s^t \beta_s \gamma_{y,s}) C_{se2} \quad (4.160)$$

$$a_{NW}^{t,\xi} = -(\tilde{D}_w^t \beta_w \gamma_{x,w} + \tilde{D}_n^t \beta_n \gamma_{y,n}) C_{nw4} \quad (4.161)$$

$$a_{SW}^{t,\xi} = (\tilde{D}_w^t \beta_w \gamma_{x,w} + \tilde{D}_s^t \beta_s \gamma_{y,s}) C_{sw1} \quad (4.162)$$

where,

$$\tilde{D}_e^t = \frac{\rho_e D_e^{AB} A_e (\bar{h}_W - \bar{h}_{\text{LiBr}})_e}{(ds)_e} \quad \tilde{D}_w^t = \frac{\rho_w D_w^{AB} A_w (\bar{h}_W - \bar{h}_{\text{LiBr}})_w}{(ds)_w}$$

$$\tilde{D}_n^t = \frac{\rho_n D_n^{AB} A_n (\bar{h}_W - \bar{h}_{\text{LiBr}})_n}{(dt)_n} \quad \tilde{D}_s^t = \frac{\rho_s D_s^{AB} A_s (\bar{h}_W - \bar{h}_{\text{LiBr}})_s}{(dt)_s} \quad (4.163)$$

$$b_P^t = \left(\frac{\rho_P C_{PP} \bar{V}_P}{\Delta t} \right) T_P^o \quad (4.164)$$

4.3.1.5 Liquid Phase Mass Fraction Equation

Equation (2.25) yields to the following equation for conservation of mass in the liquid:

$$\frac{(\rho_P \nabla_P)}{\Delta t} (\xi_{WP} - \xi_{WP}^o) + \dot{m}_e \xi_{W_e} - \dot{m}_\xi \xi_{W_w} + \dot{m}_n \xi_{W_n} - \dot{m}_s \xi_{W_s} = D_e^\xi \frac{\partial \xi_W}{\partial n} \Big|_e - D_w^\xi \frac{\partial \xi_W}{\partial n} \Big|_w + D_n^\xi \frac{\partial \xi_W}{\partial n} \Big|_n - D_s^\xi \frac{\partial \xi_W}{\partial n} \Big|_s \quad (4.165)$$

where $D_f^\xi = \rho_f D_f^{AB}$. Discretisation of Equation (4.165) yields to:

$$a_P^{\xi,\xi} \xi_{WP} + \sum a_{NB8}^{\xi,\xi} \xi_{WNB8} = b_P^\xi \quad (4.166)$$

The derivations of $a_P^{\xi,\xi}$ and $a_{NB8}^{\xi,\xi}$ are analogous to those for the U velocity coefficients in x -momentum equation using $\rho_f D_f^{AB}$ instead of μ_f .

4.3.2 Algebraic Interface Equations

At the liquid-gas interface, one equation is required to form an algebraic equation for each of the field variables at either the liquid or gas side. In these algebraic equations, the nodes on both liquid and gas sides of the interface along with the adjacent nodes in both regions are involved. Figure 4.2 shows the indexing notation of the interface nodes and their neighbouring control volumes. This naming system is applied to all the algebraic form of the interface equations.

4.3.2.1 Normal Force Balance

The normal force balance, Equation (2.30), is used as an equation for P on the liquid interface ($j = j_{EL} + 1$). The 2D stress tensor τ is defined in terms of the normal and shear stress:

$$\tau = \begin{pmatrix} \tau_{xx} & \tau_{yx} \\ \tau_{xy} & \tau_{yy} \end{pmatrix} \quad (4.167)$$

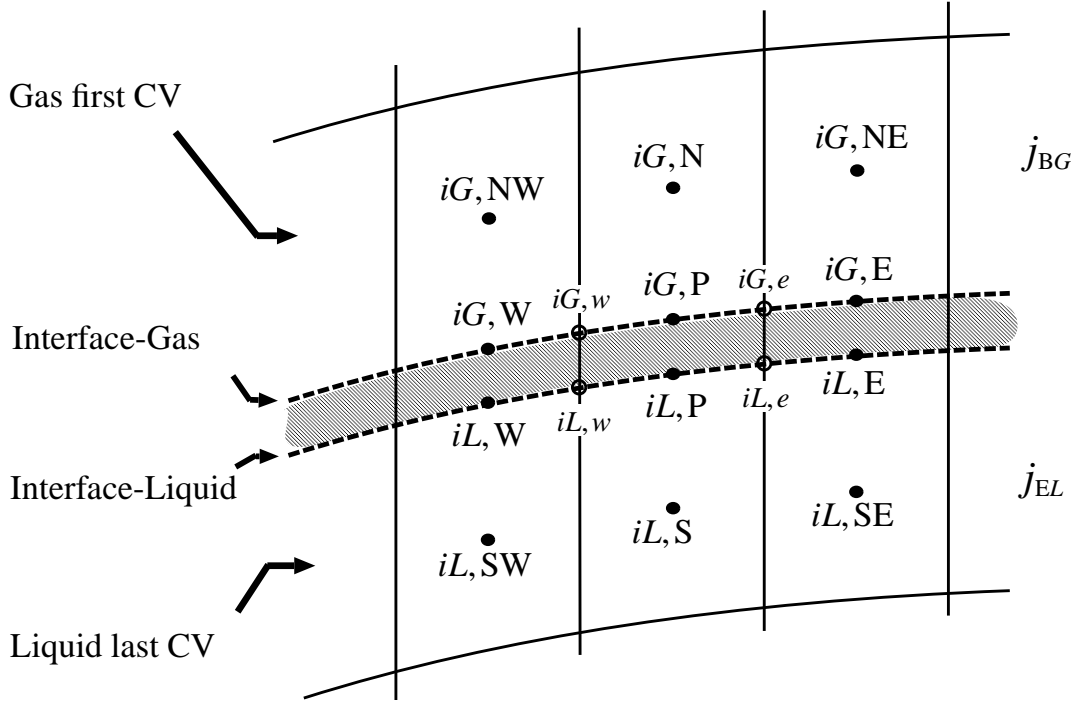


Figure 4.2: Indexing notation for interface and neighbouring control volumes; the spacing between the nodes at the interface is exaggerated for illustration purposes.

For incompressible fluids, the stress tensor can be written in the compact form of:

$$\tau_{ij} = -P \delta_{ij} + \mu \left(\frac{\partial U_i}{\partial x_j} + \frac{\partial U_j}{\partial x_i} \right) \quad (4.168)$$

where i and j refer to the coordinates x and y and δ_{ij} in the index notation is the Kronecker delta.

Substitution of Equation (4.167) in Equation (2.30) results in the following equation:

$$\left(\tau_{xx} n_x^2 + 2 \tau_{xy} n_x n_y + \tau_{yy} n_y^2 \right)_{L,\text{intf}} + \sigma K = \left(\tau_{xx} n_x^2 + 2 \tau_{xy} n_x n_y + \tau_{yy} n_y^2 \right)_{G,\text{intf}} \quad (4.169)$$

Substitution of all stresses in Equation (4.169) results in:

$$\begin{aligned} \left(-P + 2 \mu \left(\frac{\partial U}{\partial x} \right) n_x^2 + 2 \mu \left(\frac{\partial U}{\partial r} + \frac{\partial V}{\partial x} \right) n_x n_y + 2 \mu \left(\frac{\partial V}{\partial y} \right) n_y^2 \right)_{L,\text{intf}} + \sigma K = \\ \left(-P + 2 \mu \left(\frac{\partial U}{\partial x} \right) n_x^2 + 2 \mu \left(\frac{\partial U}{\partial y} + \frac{\partial V}{\partial x} \right) n_x n_y + 2 \mu \left(\frac{\partial V}{\partial y} \right) n_y^2 \right)_{G,\text{intf}} \end{aligned} \quad (4.170)$$

The velocity derivatives are evaluated based on central differencing scheme. One-dimensional interpolation is employed to determine the corner values (U_{ne} and U_{nw}) for the liquid side of the interface and (U_{se} and U_{sw}) for the gas side of the interface from its interfacial two neighbours. For example, U_{ne} at the liquid side of the interface is determined by ($U_{ne} = f_{ne} U_N + (1 - f_{ne}) U_{NE}$) where f_{ne} is a linear interpolation factor based on the grid spacing. The derivatives at the interface for any transport variable can be given in general forms by the following expressions:

$$\left. \frac{\partial \Phi}{\partial x} \right|_{L, \text{intf}} = \left(\frac{\partial \Phi}{\partial x} \right)_{iL, S} = A_{x1} \Phi_{iL, S} + A_{x2} \Phi_{iL, P} + A_{x3} \Phi_{iL, E} + A_{x4} \Phi_{iL, W} \quad (4.171)$$

$$\left. \frac{\partial \Phi}{\partial y} \right|_{L, \text{intf}} = \left(\frac{\partial \Phi}{\partial y} \right)_{iL, S} = A_{y1} \Phi_{iL, S} + A_{y2} \Phi_{iL, P} + A_{y3} \Phi_{iL, E} + A_{y4} \Phi_{iL, W} \quad (4.172)$$

$$\left. \frac{\partial \Phi}{\partial x} \right|_{G, \text{intf}} = \left(\frac{\partial \Phi}{\partial x} \right)_{iG, N} = B_{x1} \Phi_{iG, N} + B_{x2} \Phi_{iG, P} + B_{x3} \Phi_{iG, E} + B_{x4} \Phi_{iG, W} \quad (4.173)$$

$$\left. \frac{\partial \Phi}{\partial y} \right|_{G, \text{intf}} = \left(\frac{\partial \Phi}{\partial y} \right)_{iG, N} = B_{y1} \Phi_{iG, N} + B_{y2} \Phi_{iG, P} + B_{y3} \Phi_{iG, E} + B_{y4} \Phi_{iG, W} \quad (4.174)$$

For the purpose of brevity, the liquid and the gas interfaces are shown with iL and iG , respectively in the interface algebraic equations. iL, S and iG, N are the last and first control volumes in the liquid and gas phases, respectively. The coefficients in Equations (4.171) to (4.174) are:

$$\begin{aligned} A_{x1} &= \frac{1}{\Psi_n} \left[\frac{s_{yn}}{(dt)_n} \right]_{iL, S} & A_{x2} &= \frac{1}{\Psi_n} \left[\frac{t_{yn}}{(ds)_n} (f_{ne} - (1 - f_{nw})) - \frac{s_{yn}}{(dt)_n} \right]_{iL, S} \\ A_{x3} &= \frac{1}{\Psi_n} \left[\frac{t_{yn}}{(ds)_n} (1 - f_{ne}) \right]_{iL, S} & A_{x4} &= -\frac{1}{\Psi_n} \left[\frac{t_{yn}}{(ds)_n} f_{nw} \right]_{iL, S} \end{aligned} \quad (4.175)$$

$$\begin{aligned} A_{y1} &= -\frac{1}{\Psi_n} \left[\frac{s_{xn}}{(dt)_n} \right]_{iL, S} & A_{y2} &= \frac{1}{\Psi_n} \left[\frac{s_{xn}}{(dt)_n} - \frac{t_{xn}}{(ds)_n} (f_{ne} - (1 - f_{nw})) \right]_{iL, S} \\ A_{y3} &= -\frac{1}{\Psi_n} \left[\frac{t_{xn}}{(ds)_n} (1 - f_{ne}) \right]_{iL, S} & A_{y4} &= \frac{1}{\Psi_n} \left[\frac{t_{xn}}{(ds)_n} f_{nw} \right]_{iL, S} \end{aligned} \quad (4.176)$$

$$\begin{aligned} B_{x1} &= -\frac{1}{\Psi_s} \left[\frac{s_{ys}}{(dt)_s} \right]_{iG, N} & B_{x2} &= \frac{1}{\Psi_s} \left[\frac{t_{ys}}{(ds)_s} (f_{se} - (1 - f_{sw})) + \frac{s_{ys}}{(dt)_s} \right]_{iG, N} \\ B_{x3} &= \frac{1}{\Psi_s} \left[\frac{t_{ys}}{(ds)_s} (1 - f_{se}) \right]_{iG, N} & B_{x4} &= -\frac{1}{\Psi_s} \left[\frac{t_{ys}}{(ds)_s} f_{sw} \right]_{iG, N} \end{aligned} \quad (4.177)$$

$$\begin{aligned}
 B_{y1} &= \frac{1}{\Psi_s} \left[\frac{s_{xs}}{(dt)_s} \right]_{iG,N} & B_{y2} &= \frac{1}{\Psi_s} \left[\frac{-s_{xs}}{(dt)_s} - \frac{t_{xs}}{(ds)_s} (f_{se} - (1 - f_{sw})) \right]_{iG,N} \\
 B_{y3} &= -\frac{1}{\Psi_s} \left[\frac{t_{xs}}{(ds)_s} (1 - f_{se}) \right]_{iG,N} & B_{y4} &= \frac{1}{\Psi_s} \left[\frac{t_{xs}}{(ds)_s} f_{sw} \right]_{iG,N}
 \end{aligned} \tag{4.178}$$

The geometrical terms, Ψ_n and Ψ_s , are defined as:

$$\Psi_n = (s_{xn} t_{yn} - t_{xn} s_{yn})_{iL,S} \quad \Psi_s = (s_{xs} t_{ys} - t_{xs} s_{ys})_{iG,N} \tag{4.179}$$

Applying the velocity gradient definitions, Equation (4.170) can be written as:

$$\begin{aligned}
 & -P_{iL} + 2 (\mu n_x^2)_{iL,P} (A_{x1} U_{iL,S} + A_{x2} U_{iL,P} + A_{x3} U_{iL,E} + A_{x4} U_{iL,W}) \\
 & + 2 (\mu n_x n_y)_{iL,P} (A_{y1} U_{iL,S} + A_{y2} U_{iL,P} + A_{y3} U_{iL,E} + A_{y4} U_{iL,W}) \\
 & + 2 (\mu n_x n_y)_{iL,P} (A_{x1} V_{iL,S} + A_{x2} V_{iL,P} + A_{x3} V_{iL,E} + A_{x4} V_{iL,W}) \\
 & + 2 (\mu n_y^2)_{iL,P} (A_{y1} V_{iL,S} + A_{y2} V_{iL,P} + A_{y3} V_{iL,E} + A_{y4} V_{iL,W}) + \sigma K = \\
 & -P_{iG} + 2 (\mu n_x^2)_{iG,P} (B_{x1} U_{iG,N} + B_{x2} U_{iG,P} + B_{x3} U_{iG,E} + B_{x4} U_{iG,W}) \\
 & + 2 (\mu n_x n_y)_{iG,P} (B_{y1} U_{iG,N} + B_{y2} U_{iG,P} + B_{y3} U_{iG,E} + B_{y4} U_{iG,W}) \\
 & + 2 (\mu n_x n_y)_{iG,P} (B_{x1} V_{iG,N} + B_{x2} V_{iG,P} + B_{x3} V_{iG,E} + B_{x4} V_{iG,W}) \\
 & + 2 (\mu n_y^2)_{iG,P} (B_{y1} V_{iG,N} + B_{y2} V_{iG,P} + B_{y3} V_{iG,E} + B_{y4} V_{iG,W})
 \end{aligned} \tag{4.180}$$

The final form of the normal force balance algebraic equation to calculate the liquid interface pressure is:

$$\begin{aligned}
 & a_{iL,P}^{c,p} P_{iL,P} + a_{iL,N}^{c,p} P_{iG,P} + a_{iL,P}^{c,u} U_{iL,P} + a_{iL,E}^{c,u} U_{iL,E} + a_{iL,W}^{c,u} U_{iL,W} + a_{iL,S}^{c,u} U_{iL,S} + \\
 & a_{iL,P}^{c,v} V_{iL,P} + a_{iL,E}^{c,v} V_{iL,E} + a_{iL,W}^{c,v} V_{iL,W} + a_{iL,S}^{c,v} V_{iL,S} + a_{iL,N}^{c,u} U_{iG,P} + a_{iL,NE}^{c,u} U_{iG,E} + \\
 & a_{iL,NW}^{c,u} U_{iG,W} + a_{iL,N}^{c,v} V_{iG,P} + a_{iL,NE}^{c,v} V_{iG,E} + a_{iL,NW}^{c,v} V_{iG,W} = b_{iL,P}^c \tag{4.181}
 \end{aligned}$$

The coefficients of Equation (4.181) are given in Appendix E, Section E.1.

4.3.2.2 Zero Pressure Gradient

This condition is employed on the gas interface ($j = j_{BG} - 1$) to govern the pressure $P_{iG,P}$. Discretisation of Equation (2.38) leads to the algebraic form as follows:

$$\frac{\partial P}{\partial n} \Big|_{iG,P} = (B_{x2}P_{iG,P} + B_{x3}P_{iG,E} + B_{x4}P_{iG,W} + B_{x1}P_{iG,N})n_{xs}|_{iG,N} + (B_{y2}P_{iG,P} + B_{y3}P_{iG,E} + B_{y4}P_{iG,W} + B_{y1}P_{iG,N})n_{ys}|_{iG,N} = 0 \quad (4.182)$$

which leads to:

$$a_{iG,P}^{c,P} P_{iG,P} + a_{iG,N}^{c,P} P_{iG,N} + a_{iG,W}^{c,P} P_{iG,W} + a_{iG,E}^{c,P} P_{iG,E} = 0 \quad (4.183)$$

The coefficients of Equation (4.183) are given in Appendix E, Section E.2.

4.3.2.3 Tangential Force Balance

The algebraic tangential force balance condition is used for the calculation of gas interface velocity, $U_{iG,P}$. Equation (2.31) can be written in terms of the normal and shear stresses at the interface as follows:

$$\left(\tau_{xx} n_x s_x + \tau_{xy} (n_y s_x + n_x s_y) + \tau_{yy} n_y s_y \right)_{L,intf} - \frac{\partial \sigma}{\partial s} \Big|_{L,intf} = \left(\tau_{xx} n_x s_x + \tau_{xy} (n_y s_x + n_x s_y) + \tau_{yy} n_y s_y \right)_{G,intf} \quad (4.184)$$

Equation (4.184) can be expressed in terms of velocity gradients:

$$\left(2 \mu \left(\frac{\partial U}{\partial x} \right) n_x s_x + \mu \left(\frac{\partial U}{\partial y} + \frac{\partial V}{\partial x} \right) (n_y s_x + n_x s_y) + 2 \mu \left(\frac{\partial V}{\partial y} \right) n_y s_y \right)_{L,intf} - \frac{\partial \sigma}{\partial s} \Big|_{L,intf} = \left(2 \mu \left(\frac{\partial U}{\partial x} \right) n_x s_x + \mu \left(\frac{\partial U}{\partial y} + \frac{\partial V}{\partial x} \right) (n_y s_x + n_x s_y) + 2 \mu \left(\frac{\partial V}{\partial y} \right) n_y s_y \right)_{G,intf} \quad (4.185)$$

Using the Equations (4.171) to (4.174), Equation (4.185) can be simplified as follows:

$$\begin{aligned}
 & 2 (\mu n_x s_x)_{iL,P} (A_{x1} U_{iL,S} + A_{x2} U_{iL,P} + A_{x3} U_{iL,E} + A_{x4} U_{iL,W}) \\
 & + \left[\mu (n_y s_x + n_x s_y) \right]_{iL,P} (A_{y1} U_{iL,S} + A_{y2} U_{iL,P} + A_{y3} U_{iL,E} + A_{y4} U_{iL,W}) \\
 & + \left[\mu (n_y s_x + n_x s_y) \right]_{iL,P} (A_{x1} V_{iL,S} + A_{x2} V_{iL,P} + A_{x3} V_{iL,E} + A_{x4} V_{iL,W}) \\
 & + 2 (\mu n_y s_y)_{iL,P} (A_{y1} V_{iL,S} + A_{y2} V_{iL,P} + A_{y3} V_{iL,E} + A_{y4} V_{iL,W}) - \left. \frac{\partial \sigma}{\partial s} \right|_{L, \text{intf}} = \\
 & 2 (\mu n_x s_x)_{iG,P} (B_{x1} U_{iG,N} + B_{x2} U_{iG,P} + B_{x3} U_{iG,E} + B_{x4} U_{iG,W}) \\
 & + \left[\mu (n_y s_x + n_x s_y) \right]_{iG,P} (B_{y1} U_{iG,N} + B_{y2} U_{iG,P} + B_{y3} U_{iG,E} + B_{y4} U_{iG,W}) \\
 & + \left[\mu (n_y s_x + n_x s_y) \right]_{iG,P} (B_{x1} V_{iG,N} + B_{x2} V_{iG,P} + B_{x3} V_{iG,E} + B_{x4} V_{iG,W}) \\
 & + 2 (\mu n_y s_y)_{iG,P} (B_{y1} V_{iG,N} + B_{y2} V_{iG,P} + B_{y3} V_{iG,E} + B_{y4} V_{iG,W})
 \end{aligned} \tag{4.186}$$

The algebraic equation for tangential force balance that is used to calculate the $U_{iG,P}$ at the gas interface can be written as:

$$\begin{aligned}
 & a_{iG,P}^{u,u} U_{iG,P} + a_{iG,E}^{u,u} U_{iG,E} + a_{iG,W}^{u,u} U_{iG,W} + a_{iG,N}^{u,u} U_{iG,N} + \\
 & a_{iG,P}^{u,v} V_{iG,P} + a_{iG,E}^{u,v} V_{iG,E} + a_{iG,W}^{u,v} V_{iG,W} + a_{iG,N}^{u,v} V_{iG,N} + a_{iG,S}^{u,u} U_{iL,P} + a_{iG,SE}^{u,u} U_{iL,E} + \\
 & a_{iG,SW}^{u,u} U_{iL,W} + a_{iG,S}^{u,v} V_{iL,P} + a_{iG,SE}^{u,v} V_{iL,E} + a_{iG,SW}^{u,v} V_{iL,W} = b_{iG,P}^u \tag{4.187}
 \end{aligned}$$

The coefficients of Equation (4.187) are given in Appendix E, Section E.3.

4.3.2.4 Tangential Velocity Equality

The continuity of tangential velocity at the interface, Equation (2.32), can be written based on the velocity and tangent vectors and used to calculate $U_{iL,P}$:

$$(U \hat{i} + V \hat{j})_{iG} \cdot (s_x \hat{i} + s_y \hat{j})_{iG} = (U \hat{i} + V \hat{j})_{iL} \cdot (s_x \hat{i} + s_y \hat{j})_{iL} \tag{4.188}$$

The algebraic form of Equation (4.188) is:

$$a_{iL,P}^{u,u} U_{iL,P} + a_{iL,N}^{u,u} U_{iG,P} + a_{iL,P}^{u,v} V_{iL,P} + a_{iL,N}^{u,v} V_{iG,P} = 0 \quad (4.189)$$

The coefficients of Equation (4.189) are given in Appendix E, Section E.4.

4.3.2.5 Continuity of Mass at the Interface

Equation (2.34) is used to calculate $V_{iG,P}$. Continuity of mass at the interface can be written as:

$$\left(\rho A \vec{V} \cdot \hat{n} \right)_{iL,P} = \left(\rho A \vec{V} \cdot \hat{n} \right)_{iG,P} \quad (4.190)$$

Simple calculation of the dot product results in:

$$a_{iG,P}^{v,u} U_{iG,P} + a_{iG,S}^{v,u} U_{iL,P} + a_{iG,P}^{v,v} V_{iG,P} + a_{iG,S}^{v,v} V_{iL,P} = 0 \quad (4.191)$$

The coefficients of Equation (4.191) are given in Appendix E, Section E.5.

4.3.2.6 Continuity of Energy at the Interface

The energy continuity at the interface, Equation (2.35), is used as the governing equation for $V_{iL,P}$.

This equation can be written in terms of velocity and normal unit vectors as:

$$\left(\rho A \vec{V} \cdot \hat{n} \right)_{iL,P} = \dot{m}_{\text{intf}} = \frac{A_{iL,P}}{H_a} \left(-k_{iL,P} \frac{\partial T}{\partial n} \Big|_{iL,P} + k_{iG,P} \frac{\partial T}{\partial n} \Big|_{iG,P} \right) \quad (4.192)$$

Applying previous approaches for the evaluation of the gradients and calculation of dot product of vectors gives the algebraic form of Equation (4.192) as:

$$a_{iL,P}^{v,u} U_{iL,P} + a_{iL,P}^{v,v} V_{iL,P} + a_{iL,P}^{v,t} T_{iL,P} + a_{iL,E}^{v,t} T_{iL,E} + a_{iL,W}^{v,t} T_{iL,W} + a_{iL,S}^{v,t} T_{iL,S} + a_{iL,N}^{v,t} T_{iG,P} + a_{iL,NE}^{v,t} T_{iG,E} + a_{iL,NW}^{v,t} T_{iG,W} = b_{iL,P}^v \quad (4.193)$$

The coefficients of Equation (4.193) are given in Appendix E, Section E.6.

4.3.2.7 Equilibrium Condition at the Interface

The gas-liquid interface obeys the equilibrium condition described by Equation (2.33). The equilibrium temperature is a function of the liquid pressure and mass fraction at the interface. The equilibrium temperature function, described in Appendix A, can be written as follows using the Newton-Raphson linearisation:

$$T_{iL} = T_{iL}^o + \frac{\partial T_{\text{Eq}}}{\partial \xi_W} (\xi_W - \xi_W^o) + \frac{\partial T_{\text{Eq}}}{\partial P_{iL}} (P_{iL} - P_{iL}^o) \quad (4.194)$$

The liquid interface temperature, $T_{iL,P}$, algebraic equation is:

$$a_{iL,P}^{t,t} T_{iL,P} + a_{iL,P}^{t,\xi} \xi_{W,iL,P} + a_{iL,P}^{t,p} P_{iL,P} = b_{iL,P}^t \quad (4.195)$$

The coefficients of Equation (4.195) are given in Appendix E, Section E.7.

4.3.2.8 Temperature Equality at the Interface

The gas phase interface temperature equation is the equality of $T_{iG,P}$ and $T_{iL,P}$. The algebraic equation for $T_{iG,P}$ is as follows:

$$a_{iG,P}^{t,t} T_{iG,P} + a_{iG,S}^{t,t} T_{iL,P} = 0 \quad (4.196)$$

The coefficients of Equation (4.196) are given in Appendix E, Section E.8.

4.3.2.9 Impermeability of LiBr

Newton-Raphson linearisation is applied to ($\dot{m}_{\text{intf}} \xi_W$) term in Equation (2.37).

$$\dot{m}_{\text{intf}} \xi_W = (\rho A n_x)_{iL,P} [U \xi_W^o + U^o \xi_W - U^o \xi_W^o]_{iL,P} + (\rho A n_y)_{iL,P} [V \xi_W^o + V^o \xi_W - V^o \xi_W^o]_{iL,P} \quad (4.197)$$

By Applying Equation (4.197) and the approximation of the gradient term, the ξ_W interface linear equation is formed:

$$a_{iL,P}^{\xi,\xi} \xi_{W,iL,P} + a_{iL,E}^{\xi,\xi} \xi_{W,iL,E} + a_{iL,W}^{\xi,\xi} \xi_{W,iL,W} + a_{iL,S}^{\xi,\xi} \xi_{W,iL,S} + a_{iL,P}^{\xi,u} U_{iL,P} + a_{iL,P}^{\xi,v} V_{iL,P} = b_{iL,P}^{\xi} \quad (4.198)$$

The coefficients of Equation (4.198) are given in Appendix E, Section E.9.

4.3.3 Boundary Condition Equations Implementation

Boundary conditions are imposed by means of utilizing zero-width boundary control volumes. The boundary integration points are located at the centre of the face of these control volumes. A linear algebraic equation is used to define the boundary nodal value. When the coefficients of the linear equation are determined so that they prescribe the required boundary condition, these linear equations are substituted into the algebraic equations of the control volumes next to the boundaries (algebraic absorption of the boundary condition into the nearest interior nodal equation). Two types of boundary conditions are used in this work: Dirichlet and Neumann. A detailed description of formulation and implementation of these boundary conditions is presented for a general variable $\Phi = U, V, T, \xi_W$ in this section. The pressure at the boundary nodes is calculated by performing linear extrapolation of the pressure of interior nodes toward the boundaries. The extrapolation relations for pressures on the boundaries are subsequently used in all algebraic equations with implicit pressure terms.

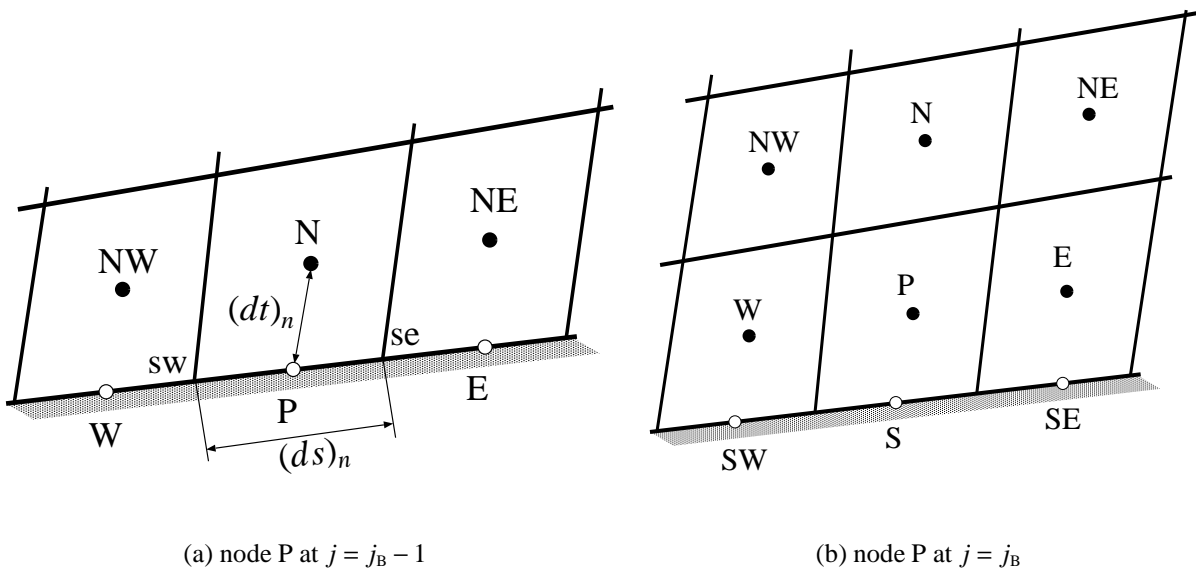


Figure 4.3: South boundary computational molecule.

The south boundary is used to illustrate the formulation of boundary conditions. Figure 4.3(a)

shows a typical boundary node and its neighbours on the south boundary of the solution domain ($i, j = j_B - 1$). The algebraic equation that connects boundary node P to its adjacent internal node is as:

$$a_{P(i, j_B-1)}^{\phi, \phi} \Phi_{P(i, j_B-1)} + a_{N(i, j_B-1)}^{\phi, \phi} \Phi_{N(i, j_B-1)} = b_{(i, j_B-1)}^{\phi} \quad (4.199)$$

The coefficients of Equation (4.199) are set to the desired boundary conditions at the south boundary. The setting of these coefficients for the two boundary condition types is given below.

4.3.3.1 Dirichlet

This boundary condition is prescribed when the value of the variable Φ at the boundary is given. For Dirichlet boundary condition, the coefficients of Equation (4.199) are set to:

$$\begin{aligned} a_{P(i, j_B-1)}^{\phi, \phi} &= 1 \\ a_{N(i, j_B-1)}^{\phi, \phi} &= 0 \\ b_{(i, j_B-1)}^{\phi} &= \Phi_{\text{bnd}} \end{aligned} \quad (4.200)$$

where Φ_{bnd} is the Φ value at boundary.

4.3.3.2 Neumann

A Neumann boundary condition is applied when the gradient of a variable is prescribed at the boundary (e.g. $\frac{\partial \Phi}{\partial x} = \Gamma_{\text{bnd}}^{\phi}$). In the case of a non-orthogonal grid, $\frac{\partial \Phi}{\partial x}$ and $\frac{\partial \Phi}{\partial y}$ are specified in terms of the gradients along the unit vector directions, \hat{s} and \hat{t} . The gradients along the west to east direction, \hat{s} , and south to north direction, \hat{t} , can be expressed in a chain rule as follows:

$$\frac{\partial \Phi}{\partial s} = \frac{\partial \Phi}{\partial x} \frac{\partial x}{\partial s} + \frac{\partial \Phi}{\partial y} \frac{\partial y}{\partial s} \quad (4.201)$$

$$\frac{\partial \Phi}{\partial t} = \frac{\partial \Phi}{\partial x} \frac{\partial x}{\partial t} + \frac{\partial \Phi}{\partial y} \frac{\partial y}{\partial t} \quad (4.202)$$

The gradient of Φ in the x direction can be evaluated using Cramer's rule:

$$\frac{\partial \Phi}{\partial x} = \frac{\begin{vmatrix} \frac{\partial \Phi}{\partial s} & \frac{\partial y}{\partial s} \\ \frac{\partial \Phi}{\partial t} & \frac{\partial y}{\partial t} \end{vmatrix}}{\begin{vmatrix} \frac{\partial x}{\partial s} & \frac{\partial y}{\partial s} \\ \frac{\partial x}{\partial t} & \frac{\partial y}{\partial t} \end{vmatrix}} = \frac{\frac{\partial \Phi}{\partial s} \frac{\partial y}{\partial t} - \frac{\partial \Phi}{\partial t} \frac{\partial y}{\partial s}}{\frac{\partial x}{\partial s} \frac{\partial y}{\partial t} - \frac{\partial y}{\partial s} \frac{\partial x}{\partial t}} \quad (4.203)$$

The gradient at the east face of a control volume becomes:

$$\left. \frac{\partial \Phi}{\partial x} \right|_e = \frac{\left. \frac{\partial \Phi}{\partial s} \right|_e \left. \frac{\partial y}{\partial t} \right|_e - \left. \frac{\partial \Phi}{\partial t} \right|_e \left. \frac{\partial y}{\partial s} \right|_e}{\left. \frac{\partial x}{\partial s} \right|_e \left. \frac{\partial y}{\partial t} \right|_e - \left. \frac{\partial y}{\partial s} \right|_e \left. \frac{\partial x}{\partial t} \right|_e} = \frac{\left. \frac{\partial \Phi}{\partial s} \right|_e t_{ye} - \left. \frac{\partial \Phi}{\partial t} \right|_e s_{ye}}{s_{xe} t_{ye} - t_{xe} s_{ye}} \quad (4.204)$$

A similar approach to Equation (4.204) can be applied to the north face of a control volume:

$$\left. \frac{\partial \Phi}{\partial x} \right|_n = \frac{\left. \frac{\partial \Phi}{\partial s} \right|_n \left. \frac{\partial y}{\partial t} \right|_n - \left. \frac{\partial \Phi}{\partial t} \right|_n \left. \frac{\partial y}{\partial s} \right|_n}{\left. \frac{\partial x}{\partial s} \right|_n \left. \frac{\partial y}{\partial t} \right|_n - \left. \frac{\partial y}{\partial s} \right|_n \left. \frac{\partial x}{\partial t} \right|_n} = \frac{\left. \frac{\partial \Phi}{\partial s} \right|_n t_{yn} - \left. \frac{\partial \Phi}{\partial t} \right|_n s_{yn}}{s_{xn} t_{yn} - t_{xn} s_{yn}} \quad (4.205)$$

The change in Φ in the y direction can be evaluate as:

$$\frac{\partial \Phi}{\partial y} = \frac{\begin{vmatrix} \frac{\partial x}{\partial s} & \frac{\partial \Phi}{\partial s} \\ \frac{\partial x}{\partial t} & \frac{\partial \Phi}{\partial t} \end{vmatrix}}{\begin{vmatrix} \frac{\partial x}{\partial s} & \frac{\partial y}{\partial s} \\ \frac{\partial x}{\partial t} & \frac{\partial y}{\partial t} \end{vmatrix}} = \frac{\frac{\partial \Phi}{\partial t} \frac{\partial x}{\partial s} - \frac{\partial \Phi}{\partial s} \frac{\partial x}{\partial t}}{\frac{\partial x}{\partial s} \frac{\partial y}{\partial t} - \frac{\partial y}{\partial s} \frac{\partial x}{\partial t}} \quad (4.206)$$

Equation (4.206) can be written for the east and north face of a control volume as:

$$\left. \frac{\partial \Phi}{\partial y} \right|_e = \frac{\left. \frac{\partial \Phi}{\partial t} \right|_e \left. \frac{\partial x}{\partial s} \right|_e - \left. \frac{\partial \Phi}{\partial s} \right|_e \left. \frac{\partial x}{\partial t} \right|_e}{\left. \frac{\partial x}{\partial s} \right|_e \left. \frac{\partial y}{\partial t} \right|_e - \left. \frac{\partial y}{\partial s} \right|_e \left. \frac{\partial x}{\partial t} \right|_e} = \frac{\left. \frac{\partial \Phi}{\partial t} \right|_e s_{xe} - \left. \frac{\partial \Phi}{\partial s} \right|_e t_{xe}}{s_{xe} t_{ye} - t_{xe} s_{ye}} \quad (4.207)$$

$$\left. \frac{\partial \Phi}{\partial y} \right|_n = \frac{\frac{\partial \Phi}{\partial t} \Big|_n \frac{\partial x}{\partial s} \Big|_n - \frac{\partial \Phi}{\partial s} \Big|_n \frac{\partial x}{\partial t} \Big|_n}{\frac{\partial x}{\partial s} \Big|_n \frac{\partial y}{\partial t} \Big|_n - \frac{\partial y}{\partial s} \Big|_n \frac{\partial x}{\partial t} \Big|_n} = \frac{\frac{\partial \Phi}{\partial t} \Big|_n s_{xn} - \frac{\partial \Phi}{\partial s} \Big|_n t_{xn}}{s_{xn} t_{yn} - t_{xn} s_{yn}} \quad (4.208)$$

To implement the Neumann boundary condition on the south boundary of the domain, $\frac{\partial \Phi}{\partial y}$ on the north face of the zero-width boundary control volume must be set. The derivatives in Equation (4.208) are evaluated using nodal and corner values of Φ :

$$\left. \frac{\partial \Phi}{\partial y} \right|_{n(i, j_B-1)} = \Gamma_{\text{bnd}}^\phi = \frac{\frac{\Phi_N - \Phi_P}{(dt)_n} s_{xn} - \frac{\Phi_{ne} - \Phi_{nw}}{(ds)_n} t_{xn}}{s_{xn} t_{yn} - t_{xn} s_{yn}} \quad (4.209)$$

Equation (4.209) can be rearranged into the form of a linear algebraic equation:

$$\Phi_P - \Phi_N = -(\Phi_{ne} - \Phi_{nw}) \frac{(dt)_n t_{xn}}{(ds)_n s_{xn}} - \Gamma_{\text{bnd}}^\phi (dt)_n \frac{s_{xn} t_{yn} - t_{xn} s_{yn}}{s_{xn}} \quad (4.210)$$

The coefficients of Equation (4.210) are as follows:

$$\left. \begin{aligned} a_{P(i, j_B-1)}^{\phi, \phi} &= 1, & a_{N(i, j_B-1)}^{\phi, \phi} &= -1 \\ b_{(i, j_B-1)}^\phi &= -(\Phi_{ne} - \Phi_{nw}) \frac{(dt)_n t_{xn}}{(ds)_n s_{xn}} - \Gamma_{\text{bnd}}^\phi (dt)_n \frac{s_{xn} t_{yn} - t_{xn} s_{yn}}{s_{xn}} \end{aligned} \right\} \quad (4.211)$$

The corner values in Equation (4.211) are determined by performing linear interpolation between the nearest boundary nodal values. Under the circumstances where the control volume is at the corner of the domain, i.g. (i_B, j_B) and both boundaries are Neumann type, then $\Phi_{se} = \Phi(i_B, j_B)$. If one of the boundaries has Dirichlet boundary condition, then $\Phi_{se} = \Phi_{\text{bnd}}$.

4.3.3.3 Algebraic Absorption of the Boundary Conditions

The boundary nodes can be eliminated from the solution fields by being substituted to the algebraic equations of the interior nodes adjacent to the boundaries. To illustrate the process, Equation (4.124) is rewritten for node P adjacent to the south boundary in Figure 4.3(b):

$$\begin{aligned} a_{P(i, j_B)}^{\phi, \phi} \Phi_{P(i, j_B)} + a_{E(i, j_B)}^{\phi, \phi} \Phi_{E(i, j_B)} + a_{W(i, j_B)}^{\phi, \phi} \Phi_{W(i, j_B)} + a_{N(i, j_B)}^{\phi, \phi} \Phi_{N(i, j_B)} + a_{S(i, j_B)}^{\phi, \phi} \Phi_{S(i, j_B)} \\ + a_{NE(i, j_B)}^{\phi, \phi} \Phi_{NE(i, j_B)} + a_{NW(i, j_B)}^{\phi, \phi} \Phi_{NW(i, j_B)} + a_{SE(i, j_B)}^{\phi, \phi} \Phi_{SE(i, j_B)} + a_{SW(i, j_B)}^{\phi, \phi} \Phi_{SW(i, j_B)} = b_{(i, j_B)}^\phi \end{aligned} \quad (4.212)$$

The nodes SW, S, and SE are located at the boundary and controlled by the boundary conditions. For these nodes, the algebraic boundary condition equation, Equation (4.199), can be rewritten as:

$$a_{P(i-1,j_B-1)}^\phi \Phi_{SW(i,j_B)} + a_{N(i-1,j_B-1)}^\phi \Phi_{W(i,j_B)} = b_{(i-1,j_B-1)}^\phi \quad (4.213)$$

$$a_{P(i,j_B-1)}^\phi \Phi_S(i,j_B) + a_{N(i,j_B-1)}^\phi \Phi_P(i,j_B) = b_{(i,j_B-1)}^\phi \quad (4.214)$$

$$a_{P(i+1,j_B-1)}^\phi \Phi_{SE(i,j_B)} + a_{N(i+1,j_B-1)}^\phi \Phi_E(i,j_B) = b_{(i+1,j_B-1)}^\phi \quad (4.215)$$

The boundary nodes Φ_{SW} , Φ_S , and Φ_{SE} in Equation (4.212) are replaced with Equations (4.213) to (4.215) in order to eliminate boundary nodes. This substitution results in the following equation:

$$\begin{aligned} \left(a_{P(i,j_B)}^{\phi,\phi}\right)^\oplus \Phi_{P(i,j_B)} + \left(a_{E(i,j_B)}^{\phi,\phi}\right)^\oplus \Phi_{E(i,j_B)} + \left(a_{W(i,j_B)}^{\phi,\phi}\right)^\oplus \Phi_{W(i,j_B)} + a_{N(i,j_B)}^{\phi,\phi} \Phi_{N(i,j_B)} \\ + a_{NE(i,j_B)}^{\phi,\phi} \Phi_{NE(i,j_B)} + a_{NW(i,j_B)}^{\phi,\phi} \Phi_{NW(i,j_B)} = \left(b_{(i,j_B)}^\phi\right)^\oplus \end{aligned} \quad (4.216)$$

The new coefficients of Equation (4.216) are:

$$\left. \begin{aligned} \left(a_{P(i,j_B)}^{\phi,\phi}\right)^\oplus &= a_{P(i,j_B)}^{\phi,\phi} - a_{S(i,j_B)}^{\phi,\phi} \frac{a_{N(i,j_B-1)}^{\phi,\phi}}{a_{P(i,j_B-1)}^{\phi,\phi}} \\ \left(a_{N(i,j_B)}^{\phi,\phi}\right)^\oplus &= a_{E(i,j_B)}^{\phi,\phi} - a_{SE(i,j_B)}^{\phi,\phi} \frac{a_{N(i+1,j_B-1)}^{\phi,\phi}}{a_{P(i+1,j_B-1)}^{\phi,\phi}} \\ \left(a_{S(i,j_B)}^{\phi,\phi}\right)^\oplus &= a_{W(i,j_B)}^{\phi,\phi} - a_{SW(i,j_B)}^{\phi,\phi} \frac{a_{N(i-1,j_B-1)}^{\phi,\phi}}{a_{P(i-1,j_B-1)}^{\phi,\phi}} \\ \left(b_{(i,j_B)}^\phi\right)^\oplus &= b_{(i,j_B)}^\phi - a_{S(i,j_B)}^{\phi,\phi} \frac{b_{(i,j_B-1)}^\phi}{a_{P(i,j_B-1)}^{\phi,\phi}} \\ &\quad - a_{SE(i,j_B)}^{\phi,\phi} \frac{b_{(i+1,j_B-1)}^\phi}{a_{P(i+1,j_B-1)}^{\phi,\phi}} - a_{SW(i,j_B)}^{\phi,\phi} \frac{b_{(i-1,j_B-1)}^\phi}{a_{P(i-1,j_B-1)}^{\phi,\phi}} \end{aligned} \right\} \quad (4.217)$$

After the modification of the interior node coefficients to implement the boundary conditions,

$a_{SW(i,j_B)}^{\phi,\phi}$, $a_{S(i,j_B)}^{\phi,\phi}$, and $a_{SE(i,j_B)}^{\phi,\phi}$ are set to zero.

4.3.3.4 Face Velocity Boundary Conditions

The face velocity boundary conditions are derived using the nodal boundary conditions and implemented using the coefficients of the continuity equation. The south boundary is used as an example to illustrate the derivation of the face velocity boundary condition. The continuity equation for node P in Figure 4.3(b), can also be applied on the south boundary as follows:

$$\begin{aligned} & \left(a_{e(i,j_B-1)}^{c,u} U_e + a_{e(i,j_B-1)}^{c,v} V_e \right) + \left(a_{w(i,j_B-1)}^{c,u} U_w + a_{w(i,j_B-1)}^{c,v} V_w \right) \\ & + \left(a_{n(i,j_B-1)}^{c,u} U_n + a_{n(i,j_B-1)}^{c,v} V_n \right) + \left(a_{s(i,j_B-1)}^{c,u} U_s + a_{s(i,j_B-1)}^{c,v} V_s \right) = b_{P(i,j_B-1)}^c \end{aligned} \quad (4.218)$$

One can use Equation (4.218) to produce separate equations for U_s and V_s :

$$\begin{aligned} U_s = \frac{-1}{a_{s(i,j_B-1)}^{c,u}} & \left[\left(a_{e(i,j_B-1)}^{c,u} U_e + a_{e(i,j_B-1)}^{c,v} V_e \right) + \left(a_{w(i,j_B-1)}^{c,u} U_w + a_{w(i,j_B-1)}^{c,v} V_w \right) \right. \\ & \left. + \left(a_{n(i,j_B-1)}^{c,u} U_n + a_{n(i,j_B-1)}^{c,v} V_n \right) + a_{s(i,j_B-1)}^{c,v} V_s - b_{P(i,j_B-1)}^c \right] \end{aligned} \quad (4.219)$$

$$\begin{aligned} V_s = \frac{-1}{a_{s(i,j_B-1)}^{c,v}} & \left[\left(a_{e(i,j_B-1)}^{c,u} U_e + a_{e(i,j_B-1)}^{c,v} V_e \right) + \left(a_{w(i,j_B-1)}^{c,u} U_w + a_{w(i,j_B-1)}^{c,v} V_w \right) \right. \\ & \left. + \left(a_{n(i,j_B-1)}^{c,u} U_n + a_{n(i,j_B-1)}^{c,v} V_n \right) + a_{s(i,j_B-1)}^{c,u} U_s - b_{P(i,j_B-1)}^c \right] \end{aligned} \quad (4.220)$$

The coefficients $a_{s(i,j_B-1)}^{c,u}$ and $a_{s(i,j_B-1)}^{c,v}$ are set to be -1 and moved to act as a source term in Equations (4.219) and (4.220), respectively:

$$\begin{aligned} U_s = & \left(a_{e(i,j_B-1)}^{c,u} U_e + a_{e(i,j_B-1)}^{c,v} V_e \right) + \left(a_{w(i,j_B-1)}^{c,u} U_w + a_{w(i,j_B-1)}^{c,v} V_w \right) \\ & + \left(a_{n(i,j_B-1)}^{c,u} U_n + a_{n(i,j_B-1)}^{c,v} V_n \right) + a_{s(i,j_B-1)}^{c,v} V_s + a_{s(i,j_B-1)}^{c,u} \end{aligned} \quad (4.221)$$

$$\begin{aligned} V_s = & \left(a_{e(i,j_B-1)}^{c,u} U_e + a_{e(i,j_B-1)}^{c,v} V_e \right) + \left(a_{w(i,j_B-1)}^{c,u} U_w + a_{w(i,j_B-1)}^{c,v} V_w \right) \\ & + \left(a_{n(i,j_B-1)}^{c,u} U_n + a_{n(i,j_B-1)}^{c,v} V_n \right) + a_{s(i,j_B-1)}^{c,u} U_s + a_{s(i,j_B-1)}^{c,v} \end{aligned} \quad (4.222)$$

Only south and north mass flow rates in control volume P are needed to set the south boundary condition and the U and V velocity boundary conditions are set independently. These two requirements change Equations (4.221) and (4.222) as follows:

$$U_s - a_{n(i,j_B-1)}^{c,u} U_n = a_{s(i,j_B-1)}^{c,u} \quad (4.223)$$

$$V_s - a_{n(i,j_B-1)}^{c,v} V_n = a_{s(i,j_B-1)}^{c,v} \quad (4.224)$$

To obtain the Dirichlet boundary condition for U and V on the south boundary, the coefficients of Equations (4.223) and (4.224) are set as:

$$\left. \begin{aligned} a_{n(i,j_B-1)}^{c,u} &= 0 \\ a_{s(i,j_B-1)}^{c,u} &= U_{\text{bnd}} \end{aligned} \right\} \quad (4.225)$$

$$\left. \begin{aligned} a_{n(i,j_B-1)}^{c,v} &= 0 \\ a_{s(i,j_B-1)}^{c,v} &= V_{\text{bnd}} \end{aligned} \right\} \quad (4.226)$$

To obtain the Neumann boundary condition for U and V on the south boundary, the $\frac{\partial \Phi}{\partial y}$ is approximated from face to face across the control volume P:

$$\left. \frac{\partial \Phi}{\partial y} \right|_{(i,j_B)} = \Gamma_{\text{bnd}}^{\phi} = \frac{\frac{\Phi_n - \Phi_s}{(dt)_P} s_{xs} - \frac{\Phi_{se} - \Phi_{sw}}{(ds)_s} t_{xP}}{s_{xs} t_{yP} - t_{xP} s_{ys}} \quad (4.227)$$

Rearranging Equation (4.227) for Φ_s leads to:

$$\Phi_s - \Phi_n = -(\Phi_{se} - \Phi_{sw}) \frac{(dt)_P t_{xP}}{(ds)_s s_{xs}} - \Gamma_{\text{bnd}}^{\phi} (dt)_P \frac{s_{xs} t_{yP} - t_{xP} s_{ys}}{s_{xs}} \quad (4.228)$$

The coefficients in Equations (4.223) and (4.224) for U and V Neumann boundary conditions respectively are defined as:

$$\left. \begin{aligned} a_{n(i,j_B-1)}^{c,u} &= 1 \\ a_{s(i,j_B-1)}^{c,u} &= -(\Phi_{se} - \Phi_{sw}) \frac{(dt)_P t_{xP}}{(ds)_s s_{xs}} - \Gamma_{\text{bnd}}^u (dt)_P \frac{s_{xs} t_{yP} - t_{xP} s_{ys}}{s_{xs}} \end{aligned} \right\} \quad (4.229)$$

$$\left. \begin{aligned} a_{n(i,j_B-1)}^{c,v} &= 1 \\ a_{s(i,j_B-1)}^{c,v} &= -(\Phi_{se} - \Phi_{sw}) \frac{(dt)_P t_{xP}}{(dS)_s s_{xs}} - \Gamma_{\text{bnd}}^v (dt)_P \frac{s_{xs} t_{yP} - t_{xP} s_{ys}}{s_{xs}} \end{aligned} \right\} \quad (4.230)$$

The rest of the coefficients in Equation (4.218) are then set to zero.

To algebraically absorb the face boundary conditions into the interior nodal equations, Equations (4.223) and (4.224) are substituted to the continuity equation for node P:

$$\begin{aligned} & \left(a_{e(i,j_B)}^{c,u} U_e + a_{e(i,j_B)}^{c,v} V_e \right) + \left(a_{w(i,j_B)}^{c,u} U_w + a_{w(i,j_B)}^{c,v} V_w \right) + \left(a_{n(i,j_B)}^{c,u} U_n + a_{n(i,j_B)}^{c,v} V_n \right) \\ & + a_{s(i,j_B)}^{c,u} \left(a_{n(i,j_B-1)}^{c,u} U_n + a_{s(i,j_B-1)}^{c,u} \right) + a_{s(i,j_B)}^{c,v} \left(a_{n(i,j_B-1)}^{c,v} V_n + a_{s(i,j_B-1)}^{c,v} \right) = b_{P(i,j_B)}^c \end{aligned} \quad (4.231)$$

Collecting terms yields:

$$\left(a_{e(i,j_B)}^{c,u} U_e + a_{e(i,j_B)}^{c,v} V_e \right) + \left(a_{w(i,j_B)}^{c,u} U_w + a_{w(i,j_B)}^{c,v} V_w \right) + \left(a_{n(i,j_B)}^{c,u} \right)^\oplus U_n + \left(a_{n(i,j_B)}^{c,v} \right)^\oplus V_n = \left(b_{P(i,j_B)}^c \right)^\oplus \quad (4.232)$$

The new coefficients are then defined as:

$$\left. \begin{aligned} \left(a_{n(i,j_B)}^{c,u} \right)^\oplus &= a_{n(i,j_B)}^{c,u} + a_{s(i,j_B)}^{c,u} a_{n(i,j_B-1)}^{c,u} \\ \left(a_{n(i,j_B)}^{c,v} \right)^\oplus &= a_{n(i,j_B)}^{c,v} + a_{s(i,j_B)}^{c,v} a_{n(i,j_B-1)}^{c,v} \\ \left(b_{P(i,j_B)}^c \right)^\oplus &= b_{P(i,j_B)}^c - a_{s(i,j_B)}^{c,u} a_{s(i,j_B-1)}^{c,u} - a_{s(i,j_B)}^{c,v} a_{s(i,j_B-1)}^{c,v} \end{aligned} \right\} \quad (4.233)$$

4.3.4 E-factor

In development of the elliptic model in this work, the governing equations are made fully implicit. Although the steady-state solution is required in this study, the transient terms are used in the equations as relaxation in the solution of the coupled non-linear equations.

Van Doormaal and Raithby [53] recommended replacing the transient term with a distorted transient term. This distorted transient scheme uses a so-called E-factor, E . To use this scheme,

$a_P^{u,u}$ equation, Equation (4.125), is rewritten as:

$$(a_P^{u,u}) = \frac{\rho_P \bar{V}_P}{\Delta t} + (a_P^{u,u})^* \quad (4.234)$$

The transient term in Equation (4.125) is redefined using the E-factor:

$$\frac{\rho_P \bar{V}_P}{\Delta t} = \frac{(a_P^{u,u})^*}{E^u} \quad (4.235)$$

Substituting Equation (4.235) into Equations (4.234) and (4.164) produces new definitions for $a_P^{u,u}$ and b_P^u coefficients:

$$(a_P^{u,u}) = (a_P^{u,u})^* + \frac{(a_P^{u,u})^*}{E^u} = \left(1 + \frac{1}{E^u}\right) (a_P^{u,u})^* \quad (4.236)$$

$$b_P^u = \frac{(a_P^{u,u})^*}{E^u} U_P^o + \rho_P g_x \bar{V}_P \quad (4.237)$$

A similar definition is used for the V , T , and ξ_w equations.

The E-factor allows taking a different Δt in each control volume (if control volumes have different sizes), which can lead to faster convergence. In the computer code implementation of the coefficient calculations, both the E-factor and true transient formulations are available and are selected through the specification of E and Δt values.

4.3.5 Interface Movement Procedure

The interface location is determined by imposing the mass balance at each column of the liquid region using the ILMB method. Equation (4.238) balances the mass crossing the east, west, and interface of the liquid column shaded in Figure 4.4.

$$\underbrace{\int_0^{h_{L,e}} \rho_{L,e} (\vec{V} \cdot \hat{n})_e dh}_{\dot{m}'_e} = \underbrace{\int_0^{h_{L,w}} \rho_{L,w} (\vec{V} \cdot \hat{n})_w dh}_{\dot{m}'_w} + \underbrace{\dot{m}'_{\text{intf}}}_{\text{mass crossing the interface}} \quad (4.238)$$

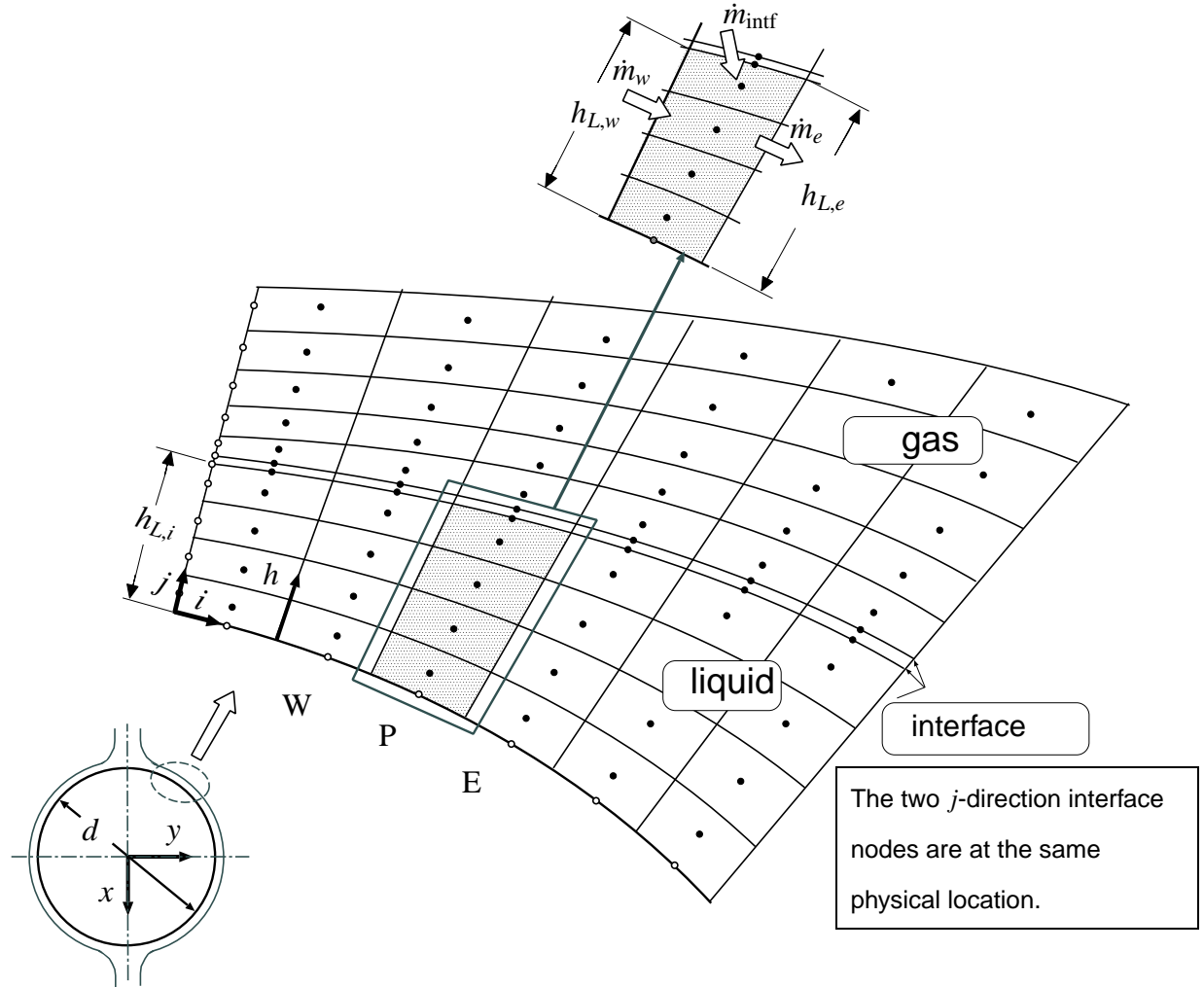


Figure 4.4: Nomenclature used in the ILMB method. The interface node spacing is exaggerated for illustration purposes.

where $h_{L,w}$ and $h_{L,e}$ are the distance of the interface from the domain south boundary at the west and east side of the liquid column. The integrals in Equation (4.238) can be converted using a single integration point at each face of the control volumes.

$$\sum_{j=j_{BL}}^{j_{EL}} \rho_{L_e} (U_e n_{xe} + V_e n_{ye}) \Delta h_{L,e} = \sum_{j=j_{BL}}^{j_{EL}} \rho_{L_w} (U_w n_{xw} + V_w n_{yw}) \Delta h_{L,w} + \dot{m}'_{intf} \quad (4.239)$$

For uniform spacing in the h direction: $h_{L,e} = N_{y,L} \Delta h_{L,e}$. Rearrangement of Equation (4.239) for uniform spacing gives:

$$\frac{1}{N_{y,L}} \left[\sum_{j=j_{BL}}^{j_{EL}} \rho_{L_e} (U_e n_{xe} + V_e n_{ye}) \right] h_{L,e} = \frac{1}{N_{y,L}} \left[\sum_{j=j_{BL}}^{j_{EL}} \rho_{L_w} (U_w n_{xw} + V_w n_{yw}) \right] h_{L,w} + \dot{m}'_{\text{intf}} \quad (4.240)$$

Equation (4.240) the interface height at east and west side of each liquid column. The position of the first node on the interface is fixed and used as $h_{L,w}$. Therefore, applying forward marching gives the position of the interface at the successive stations along the domain south boundary. The application of the ILMB is enabled by not solving the continuity equations in the row of the control volumes adjacent to the interface in the liquid.

4.3.6 Solution Method

Applying a finite volume method with the described techniques results in implicitly coupled algebraic equations. Using the non-orthogonal grid produces a nine-point computational molecule, consisting of the central node and its eight neighbouring nodes, for each field variable (U , V , P , and T in both phases, and ξ_w in the liquid phase). Therefore, the coefficients for each node are stored in a nine-banded 5-block matrix. Then all the coefficients are assembled in a sparse matrix. The interface condition coefficients are also added to the sparse matrix. An in-house computer code implements this numerical solution approach. The coupled algebraic equations are all solved together simultaneously using the parallelized SuperLU-DIST [54] direct solver within the PETSc software library.

4.3.6.1 Convergence Criteria

The numerical solution of the algebraic equations is repeated until a converged solution is obtained for the field variables and the interface movement. At each iteration the matrix equation is solved on a fixed mesh. Before repeating the numerical solution, the interface is moved based on the most

recent interface height calculations and the entire domain grid is recalculated. The next iteration of the numerical solution begins with updating the coefficient matrix based on the most recent field variables and domain grid. The computation proceeds until the desired convergence is obtained.

The steady-state convergence of the field variables is checked using the following:

$$\left| \frac{\Phi_{(i,j)}^n - \Phi_{(i,j)}^{n-1}}{\max(\Phi_{all(i,j)}^n) - \min(\Phi_{all(i,j)}^n)} \right| \leq \epsilon^\phi \quad (4.241)$$

where ϵ^ϕ is the steady-state convergence criterion for the field variable Φ and n is the iteration number. In this study, $\epsilon^U = \epsilon^V = \epsilon^P = \epsilon^{\xi w} = 10^{-7}$ and $\epsilon^T = 10^{-4}$. Convergence of the interface height is declared when the maximum of all absolute changes in interface node locations between two consecutive iterations is less than 10^{-10} m for the entire domain.

The residual of the linearised governing equations are also investigated during the computation process using the following equation:

$$\{\mathcal{R}^n\} = \{|b\} - [A] \cdot \{\Phi^n\} \leq \mathcal{R}_{\text{spec}}^\phi \quad (4.242)$$

where \mathcal{R}^n is the absolute residual of variable Φ algebraic equation and $\mathcal{R}_{\text{spec}}^\phi$ is the specified residual criterion for each field variable. For a typical case in this study, $\mathcal{R}_{\text{spec}}^U = \mathcal{R}_{\text{spec}}^V = \mathcal{R}_{\text{spec}}^P = \mathcal{R}_{\text{spec}}^{\xi w} = 10^{-6}$ and $\mathcal{R}_{\text{spec}}^T = 10^{-4}$. The time step size of $\Delta t = 10^{-3}$ s was used in the simulation of the elliptic model. No change in the converged solution was observed with variation of the time step size.

Chapter 5

Parallel-Plate Channels: Parabolic Model

5.1 Introduction

The results of the parabolic numerical model are presented in this chapter. Detailed results are compared with the literature to demonstrate the validity of the present approach. The temperature, mass fraction and velocity profiles are presented for the single phase application of the model. The numerical model is then applied to the two-phase problem of simultaneous heat and mass transfer in and between the liquid and vapour phases. The effect of the liquid phase inlet Reynolds number, mass fraction, and cold wall temperature on absorption process are examined. New results are presented to investigate the gas phase effect on mass absorption and liquid film thickness development.

5.2 Grid Independence Study

A grid independence study was conducted using a typical case studied in this work (Comparison Case C2 described in Section 5.3). The axial variation of the interfacial mass fraction was used to assess the grid independence.

The number of nodes in the x and y directions for Comparison Case C2 considered were as follows: $40 \leq N_{y,L} \leq 100$, $40 \leq N_{y,G} \leq 100$, and $300 \leq N_x \leq 700$. A grid with $N_{y,L} = 80$, $N_{y,G} = 80$, and $N_x = 500$ was used which had a maximum difference of 0.16% from the finest grid ($N_{y,L} = 100$, $N_{y,G} = 100$, and $N_x = 700$).

5.3 Comparisons with Previous Work

The validity of the parabolic numerical code is demonstrated by comparing the results with three earlier works conducted for the absorption of water vapour into a LiBr-water solution flowing on a vertical plate. Due to the lack of published experimental measurements of absorption in a vertical channel in the literature, the three numerical works by Andberg and Vliet [10], Kawae et al. [11], and Mittermaier and Ziegler [13] were selected to assess the present numerical method. In all these studies, only the liquid solution film is modelled. Therefore, for the purpose of comparison, the vapour effect on the steady, laminar thin falling film solution was minimized by modifying the gas phase velocity boundary conditions and properties as follows, Figure 2.1:

- At $y = H$, $\frac{\partial U_G}{\partial y} = 0$ and $\frac{\partial V_G}{\partial y} = 0$ to permit entrainment of the quiescent vapour.
- The water vapour density and dynamic viscosity were specified to be $7.7353 \times 10^{-1} \text{ kg m}^{-3}$ and $8.2947 \times 10^{-8} \text{ kg m}^{-1} \text{ s}^{-1}$, respectively, to keep the gas phase velocity small and diminish the vapour shear force at the interface.

The parameters used for the comparison cases are summarized in Tables 5.1 and 5.2. The conditions in Table 5.1 are either stated in each reference or calculated based on the information provided in them. The value of ΔT_{sub} was chosen in each case so that the value of $T_{L,\text{in}}$ based on the equilibrium condition of McNeely [1] and the P_{in} and $\xi_{\text{LiBr},\text{in}}$ from the reference article matched the value of $T_{L,\text{in}}$ given in the article.

5.3.1 Comparison Case C1: Andberg and Vliet [10]

Development of temperature and mass fraction profiles in the falling film of LiBr over a cooled plate was modelled by Andberg and Vliet [10]. In order to model this case, the inlet operating conditions were specified according to Table 5.1. To reproduce the same case treated in Andberg

Table 5.1: Operating parameters and physical properties in comparison cases.

Reference	$Re_{L,in}$	T_{wall}	$T_{L,in}$	$\xi_{LiBr,in}$	P	δ_{in}	ΔT_{sub}	H_a
	–	[°C]	[°C]	–	[kPa]	[mm]	[K]	[J kg ⁻¹]
Andberg and Vliet [10]	10	35	44.44	0.6	0.9348	0.1719	1	2.6605×10^6
Kawae et al. [11]	10.6	35	46.50	0.6	1	0.2	0.15	2.7727×10^6
Mittermaier and Ziegler [13]	52.174	29.09	35.08	0.5	1.5	0.2359	0.01	$(h_v - \bar{h}_w)_{intf}$
Mittermaier and Ziegler [13]	52.174	29.09	35.08	0.5	1.5	0.076	0.01	$(h_v - \bar{h}_w)_{intf}$

Table 5.2: Comparison case parameters.

Reference	L	H	N_x	$N_{y,L}$	$N_{y,G}$	$U_{L,in}^a$	δ^b	Equilibrium Condition
	[m]	[m]	–	–	–	[m s ⁻¹]	–	–
Andberg and Vliet [10]	2	0.06227	400	80	80	FD	AE	McNeely [1]
Kawae et al. [11]	10	0.06227	500	80	80	FD	AE	McNeely [1]
Mittermaier and Ziegler [13]	0.1	0.06227	300	80	80	FD	NS	Mittermaier et al. [12]
Mittermaier and Ziegler [13]	0.1	0.06227	300	40	80	UF	NS	Mittermaier et al. [12]

^a FD: fully developed; UF: uniform

^b AE: analytical equation; NS: numerical solution

and Vliet [10], the geometry parameters presented in Table 5.2 are applied to a two-dimensional vertical channel. The liquid phase governing equations and the interface boundary conditions were altered to make the current model as close as possible to that of Andberg and Vliet [10]. The x -direction convection term including the partial enthalpies of the components in Equation (2.3) and the y -direction convection terms in Equations (2.3) and (2.4) were neglected. The partial enthalpies of LiBr, \bar{h}_{LiBr} , and water, \bar{h}_w , in the right-hand side of Equation (2.3) were replaced with $C_{p,LiBr}T_L$ and $C_{p,w}T_L$, respectively. Finally, the interface mass diffusion equation, Equation (2.11), and the

energy balance equation, Equation (2.12), were changed as follows:

$$\rho_L D_L^{AB} \frac{\partial \xi_{\text{LiBr}}}{\partial y} = \dot{m}_{\text{intf}}'' \quad (5.1)$$

$$k_L \frac{\partial T_L}{\partial y} = -\dot{m}_{\text{intf}}'' H_a \quad (5.2)$$

Based on the liquid film Reynolds number $\text{Re}_{L,\text{in}} = 10$, the inlet Froude number is $\text{Fr}_{L,\text{in}} = 0.83$ and the film is subcritical. The vapour enters the channel beside the liquid film solution with a mass flow rate per unit depth of $\dot{m}'_{G,\text{in}} = 7.1 \times 10^{-4} \text{ kg m}^{-1} \text{ s}^{-1}$. This value is chosen to provide enough vapour mass to advance the solution to $L = 2 \text{ m}$. A sufficient number of grid cells were allocated in the x and y directions as shown in Table 5.2 to ensure the grid independence based on the grid examination explained in Section 5.2.

In Figures 5.1 (a) and (b), the axial variation of the interfacial temperature and LiBr mass fraction obtained by the parabolic two-phase model is compared with the results in Andberg and Vliet [10]. The fully developed LiBr solution enters the channel with $\xi_{\text{LiBr}} = 0.6$. In the solution of the set of control volumes at the first station after the inlet, the node next to the interface remained unchanged from the inlet conditions (inlet mass fraction of 0.60 and temperature of 44.44°C). Because of the subcooling, the solution to the energy balance and equilibrium conditions at the interface yield ξ_{LiBr} of 0.5954 and a temperature of 44.548°C . Note that the interface temperature is consistent with the equilibrium condition and it is slightly larger than the inlet temperature, so energy is transferred to the film by conduction. In the second column of control volumes, there is a high gradient of mass fraction at the interface which causes a high mass absorption rate and energy transfer to the liquid. The energy transfer rate at the interface is higher than what is conducted to the film, so the interface temperature increases to 44.570°C . According to the equilibrium condition at the interface, ξ_{LiBr} increases to 0.5956. The increases in interface temperature and LiBr mass fraction continue until the energy is transferred more rapidly to the film at approximately $x = 4 \times 10^{-4} \text{ m}$, after which the interface temperature and LiBr mass fraction both decrease. The initial increases in the interface temperature and mass fraction due to subcooling were also observed by Mittermaier and Ziegler [15]. Detailed investigation of the subcooling effect in the

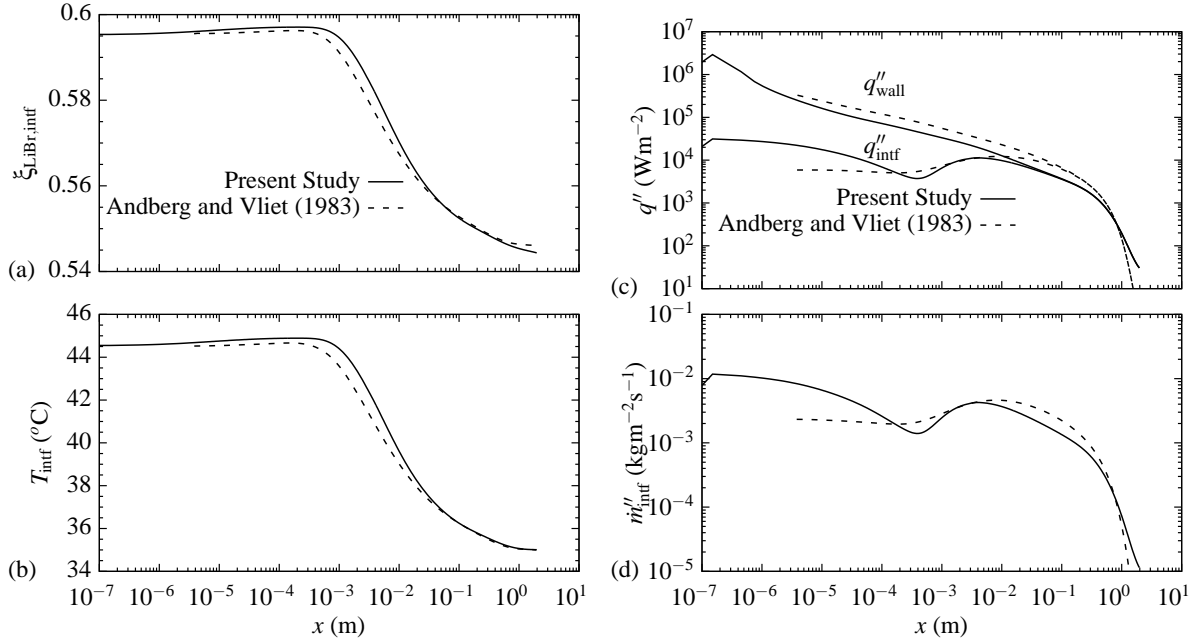


Figure 5.1: Axial variation of (a) interface mass fraction, (b) interface temperature, (c) interface and wall heat flux, and (d) interface mass flux for Comparison Case C1.

present work showed that, although subcooling causes relatively more initial water absorption at the inlet of the channel and affects the evolution of temperature, mass fraction, and mass absorption in the initial part of the channel, practically the same solution was obtained after $x = 3 \times 10^{-3}$ m for Case C1 with or without inlet subcooling. After undergoing this initial stage near the entrance, at $x = 3 \times 10^{-3}$ m the LiBr mass fraction decreases considerably and the interface temperature decreases according to the equilibrium relation at the interface. After this point, the present model predicts higher values for temperature and mass fraction in comparison to Andberg and Vliet [10]. As the interfacial temperature approaches the wall temperature (35°C in this case), the temperature gradient across the film approaches zero and the interface ξ_{LiBr} approaches a constant value. The discrepancy between the two results could be related to Andberg and Vliet having a constant pressure, whereas the pressure changes along the channel in the present model. In addition, Andberg and Vliet [10] used 19 nodes in the y direction for the liquid film compared to 80 for the present model.

Axial variations of the interfacial and wall heat fluxes and the interface mass flux are shown in Figures 5.1(c) and (d). In the present model, a larger amount of water vapour is absorbed into the liquid solution at the initial section of the channel compared to that of Andberg and Vliet [10]. At this location, the large temperature difference between the wall and the film uniform temperature causes a noticeable heat transfer at the wall while the temperature gradient is small at the interface. As the liquid temperature establishes a linear profile further down the channel, the heat released at the interface is conducted to the wall. A high temperature gradient at the interface results an increase in the interfacial heat and mass transfer between $x = 5 \times 10^{-4}$ m and $x = 5 \times 10^{-3}$ m. The wall and the interface heat transfer become nearly equal further down the channel and mass absorption drops to a very small amount because the interface temperature gradient is significantly reduced as flow advances down the channel.

5.3.2 Comparison Case C2: Kawae et al. [11]

The numerical model presented by Andberg and Vliet [10] was implemented by Kawae et al. [11] and tested for relatively higher falling film inlet temperature, pressure, film thickness and Reynolds number. To validate the current model regarding the transverse variations in the liquid film, a new test case was prepared according to the characteristics provided in Kawae et al. [11], as shown in Table 5.1. The liquid film Reynolds and Froude number for this case are $Re_{L,in} = 10.6$ and $Fr_{L,in} = 0.88$, respectively. As presented in Table 5.2, the number of nodes in the axial direction was increased to ensure the accuracy of the results.

The comparison of the axial variations of the interface mass fraction and interface and wall heat flux are presented in Figures 5.2 (a) and (b), respectively. The current model results are in a good agreement with the results predicted by Kawae et al. [11] except for a slight difference in the interface mass fraction at the end of the channel. This discrepancy is a result of a small difference in the interface temperature which is not presented here. Figure 5.2 (b) shows that the present model predicts higher heat flux caused by higher mass at the interface at $x = 10^{-5}$ m in comparison

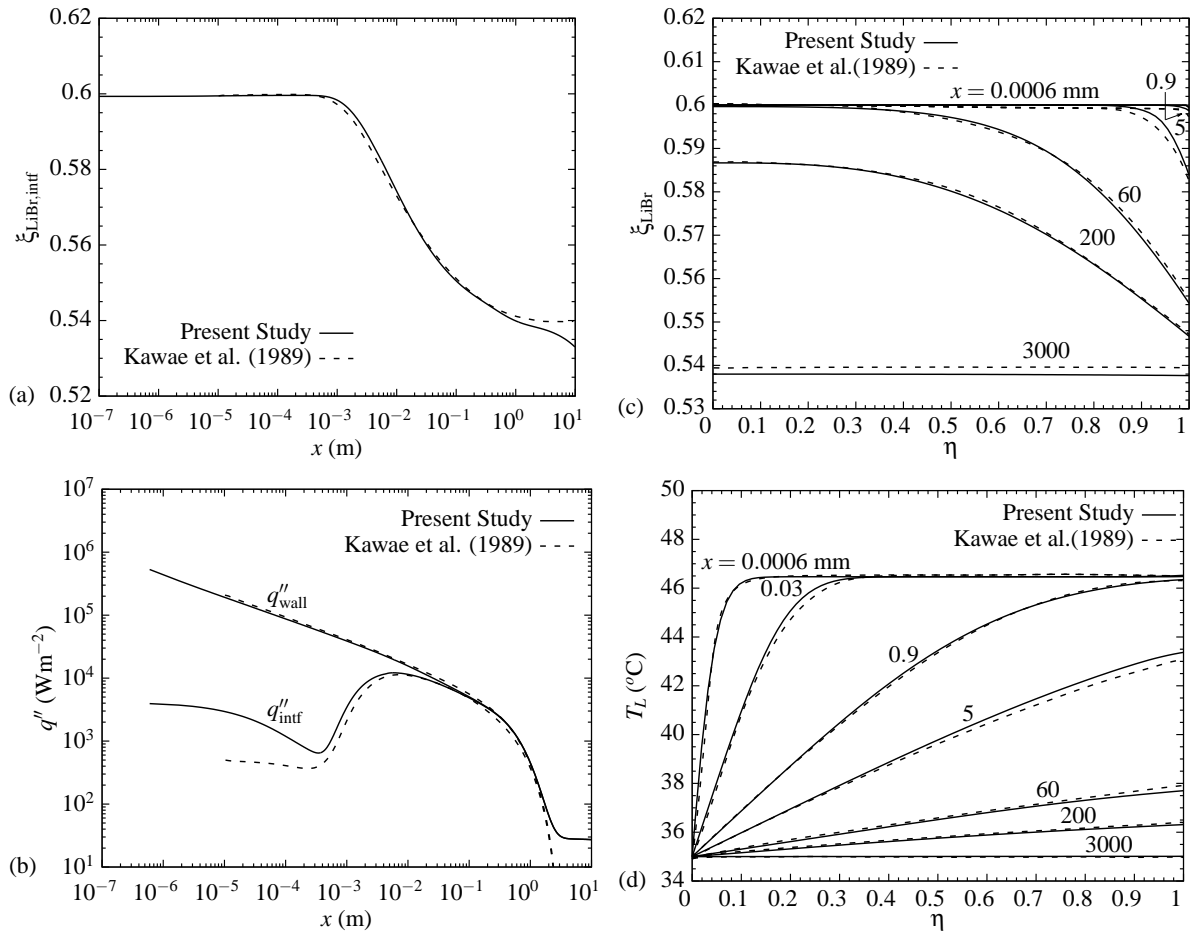


Figure 5.2: Comparison Case C2: axial variation of (a) interface mass fraction and (b) interface and wall heat flux; transverse-direction profiles at selected axial locations of (c) LiBr mass fraction and (d) liquid temperature.

to Kawae et al. [11]. This difference occurs because of the interfacial mass fraction gradient at the very beginning of the channel, the details of this gradient are shown in Figure 5.2 (c). After reaching a maximum near $x = 5 \times 10^{-3}$ m, the interface heat flux of the current model become nearly equal to that of Kawae et al. [11]. For $x > 2$ m, no data were presented by Kawae et al. [11] but the current results show that mass absorption and heat transfer continues at nearly constant values to the end of the channel.

Transverse distributions of the liquid film mass fraction and temperature at different axial locations are compared to Kawae et al. [11] in Figures 5.2 (c) and (d), respectively. The present results agree well with the single-phase model presented by Kawae et al. [11]. Figure 5.2 (c) shows that near the inlet (at $x = 0.0006$ mm) the LiBr mass fraction drops sharply at the interface while staying at the uniform inlet value $\xi_{\text{LiBr,in}} = 0.6$ across most of the film. This behaviour is due to the absorption of water at the interface. Further along the channel, absorption of water causes a continual drop in the LiBr mass fraction at the interface. The reduction is observed to be closer to the interface because the water has not diffused yet into the film. Figure 5.2 (d) shows that near the inlet, the temperature difference between the isothermal wall and the inlet film flow produces a noticeable temperature gradient close to the wall. Flow close to the interface is not yet affected by the cold wall and is still at a uniform temperature. Further down the channel, the flow becomes affected by the cooling wall and the temperature gradient approaches to a linear profile. The temperature and mass fraction profiles become almost uniform near the exit of the channel.

5.3.3 Comparison Case C3: Mittermaier and Ziegler [13]

The current model results for a liquid film with $Re_{L,\text{in}} = 52.174$ with either a fully developed or a uniform inlet velocity profile was compared to the results presented in Mittermaier and Ziegler [13]. The variable thermophysical properties and equilibrium relation provided by Mittermaier et al. [12] were used (Appendix A.4 and Appendix F). Note that some corrections are made to equilibrium condition and $C_{p,L}$ given by Mittermaier et al. [12]. Equation (5.2) was applied for the energy balance at the interface.

Figures 5.3 (a) and (b) compare the present model results for the axial variation of the absorption mass flux and the film thickness, respectively, with the results of Mittermaier and Ziegler [13] for the fully developed inlet velocity case. Just after the inlet, a sudden change in the conditions from the inlet causes a significant temperature gradient which leads to absorption of a significant amount of mass at the interface. While the interface temperature and mass fraction go through the

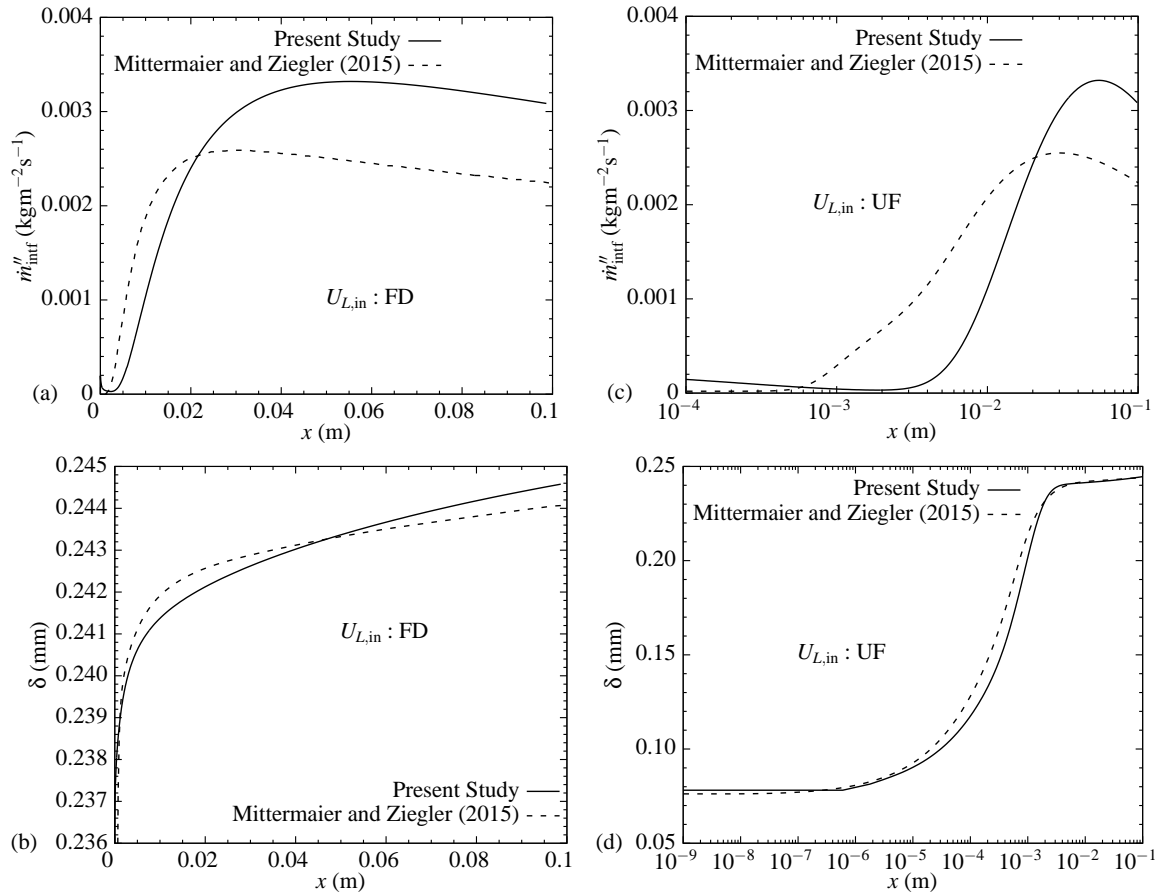


Figure 5.3: Comparison Case C3: axial variation of (a) interface mass flux and (b) liquid film thickness with a fully developed inlet velocity profile; axial variation of (c) interface mass flux and (d) liquid film thickness with a uniform inlet velocity profile.

adjustment in the equilibrium condition, a very localized non-physical reduction in the interface mass flux occurs in the beginning of the channel. This reduction in the interface mass flux does not affect the results further down the channel. After reaching a minimum, the mass flux increases for roughly half the channel length and then decrease slightly. Less mass absorption is predicted by the present model in the beginning of the channel compared to Mittermaier and Ziegler [13], so the liquid film is thinner at this section. The opposite behaviour is observed farther down the channel.

In Figures 5.3 (c) and (d), the current model is compared with the results of Mittermaier and Ziegler [13] for the uniform inlet velocity case. Figure 5.3 (c) shows that the present model predicts a qualitatively similar axial variation of interface mass flux compared to Mittermaier and Ziegler [13]. Figure 5.3 (d) presents the film thickness change in the x direction. Good agreement in value and trend is observed, with greatest deviation occurring between $x = 10^{-4}$ m and $x = 10^{-3}$ m.

Figure 5.4 (a) shows that, for the fully developed inlet case, the inlet and outlet velocity profiles of the present results and those of the Mittermaier and Ziegler [13] fully developed case are in good agreement. Figure 5.4 (b) shows reasonable agreement between the mass fraction profiles at $x = 0.1$ m. The interface mass fraction predicted by the present model is 1.0% greater than that of Mittermaier and Ziegler [13].

5.3.4 Summary of Comparison Cases

The numerical results of the present model were compared to the single-phase models presented by Andberg and Vliet [10], Kawae et al. [11], and Mittermaier and Ziegler [13] by minimizing the gas phase effects. The governing equations were simplified to implement a closer model to the studies by Andberg and Vliet [10] and Kawae et al. [11]. The results showed good agreement with these two works for the axial variation and for the transverse-direction profiles of variables within the liquid film. Applying the present model (with only the gas-phase modifications) to the cases studied by Mittermaier and Ziegler [13] showed that the present model is capable of producing good results for both the fully developed and uniform inlet velocity cases investigated in Mittermaier and Ziegler [13]. In the next section, the full model is implemented for the problem of two-phase absorption to investigate the effects of changing some of the operating parameters and the gas phase velocity.

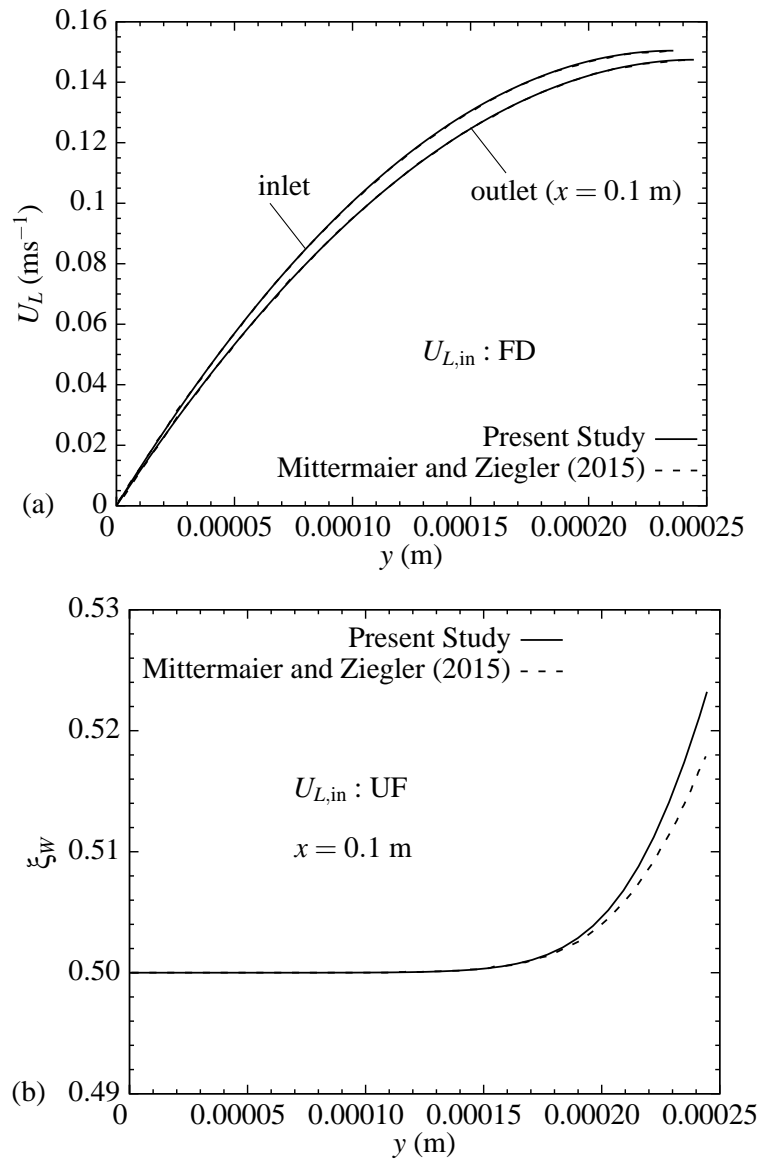


Figure 5.4: Comparison Case C3: (a) liquid velocity profile at x values of 0 m and 0.1 m with a fully developed inlet velocity profile and (b) water mass fraction profile at $x = 0.1$ m with a uniform inlet velocity profile.

5.4 New Results for the Parabolic Two-Phase Absorption Model

Co-current fully developed flow of liquid film and water vapour with interfacial shear stress is modelled to investigate the impact of the operating parameters and the gas phase on the absorption process inside a parallel plate vertical channel. The analytical equations presented in Saleh and Ormiston [44] were used to determine the liquid and gas phase fully developed velocities and the corresponding film inlet thickness and pressure gradient. Variable thermophysical properties [12] were used for the liquid film. The equilibrium relation of McNeely [1] was applied at the interface as given in A.1. The functions for the enthalpy of the vapour and partial enthalpies of the solution components were given in Florides et al. [55] and Pátek and Klomfar [56], respectively. Constant properties were used for the vapour [47].

5.4.1 Effect of Changing the Operating Parameters

The effects of changing the inlet film mass fraction, the inlet film Reynolds number, and the wall temperature impact were examined by formulating the eight new cases listed in Table 5.3. For all these cases, the following conditions were used: $L = 5$ m, $H = 0.01$ m, $P_{\text{in}} = 1.5$ kPa, $\Delta T_{\text{sub}} = 1$ K, $T_{G,\text{in}} = 20^\circ\text{C}$, $\text{Re}_{G,\text{in}} = 1000$, $\rho_G = 7.7353 \times 10^{-3}$ kg m⁻³, $\mu_G = 8.2947 \times 10^{-6}$ kg m⁻¹ s⁻¹, $N_{y,L} = 80$, $N_{y,G} = 320$, and $N_x = 2500$. The end of the channel occurs at $(x/H) = 500$. The value of $\dot{m}''_{L,\text{in}}$ in Table 5.3 is the product of the inlet density and the inlet average velocity.

In general, two types of behaviour were observed in these cases. In some cases (Case 2, Case 6, and Case 8), nearly all the vapour available in the gas phase was absorbed to the LiBr-water solution before reaching either the end of absorption or the end of the channel. In other cases, the interface temperature became very close to the wall temperature at a specific distance from the inlet. In the latter situation, a fraction of vapour mass remains and because no more absorption occurs at the interface; the numerical solution was terminated at this point. This point is referred to here as the end of absorption; in this situation $T_{\text{intf}} = T_{\text{wall}}$ and $\xi_{W,\text{intf}} = \xi_{W,\text{eoa}}$.

Table 5.3: Operating parameters for two-phase model test cases.

Properties	Case 1	Case 2	Case 3	Case 4	Case 5	Case 6	Case 7	Case 8
$\xi_{W,in}$	0.5	0.45	0.5	0.45	0.5	0.45	0.5	0.45
$T_{L,in}$ [°C]	34.02	42.77	34.02	42.77	34.02	42.77	34.02	42.77
T_{wall} [°C]	30	30	30	30	28	28	28	28
$T_{L,in}-T_{wall}$ [°C]	4.02	12.77	4.02	12.77	6.02	14.77	6.02	14.77
$Re_{L,in}$	50	50	25	25	50	50	25	25
δ_{in} [mm]	0.2262	0.2487	0.1779	0.1957	0.2262	0.2487	0.1779	0.1957
$\dot{m}''_{L,in}$ [kg m ⁻² s ⁻¹]	155.45	170.40	98.85	108.23	155.45	170.40	98.85	108.23

The ratio of the total absorbed mass to the inlet vapour mass is presented in Figure 5.5 (a). The vapour absorption rate is noticeably rapid in the beginning of the channel for the cases which are poorer in water ($\xi_{W,in} = 0.45$). Between 40% to 50% of the inlet vapour mass is absorbed by this group of liquid films by $x/H = 50$. Very close to the inlet of the channel, in cases with identical inlet mass fraction, slower films in contact with colder walls (Cases 7 and 8) absorb larger amounts of vapour mass. In a longer distance from the inlet, the rate of mass absorption in films with higher $Re_{L,in}$ (e.g., Case 1 and Case 2), increases faster and reaches a higher value in comparison to Case 7 and Case 8, respectively. In cases which face a water vapour shortage, nearly all the vapour is absorbed by the film within half of the channel length. As shown in Table 5.3, a higher value of $Re_{L,in}$ corresponds to a larger inlet film thickness. Figure 5.5 (b) illustrates the film thickness change along the channel. A considerable film thickness difference is observed between the cases with equal $Re_{L,in}$ but different $\xi_{W,in}$. For instance, Cases 2 and 6 with $\xi_{W,in} = 0.45$ begin at larger film thickness and thicken more rapidly compared to Cases 1 and 5, respectively. Flowing over a colder wall increases the interface height of a film for a given $Re_{L,in}$ and $\xi_{W,in}$ combination, as seen

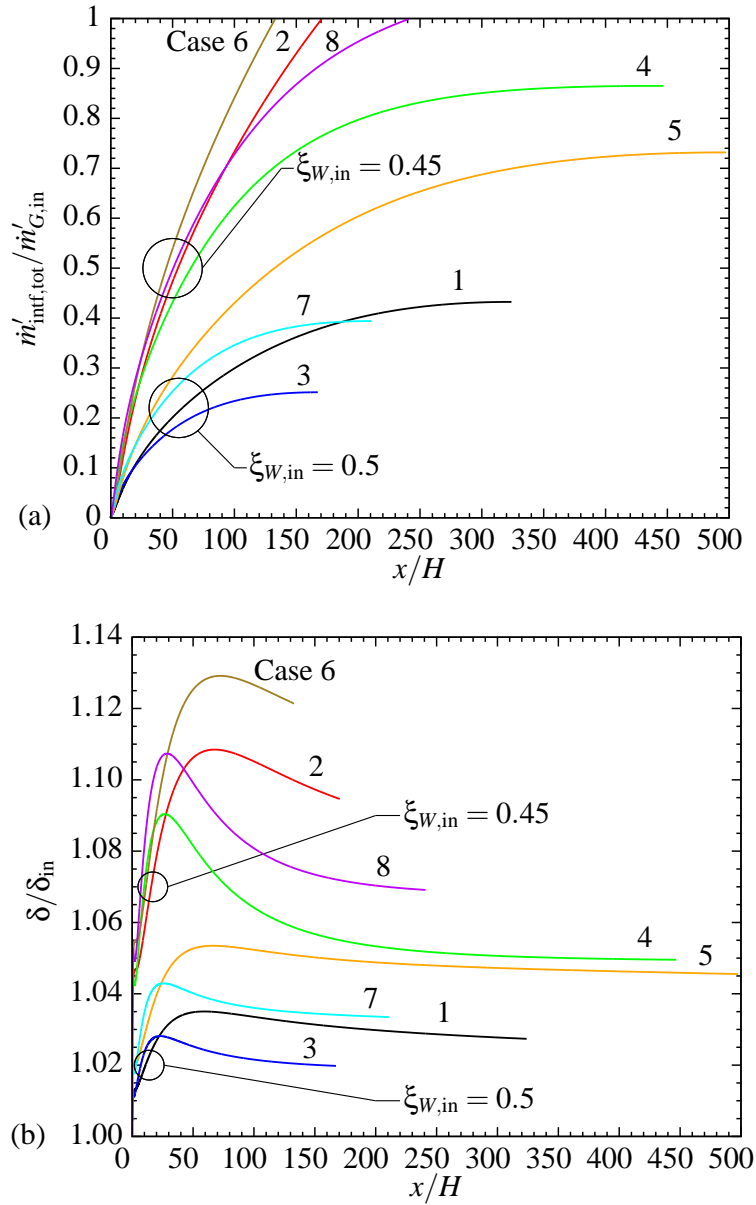


Figure 5.5: Comparison of (a) total absorbed mass ratio to the inlet vapour mass and (b) liquid film thickness.

by comparing Cases 1 and 5. This trend is due to a larger amount of water vapour absorption in the case of the colder wall. As mass absorption decreases at the interface, the liquid film thickness approaches a constant value except in the cases where all the vapour was absorbed at a relatively

short distance along the channel.

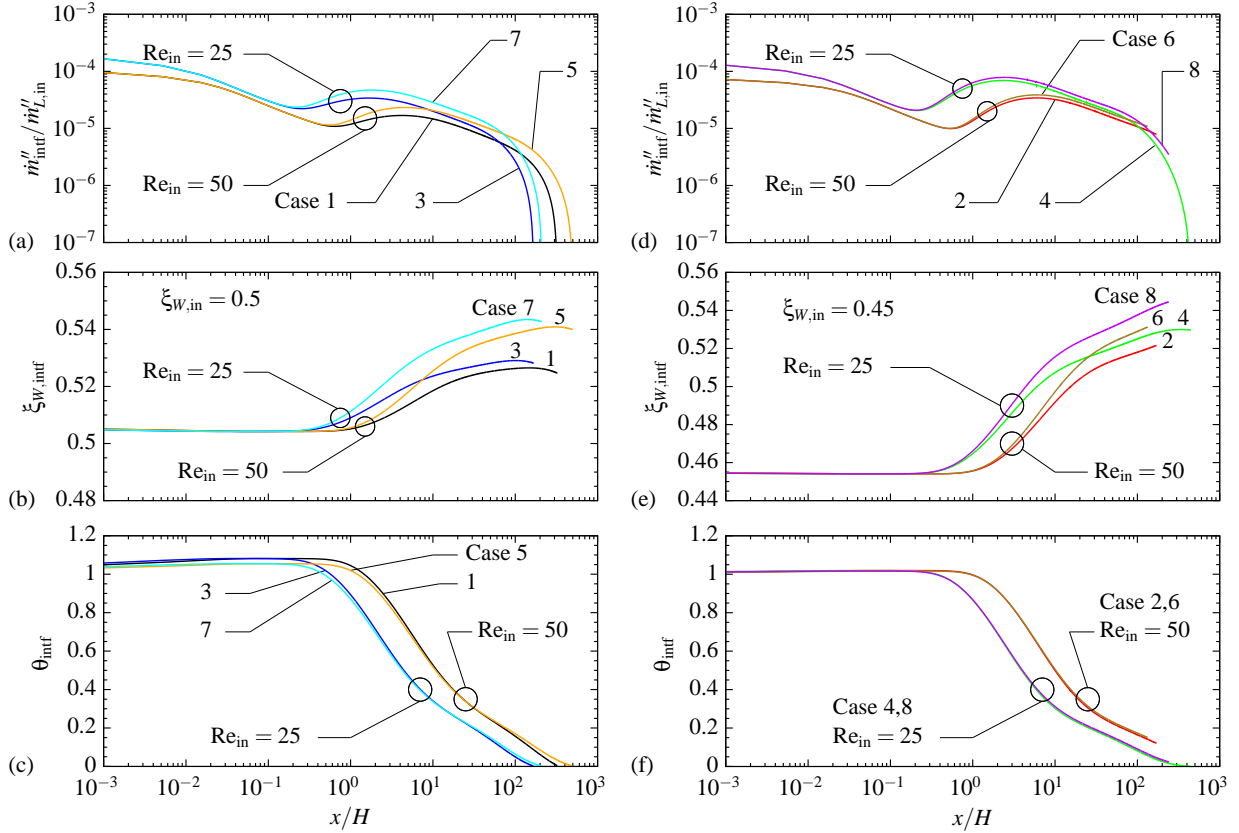


Figure 5.6: Comparison of interfacial (a) mass flux, (b) mass fraction, and (c) temperature in cases with $\xi_{W,\text{in}} = 0.5$; comparison of interfacial (d) mass flux, (e) mass fraction, and (f) temperature in cases with $\xi_{W,\text{in}} = 0.45$.

Figures 5.6 (a), (b), and (c) show the axial variation of the interface mass flux, mass fraction and temperature, respectively for the cases with $\xi_{W,\text{in}} = 0.5$. The inlet temperature and mass flux of the liquid films are also given in Table 5.3. In all the cases with $\xi_{W,\text{in}} = 0.5$ presented in Figure 5.6, a considerable amount of mass is absorbed just after the inlet because of the large gradient of water mass fraction at the interface. Over the initial part of the channel, a slightly higher amount of mass, \dot{m}''_{intf} , is absorbed into the liquid film for cases with larger $Re_{L,\text{in}}$. Between the inlet and $x/H = 10^{-3}$ (not shown) the interface temperature and mass fraction increase slightly and

remain nearly constant after $x/H = 10^{-3}$ as the interface mass absorption and mass fraction gradient decrease. When the interface experiences an increase in water mass fraction gradient, the rate of mass absorption increases (e.g., between $x/H = 0.6$ and $x/H = 9$ in Case 1). Over this section, the interfacial mass fraction of water rises and makes the interfacial temperature decline. Other cases with $\xi_{W,in} = 0.5$ shown in Figure 5.6 exhibit the same behaviour.

Over the last section of the channel, the rate of mass absorption at the interface drops gradually because the water mass fraction gradient becomes smaller at the interface. Meanwhile, the interface temperature approaches the wall temperature and mass fraction approaches a constant value across the film, $\xi_{W,ea}$. Figure 5.6 (c) shows that the cases with identical $\xi_{W,in}$ and $Re_{L,in}$ have very similar profiles of Θ and the wall temperatures do not affect Θ except at the end of absorption. Although changes in $Re_{L,in}$ and T_{wall} do not affect the interface mass fraction near the inlet of the channel, changing the wall temperature has a substantial impact on the interfacial mass fraction over the remainder of the channel length. For the cases with equal values of $(T_{L,in} - T_{wall})$, (e.g., Cases 1 and 3), the film with the higher Reynolds number absorbs a greater amount of mass and experiences lower diffusion across the film in comparison with convection in the x direction. Consequently, the wall temperature is reached in a shorter distance by the slower liquid film.

The interfacial mass absorption, mass fraction, and temperature for cases with $\xi_{W,in} = 0.45$ are compared in Figures 5.6 (d), (e), and (f), respectively. This group of cases shows similar axial variations to the group of cases with higher inlet water mass fraction (presented in Figure 5.6) except that a higher rate of mass absorption at the interface causes a shortage of vapour in Cases 2, 6, and 8. In those cases, the interface mass fraction rises at a steeper trend in comparison to similar cases in Figure 5.6 (b).

The water mass fraction change across the liquid film in Case 1 is shown at various axial locations in Figure 5.7 (a). At $x/H = 0.001$, the mass fraction is at the uniform inlet value of $\xi_W = 0.5$ across the film except very close to the interface. This sharp mass fraction gradient at the interface at this location causes a relatively large rate of mass absorption into the liquid film.

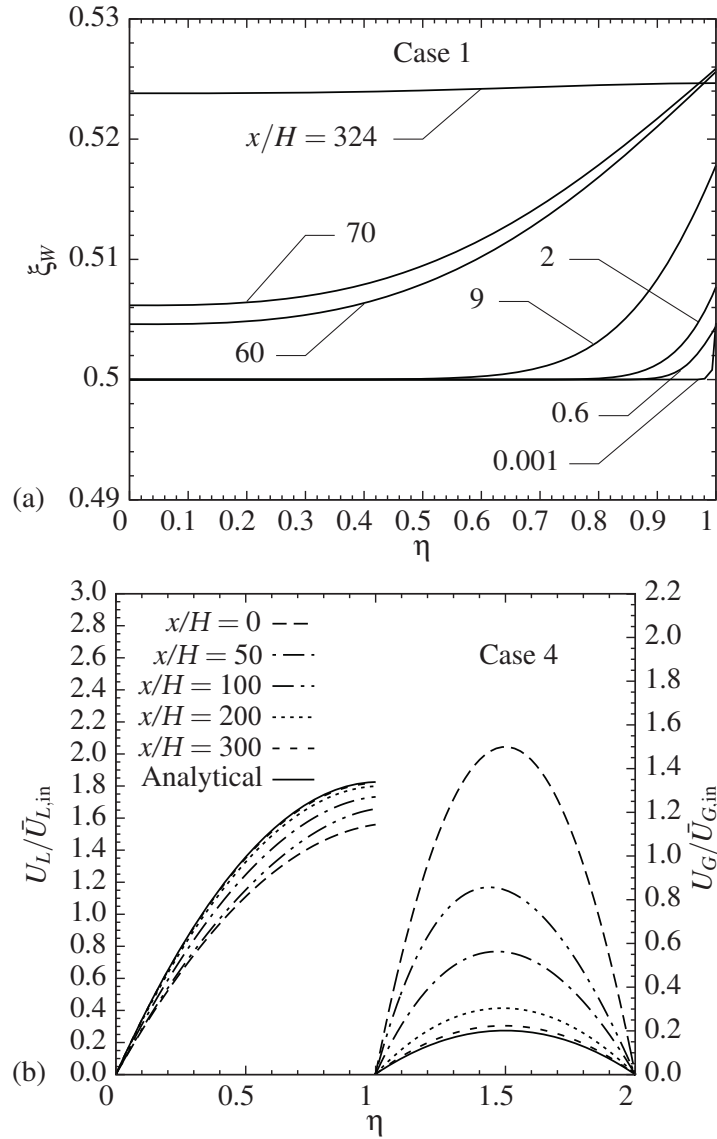


Figure 5.7: (a) mass fraction variation across the film in Case 1 and (b) liquid film and vapour velocity profiles at different axial locations in Case 4.

Between $x/H = 0.6$ and $x/H = 9$, the water mass fraction and its gradient at the interface both increase and a larger portion of the film deviates from the inlet mass fraction value. This trend leads to the increase in mass absorption at the interface seen in Figure 5.6 as discussed earlier. As more water is diffused into the film between $x/H = 9$ and $x/H = 70$, the water mass fraction

changes near the wall and the gradient of water mass fraction decreases at the interface. Farther down the channel the mass fraction approaches $\xi_{W,EOA}$ across the film and the absorption process ends at $x/H = 324$.

Figure 5.7 (b) compares the velocity profiles in the liquid film and gas phases at selected axial locations along the channel for Case 4. The values used to normalise the velocities in the two phases are $\bar{U}_{L,in} = 0.0675 \text{ m s}^{-1}$ and $\bar{U}_{G,in} = 54.7 \text{ m s}^{-1}$; the liquid and gas velocities are equal at the interface ($\eta = 1$). The profiles show that the mass transfer at the interface causes an increase in the liquid film velocity and a significant decrease in the vapour velocity. At the end of absorption, the velocity profiles approach the anticipated analytical profiles. These analytical profiles use the end of absorption film thickness and pressure gradient with the analytical solution of fully developed downward laminar two-phase flow in a parallel plate channel presented by Saleh and Ormiston [44].

5.4.2 Effect of the Gas Phase

In this section the impact of gas phase velocity and temperature on the absorption of water vapour into a LiBr-water solution is investigated.

Three gas flow rates (corresponding to $Re_{G,in}$ values of 1000, 2000, and 3000) were chosen and the liquid film conditions are as described in Case 4. The gas temperature and properties are those mentioned in the previous section.

The interface velocity variation in the axial direction is shown in Figure 5.8 (a) for the three $Re_{G,in}$ values. For the cases of $Re_{G,in}$ equal to 1000, 2000, and 3000, the mean inlet velocity of the liquid film, $\bar{U}_{L,in}$, was 0.0675 m s^{-1} , 0.0703 m s^{-1} , and 0.0731 m s^{-1} , respectively. Just after the inlet, the velocity at the interface reaches a minimum because the thin liquid film slows down the faster moving vapour. The noticeable gas velocity gradient at the interface, which is maximum near the inlet, forces the liquid film to speed up. As mass leaves the vapour and gets absorbed to

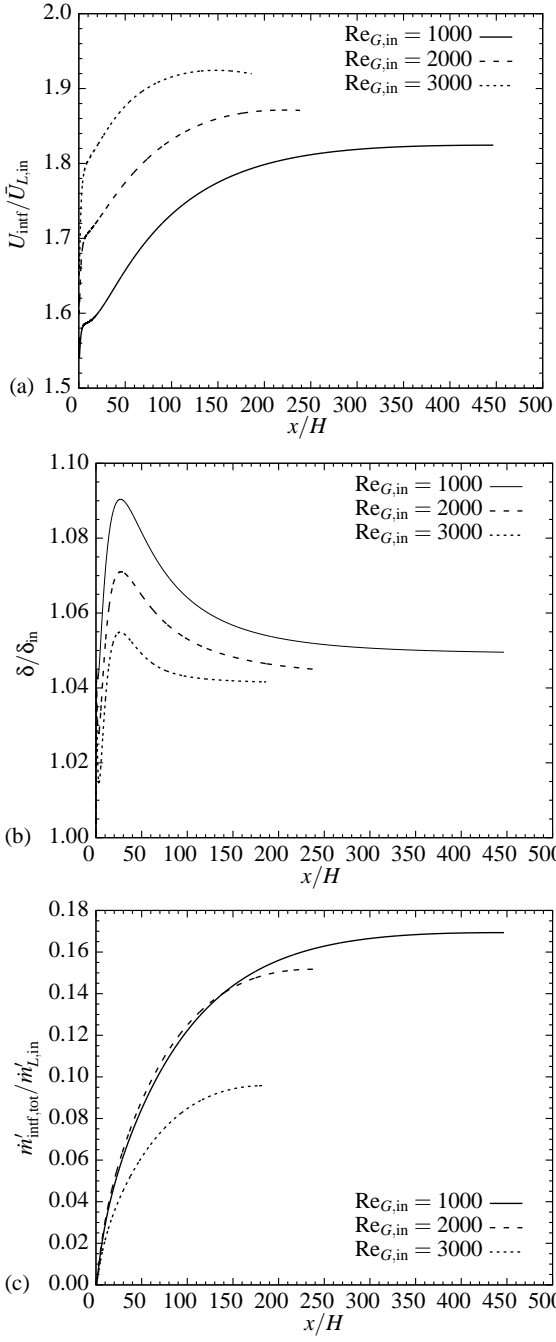


Figure 5.8: Effect of $Re_{G,in}$ change on (a) interface velocity, (b) film thickness, and (c) mass absorption rate in Case 4.

the liquid film, the interface velocity increases gradually. The higher the $Re_{G,in}$ value, the faster liquid film is dragged on by the vapour.

The axial variation of the liquid film height for the three values of $Re_{G,in}$ is presented in Figure 5.8 (b). The inlet film thickness, which corresponds to the fully developed liquid and vapour flows, is larger for smaller $Re_{G,in}$; δ_{in} had values of 0.1957 mm, 0.1878 mm, and 0.1806 mm for $Re_{G,in}$ equal to 1000, 2000, and 3000, respectively. Because of the initial sudden high rate of absorption of water, the film thickness increases rapidly. Following that rise, the liquid film thins due to the significant shear stress at the interface. As shown in Figure 5.8 (b), a lower inlet gas Reynolds number leads to a greater relative decrease relative to the peak film thickness. As the mass transfer rate decreases along the channel, the film thickness approaches a constant value.

Figure 5.8 (c) compares the total amount of mass added to the liquid film by the absorption relative to the liquid inlet mass flow rate $\dot{m}'_{L,in} = 2.119 \times 10^{-2} \text{ kg m}^{-1} \text{ s}^{-1}$. The case with higher gas Reynolds number, reaches the end of absorption state in a shorter distance from the inlet. In the case with $Re_{G,in} = 1000$, thicker liquid film flows down the channel for a longer distance and absorbs more water relative to the inlet liquid mass flow when compared to the two other cases.

In Figure 5.9, the interface mass flux and the interface and wall heat fluxes are compared for different gas Reynolds numbers. The reference values used for to normalise the cases of $Re_{G,in}$ equal to 1000, 2000, and 3000 were $\dot{m}''_{L,in}$ values of $108.23 \text{ kg m}^{-2} \text{ s}^{-1}$, $112.77 \text{ kg m}^{-2} \text{ s}^{-1}$, and $117.27 \text{ kg m}^{-2} \text{ s}^{-1}$ and q''_{ref} values of $2.30 \times 10^4 \text{ W m}^{-2}$, $3.05 \times 10^4 \text{ W m}^{-2}$, and $3.17 \times 10^4 \text{ W m}^{-2}$, respectively. There is a strong similarity between the graphs in the region up to $x/H = 50$ for different values of $Re_{G,in}$. Downstream of this section, for higher values of $Re_{G,in}$, the thinner film causes higher rate of mass and temperature diffusion into the film. As a result, energy diffusion in the y direction happens faster for a thinner liquid film and the liquid film approaches the wall temperature in a shorter distance. The case with the highest value of $Re_{G,in}$ reaches the end of absorption at a shorter distance along the channel compared to the other two cases.

The effect of changing the gas phase temperature was examined while maintaining all of the

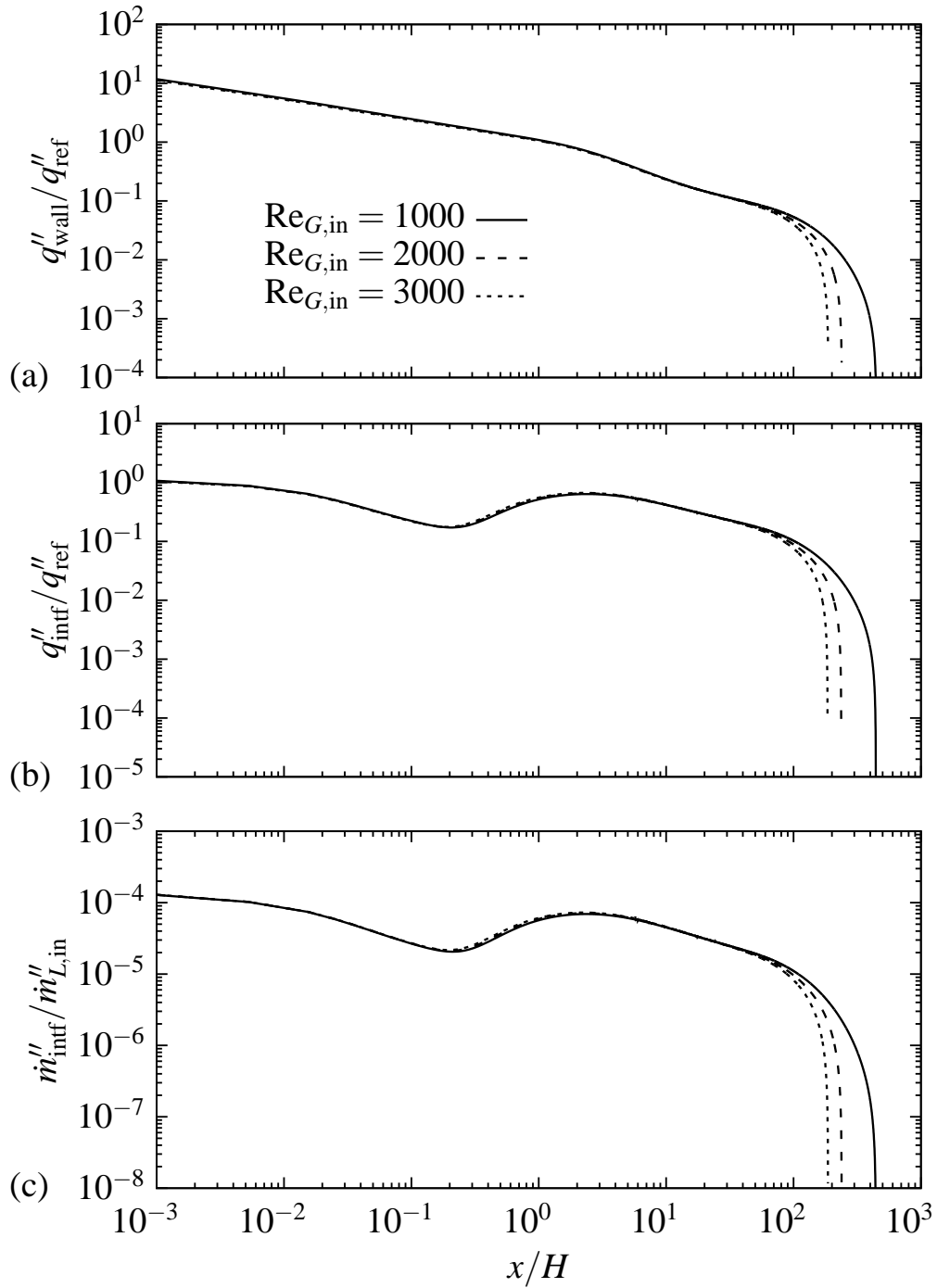


Figure 5.9: Effect of $\text{Re}_{G,\text{in}}$ change on mass and heat fluxes in Case 4.

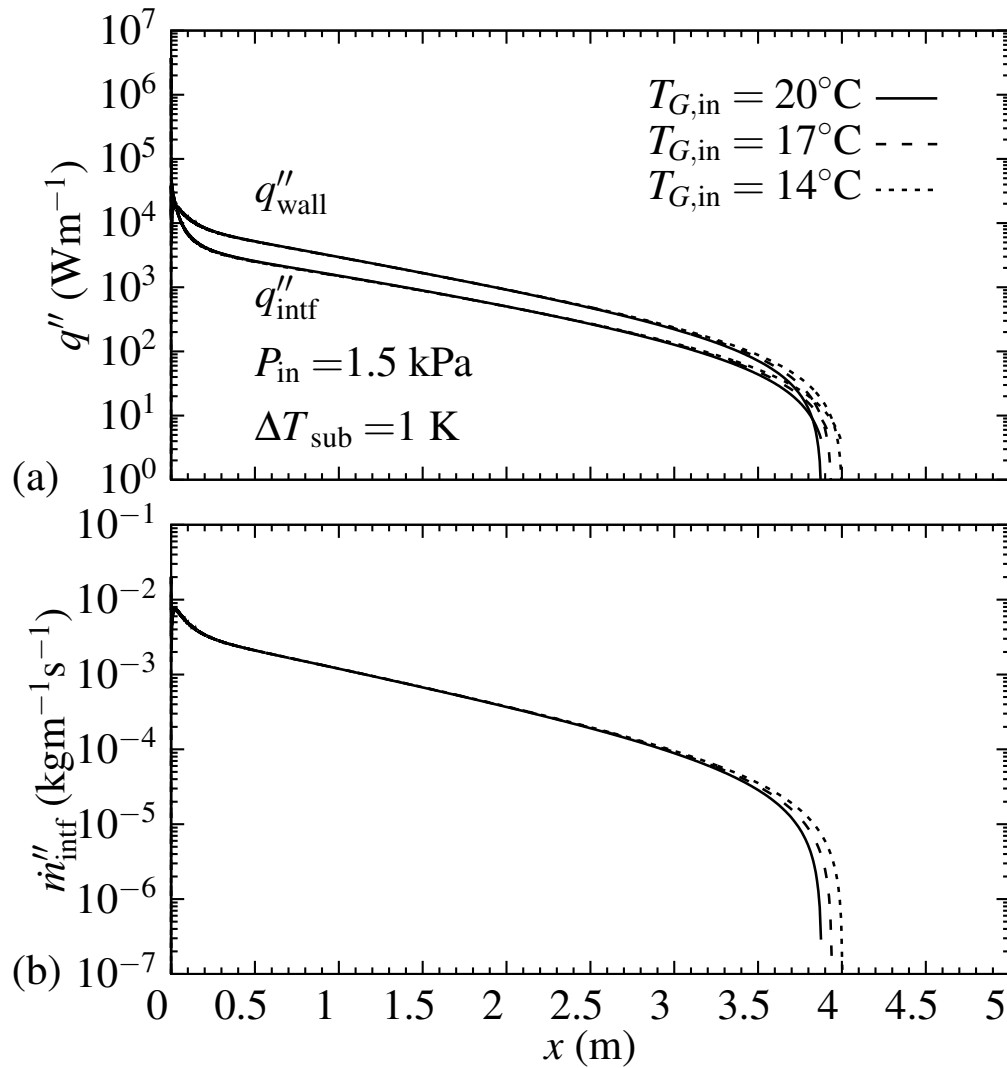


Figure 5.10: Vapour inlet temperature effect on (a) interface and wall heat fluxes and (b) interface mass flux in Case 4.

parameters as in Case 4 in Section 5.4.1 except that the gas phase constant properties were taken from [57]. Figure 5.10 shows the mass and heat flux at the interface and the heat flux at the isothermal wall. For most of the channel length, the cases with different $T_{G,\text{in}}$ show very similar behaviour for interfacial mass and heat transfer. At $x = 3$ m, the interface mass and heat flux for the case with higher vapour temperature, $T_{G,\text{in}} = 20^\circ\text{C}$, becomes smaller than the other two cases

and absorption ends at a slightly shorter distance from the channel entrance. Figure 5.10 (a) shows that the wall and interface heat transfer in the colder vapour case, become nearly equal in a longer distance from the inlet of the channel.

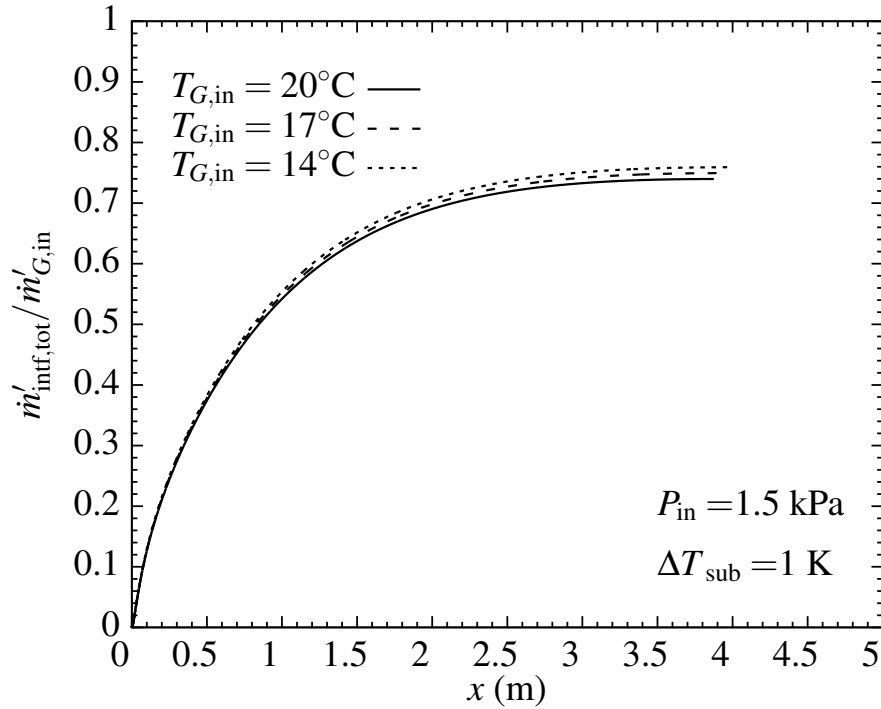


Figure 5.11: Vapour inlet temperature effect on total absorbed mass ratio to the inlet vapour mass in Case 4.

In the cases compared in Figure 5.11, the water vapour enters the channel at almost equal mass flow rates, $\dot{m}'_{G,\text{in}} = 0.0047 \text{ kg m}^{-1} \text{ s}^{-1}$. The total mass absorbed at the interface is only 0.6 % higher in the case with $T_{G,\text{in}} = 14^\circ\text{C}$ relative to the case with $T_{G,\text{in}} = 20^\circ\text{C}$. The liquid film thickness change along the channel is compared for different $T_{G,\text{in}}$ cases in Figure 5.12. Higher rate of mass absorption in the initial part of the channel causes a sharp increase in the film thickness from $\delta_{\text{in}} = 0.197 \text{ mm}$ to nearly $\delta = 0.214 \text{ mm}$. As the mass absorption rate decreases at the interface, the liquid film thickness approaches a constant value. The cases in Figure 5.12 show similar growth of the film thickness due to the nearly equal amount of mass absorption.

The gas phase temperature distribution at selected axial locations is illustrated in Figure 5.13.

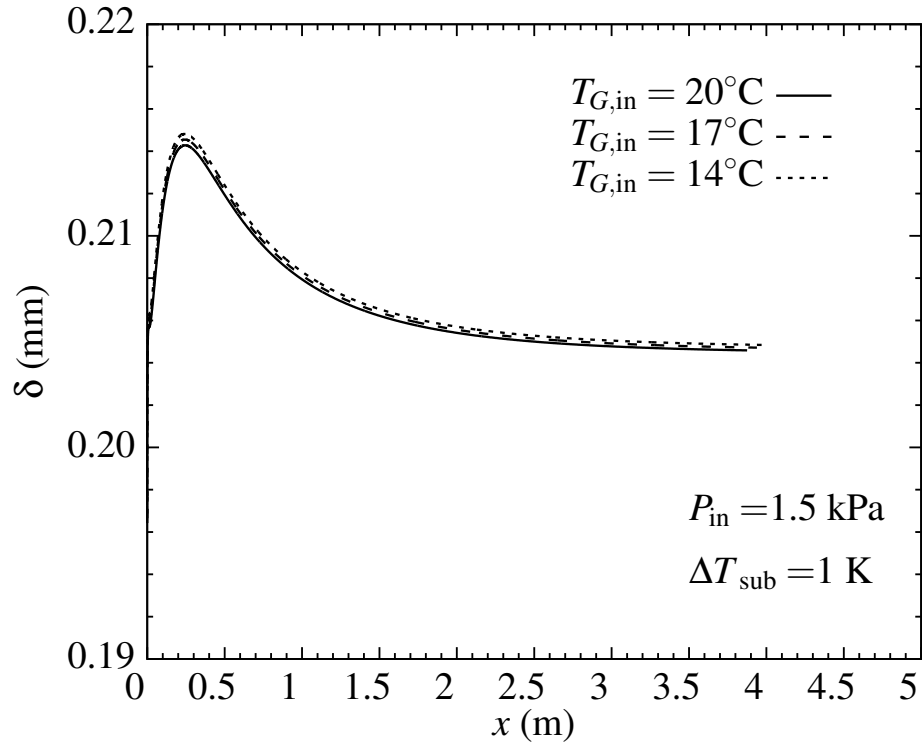


Figure 5.12: Vapour inlet temperature effect on liquid film thickness in Case 4.

At $x = 10^{-5}$ m, the gas phase temperature changes from 43°C at the interface ($\eta = 1$) to the gas inlet temperature at the adiabatic wall ($\eta = 2$). In the case of $T_{G,\text{in}} = 20^{\circ}\text{C}$, the temperature gradient is smaller because the gas bulk temperature is closer to the interface equilibrium temperature. Although, the cases with different $T_{G,\text{in}}$ experience different gas phase temperature change along the channel, they all reach the wall temperature farther down the channel at $x = 3.6$ m.

Figure 5.14 shows that the colder vapour case approaches the wall temperature at a steeper temperature gradient. This happens due to more heat conduction to the gas phase in the case with $T_{G,\text{in}} = 14^{\circ}\text{C}$, especially in the beginning of the channel.

Figures 5.15 and 5.16 illustrate the axial variation of pressure and pressure gradient. There is a pressure drop between the inlet and last point of absorption in Figure 5.15. The pressure drop is caused by momentum change and shear force at the walls. The pressure drop is slightly

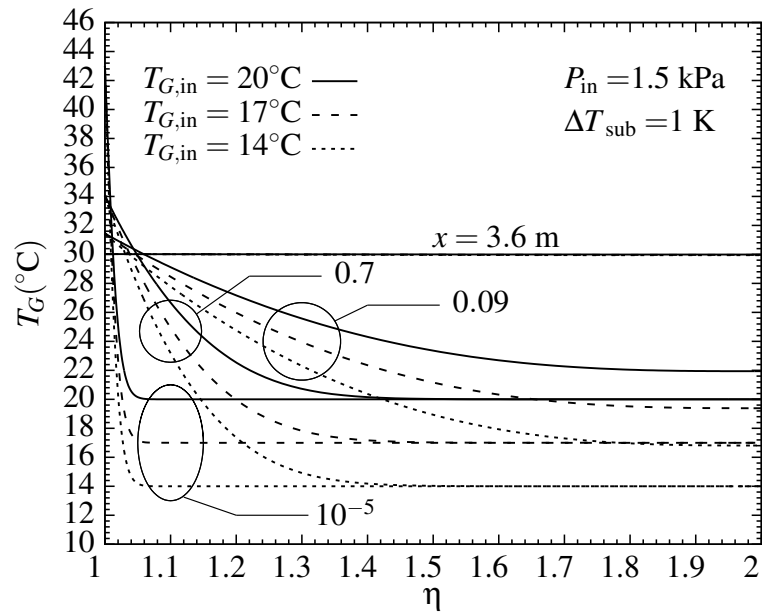


Figure 5.13: Vapour inlet temperature effect on vapour temperature distribution across the channel in Case 4.

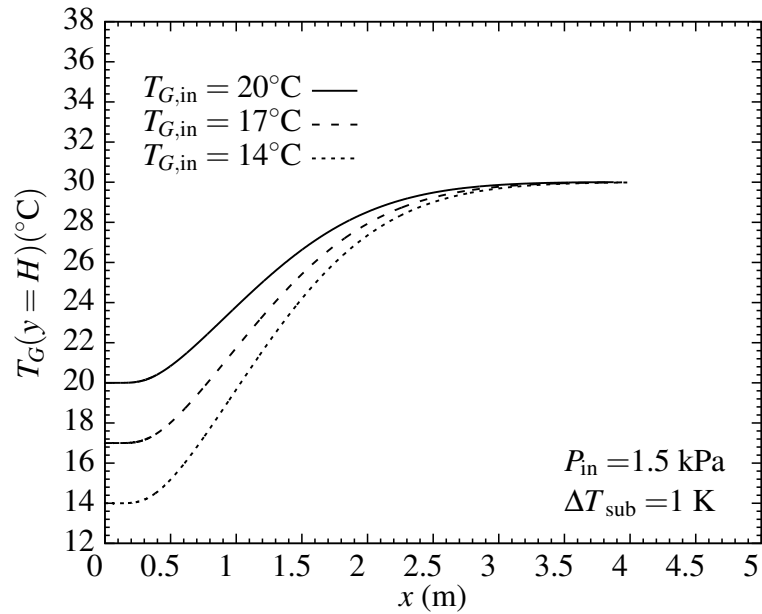


Figure 5.14: Vapour inlet temperature effect on adiabatic wall temperature variation in Case 4.

higher for higher $T_{G,in}$. This very small difference is not enough to make a noticeable difference in the interface temperature and mass fraction in these cases. As seen in Figure 5.16, the pressure gradient is initially positive due to mass depletion, then becomes negative mainly due to increased wall shear in the liquid film.

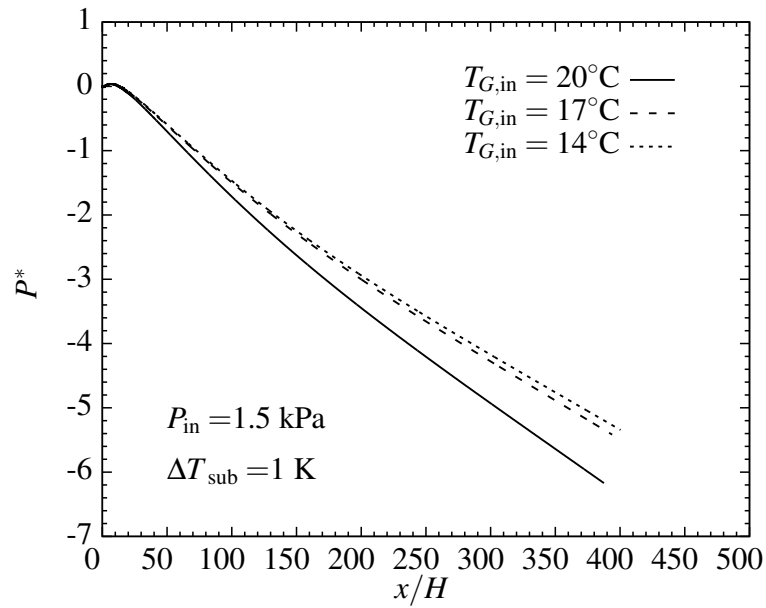


Figure 5.15: Vapour inlet temperature effect on axial variation of pressure in Case 4.

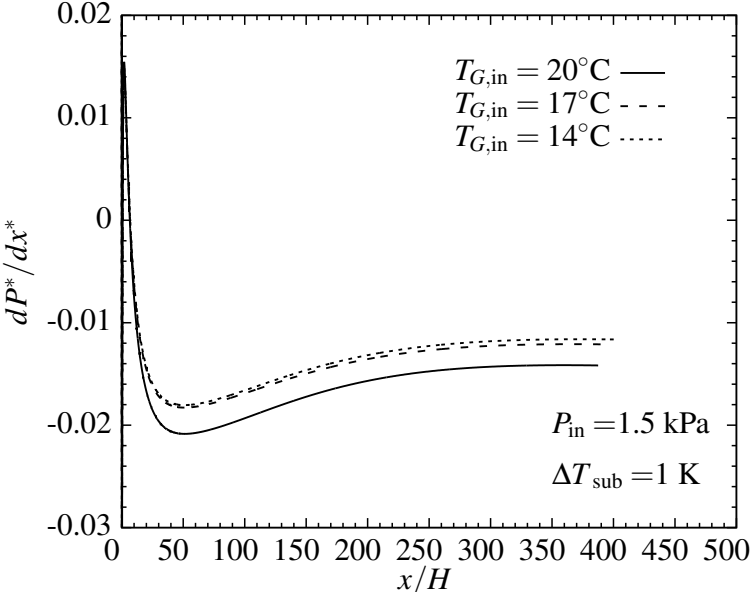


Figure 5.16: Vapour inlet temperature effect on axial variation of pressure gradient in Case 4.

Chapter 6

Parallel-Plate Channels: Elliptic Model

6.1 Introduction

In this chapter detailed comparisons of the elliptic model with Habib and Wood [18] and the parabolic method (described in earlier chapters and published as Abbasi Havestini and Ormiston [58]) are conducted to demonstrate the validity of the current work and also differentiate the characteristics of two-phase elliptic and parabolic approaches. The effect of changing the LiBr solution mass diffusion coefficient, the interface heat of absorption and mass fraction condition are studied in these comparisons. These results can be a useful benchmark results for future detailed two-phase analysis of absorption. New results are also presented to investigate the pressure change effect on the interface heat and mass transfer and the liquid film development along the channel.

6.2 Grid Independence Study

A grid independence test was conducted using a typical case studied in this work (Case E2 described later in Section 6.3) and was based on the variation of the film thickness. The number of nodes considered in the x and y directions for Case E2 were as follows: $20 \leq N_{y,L} \leq 60$, $45 \leq N_{y,G} \leq 135$, and $250 \leq N_x \leq 750$. A grid with $N_{y,L} = 40$, $N_{y,G} = 90$, and $N_x = 500$ was used which had a maximum difference of 0.08% from the finest grid ($N_{y,L} = 60$, $N_{y,G} = 135$, and $N_x = 750$).

6.3 Comparisons with Previous Work

6.3.1 Definition of Comparison Cases

In this section, the results of the present elliptic model are compared to Habib and Wood [18] and the parabolic model of Abbasi Havestini and Ormiston [58]. Because values for the liquid and gas properties and the heat of absorption were not readily available in Habib and Wood [18], initially, the standard values (based on values that have appeared in the literature) were used to produce the elliptic model results. Comparison of the initial results from the present model with Habib and Wood [18] demonstrated the deviation of the elliptic model results from Habib and Wood [18] because of the impact of the LiBr solution diffusion coefficient, D_L^{AB} , and the heat of absorption, H_a . Therefore, D_L^{AB} and H_a were changed to alternative values as explained later.

For the purpose of comparison, the liquid phase energy equation, Equation (2.24), is altered to make the elliptic model as close as possible to that of Habib and Wood [18]. The x and y -direction convection and mass diffusion terms including the partial enthalpies of the solution components were therefore neglected. These changes were also made to the parabolic model presented in Abbasi Havestini and Ormiston [58]. In the comparison with the work of Habib and Wood [18], the effect of two parameters and one interface condition are studied. In the cases shown in Table 6.1, the heat of absorption is either $2.7602 \times 10^6 \text{ J kg}^{-1}$ (calculated based on Lemmon et al. [57] and Pátek and Klomfar [56]) or $4.2500 \times 10^5 \text{ J kg}^{-1}$ (deduced from Figure 6 and 7 in Habib and Wood [18]). The liquid phase diffusion coefficient, D_L^{AB} is either $1.3617 \times 10^{-9} \text{ m}^2 \text{ s}^{-1}$ (Mittermaier et al. [12]), or a value five times smaller (a value which is caused the present prediction of the interface mass fraction and temperature to match Habib and Wood [18] better). Finally, the LiBr impermeability condition at the interface, Equation (2.37), was changed to the alternate interface boundary condition for mass fraction stated in Habib and Wood [18] as follows:

$$-\rho_L D_L^{AB} \left. \frac{\partial \xi_W}{\partial n} \right|_{L,\text{intf}} = \dot{m}''_{\text{intf}} \quad (6.1)$$

For all the cases presented in Table 6.1, following conditions were used: $L = 1 \text{ m}$,

$H = 0.06$ m, $\delta_{\text{in}} = 0.2545$ mm, $P_{\text{in}} = 0.936$ kPa, $T_{G,\text{in}} = 20^\circ\text{C}$, $T_{L,\text{in}} = 44.15^\circ\text{C}$, $\Delta T_{\text{sub}} = 0$ K, $\xi_{W,\text{in}}=0.4$, $T_{\text{wall}} = 35^\circ\text{C}$, $\text{Re}_{G,\text{HW},\text{in}} = 30$, $\text{Re}_{L,\text{in}} = 30$, $N_{y,L} = 40$, $N_{y,G} = 90$, and $N_x = 500$. The kinematic viscosity of the LiBr solution, $\nu_L = 2.6805 \times 10^{-6}$ m² s⁻¹, was calculated based on the Reynolds number and initial film thickness found in Habib and Wood [18], and was used along with density, $\rho_L = 1.7005 \times 10^3$ kg m⁻³ (Mittermaier et al. [12]), to obtain the viscosity, $\mu_L = 4.5582 \times 10^{-3}$ kg m⁻¹ s⁻¹. Other properties obtained by using the functions provided by Mittermaier et al. [12] are as follows: $C_{p,L} = 1.9573 \times 10^3$ J kg⁻¹ K⁻¹ (using the corrected version given in Appendix F.3) and $k_L = 4.3364 \times 10^{-1}$ W m⁻¹ K⁻¹. The constant properties (Lemmon et al. [57]) used for the gas phase are as follows : $\rho_G = 6.9213 \times 10^{-3}$ kg m⁻³, $\mu_G = 9.5479 \times 10^{-6}$ kg m⁻¹ s⁻¹, $C_{p,G} = 1.8744 \times 10^3$ J kg⁻¹ K⁻¹, and $k_G = 1.8089 \times 10^{-2}$ W m⁻¹ K⁻¹. The liquid film and water vapour enter the channel at uniform velocities and the equilibrium condition of Siebe [3], as given in A.3, was applied at their interface.

Table 6.1: Definition of comparison cases.

Case	Solution method	H_a [J kg ⁻¹]	D_L^{AB} [m ² s ⁻¹]	Interface mass fraction condition
Case E1	Elliptic	2.7602×10^6	1.3617×10^{-9}	Equation (6.1)
Case E2	Elliptic	4.2500×10^5	2.7235×10^{-10}	Equation (6.1)
Case P1	Parabolic	2.7602×10^6	1.3617×10^{-9}	Equation (6.1)
Case P2	Parabolic	4.2500×10^5	2.7235×10^{-10}	Equation (6.1)
Case E3	Elliptic	2.7602×10^6	1.3617×10^{-9}	Equation (2.37)

6.3.2 Axial Variations

In Figure 6.1, the axial variation of the interfacial temperature and LiBr mass fraction obtained by the present two-phase elliptic model and the Abbasi Havestini and Ormiston [58] parabolic model are compared to the results of Habib and Wood [18]. In these cases, the LiBr solution enters the channel with $T_{L,\text{in}} = 44.15^\circ\text{C}$ and $\xi_{\text{LiBr},\text{in}}=0.6$. At the initial part of the channel, the interface

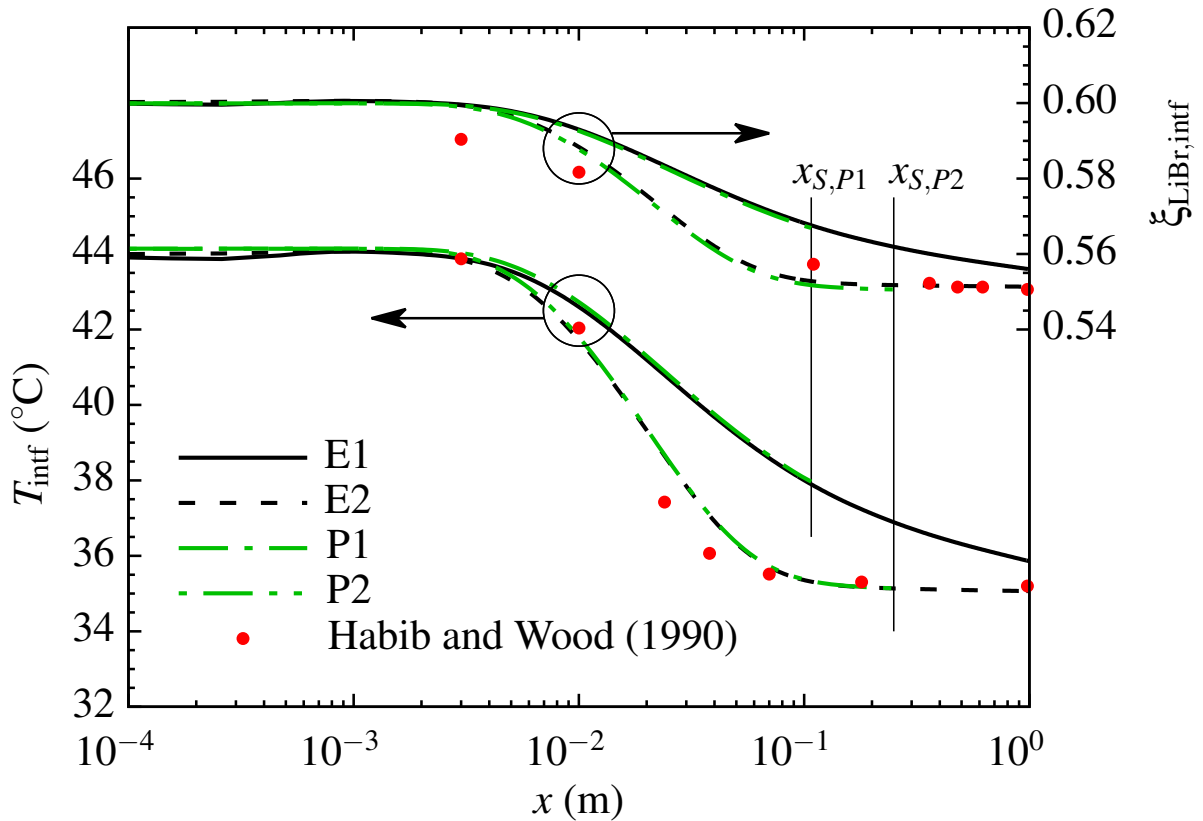


Figure 6.1: Comparison of axial variation of interface temperature and mass fraction for Cases E1, E2, P1, and P2 with Habib and Wood [18].

temperature and mass fraction change slightly from the inlet values. After this initial section, when more water is absorbed, the interface LiBr mass fraction decreases along the channel. While the energy released at the interface is eventually passed to the cold wall through the liquid film, the interface temperature decreases following the decrease in the LiBr mass fraction according to the equilibrium relation at the interface.

The parabolic model of Abbasi Havestini and Ormiston [58] produced results that predicted absorption of a great fraction of vapour mass into the LiBr-water solution in Cases P1 and P2 at an axial location before the prescribed channel length. In this situation, the lack of enough vapour mass for continuation of the absorption process caused the onset of negative velocities in

the gas phase and termination of parabolic model computation. The stopping points for Cases P1 and P2 are $x_{S,P1} = 1.07 \times 10^{-1}$ m and $x_{S,P2} = 2.72 \times 10^{-1}$ m at which 75% and 91% of the inlet vapour mass was absorbed into the liquid film, respectively. The elliptic model, however, produces converged solutions for the entire channel. The elliptic model has the capability of pulling mass from the channel outlet when the most of the available vapour in the gas phase is absorbed. At those points where the vapour mass enters the channel at $x = L$, the gas phase temperature outlet boundary condition is changed to $T = T_{\text{wall}} = 35^\circ\text{C}$.

At the initial part of the channel, the interface temperatures in the elliptic cases are slightly smaller than the parabolic cases. This occurs because of the slight decrease in the LiBr mass fraction (not noticeable in Figure 6.1) due to mass leaving the liquid film at the interface in a very short distance; this phenomenon will be discussed shortly with respect to Figure 6.2. At this initial stage near the entrance of the channel, when water leaves the liquid film at the interface and enters the gas phase, the interface LiBr mass fraction decreases. Because of the interfacial equilibrium relation between the mass fraction and the temperature, the decrease in the LiBr mass fraction causes a small temperature decrease in the elliptic cases at the initial part of the channel. In Cases E1 and P1, which use larger values of H_a and D_L^{AB} , the decreases in the interface LiBr mass fraction and temperature in the x -direction occur more slowly compared to other cases, between $x = 3 \times 10^{-3}$ m and $x = 6 \times 10^{-2}$ m. As a result, Cases E1 and P1 predict higher values of $\xi_{\text{LiBr,inf}}$ and T_{inf} in this section of the channel compared to Cases E2 and P2. The discrepancy between the results of E1 and P1 and those of Habib and Wood [18] is significant in Figure 6.1 because they use the standard value of H_a rather than the smaller value used in Habib and Wood [18]. The smaller value of H_a was deduced from Figures 6 and 7 in Habib and Wood [18] and applied to Cases E2 and P2. Also, D_L^{AB} was reduced in Cases E2 and P2 to investigate its effect on altering the results of Cases E1 and P1 and making them closer to those of Habib and Wood [18]. In Cases E2 and P2, the drop in the interface LiBr mass fraction and temperature is significant between $x = 10^{-2}$ m and $x = 10^{-1}$ m and the results are much closer to those presented by Habib and Wood [18]. The results of P1 and P2 are in a good agreement with the results of E1 and E2, respectively, up to

their stopping points. At the end of the channel ($x = 1$ m), in Case E2, the interface temperature and LiBr mass fraction reach the wall temperature, $T_{\text{wall}} = 35^\circ\text{C}$, and the consistent mass fraction, $\xi_{\text{LiBr}} = 0.551$, respectively, while in Case E1 the interface temperature is above the wall temperature. Case E1 would require a longer channel to reach the wall temperature at the interface.

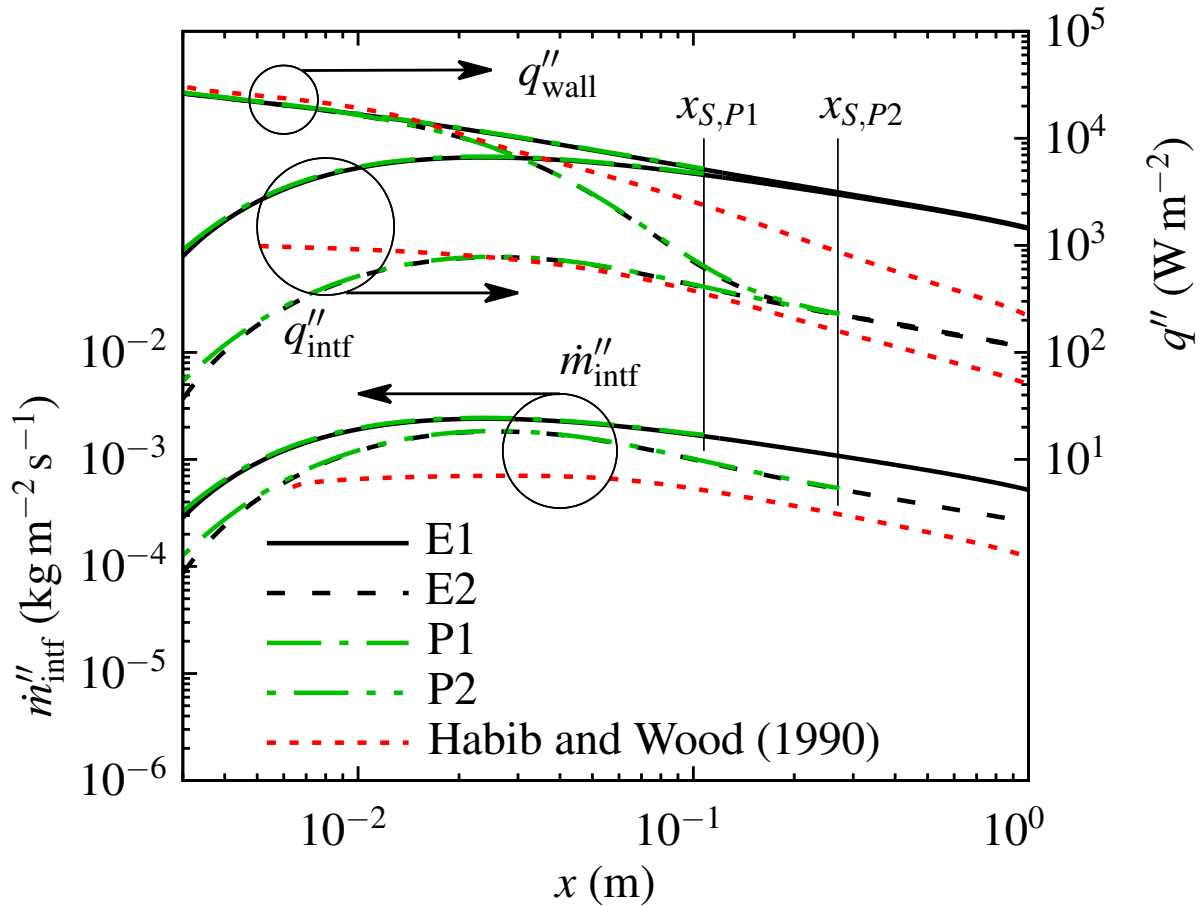


Figure 6.2: Comparison of axial variation of interface mass flux, interface and wall heat flux for Cases E1, E2, P1, and P2 with Habib and Wood [18].

Comparisons of the axial variations of the interface mass flux, interface and wall heat fluxes are presented in Figure 6.2. In the parabolic model of Abbasi Havestini and Ormiston [58], the pressure is assumed to be constant in the y direction and the global mass balance is applied as an additional constraint equation to determine the pressure gradient in the x direction, dP/dx . In

the elliptic model, the pressure field is calculated at each node over the channel and is coupled to the velocity field, U and V . In the elliptic model, a pressure drop is observed at the interface in the beginning of the channel where the mass fraction is at nearly the inlet value. According to equilibrium condition, a decrease in the pressure at a specific mass fraction results in a decrease in the temperature. A slight pressure drop occurs initially for Case E1, and this leads to a temperature gradient at the liquid interface that is negative and consequently the energy and mass are transferred to the gas phase. This situation occurs at the first 0.3% of the channel and does not have any effect on the solution field of the rest of channel. The pressure drop in the beginning of the channel is smaller in Case E2 compared to Case E1 and is not predicted by the parabolic model in Cases P1 and P2.

The cases with the higher values of the heat of absorption and the liquid diffusion coefficient, E1 and P1, predict higher mass flux at the interface. According to the mass fraction condition used at the interface of the cases in Figure 6.2, the higher diffusion coefficient increases the mass passing through the interface and also causes faster diffusion of water into the liquid film. Faster diffusion of water keeps the interface LiBr mass fraction at a higher value and water is more readily absorbed (Figure 6.1). The parabolic cases results, up to the stopping point, are very similar to the corresponding elliptic cases. Although using smaller values of H_a and D_L^{AB} brings the interface mass and heat flux results in Cases E2 and P2 closer to those of Habib and Wood [18], it is not the case for the heat flux at the wall. At $x = 3 \times 10^{-3}$ m (the start of the x axis in Figure 6.2), the wall heat flux of all the model cases are close to the value of Habib and Wood [18]. The large initial difference between the interface and wall heat fluxes in Cases E2 and P2 is reduced by the rapid drop in the wall heat flux to reach the interface heat flux at $x = 2 \times 10^{-1}$ m. As the liquid film and vapour are flowing downward in the channel and the interface temperature approaches the wall temperature, the wall heat flux converges toward the interface heat flux in Cases E1, E2, P1, and P2. However, this expected pattern of behaviour was not established in the work of Habib and Wood [18].

6.3.3 Transverse Profiles

Figure 6.3 shows the transverse-direction profiles of LiBr mass fraction in Cases E1 and E2 compared to Habib and Wood [18]. Near the inlet (at $x = 0.003$ m), most of the liquid film is at the inlet

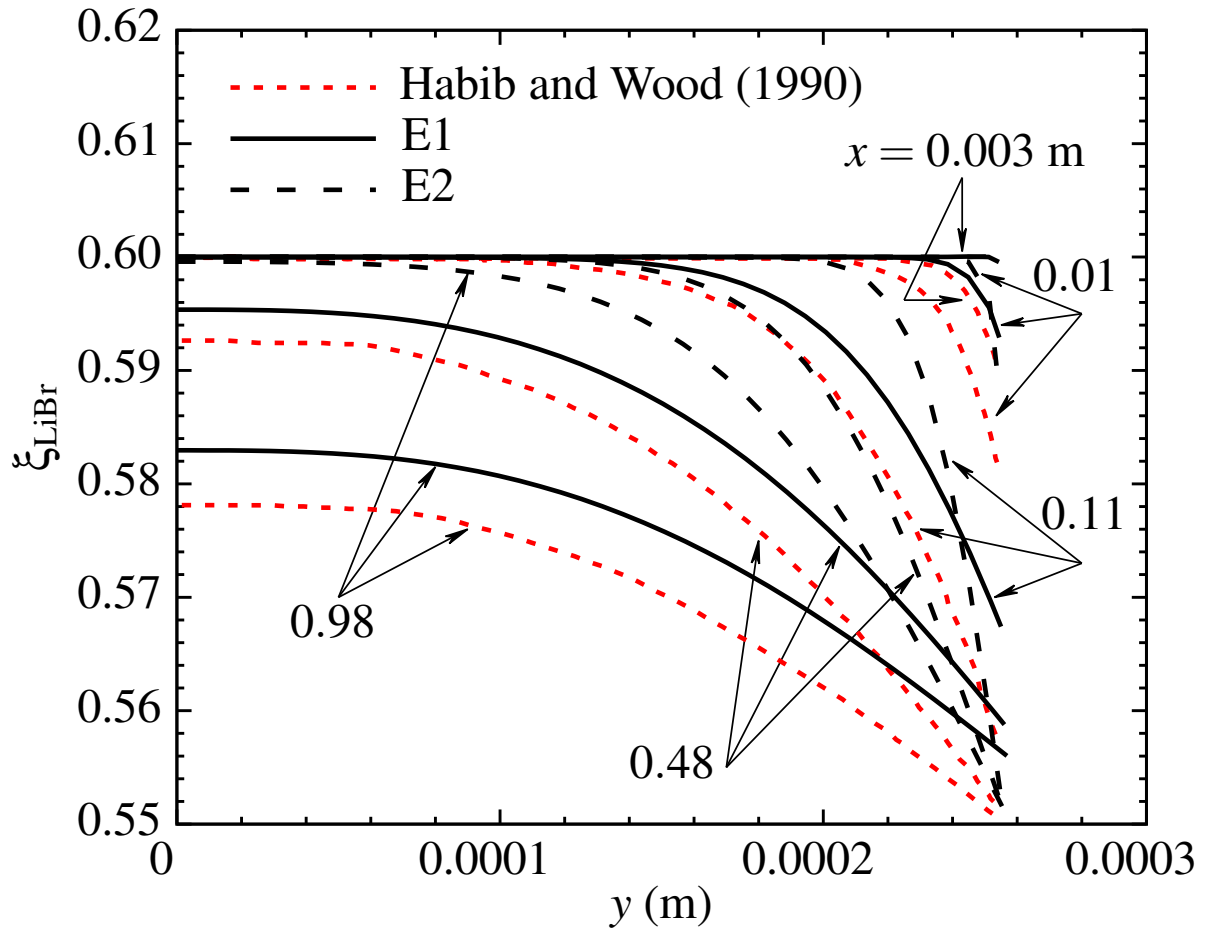


Figure 6.3: Comparison of LiBr mass fraction distribution for Cases E1 and E2 with Habib and Wood [18].

value of mass fraction $\xi_{\text{LiBr}}=0.6$ in all the cases. At this axial location, because of the absorption of water at the interface, the LiBr mass fraction drops at the interface. This drop is noticeably higher in the case of Habib and Wood [18], where $\xi_{\text{LiBr,intf}}=0.59$. At $x = 0.01$ m, $\xi_{\text{LiBr,intf}}$ of Habib and Wood [18] is lower than Cases E1 and E2 and a greater portion of the film close to the interface

is affected by the absorbed mass. Between $x = 0.11$ m and $x = 0.98$ m, the interface mass fraction change in Case E2 is very similar to Habib and Wood [18] whereas Case E1 predicts significantly different values. In this section of the channel, Case E1 follows more closely the development of the mass fraction profiles in Habib and Wood [18] but predicts consistently larger values of ξ_{LiBr} . In Case E2, which uses a smaller value of D_L^{AB} , the interface LiBr mass fraction reaches the value consistent with the wall temperature ($\xi_{\text{LiBr}}=0.552$) relatively close to the inlet (at $x = 0.11$ m). At this axial location, 78% of the film thickness in Case E2 is still at the inlet value of mass fraction, $\xi_{\text{LiBr}}=0.6$. This trend is the result of the slow diffusion of absorbed water into the liquid film due to the small value of D_L^{AB} . When the flow reaches $x = 0.48$ m in Case E2, the absorbed water is diffused to a larger portion of the liquid film where ξ_{LiBr} is decreased. Near the end of the channel, at $x = 0.98$ m, the LiBr mass fraction at the wall is decreased to $\xi_{\text{LiBr}}=0.583$ and $\xi_{\text{LiBr}}=0.578$ in Case E1 and the case of Habib and Wood [18], respectively whereas nearly the third of the liquid film from the wall side is not affected by the diffusion of water in Case E2.

Figure 6.4 compares Cases E1 and E2 transverse-direction profiles of the liquid film temperature to Habib and Wood [18]. At $x = 0.003$ m, very close to the inlet of the channel, the elliptic model produces the same profiles of temperature in Cases E1 and E2 with a higher temperature distribution across the film compared to Habib and Wood [18]. As the flow develops along the channel, the decrease in the interface mass LiBr fraction decreases the interface temperature. In addition, the temperature gradient close to the wall decreases. The decrease in the temperature across the film occurs faster in the case of Habib and Wood [18] compared to Cases E1 and E2, most notably between $x = 0.024$ m and $x = 0.038$ m. The temperature profiles of Case E2 and Habib and Wood [18] become almost uniform at $T = T_{\text{wall}} = 35^\circ\text{C}$ near the exit of the channel.

Figure 6.5 shows the transverse-direction profiles of the gas phase temperature in Cases E1 and E2 compared to the results of Habib and Wood [18]. At $x = 0.003$ m, the difference between the water vapour inlet temperature $T_{G,\text{in}} = 20^\circ\text{C}$ and the interface temperature $T_{\text{intf}} = 44.15^\circ\text{C}$ produces a sharp gradient close to the interface. Near the inlet, the model of Habib and Wood [18] predicts higher temperatures near the interface compared to Cases E1 and E2. Further down the

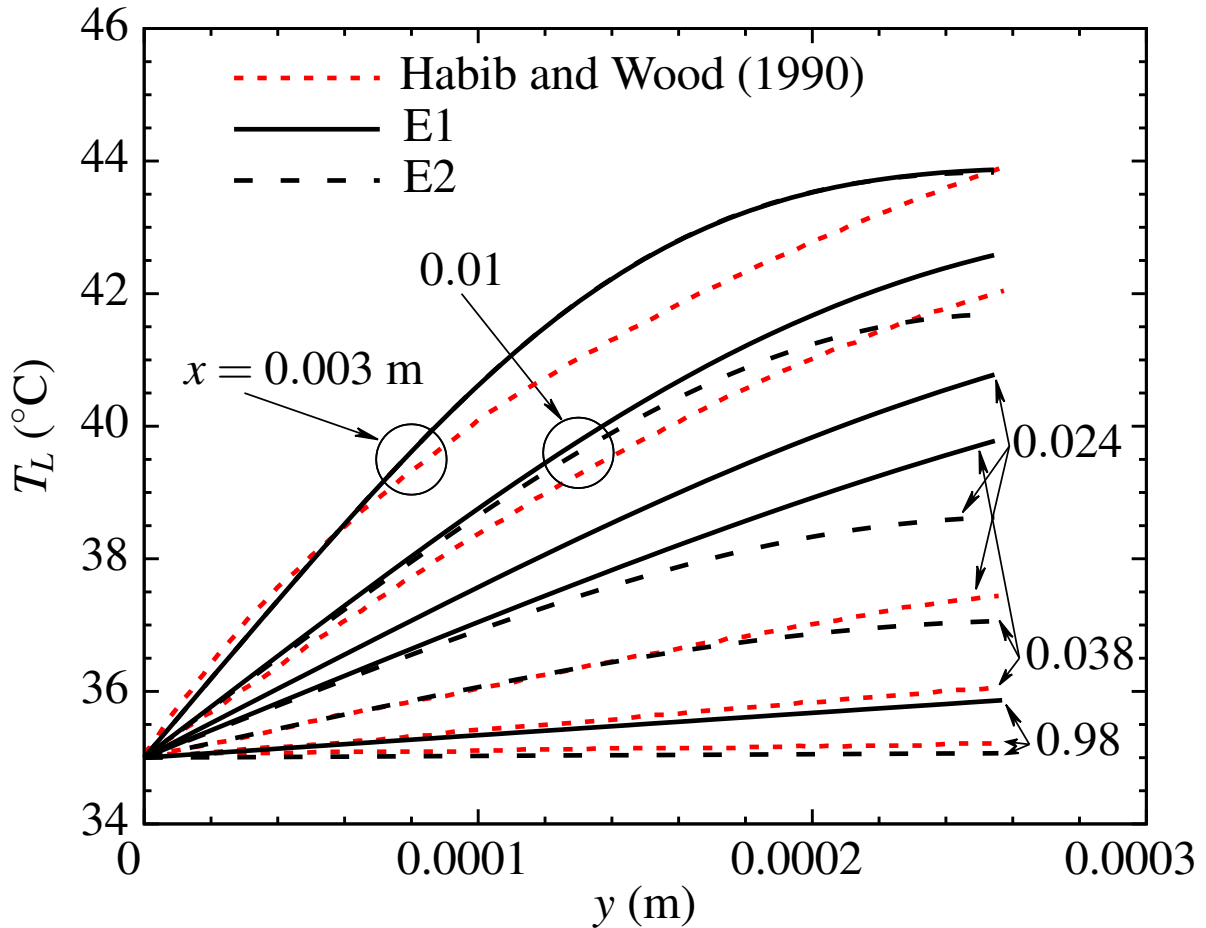


Figure 6.4: Comparison of temperature distribution in the liquid film for Cases E1 and E2 with Habib and Wood [18].

channel, due to the heat transfer from the interface to the gas region, the temperature in the gas phase increases and the adiabatic wall temperature approaches the interface temperature, which had been changing axially from the inlet liquid temperature to approach the cooled wall temperature. In Cases E1 and E2, because the vapour flow at the wall temperature is pulled in through the outlet of the channel, the gas region temperature approaches the interface final temperature very rapidly. Figure 6.2 showed that the interface mass flux is higher in Case E1 compared to Case E2, so when the flow reaches $x = 0.18$ m in Case E1, nearly all the vapour mass available in the gas phase has been absorbed to the liquid film and the gas region is already pulling mass

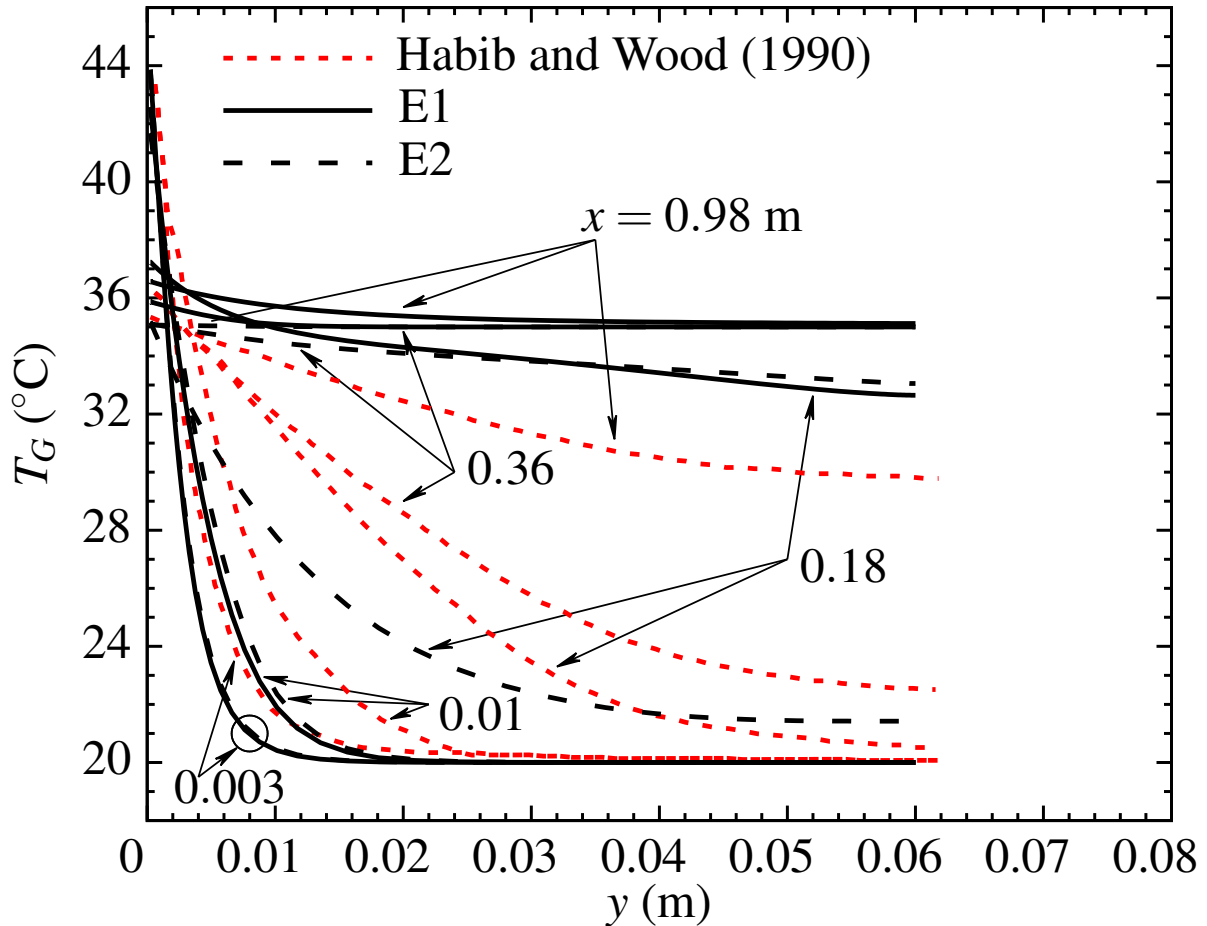


Figure 6.5: Comparison of temperature distribution in the gas phase for Cases E1 and E2 with Habib and Wood [18].

from the channel outlet. At this same point, only 69% of the vapour in Case E2 has been absorbed. The early deficit in vapour mass in Case E1 is the reason of faster advance of gas phase temperature toward the interface temperature compared to Case E2. In the case of Habib and Wood [18], the temperature gradient across the vapour decreases gradually and the adiabatic wall temperature changes to only approximately 30°C when the flow reaches the end of the channel .

The impact of the interface mass fraction condition on the absorption of water into the LiBr-water solution is investigated in Figures 6.6 to 6.8. Figure 6.6 indicates that when the imperme-

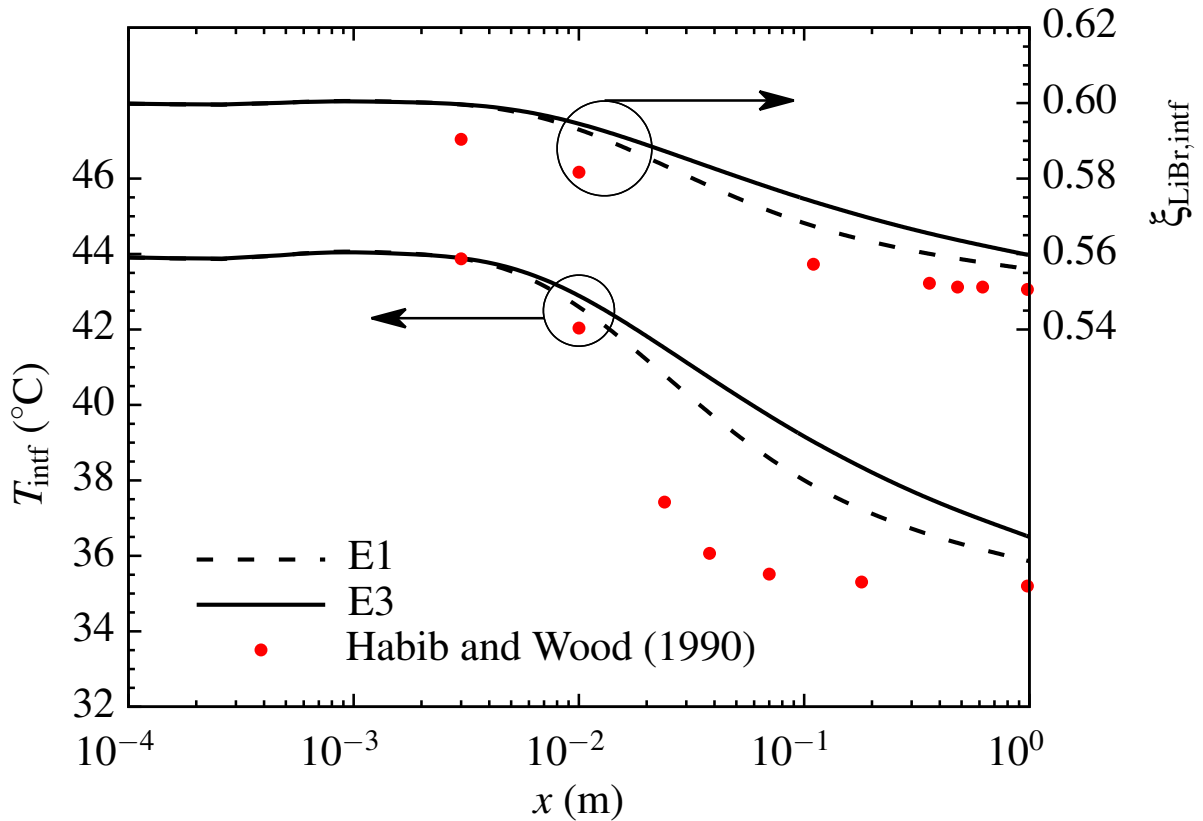


Figure 6.6: Axial variation of interface temperature and mass fraction for Cases E1 and E3.

ability of LiBr into the gas phase is applied at the interface (Case E3), higher values of temperature and LiBr mass fraction are obtained at the interface compared to Case E1 and those of Habib and Wood [18]. The impermeability condition in Case E3 prevents the LiBr from passing through the interface to the gas phase. As a result, the mass of LiBr in the solution remains the same between the inlet and outlet of the channel. In Case E1, however, the mass fraction condition used at the interface does not assure the impermeability of LiBr and 2% decrease in LiBr mass in the liquid film is observed at the end of the channel relative to the inlet LiBr mass. Because of the impermeability condition, LiBr tends to build up more at the interface in Case E3 compared to Case E1. Case E3 produces higher values of interface temperature for higher values of LiBr mass fraction consistent with the equilibrium condition. Figure 6.6 shows that Case E3 has a slower rate of axial decrease

for T_{intf} and $\xi_{\text{LiBr,intf}}$ compared to Case E1 and Habib and Wood [18].

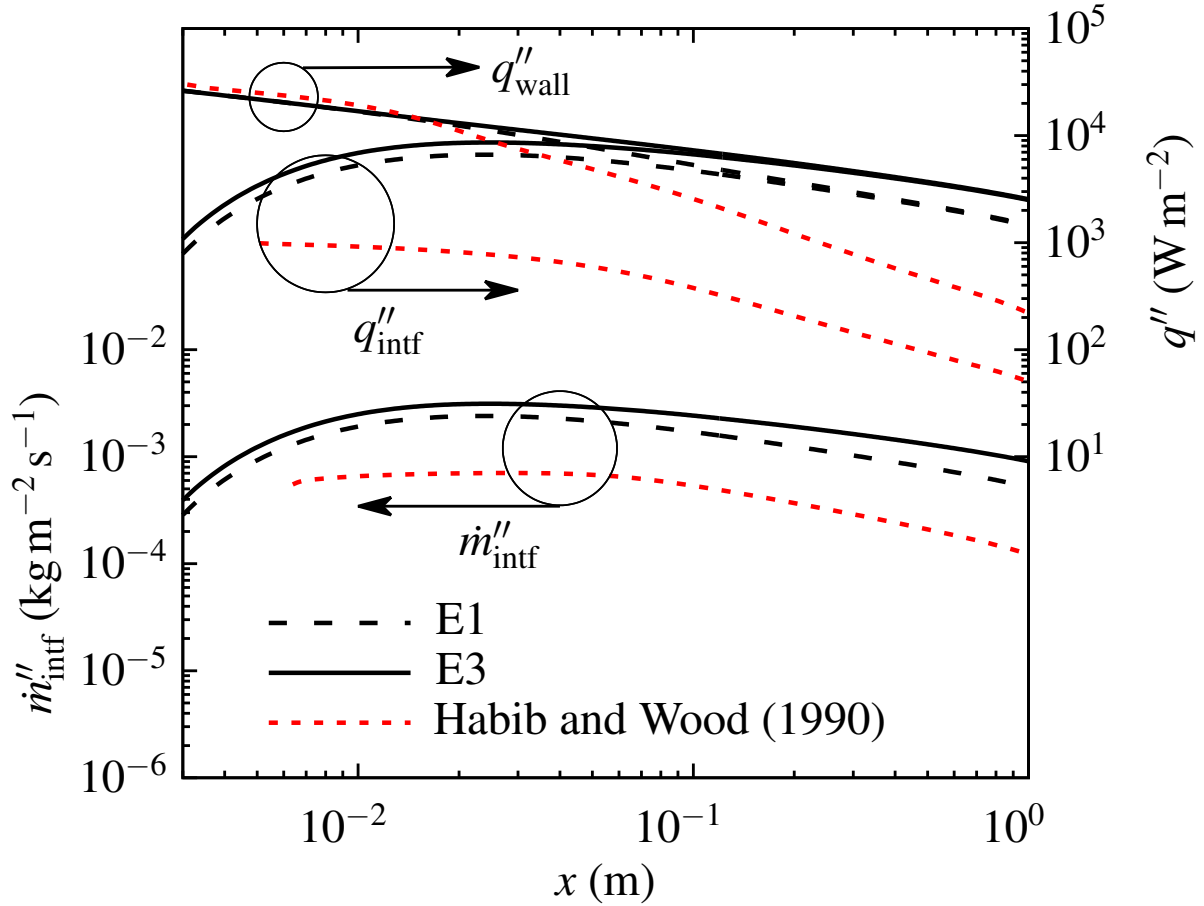


Figure 6.7: Axial variation of interface mass flux, interface and wall heat flux for Cases E1 and E3.

In Figure 6.7, Case E3 predicts higher values of heat and mass flux at the liquid-gas interface in comparison to Case E1 and shows more deviations from the case of Habib and Wood [18]. The impermeability of LiBr applied to Case E3 enables the interface to pass more water from the vapour and release more energy to the liquid film compared to the other cases. The heat flux at the isothermal wall in Case E3 is similar to Case E1 in the first part of the channel. In Case E3, however, the liquid film conducts more heat to the wall between $x = 0.03$ m and $x = 1$ m where the interface heat flux is higher than in Case E1.

Figure 6.8 presents the axial variation of both the accumulated absorbed mass ($\dot{m}'_{\text{intf,tot}}$) rel-

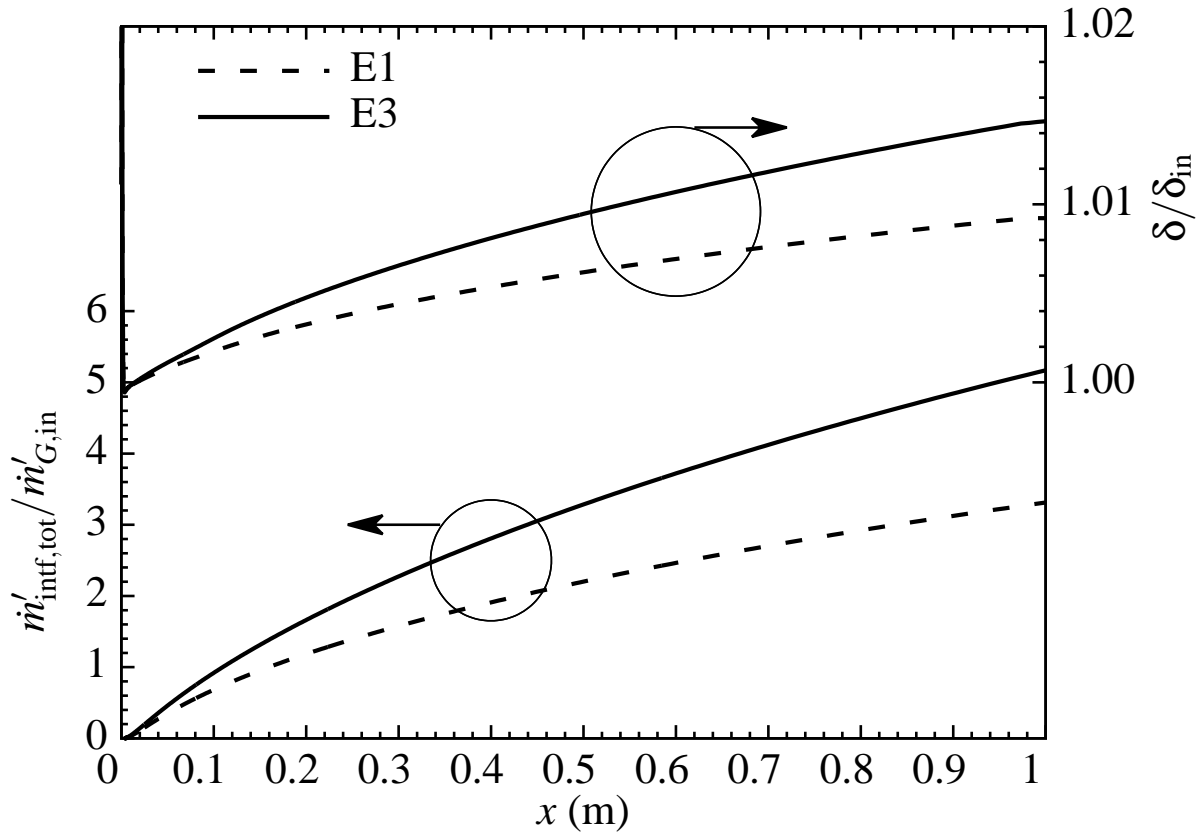


Figure 6.8: Total absorbed mass ratio to the inlet vapour mass and film thickness for Cases E1 and E3.

ative to the amount of vapour entering the channel and the film thickness relative to the inlet film thickness for Cases E1 and E3. Hereafter, the proportion of mass absorbed at the interface ($\dot{m}'_{\text{intf,tot}}/\dot{m}'_{G,\text{in}}$) will be referred as the relative amount of water absorbed. In Cases E1 and E3, nearly all of the inlet vapour is absorbed by $x = 0.15$ m and $x = 0.1$ m, respectively. To supply additional required vapour, flow enters the channel through the outlet ($x = L$). The liquid film in Case E3 absorbs a larger amount of vapour mass at each axial location and reaches the value of $\dot{m}'_{\text{intf,tot}}/\dot{m}'_{G,\text{in}} = 5.16$ by the end of the channel compared to $\dot{m}'_{\text{intf,tot}}/\dot{m}'_{G,\text{in}} = 3.31$ in Case E1. Figure 6.8 shows that the development of the film thicknesses in Cases E1 and E3 follows the trends of the mass absorption at the interface. As expected, the higher relative amount of water absorbed

in Case E3 results in a thicker film than for Case E1. At $x = 1$ m, Cases E1 and E3 reach a film thickness of $\delta = 0.2568$ mm and 0.2582 mm, respectively.

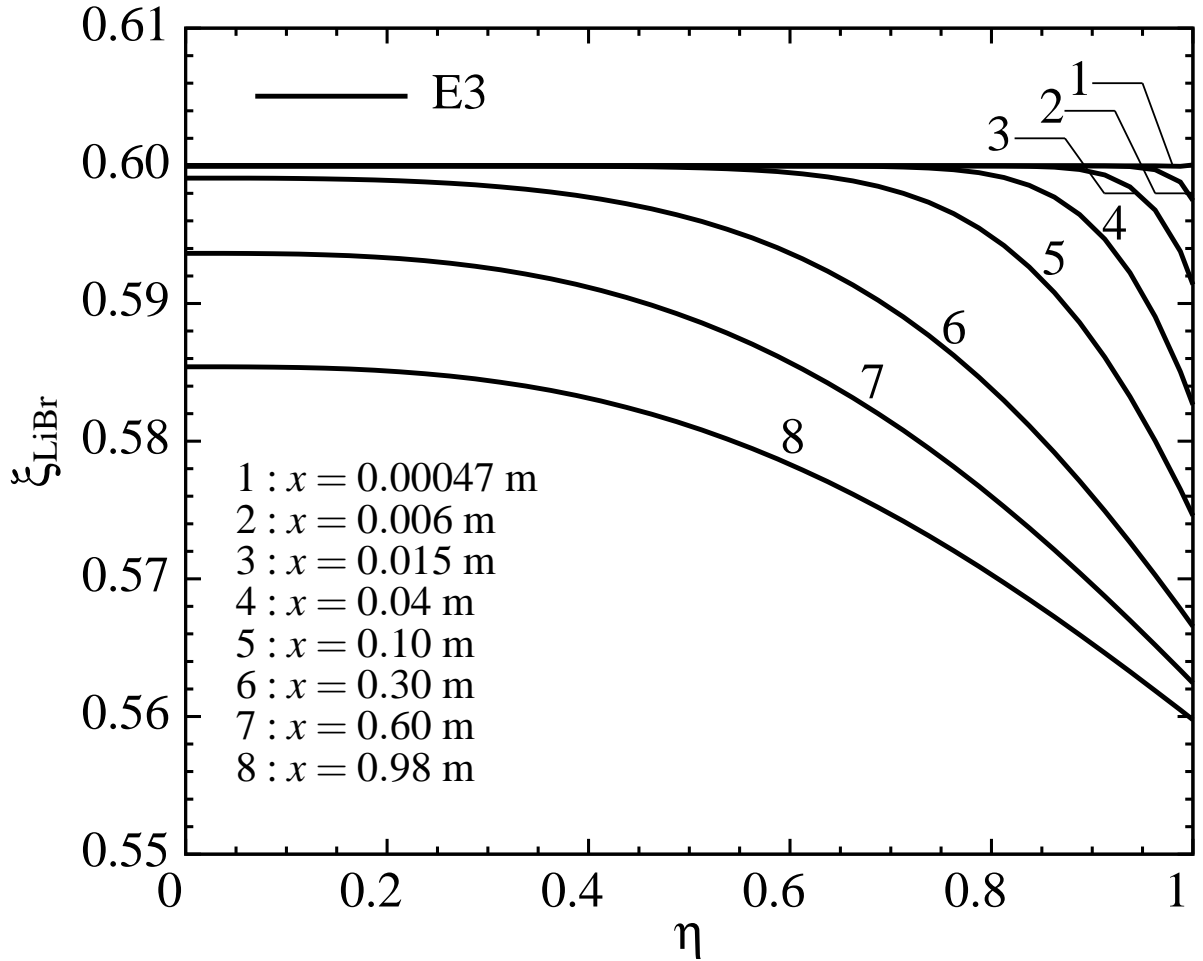


Figure 6.9: LiBr mass fraction distribution for Case E3.

The LiBr mass fraction change across the liquid film in Case E3 is shown at various axial locations in Figure 6.9. Hereafter, η will be used for the non-dimensional transverse-direction axis where needed in figures. The definition of η is:

$$\eta = \frac{y}{\delta} \quad \text{for } 0 \leq y \leq \delta, \quad (6.2)$$

$$\eta = \frac{y - \delta}{H - \delta} + 1 \quad \text{for } \delta \leq y \leq H. \quad (6.3)$$

At $x = 0.00047$ m, the mass fraction is at the uniform inlet value of $\xi_{\text{LiBr}} = 0.6$ across the liquid film. The interface mass fraction gradient increases as more water is absorbed at $x = 0.006$ m. The increase in the interface mass fraction gradient continues to the point of $x = 0.04$ m while a larger portion of the film deviates from the inlet mass fraction value. By $x = 0.3$ m, the LiBr mass fraction of the film near the wall has begun to decrease. As the LiBr solution flows down the channel, the decrease in the interface mass fraction gradient decreases the mass absorption (Figure 6.7) and the liquid flow close to the wall becomes more affected by the water diffusion in the film.

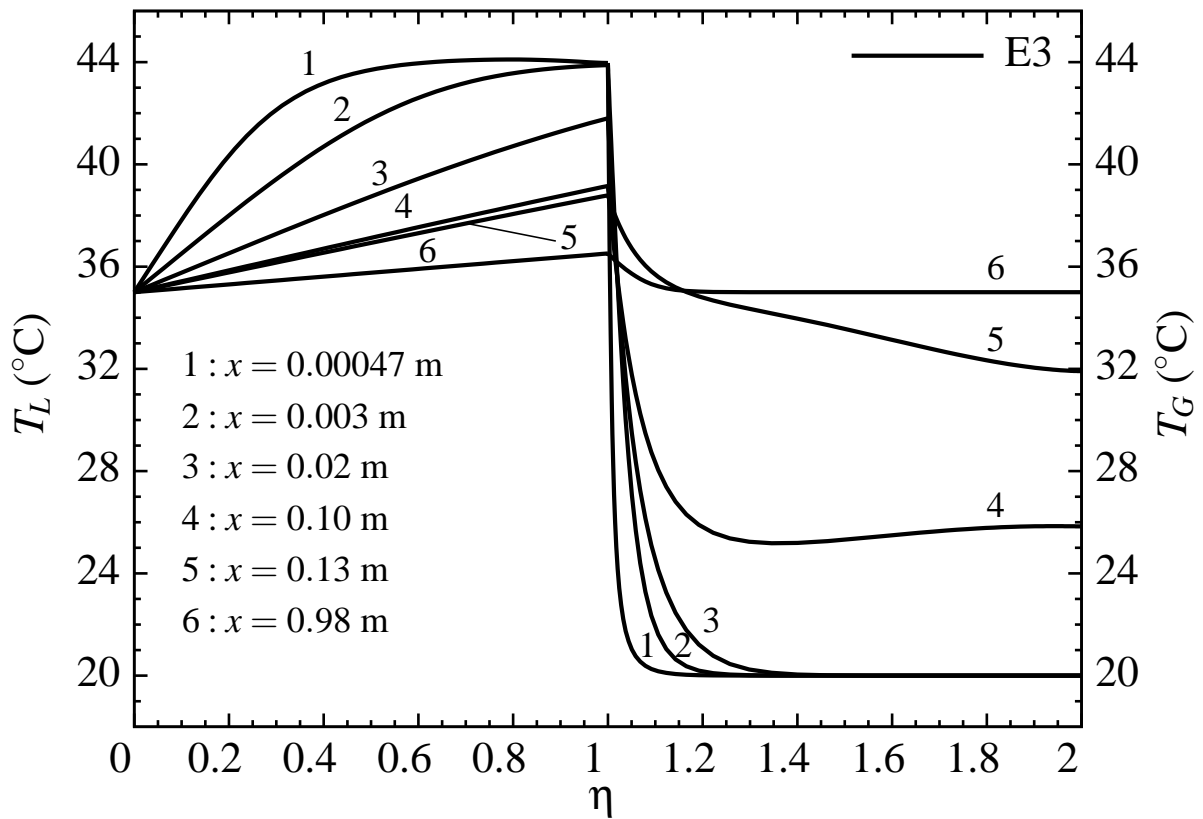


Figure 6.10: Temperature distribution in the liquid and gas phases for Case E3.

Figure 6.10 compares the temperature profiles in the liquid and gas regions at selected axial locations for Case E3. At $x = 0.00047$ m, a significant temperature gradient occurs close to the wall in the liquid because of the wall-liquid temperature difference. Also at that axial location a sharp gradient occurs near the interface in the gas because of the liquid-gas temperature difference.

Between $x = 0.0003$ m and $x = 0.02$ m, the interface temperature decreases noticeably and the film temperature profile becomes nearly linear, while a large portion of the gas region is still at the gas inlet temperature. The temperature of this part of the gas changes considerably at $x = 0.1$ m where the lack of enough vapour mass in the gas phase causes vapour to enter from the outlet. The great impact of this inflow at the outlet on the gas phase temperature is reflected in the change in gas temperature in the short distance between $x = 0.1$ m and $x = 0.13$ m. When the gradient of the liquid film temperature reaches its minimum value at $x = 0.98$ m, only in a small area close to the interface the temperature of the vapour is not at the wall temperature (which coincides with the temperature value of vapour entering the channel at $x = L$).

6.3.4 Summary of Comparison Cases

The numerical results of the present elliptic model were compared to the parabolic approach of Abbasi Havestini and Ormiston [58] and the elliptic model presented by Habib and Wood [18]. The liquid energy equation and diffusion coefficient, the interface mass fraction condition and heat of absorption were modified to emulate the conditions in the study by Habib and Wood [18]. The results of the present model were in a very good agreement with the parabolic model of Abbasi Havestini and Ormiston [58] and close to the predictions of Habib and Wood [18] for axial variations of the interface temperature and mass fraction when the modifications were applied. The change of the interface mass fraction condition also showed a noticeable effect on the absorption at the interface.

6.4 New Results for the Elliptic Two-phase Absorption Model

A new set of computations were undertaken to investigate the impact of the inlet pressure and the temperature difference between the liquid film and the isothermal wall on the absorption at the interface of co-current steady flow of the LiBr solution and water vapour. Fully developed inlet

velocity profiles of the liquid and gas phases were applied. The comprehensive form of the governing equations and the interface conditions discussed in Section 2.4 were solved. The variable thermophysical properties and the equilibrium relation presented by Mittermaier et al. [12] were applied to the LiBr solution and the interface, respectively. Constant properties were used for the gas phase as given in Lemmon et al. [57], evaluated at the inlet conditions. The heat of absorption was obtained by using the Lemmon et al. [57] function for water vapour enthalpy and the Pátek and Klomfar [56] function for water partial enthalpy in the solution. The inlet pressure and the wall temperature were changed to formulate the four new cases presented in Table 6.2. The following conditions were applied to these cases: $L = 1$ m, $H = 0.06$ m, $T_{G,in} = 20^\circ\text{C}$, $\text{Re}_{G,in} = 500$, $\text{Re}_{L,in} = 30$, $N_{y,L} = 40$, $N_{y,G} = 90$, and $N_x = 500$.

As Table 6.2 indicates, the inlet pressure was changed from $P = 1$ kPa in Case E4 to $P = 2$ kPa in Cases E5 and E6 while the wall temperature was not changed. According to equilibrium condition, the change in the pressure can be implemented either by keeping the film inlet mass fraction unchanged and finding the matching temperature, (Case E5), or by keeping the inlet temperature unchanged and finding the matching mass fraction, (Case E6). In Case E7 the wall temperature is changed to maintain the liquid-wall temperature difference the same as in Case E4 but using the same $\xi_{W,in}$ and $T_{L,in}$ as Case E5.

Table 6.2: Operating parameters for cases E4 to E7.

Case	P [kPa]	$\xi_{W,in}$ –	$T_{L,in}$ [°C]	T_{wall} [°C]	$T_{L,in} - T_{wall}$ [K]
E4	1	0.40	44.37	35	9.37
E5	2	0.40	56.40	35	21.4
E6	2	0.47	44.37	35	9.37
E7	2	0.40	56.40	47.03	9.37

Figure 6.11 presents the interface temperature and LiBr mass fraction in the flow direction for Cases E4 to E7. The temperature profiles show that the interface temperature is highly affected by

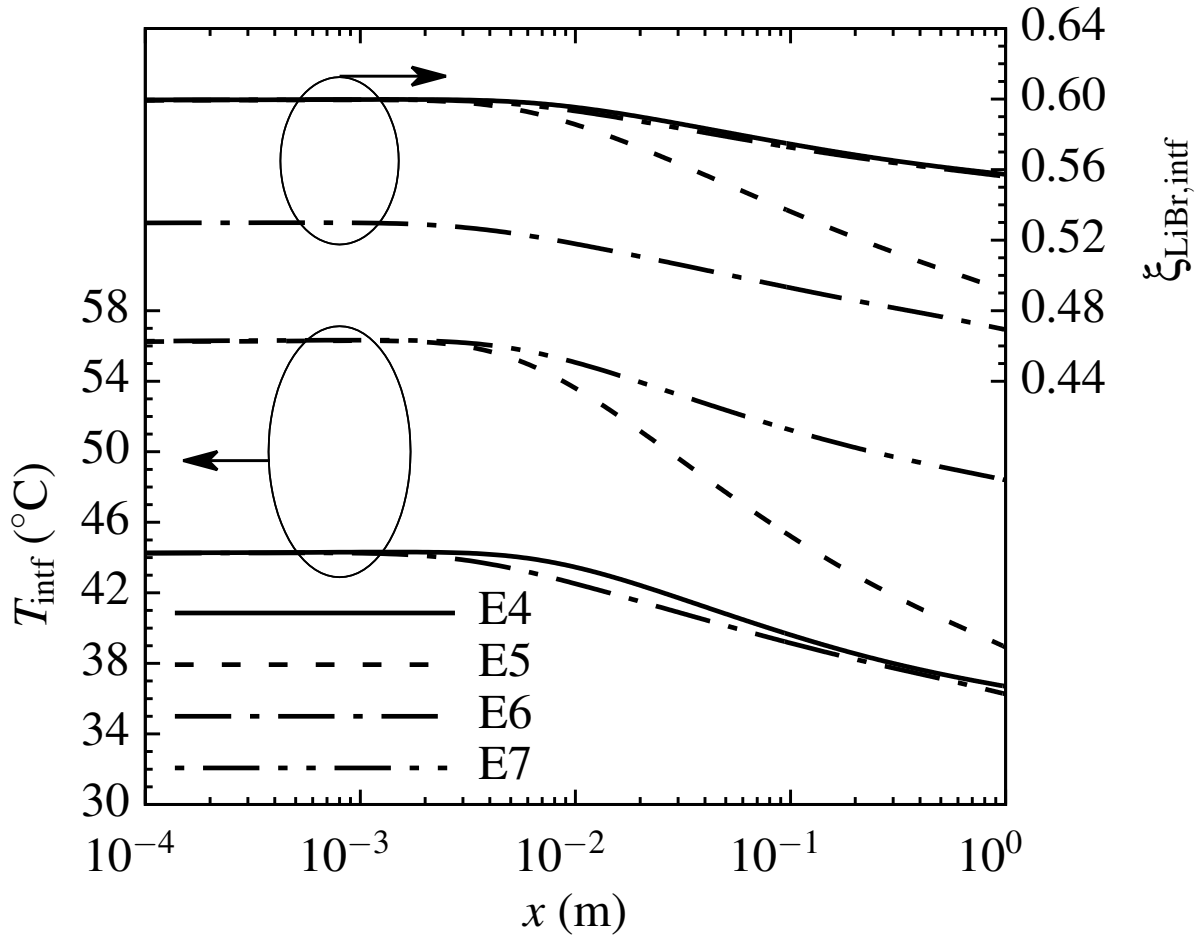


Figure 6.11: Axial variation of interface temperature and mass fraction for Cases E4 to E7.

the cold wall temperature on which the film is flowing. In Cases E4 and E6, the interface temperature decreases to approach $T_{\text{wall}} = 35^\circ\text{C}$ and the impact of the different $\xi_{W,\text{in}}$ (caused by different pressures) is only noticeable in a short portion of the channel between $x = 0.003$ m to $x = 0.2$ m. In the pair of Cases E5 and E7, which have common inlet pressure, mass fraction, and temperature, Case E5 deviates from Case E7 towards a smaller wall temperature. In Cases E4 and E7, although the inlet pressures and temperatures are different, the mass fraction profiles are similar because of the equal values of $\xi_{W,\text{in}}$ and $(T_{L,\text{in}} - T_{\text{wall}})$ in those cases. Case E5 deviates from Cases E4 and E7 and reaches a smaller ξ_{LiBr} at the end of the channel due to a larger $(T_{L,\text{in}} - T_{\text{wall}})$. In Case E6, the

interface mass fraction decrease over the channel length is about 0.06 (from $\xi_{\text{LiBr, intf}}=0.53$ to 0.47). That change is close to that for Case E4: 0.04 (from $\xi_{\text{LiBr, intf}}=0.6$ to 0.56), which is a comparable case with similar $T_{L, \text{in}}$ and T_{wall} .

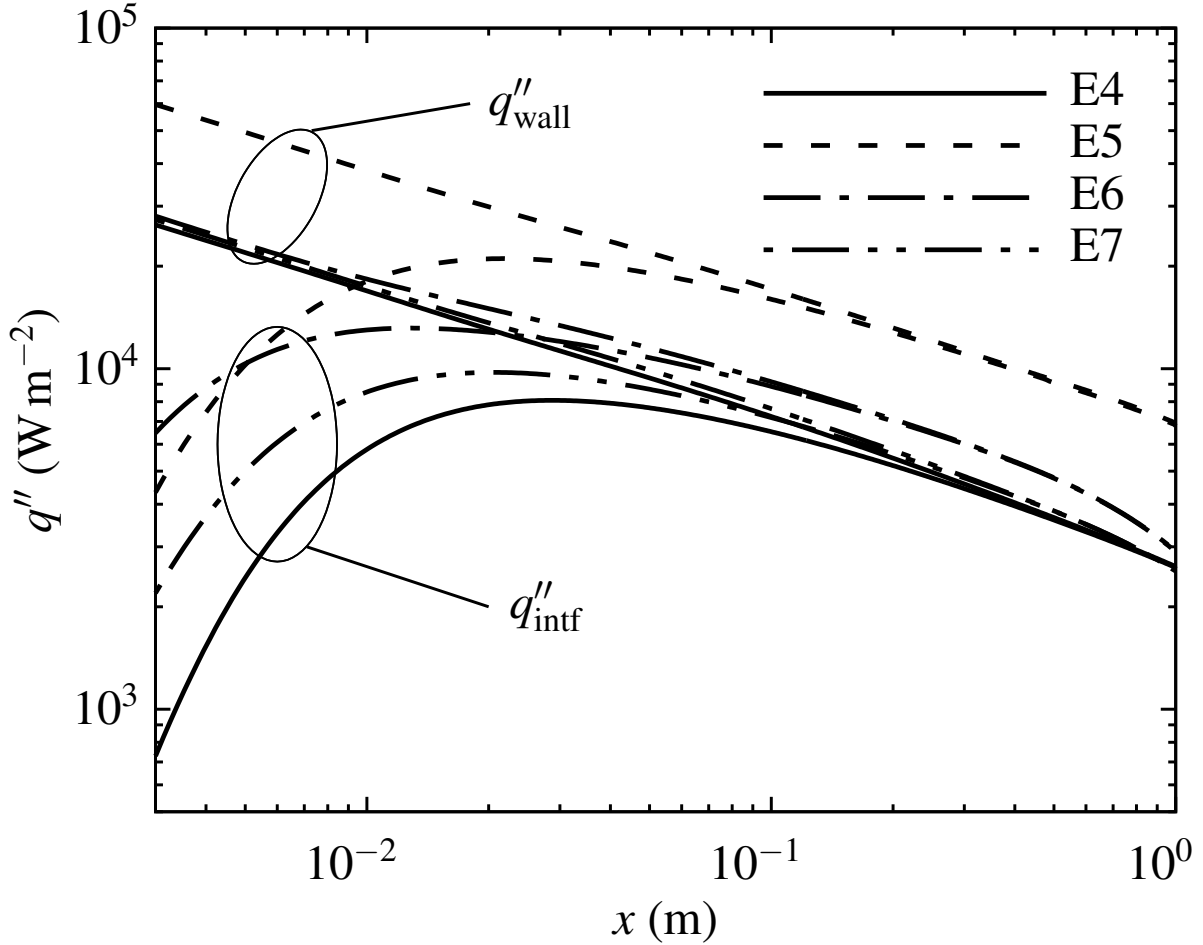


Figure 6.12: Axial variation of interface and wall heat flux for Cases E4 to E7.

In Figure 6.12 the axial variation of the interface and wall heat flux are compared in Cases E4 to E7. A noticeably higher rate of heat transfer by conduction happens at the wall of Case E5 because of the larger temperature difference between the liquid film and the wall. This temperature difference causes a sharp drop in the interface temperature and LiBr mass fraction, thus requiring more absorption of water and release of heat at the interface. The other three cases with the same value of $(T_{L, \text{in}} - T_{\text{wall}})$, E4, E6, and E7, show similar wall heat flux values at the entrance of the

channel. As was observed in Figure 6.11, the decrease in the interface LiBr mass fraction over the channel length in Case E6 was slightly more than Case E4. This reduction is the result of a greater mass flux at the interface in Case E6 compared to Case E4, which is seen as a greater heat flux for Case E6, as shown in Figure 6.12. Case E7 shows more energy release at the interface compared to Case E4 and the interface heat flux reaches the wall heat flux value in a shorter distance from the inlet.

The axial variation of the relative amount of water absorbed and the film thickness relative to the inlet film thickness for Cases E4 to E7 are shown in Figure 6.13. The water vapour enters the

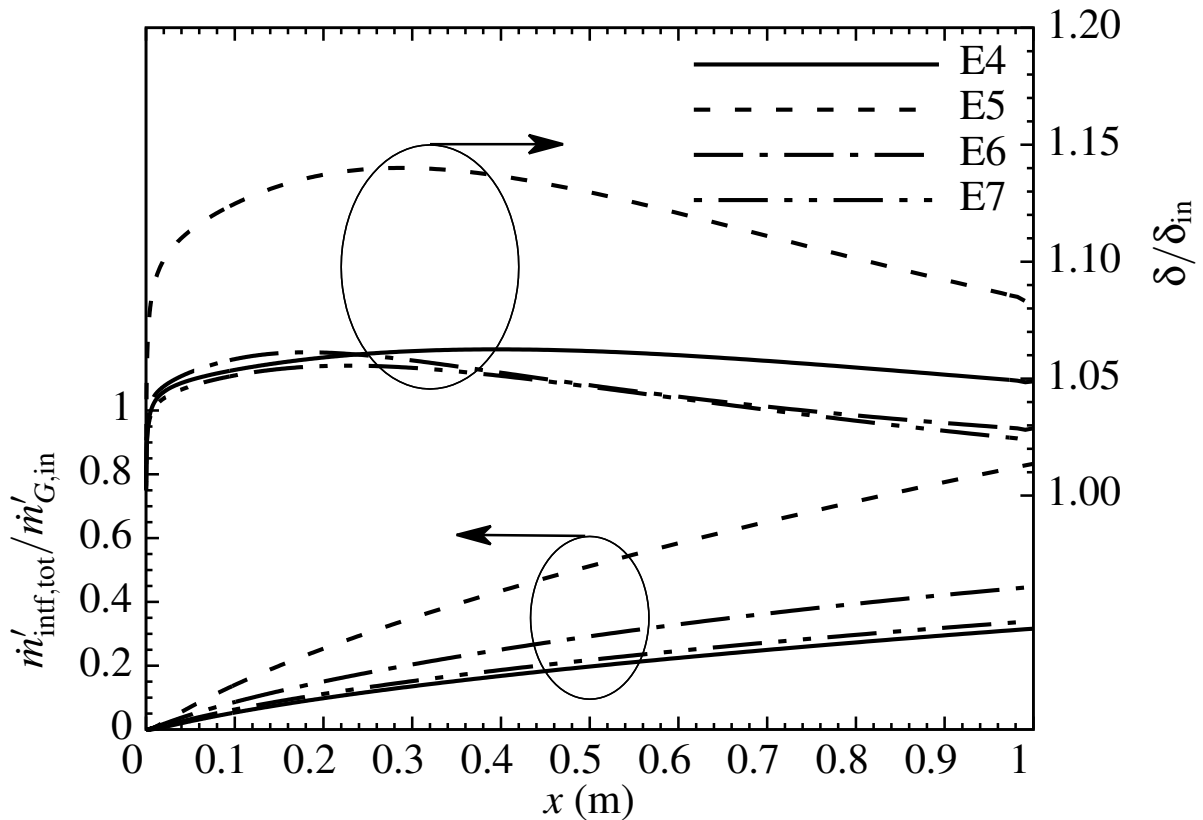


Figure 6.13: Total absorbed mass ratio to the inlet vapour mass and film thickness for Cases E4 to E7.

channel at $Re_{G,in} = 500$ in all the cases. The increase in the channel inlet pressure from $P = 1$ kPa to $P = 2$ kPa along with the increase in the liquid inlet temperature, increases the relative amount

of water absorbed from 31% in Case E4 to 83% in Case E5 at $x = 1$ m. When the pressure increase is applied at a higher $\xi_{W,in}$, the relative amount of water absorbed increases to 44% in Case E6. The relative amount of water absorbed is 33% at the end of absorption process in Case E7, which shows that the increase in the absorption pressure has a negligible effect on mass absorption when $\xi_{W,in}$ and $(T_{L,in} - T_{wall})$ are not changed. The film thickness in Cases E4 to E7 increases to a maximum value and then decreases until the film reaches the channel end. The initial film thickness, which corresponds to the fully developed flows of liquid and vapour, had values of $\delta_{in} = 0.2686, 0.2358, 0.1968,$ and 0.2358 mm for Cases E4 to E7, respectively. The highest increase in film thickness relative to the inlet film thickness, occurs in Case E5 which has a higher rate of mass absorption at the interface.

The temperature distribution in the liquid film and the water vapour for Case E6 is presented in Figure 6.14. In this case, a sufficient amount of vapour mass was available in the gas phase to be absorbed and no mass is required from the channel outlet. The temperature difference between the wall and the liquid film results in a significant temperature gradient at the wall in the entrance area of the channel. Similarly, the interface on the gas phase side experiences a sharp temperature gradient due to the temperature difference of the liquid and gas phases. At $x = 0.003$ m, when more mass is absorbed at the interface, the temperature of the liquid has decreased whereas a large portion of the gas phase remains at the inlet temperature of the vapour. The liquid film temperature profile becomes linear and approaches the wall temperature from $x = 0.003$ m to $x = 0.6$ m. At $x = 0.6$ m, the heat conducted from the interface to the vapour increases the temperature in nearly half of the gas phase region. The temperature distribution in the water vapour for Case E6 is similar to Figure 6.10 except that the gas phase temperature near the wall increased only to about $T = 21^\circ\text{C}$ by the end of the channel.

Figure 6.15 shows the local Sherwood number along the liquid-gas interface in Case E6. The liquid film Sherwood number is defined as follows:

$$\text{Sh} = \frac{C_m \delta}{D_{\text{intf}}^{AB}} \quad (6.4)$$

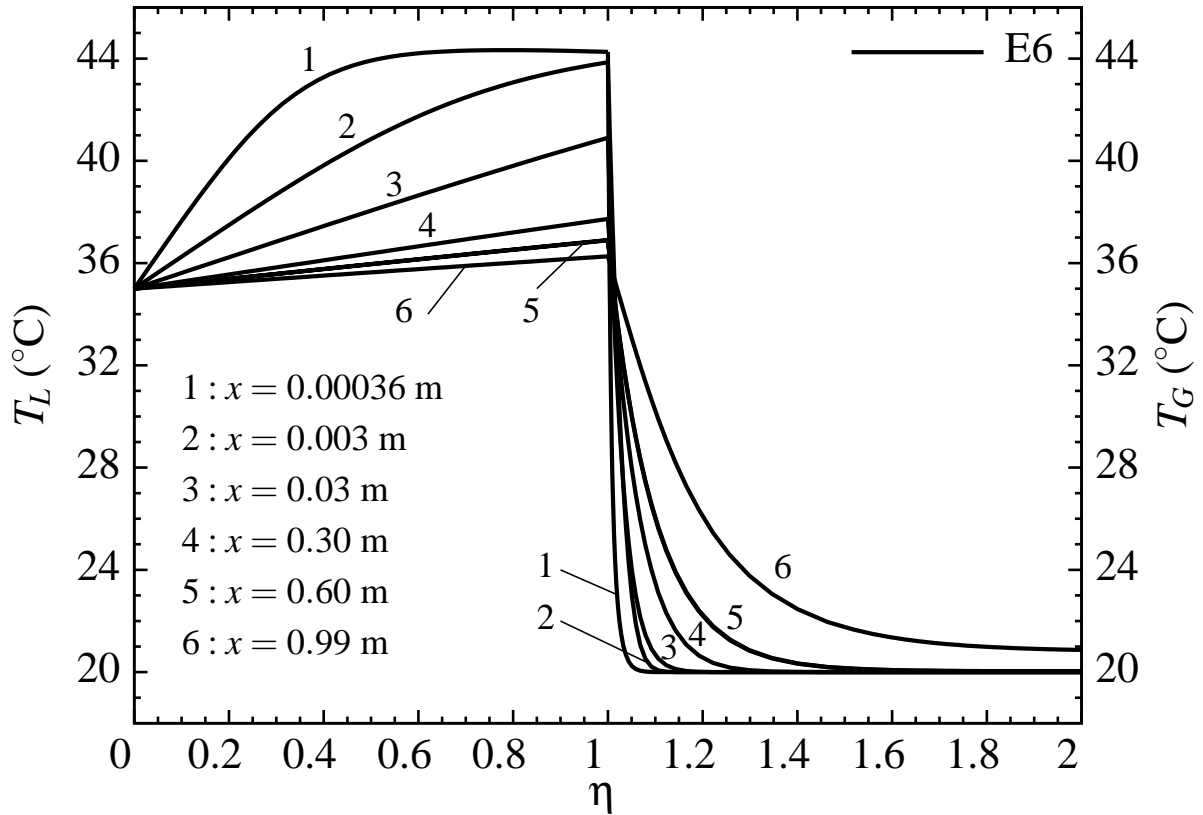


Figure 6.14: Temperature distribution in the liquid and gas phases for Case E6.

where C_m is the mass transfer coefficient and calculated by using the following equation:

$$C_m = \frac{\dot{m}''_{\text{intf}}}{\rho_{L,\text{intf}} (\xi_{W,\text{intf}} - \xi_{W,b})} \quad (6.5)$$

In Equation (6.5), $\xi_{W,b}$ is the bulk water mass fraction of the liquid film. Figure 6.15 shows that the Sherwood number decreases from 91 at the inlet to 8 at the outlet of the channel in Case E6. As the liquid film flows further downstream more of the mass absorbed at the interface diffuses across the film and the Sherwood number decreases.

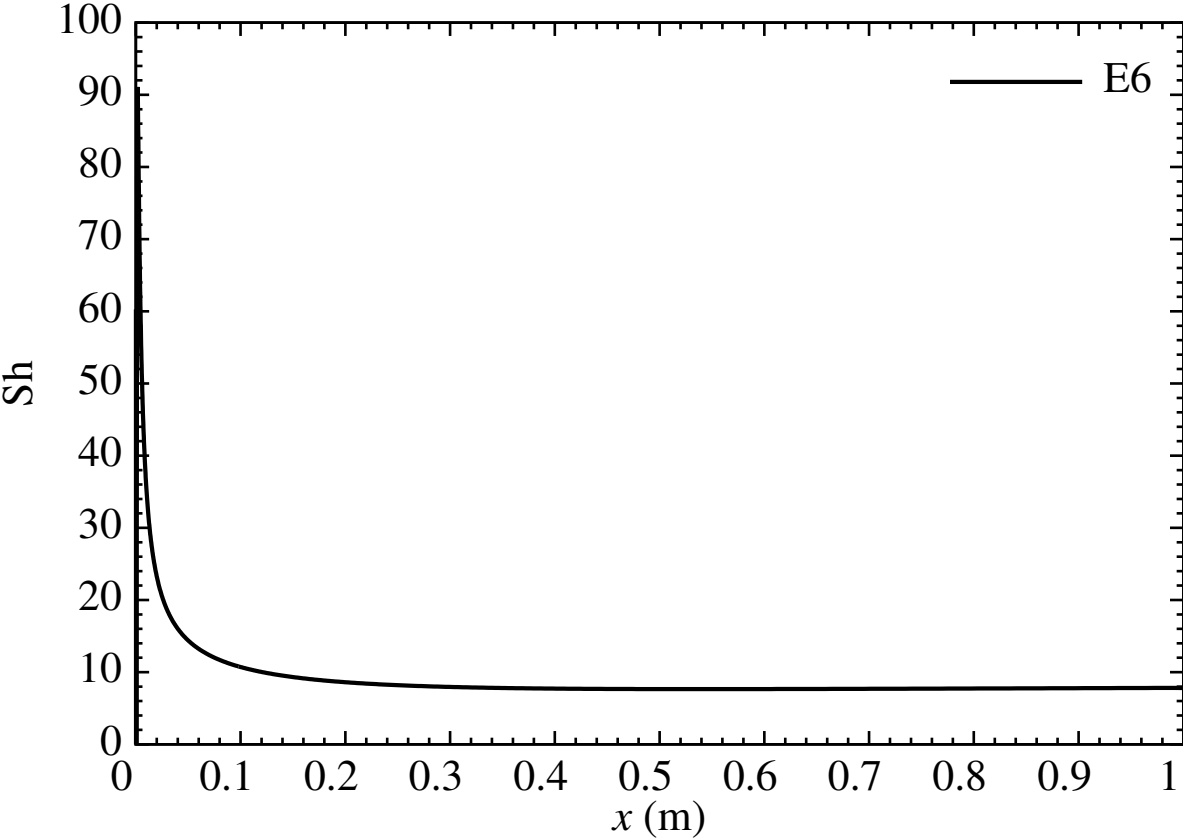


Figure 6.15: Axial variation of Sh number for Case E6.

Chapter 7

Horizontal Tubes: Elliptic Model

7.1 Introduction

In this chapter, the elliptic model that is implemented in an in-house computer code is used to model absorption of water vapour into a LiBr liquid film flowing over a horizontal tube. The accuracy of the elliptic model results is validated through comparisons with relevant numerical and experimental results from the open literature. The results of the present two-phase elliptic model are compared to the numerical two-phase model of Min and Choi [24] and the single-phase parabolic models of Papaefthimiou et al. [28] and Kyung et al. [30]. The experimental data of Seol and Lee [29] are used to validate the results of the present model over a range of absorber operating conditions. New numerical results are presented for a parametric study of the effect of changing the liquid film inlet Reynolds number, the film inlet temperature, the tube diameter, and the distance between the tubes on the absorption rate and the temperature and mass fraction around the tube.

7.2 Grid Independence Study

A grid independence test was conducted using one of the comparison cases (Case HT1 described in section 7.3.1) studied to investigate the performance of the elliptic model. Three sets of grids were used for the grid independence test. The number of nodes considered in the x and y directions for Case HT1 were as follows: $40 \leq N_{y,L} \leq 70$, $100 \leq N_{y,G} \leq 170$, and $610 \leq N_x \leq 910$. Values of the film thickness and the interface temperature were used to assess the effect of changing the grid. A grid with $N_{y,L} = 60$, $N_{y,G} = 140$, and $N_x = 760$ was selected because its results deviated by only -0.89% and 0.08% for the film thickness and the interface temperature, respectively, from

the finest grid ($N_{y,L} = 70$, $N_{y,G} = 170$, and $N_x = 910$).

7.3 Comparisons with Previous Work

7.3.1 Definition of Comparison Cases

In this section, the geometric and operating parameters of the comparison cases are described. Figure 7.1 shows a tube bundle and the definition of the parameters used for cases studied in this chapter. The geometric and operating parameters applied to comparison cases are summarized in Tables 7.1 and 7.2, respectively. The tube diameter is $d = 19.05$ mm ($3/4$ inch) in all the cases except in Cases HT2 and HT3 in which a tube size of $d = 8$ mm ($5/16$ inch) was used. A centre-to-centre y -direction spacing, S_T , of $9d$ is assumed in all the comparison cases. The computational domain size before and after the tubes are $L_1 = d$ and $L_2 = 5d$, respectively, except for Case HT1 ($L_1 = 0.367d$). The liquid film inlet thickness is calculated based on $Re_{L,in}$, given in the references and $Fr_{L,in}$, assumed based on the work of Min and Choi [24]. A sufficient number of grid cells were allocated in the x and y directions (as shown in Table 7.1) to ensure grid independence based on the grid examination explained in Section 7.2. In Table 7.2, P , $T_{L,in}$, $\xi_{LiBr,in}$, and T_{wall} were provided in the references and the gas phase inlet Reynolds number and temperature were assumed as $Re_{G,d,in} = 20$ and $T_{G,in} = 20^\circ\text{C}$.

As it was explained in Section 4.3.5, the interface location in the elliptic model is determined by applying an integral mass balance to the liquid film. The severe changes in the liquid film velocity at the top and bottom of the tube in the beginning of the numerical solution led to strong grid skewing in those areas. To overcome this problem, the interface location and the domain grid were not updated over a few iterations to maintain a stable numerical solution. When the desired minimum change in the velocity field was achieved, the interface location was calculated and the grid was regenerated for the following iterations of the solution.

To incorporate the surface tension effect in the elliptic model, the liquid film curvature around the tube was explicitly computed and the surface tension force was added to the interface force balance. This effort did not lead to a stable solution. Therefore, the surface tension force at the interface is neglected in comparison cases studied in this section.

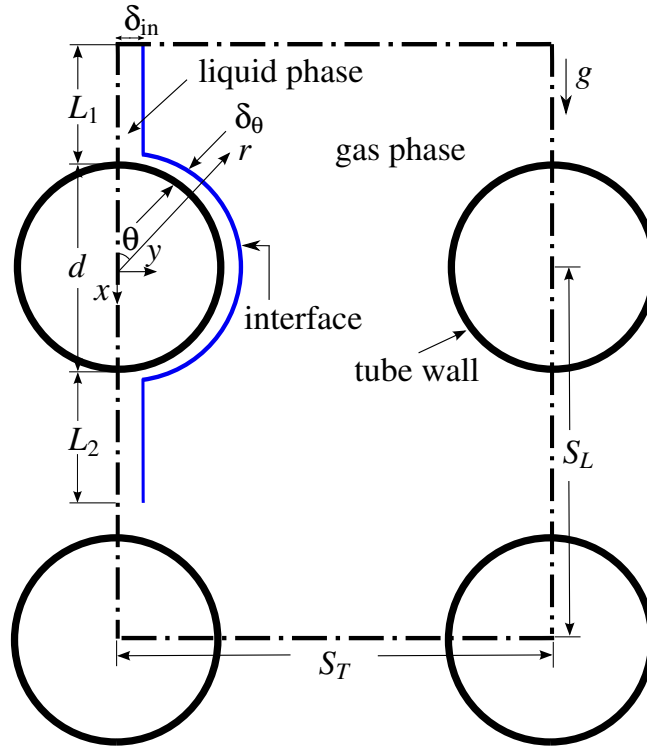


Figure 7.1: Geometric parameters definition for horizontal tubes studied using the elliptic model.

7.3.2 Comparison Case HT1: Min and Choi [24]

To make the elliptic model in Case HT1 as close as possible to Min and Choi [24], the x and y -direction convection and mass diffusion terms in the liquid energy equation including the partial enthalpies of the solution components were neglected. The liquid properties and the heat of absorption are assumed to be constant. Dimensionless numbers $Re_{L,MC} = 16.7$, $Fr_L = 19.9$, $Sc = 2456$, $Pr = 21.4$, and $Ja = 0.058$ are given in Min and Choi [24]. These dimensionless numbers along

Table 7.1: Geometric parameters in comparison cases.

Reference	Case	d [mm]	S_T/d –	L_1/d –	L_2/d –	δ_{in} [mm]	N_x –	$N_{y,L}$ –	$N_{y,G}$ –
Min and Choi [24]	HT1	19.05	9	0.367	5	0.2564	760	60	140
Papaefthimiou et al. [28]	HT2	8	9	1	5	0.0512	550	40	140
Papaefthimiou et al. [28]	HT3	8	9	1	5	0.0407	550	40	140
Kyung et al. [30]	HT4	19.05	9	1	5	0.0563	800	50	140
Seol and Lee [29]	HT5	19.05	9	1	5	0.0750	800	50	140

Table 7.2: Operating parameters in comparison cases.

Reference	Case	$Re_{L,in}$ –	$Fr_{L,in}$ –	$Re_{G,d,in}$ –	P [kPa]	$T_{L,in}$ [°C]	$\xi_{LiBr,in}$ –	T_{wall} [°C]	$T_{G,in}$ [°C]
Min and Choi [24]	HT1	16.7 ^a	19.9	20	1	40	0.612	30	20
Papaefthimiou et al. [28]	HT2	20	132.93	20	1.227	50	0.6	V	20
Papaefthimiou et al. [28]	HT3	10	66.47	20	1.227	50	0.6	V	20
Kyung et al. [30]	HT4	15.8	83.86	20	1.08	47.92	0.6	V	20
Seol and Lee [29]	HT5	19.73	67.37	20	0.8, 1.07, 1.33	R	0.6	R	20

^a $Re_{L,MC}$ (defined in the nomenclature)

V: Variable (Equations (7.4) and (7.5)); R: a range of values (Table 7.3)

with the kinematic viscosity, $\nu_L = 3.4347 \times 10^{-6} \text{ m}^2 \text{ s}^{-1}$, and density, $\rho_L = 1.7288 \times 10^3 \text{ kg m}^{-3}$, of the LiBr solution from Mittermaier et al. [12] and $H_a = 2.8085 \times 10^6 \text{ J kg}^{-1}$ (calculated based on Equation (2.36) by using Lemmon et al. [57] for h_v and Pátek and Klomfar [56] for \bar{h}_W) were used to obtain the following properties of the the LiBr solution: $C_{p,L} = 1.6208 \times 10^3 \text{ J kg}^{-1} \text{ K}^{-1}$, $k_L = 4.4972 \times 10^{-1} \text{ W m}^{-1} \text{ K}^{-1}$ and $D_L^{AB} = 1.3985 \times 10^{-9} \text{ m}^2 \text{ s}^{-1}$. The magnitude of the film in-

let velocity is assumed to be the free-fall speed from the upper tube, $U_{L,in} = 0.2237 \text{ m s}^{-1}$ and the inlet film thickness based on $Re_{L,MC}$ and Fr_L is $\delta_{in} = 0.256415 \text{ mm}$. The constant properties (Lemmon et al. [57]) used for the gas phase in Case HT1 are as follows: $\rho_G = 7.3955 \times 10^{-3} \text{ kg m}^{-3}$, $\mu_G = 9.5477 \times 10^{-6} \text{ kg m}^{-1} \text{ s}^{-1}$, $C_{p,G} = 1.8754 \times 10^3 \text{ J kg}^{-1} \text{ K}^{-1}$, and $k_G = 1.8089 \times 10^{-2} \text{ W m}^{-1} \text{ K}^{-1}$. The liquid film and water vapour enter the domain at uniform velocities and the equilibrium condition of Mittermaier et al. [12], as given in Appendix A.4, was applied at their interface.

Figure 7.2 shows the liquid film shape around the tube in Case HT1. In Figure 7.2, R is the tube radius. The film becomes thinner as it reaches the top of the tube because the film accelerates at the top of the tube, right before flowing over the tube. After the upper stagnation region where the flow is brought to rest, the film thickness increases. The liquid film velocity increases when it flows around the tube and becomes thinner compared to the top of the tube. The film thickness does not change around the tube considerably and the film attains a fully developed state. The film then thickens as it reaches the bottom of the tube and is transitioned to a falling film below the tube.

The LiBr mass fraction distribution across the liquid film at various stream-wise sections for Case HT1 is shown in Figure 7.3. In this Figure, ξ_{LiBr}^* and r_θ^* are defined as following based on the work of Min and Choi [24]:

$$\xi_{LiBr}^* = \frac{\xi_{LiBr} - \xi_{LiBr}(P, T_{wall})}{\xi_{LiBr,in} - \xi_{LiBr}(P, T_{wall})}, \quad r_\theta^* = \frac{r - \frac{d}{2}}{\delta_\theta} \quad (7.1)$$

where $\xi_{LiBr}(P, T_{wall})$ is the LiBr equilibrium mass fraction at the wall temperature and δ_θ is the film thickness in the radial direction at the tube central angle θ . In Case HT1, $\xi_{LiBr}(P, T_{wall}) = 0.5124$ based on the Mittermaier et al. [12] equilibrium condition.

In Figure 7.3, the x axis begins at 0.8 because mass fraction gradient occurs only at the last 15% of the film thickness (near the liquid-gas interface) around the tube. This trend is the result of the slow diffusion of absorbed water into the film liquid over the short distance around the tube. At $\theta = 5^\circ$, a large portion of the liquid film is at the inlet mass fraction, $\xi_{LiBr,in} = 0.612$, whereas near

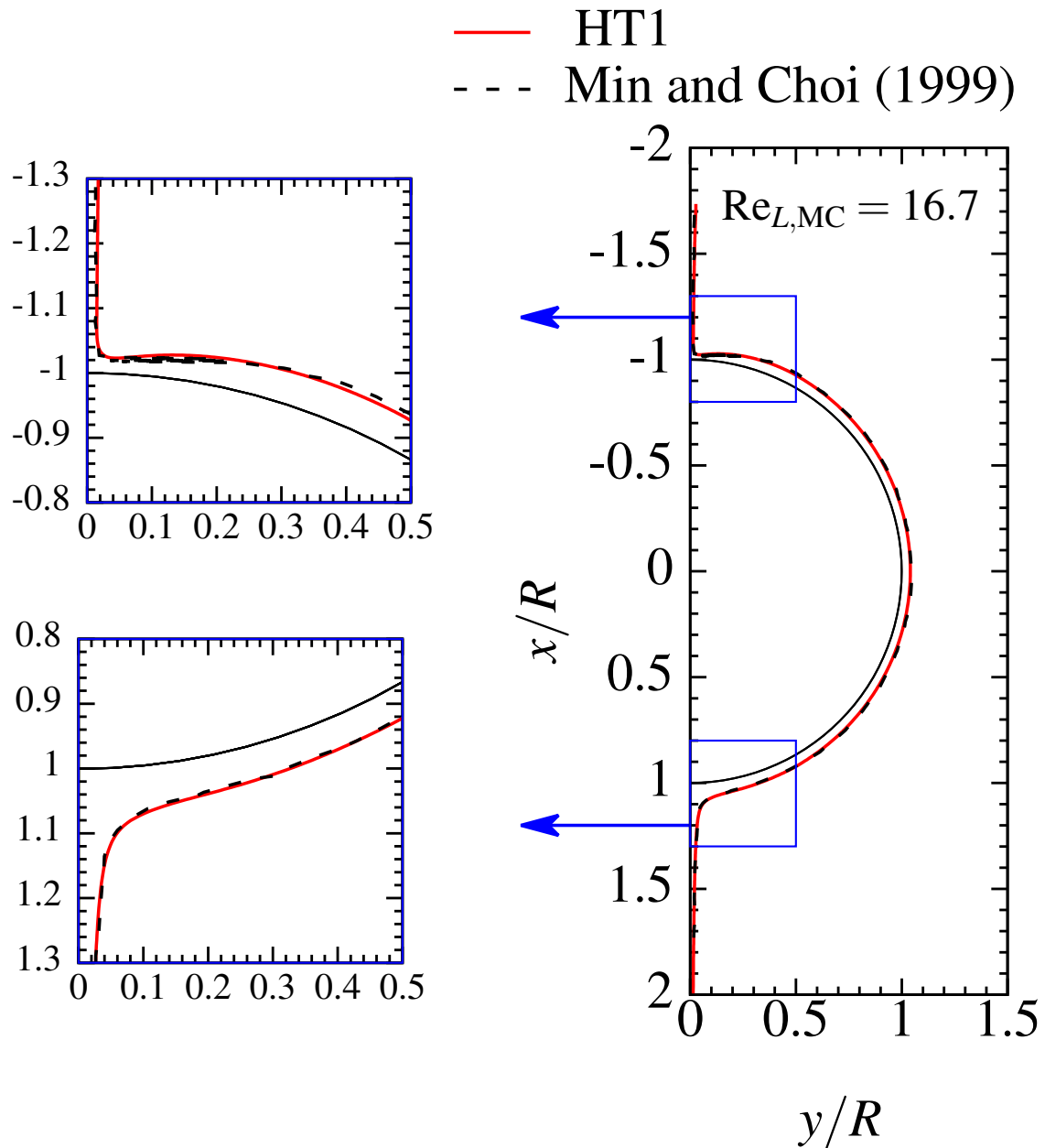


Figure 7.2: Liquid falling film shape around the tube for Case HT1 and Min and Choi [24].

the interface the LiBr mass fraction drops sharply due to the absorption of water at the interface. As the LiBr solution flows over the tube, the interface LiBr mass fraction decreases and more water is diffused to the liquid film resulting a decrease in ξ_{LiBr} close to $r_{\theta}^* = 0.9$ at $\theta = 45^\circ$. The change

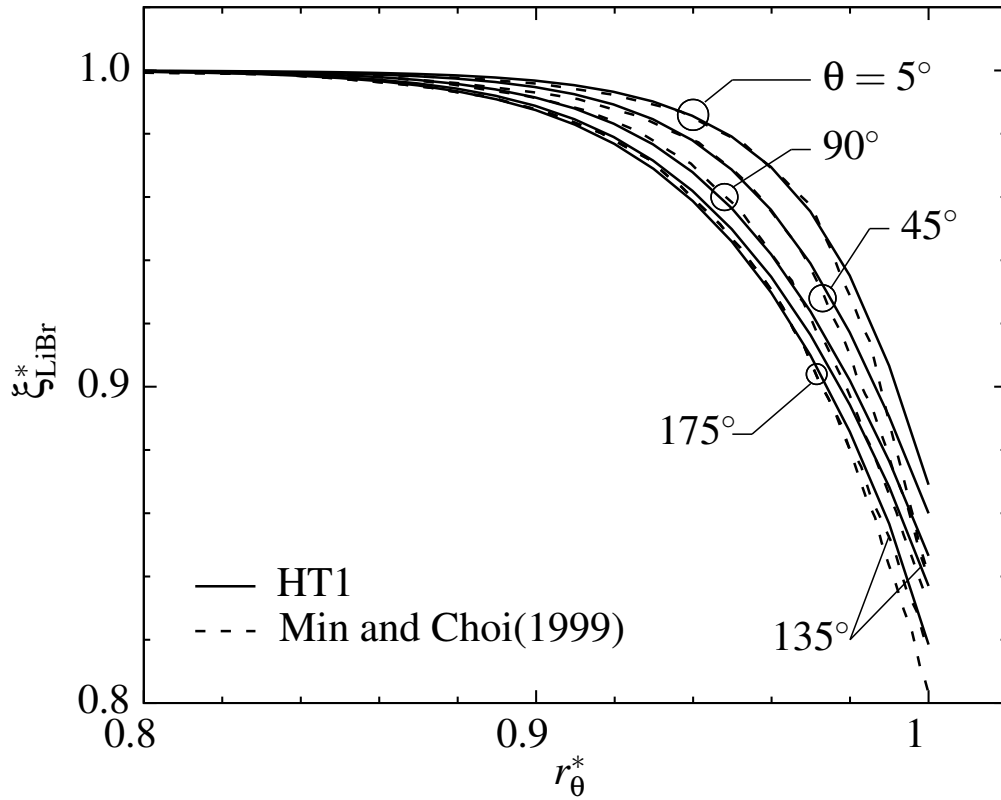


Figure 7.3: Comparison of LiBr mass fraction distribution in the liquid film for Case HT1 with Min and Choi [24].

in the LiBr mass fraction between $r_\theta^* = 0.95$ and $r_\theta^* = 1$ is more noticeable in the first half of the tube profiles, i.e. between $\theta = 5^\circ$ and $\theta = 90^\circ$. Case HT1 follows more closely the development of the mass fraction profiles in Min and Choi [24] between $r_\theta^* = 0.9$ and $r_\theta^* = 0.95$. In the region closer to the interface, between $r_\theta^* = 0.95$ and $r_\theta^* = 1$, the results of Case HT1 deviate from Min and Choi [24] and the drop at the interface LiBr mass fraction becomes smaller than those of Min and Choi [24]. The difference between the results of Case HT1 and Min and Choi [24] in this region could be related to applying a different equilibrium condition and heat of absorption, H_a , at the interface. This information was not provided by Min and Choi [24].

Figure 7.4 presents the local Sherwood number for Case HT1 and Min and Choi [24]. The local Sherwood number for the liquid film around the tube is defined as follows:

$$\text{Sh} = \frac{\dot{m}''_{L,\text{intf}} R}{\rho_L D_{\text{intf}}^{AB} (\xi_{\text{LiBr},\text{in}} - \xi_{\text{LiBr}}(P, T_{\text{wall}}))} \quad (7.2)$$

where R is the tube radius. At the top stagnation point where the liquid film thins, as seen in Figure 7.2, the temperature and mass fraction gradients increase at the interface. This will lead to

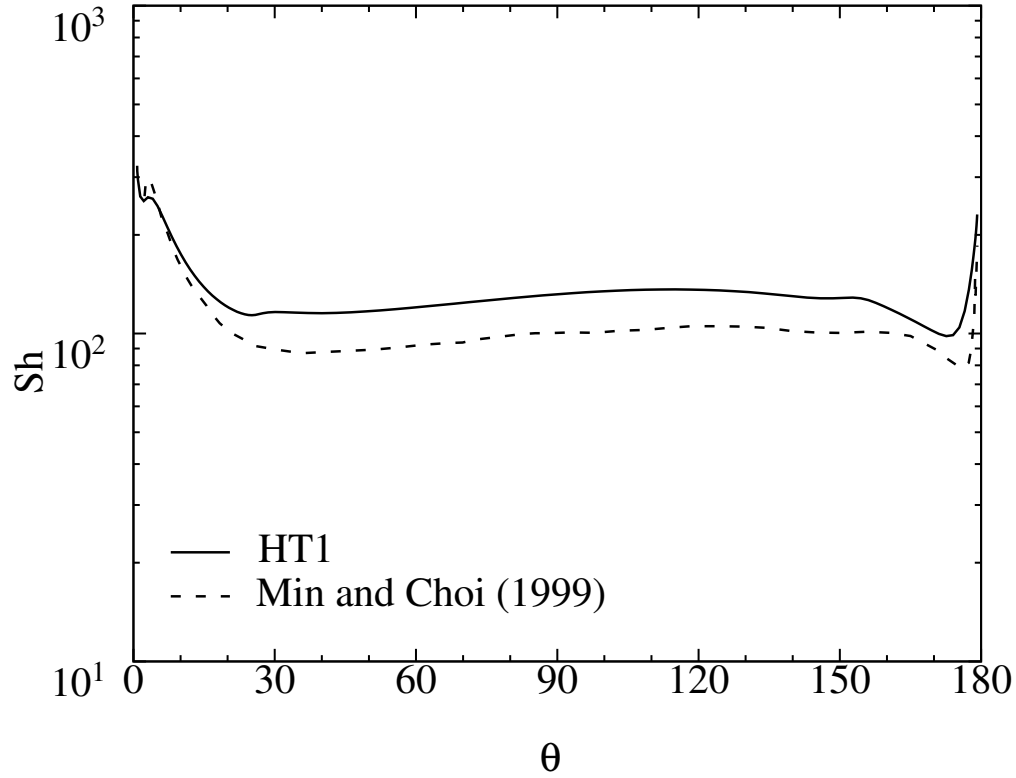


Figure 7.4: Comparison of local Sherwood number along the interface for Case HT1 with Min and Choi [24].

a higher mass absorption at the interface at $\theta = 5^\circ$ and an increase in the local Sherwood number. The thickening of the film while flowing around at the top of the tube does the opposite and the Sherwood number decreases to a smaller value at $\theta = 30^\circ$. On the side of the tube, the Sherwood number is not changed noticeably until the liquid film thickens at the bottom of the tube and the rate of mass absorption decreases. At $\theta = 175^\circ$ the Sherwood number is three times smaller compared to the top of the tube. The Sherwood number increases when the falling film thins below the

tube. Case HT1 predicts a similar trend but higher values for Sherwood number around the tube compared to Min and Choi [24].

The comparison for the local Nusselt number along the tube surface is presented in Figure 7.5.

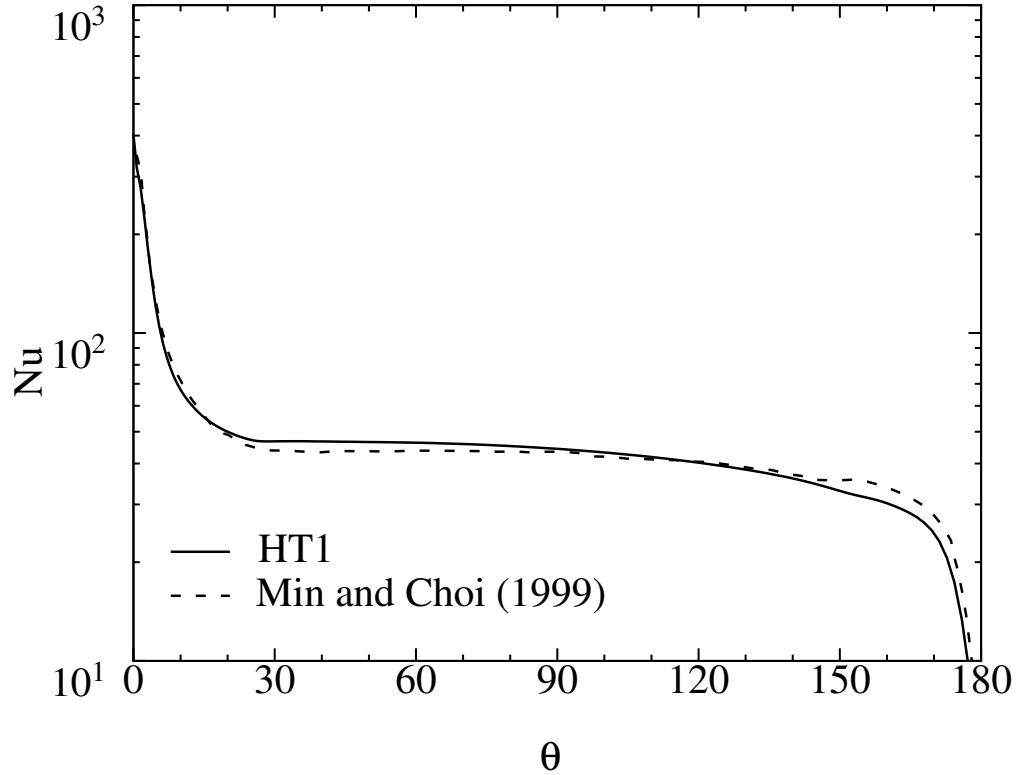


Figure 7.5: Comparison of local Nusselt number along the tube surface for Case HT1 with Min and Choi [24].

The local Nusselt number is defined as follows:

$$\text{Nu} = \frac{\dot{q}''_{\text{wall}} R}{k_L (T_{L,\text{in}} - T_{\text{wall}})} \quad (7.3)$$

Case HT1 and Min and Choi [24] predicted a similar trend for Nu variation with θ in which Nu value is maximum at the top of the tube, $\theta = 0^\circ$, and decreases toward the bottom of the tube. At $\theta = 0^\circ$, the temperature difference between the tube wall and the liquid film is at its maximum value. As the liquid film flows around the tube, more heat is transferred from the liquid film to the cold surface of the tube and the temperature of the LiBr solution decreases. The decrease in the

temperature gradient at the wall from the top of the tube to the bottom of it leads to a decrease in the wall heat flux and the local Nusselt number. Case HT1 predicted a slightly higher heat transfer to the tube wall between $\theta = 20^\circ$ and 70° .

7.3.3 Comparison Cases HT2 and HT3: Papaefthimiou et al. [28]

In order to model Cases HT2 and HT3 in Papaefthimiou et al. [28], the x - and y -direction convection and mass diffusion terms in the liquid energy equation including the partial enthalpies of the solution components were neglected. The numerical domain geometric parameters and the operating parameters in Cases HT2 and HT3 are presented in Tables 7.1 and 7.2, respectively. Constant properties from Mittermaier et al. [12] are applied to the liquid film: $\rho_L = 1.6965 \times 10^3 \text{ kg m}^{-3}$, $\mu_L = 4.4925 \times 10^{-3} \text{ kg m}^{-1} \text{ s}^{-1}$, $C_{p,L} = 1.97648 \times 10^3 \text{ J kg}^{-1} \text{ K}^{-1}$, $k_L = 4.3822 \times 10^{-1} \text{ W m}^{-1} \text{ K}^{-1}$ and $D_L^{AB} = 1.5380 \times 10^{-9} \text{ m}^2 \text{ s}^{-1}$. The equilibrium condition presented by McNeely [1] was applied to the liquid-gas interface. The variable heat of absorption, H_a , is calculated using the functions generated by curve fitting to the data sets presented in Figure 2 of Papaefthimiou et al. [28]. These functions are given in Appendix G. The tube wall boundary condition, Equation (2.41), is changed to the convection condition as follows to make Cases HT2 and HT3 closer to the cases presented in Papaefthimiou et al. [28]:

$$h(T_{\text{wall}} - T_{\text{cw}}) = k_L \left. \frac{\partial T_L}{\partial n} \right|_{\text{wall}} \quad (7.4)$$

where T_{cw} and h are the cooling water inlet temperature and the overall heat transfer coefficient between the cooling water and the tube, respectively, and n points towards the liquid film. For Cases HT2 and HT3, $T_{\text{cw}} = 30^\circ\text{C}$ as given by Papaefthimiou et al. [28]. The value for h was not given in Papaefthimiou et al. [28], so for Cases HT2 and HT3 h was estimated to be $5100 \text{ W m}^{-2} \text{ K}^{-1}$, which is a reasonable assumption for a turbulent water flow inside the tube. The constant properties (Lemmon et al. [57]) used for the gas phase in Cases HT2 and HT3 are as follows: $\rho_G = 9.0754 \times 10^{-3} \text{ kg m}^{-3}$, $\mu_G = 9.7295 \times 10^{-6} \text{ kg m}^{-1} \text{ s}^{-1}$, $C_{p,G} = 1.8790 \times 10^3 \text{ J kg}^{-1} \text{ K}^{-1}$, and $k_G = 1.8192 \times 10^{-2} \text{ W m}^{-1} \text{ K}^{-1}$.

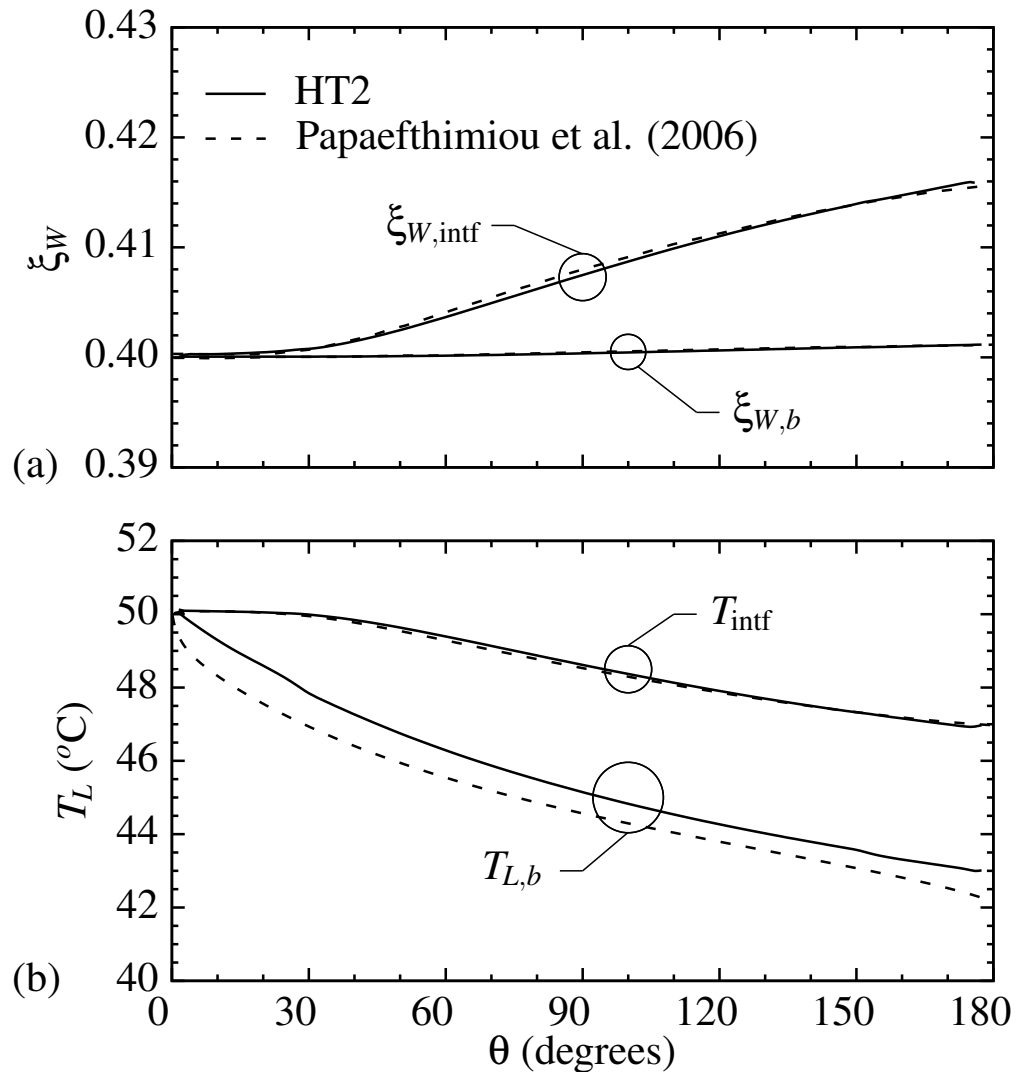


Figure 7.6: Comparison of the interface and the bulk (a) water mass fraction and (b) temperature along the flow direction for Case HT2 with Papaefthimiou et al. [28].

Figure 7.6 shows the variation of the interface and the bulk mass fraction and temperature in the flow direction in Case HT2. The liquid film reaches the tube surface at $T_L = 50^\circ\text{C}$ while absorbing water vapour at the interface. As the liquid film flows over the tube, the heat is transferred from the film to the cooling water inside the tube. The temperature at the interface decreases and according to the equilibrium condition, the water mass fraction increases at the interface. A decrease in the

interface temperature by 3°C is observed over the tube in Case HT2, whereas the bulk temperature decreased by 7°C at the bottom of the tube. In Case HT3, the tube diameter is 4 mm and the interface temperature decreases only a few degrees along the short circumference of the tube and the interface water mass fraction increases only by 3.75%. The slight change in the bulk water mass fraction shows that the water is diffused very slowly into the liquid film. The elliptic model predicts a higher bulk temperature for Case HT2 compared to Papaefthimiou et al. [28]. The discrepancy between the results could be related to the difference in the film thickness predicted by each model.

The interface and the bulk mass fraction and temperature for a film with a smaller Reynolds number are compared to Papaefthimiou et al. [28] in Figure 7.7. Case HT3 shows a larger interface temperature drop (6°C) over the tube compared to Case HT2. Similar to the interface temperature, the water mass fraction change at the interface in Case HT3 is two times more than Case HT2. The smaller film thickness and the significant decrease in the interface temperature in Case HT3 compared to Case HT2 caused a larger decrease in the bulk temperature (9.5°C) from the top to the bottom of the tube. The results of Case HT3 are close to the results produced by Papaefthimiou et al. [28].

7.3.4 Comparison Case HT4: Kyung et al. [30]

Kyung et al. [30] applied a single-phase parabolic model to a LiBr liquid film flowing over a horizontal tube. In applying the elliptic model to Case HT4, the x and y direction partial enthalpies in the liquid energy equation are neglected. The numerical domain geometric parameters and the liquid and gas inlet properties in Case HT4 are summarized in Tables 7.1 and 7.2, respectively. The following properties for the liquid film ($T_{L,\text{in}} = 47.92^{\circ}\text{C}$ and $\xi_{\text{LiBr},\text{in}} = 0.6$) were obtained from Uemura and Hasaba [2]: $\rho_L = 1.6988 \times 10^3 \text{ kg m}^{-3}$, $\mu_L = 5.2072 \times 10^{-3} \text{ kg m}^{-1} \text{ s}^{-1}$, $C_{p,L} = 1.6537 \times 10^3 \text{ J kg}^{-1} \text{ K}^{-1}$, and $k_L = 4.3174 \times 10^{-1} \text{ W m}^{-1} \text{ K}^{-1}$. The liquid diffusion coefficient was obtained from Kashiwagi [59], $D_L^{AB} = 1 \times 10^{-9} \text{ m}^2 \text{ s}^{-1}$.

The liquid inlet temperature, $T_{L,\text{in}} = 47.92^{\circ}\text{C}$, was calculated using the corrected version of Mc-

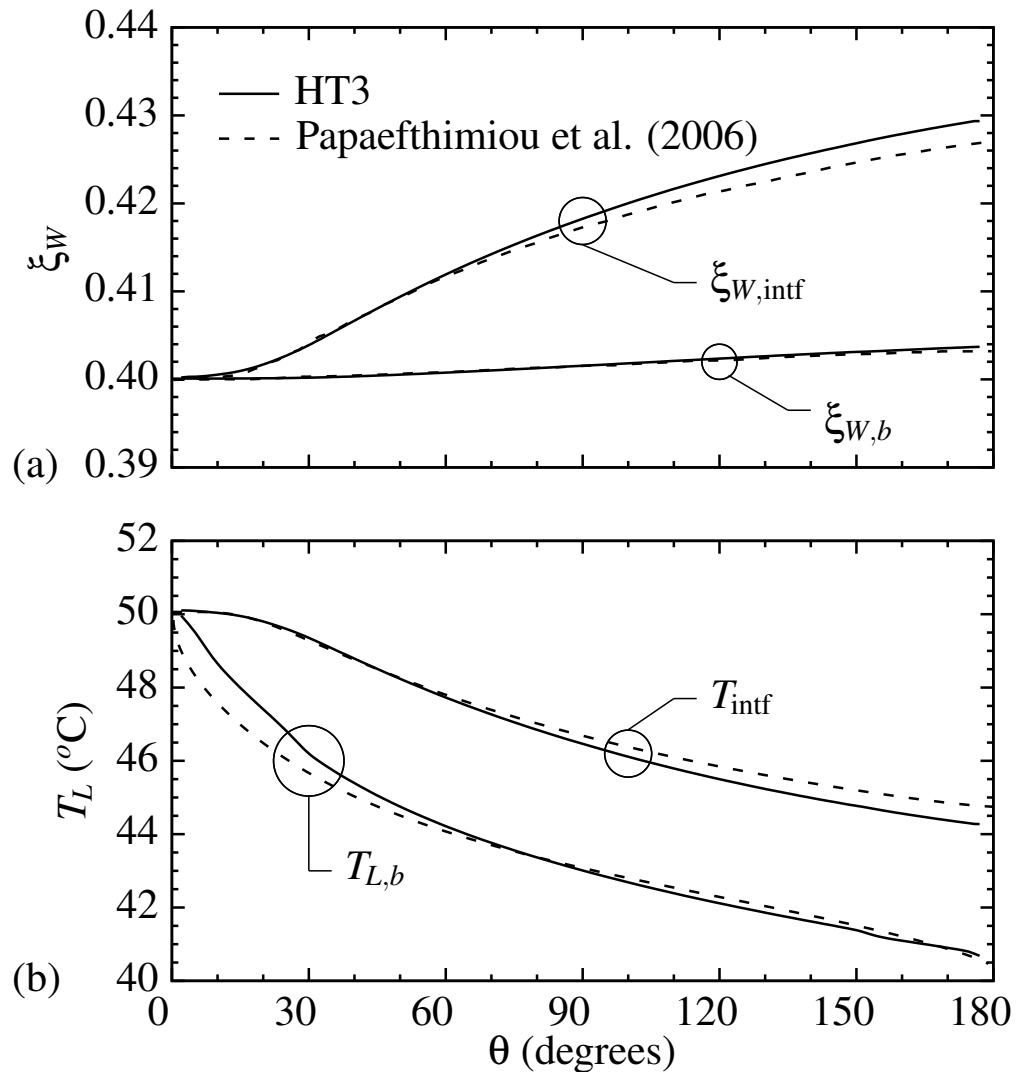


Figure 7.7: Comparison of the interface and the bulk (a) water mass fraction and (b) temperature along the flow direction for Case HT3 with Papaefthimiou et al. [28].

Neely's equilibrium condition given in Appendix A.1. The results presented by Kyung et al. [30] shows that $T_{L,in}$ is about 47°C which is closer to the temperature, $T_{L,in} = 46.94^\circ\text{C}$, obtained by the equilibrium relation presented in ASHRAE [43] (the version without the correction). The comparison Case HT4 with the corrected and uncorrected versions of McNeely's equilibrium condition applied at the interface will be referred to hereafter as Case HT4-a and Case HT4-b, respectively. A

variable heat of absorption based on Equation (2.36) by using Lemmon et al. [57] for h_v and Yuan and Herold [60] for \bar{h}_W was applied at the interface. A variable temperature was imposed as the boundary condition at the tube wall in Cases HT4-a and HT4-b to match the case presented by Kyung et al. [30]. Based on the data deduced from Figure 3 in Kyung et al. [30], a fifth order polynomial as a function of θ was used to apply the wall temperature. The wall temperature function used was:

$$T_{\text{wall}}(\theta) = -6.3667 \times 10^{-10} \theta^5 + 2.9799 \times 10^{-7} \theta^4 - 5.1603 \times 10^{-5} \theta^3 + 4.0079 \times 10^{-3} \theta^2 - 1.6089 \times 10^{-1} \theta + 39.75 \quad (7.5)$$

where θ is in degrees and T_{wall} is in $^{\circ}\text{C}$.

The constant properties used in the gas phase were: $\rho_G = 7.9875 \times 10^{-3} \text{ kg m}^{-3}$, $\mu_G = 9.7298 \times 10^{-6} \text{ kg m}^{-1} \text{ s}^{-1}$, $C_{p,G} = 1.8766 \times 10^3 \text{ J kg}^{-1} \text{ K}^{-1}$, $k_G = 1.8187 \times 10^{-2} \text{ W m}^{-1} \text{ K}^{-1}$.

The liquid film interface and bulk temperatures in Cases HT4-a and HT4-b are compared with the results of Kyung et al. [30] in Figure 7.8. The interface temperature remains almost constant until approximately 10° whereas the bulk temperature decreases noticeably in this region. This delay in the change in T_{inf} is caused by the distance needed for the cooling effect of the wall to propagate through the liquid film. Cases HT4-a and HT4-b reach the tube surface with almost 1°C temperature difference. As θ increases this difference becomes smaller and remains almost constant after 60° . A similar behaviour is observed in the bulk temperature variation in Cases HT4-a and HT4-b. The decrease in the interface and bulk temperatures occurs faster in the case of Kyung et al. [30]. Although a similar wall temperature profile to Kyung et al. [30] is applied in Cases HT4-a and HT4-b, the results presented by Kyung et al. [30] show a higher heat transfer across the film which results in a lower temperature at the interface. This might originate from the difference in the film thickness around the tube between the elliptic model and the model of Kyung et al. [30]. In case of a thicker liquid film, the effect of the cold wall is not transferred to the interface as fast as a thinner film. The larger difference between the interface and bulk temperatures in Cases HT4-a and HT4-b compared to Kyung et al. [30] corroborates the theory of thicker film in the elliptic model compared to Kyung et al. [30].

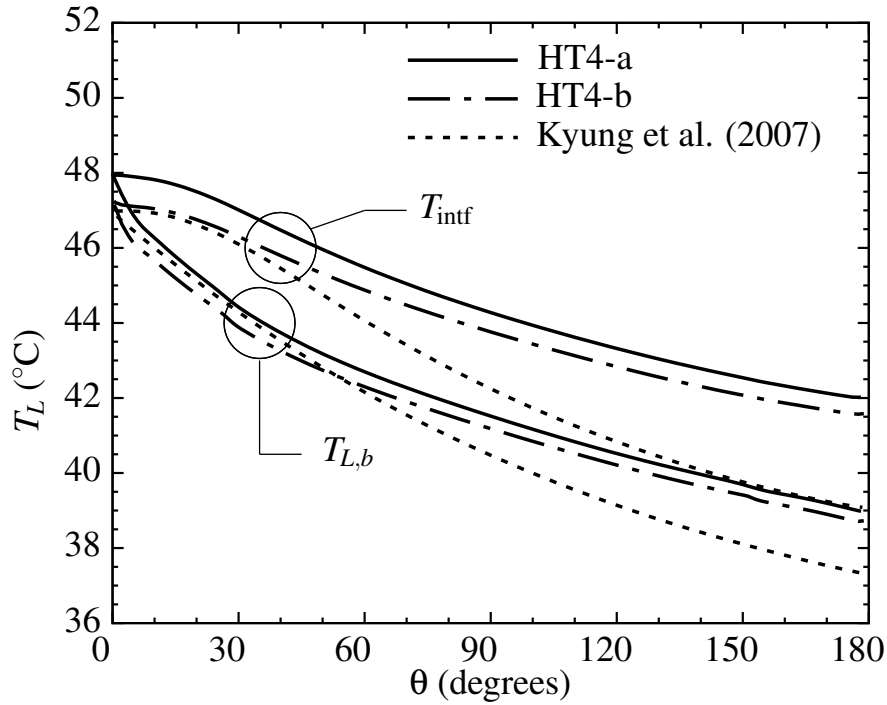


Figure 7.8: Comparison of the interface and bulk temperatures along the flow direction for Case HT4 with Kyung et al. [30].

Figure 7.9 presents the interface and bulk mass fraction in Cases HT4-a and HT4-b compared to Kyung et al. [30]. The interface water mass fraction increases with θ as more amount of water is absorbed at the interface (see Figure 7.10). The water bulk mass fraction is increased slightly from the top to the bottom of the tube because water is not diffused into the liquid film as fast as it is absorbed at the interface. Because of the difference in the interface equilibrium relation coefficients and the interface temperatures in Cases HT4-a and HT4-b, $\xi_{W,intf}$ is higher in Case HT4-a. The results of Kyung et al. [30] shows a higher increase in the interface water mass fraction over the tube.

The mass absorption rate at the interface in Cases HT4-a and HT4-b is shown in Figure 7.10. The tube wall temperature decreases from the top to the bottom of the tube due to the heat transfer from the film to the cooling water inside the tube. At the top of the tube ($0^\circ \leq \theta \leq 5^\circ$) where the

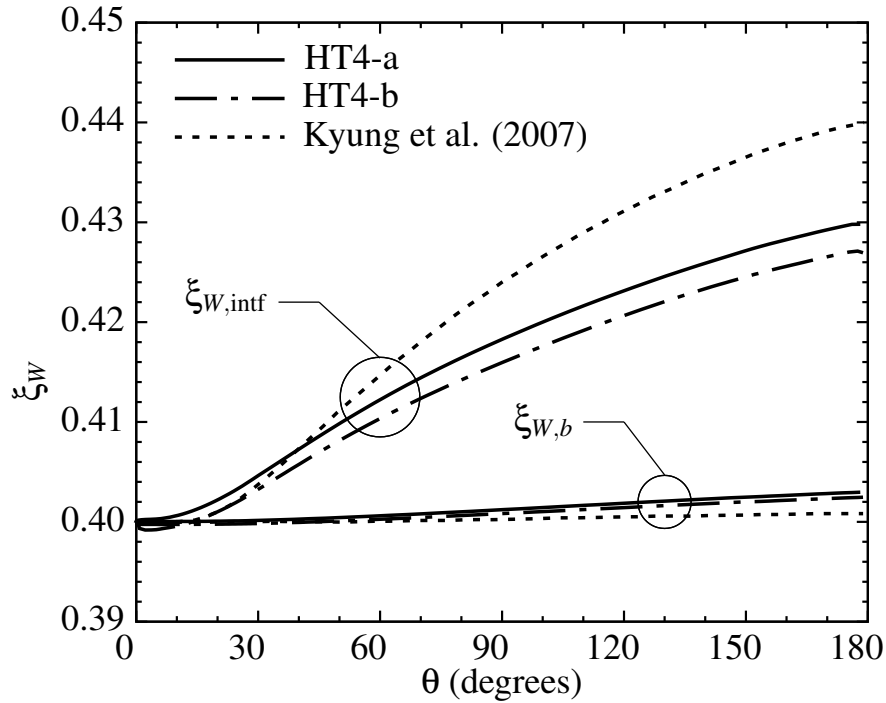


Figure 7.9: Comparison of the liquid interface and bulk mass fraction along the flow direction for Case HT4 with Kyung et al. [30].

liquid film meets the tube surface, the film becomes very thin. In this region, the mass flux at the interface becomes negative due to an adjustment of equilibrium condition that causes a reverse of the temperature gradient from the expected trend. The absorption of mass starts at the top of the tube and increases as more heat is transferred to the tube ($5^\circ \leq \theta \leq 60^\circ$). Between 60° and 150° , the water absorption rate remains almost constant. Closer to the bottom of the tube where the film thickness begins to increase, the absorption rate decreases after approximately $\theta = 150^\circ$. The elliptic model predicts a higher mass flux at the interface in comparison to Kyung et al. [30] (e.g. 217% more absorption at $\theta = 90^\circ$). The temperature difference between the interface and the tube wall is larger in Cases HT4-a and HT4-b compared to Kyung et al. [30] (see Figure 7.11 for Case HT4-b) which results in a higher interface mass flux in the elliptic model cases.

Figure 7.11 compares the temperature profiles across the liquid film for Case HT4-b

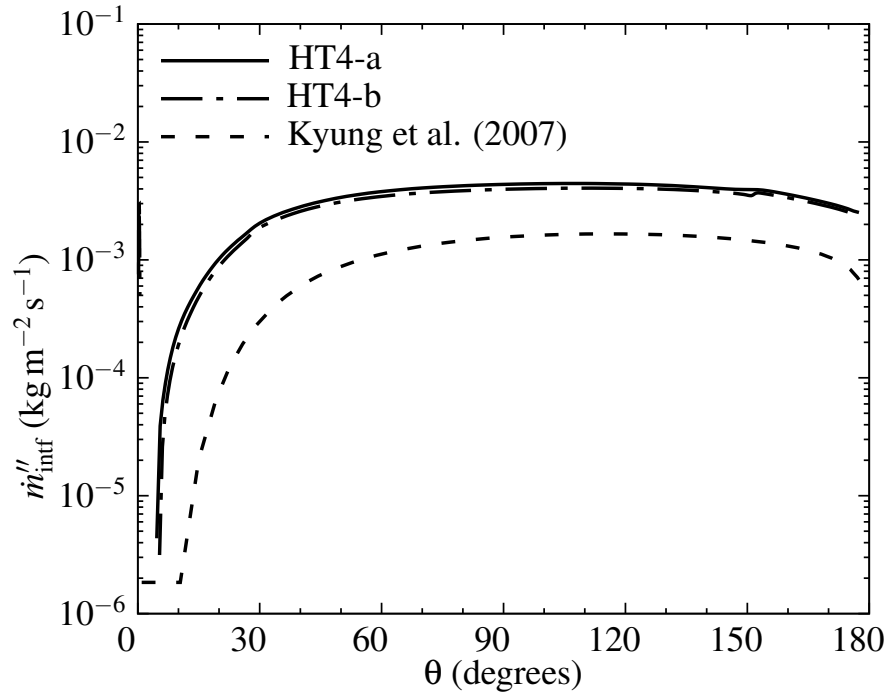


Figure 7.10: Comparison of interface mass flux along the flow direction for Case HT4 with Kyung et al. [30].

with Kyung et al. [30]. As the flow passes over the tube, the temperature decreases across the film due to heat transfer to the cooling water. At $\theta = 1^\circ$, the tube wall is at $T_{\text{wall}} = 40^\circ\text{C}$ and the temperature profile across the film is very nonlinear because the effect of the cold wall has not passed yet into the liquid film. At this point, Kyung et al. [30] model predicts a higher temperature gradient at the wall compared to the elliptic model. The decrease in the interface temperature is more noticeable after $\theta = 15^\circ$ in both models. Between $\theta = 15^\circ$ and $\theta = 45^\circ$, the temperature distribution presented by Kyung et al. [30] shows higher values. The liquid film temperature in Case HT4-b becomes larger than Kyung et al. [30] when the film passes $\theta = 90^\circ$ and flows toward the bottom of the tube. The temperature profiles are approximately linear between $\theta = 45^\circ$ and $\theta = 135^\circ$. At the bottom of the tube, $\theta = 179^\circ$, a noticeable decrease in the wall temperature causes a non-linearity in the temperature profiles in both models. This is more noticeable in Case HT4-b with the higher interface temperature. A temperature decrease of almost 8°C is observed on the

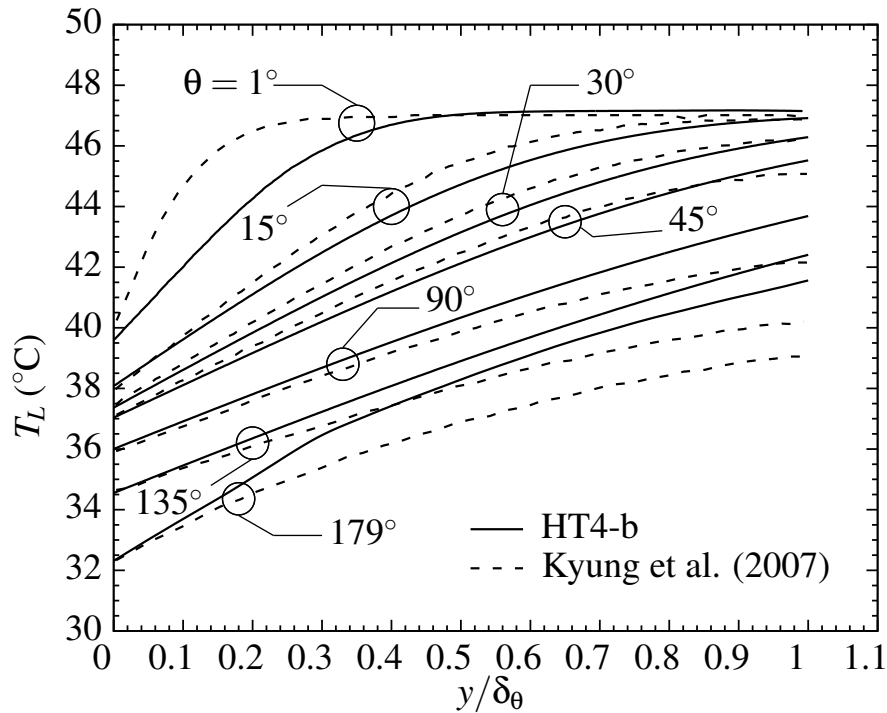


Figure 7.11: Comparison of temperature distribution in the liquid film for Case HT4 with Kyung et al. [30].

tube wall.

7.3.5 Comparison Case HT5: Seol and Lee [29]

Seol and Lee [29] used a test chamber to investigate the LiBr absorption over a horizontal tube. The concentrated LiBr solution was supplied through the nozzle array installed at the top of the horizontal tube and the water vapour was supplied to the chamber through a pair of tubes. In the test, the tube diameter and length were $d = 19.05$ mm and $L = 0.1$ m (deduced from Figure 1 in Seol and Lee [29]), respectively. A thin vertical plate was placed just below the test tube to assure sheet-drainage flow pattern at the bottom of the tube. K-type thermocouples were used to measure the LiBr solution temperature at the top of the tube and at three different points along the tube at the bottom of it. The chamber pressure was measured using a U-type mercury vacuum

manometer and a barometer.

The comprehensive form of the elliptic model including the partial enthalpies of the solution components was applied in Case HT5. The domain size and the liquid and gas flows inlet conditions are given in Table 7.1 and 7.2, respectively. The variable thermophysical properties presented by Mittermaier et al. [12] and the equilibrium relation presented by McNeely [1] were applied to the LiBr solution and the interface, respectively. The variable heat of absorption (Equation (2.36)) was obtained by using the Pátek and Klomfar [56]) function for water partial enthalpy in the LiBr solution and water vapour enthalpy from Lemmon et al. [57]. The gas phase constant properties were obtained from Lemmon et al. [57].

In Figure 7.12, the liquid film outlet temperature in Case HT5 is compared to the experimental data of Seol and Lee [29] for three different absorber pressures, i.e. $P=0.8, 1.07, \text{ and } 1.33 \text{ kPa}$. In Case HT5, the tube wall temperature is set to the average of the cooling water inlet and outlet temperatures presented in Table 2 of Seol and Lee [29]. The tube wall temperature and the liquid film inlet temperature applied to Case HT5 are presented in Table 7.3.

Table 7.3: Tube wall and liquid film inlet temperatures in Case HT5.

$P = 0.8 \text{ kPa}$		$P = 1.07 \text{ kPa}$		$P = 1.33 \text{ kPa}$	
$T_{\text{wall}} [^{\circ}\text{C}]$	$T_{L,\text{in}} [^{\circ}\text{C}]$	$T_{\text{wall}} [^{\circ}\text{C}]$	$T_{L,\text{in}} [^{\circ}\text{C}]$	$T_{\text{wall}} [^{\circ}\text{C}]$	$T_{L,\text{in}} [^{\circ}\text{C}]$
32.4	32.6	–	–	–	–
32.55	35.8	–	–	–	–
32.55	38.2	32.75	38.5	–	–
32.65	39.9	32.8	40.1	–	–
32.8	42.5	33	42.5	33.15	42.4
3.29	44.7	33.1	44.7	33.2	44.7
33	46.8	33.1	47	33.3	47.1
33	49.3	33.2	49.2	33.2	45.5

In Figure 7.12, the LiBr solution outlet temperature in Case HT5 is the liquid bulk temperature

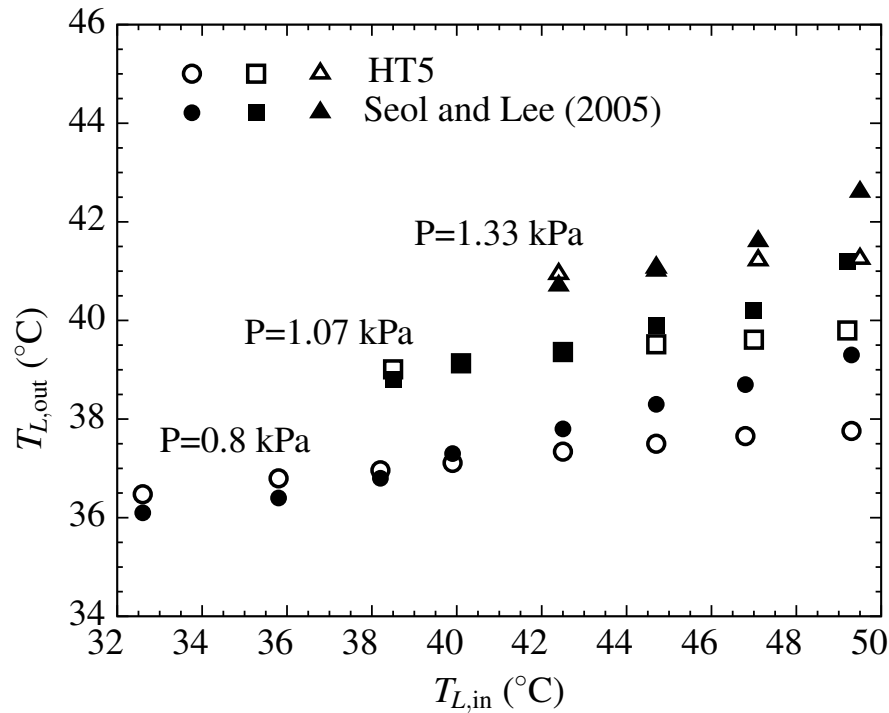


Figure 7.12: Comparison of the liquid film inlet and outlet temperature for Case HT5 with Seol and Lee [29].

calculated at 2 mm distance below the tube. As Figure 7.12 shows, the liquid film outlet temperature increases almost linearly with the solution inlet temperature at each constant pressure. When the pressure of the absorber is increased, at each almost equal tube wall and liquid inlet temperature, an increase in the liquid outlet temperature is observed. The numerical results of Case HT5 are very close to the experimental data reported by Seol and Lee [29] at lower liquid inlet temperatures at each absorber pressure. When the liquid inlet temperature increases, the numerical model predicts lower outlet temperatures for the liquid film compared to the data of Seol and Lee [29]. The liquid film outlet temperature provided by Seol and Lee [29] is the average of three outlet temperatures measured at the bottom of the tube along the tube length. In the experiment chamber, the cooling water temperature increases as it passes through the tube and receives the heat from the liquid film transferred through the tube wall. As a result, the temperature difference between

the liquid film inlet and the tube wall is lower at a longer distance from the cooling water inlet to the tube. This will lead to a higher temperature at the outlet of the liquid film. If we assume that the cooling water temperature is increasing linearly along the tube, the average of three outlet temperatures measured close to the tube inlet, in the middle of the tube, and close to the tube outlet will be higher than the outlet temperature of the the middle point (the cooling water temperature at this point is considered as the tube wall temperature in the numerical model). At higher liquid film inlet temperatures, the difference between the average outlet temperature and the middle point outlet temperature is more noticeable.

7.3.6 Summary of Comparison Cases

The numerical results of the elliptic model were compared to the elliptic model of Min and Choi [24], the single-phase parabolic approach of Papaefthimiou et al. [28] and Kyung et al. [30], and the experimental data of Seol and Lee [29]. The energy equation, the liquid properties, the tube wall temperature boundary condition, and the interface equilibrium condition were modified when required to emulate the conditions in the comparison cases. The elliptic model results were close to the numerical comparison cases and in a very good agreement with the experimental data presented by Seol and Lee [29].

7.4 New Results for the Elliptic Two-phase Absorption Over a Horizontal Tube

In this section, new results are presented to investigate the operating and geometrical parameters impact on the absorption of water vapour into the LiBr liquid film flowing over a horizontal tube. The effect of the liquid film inlet temperature and the tube wall temperature difference, $\Delta T = T_{L,in} - T_{wall}$, the liquid film inlet Reynolds number, $Re_{L,in}$, the tube diameter, d , and the transverse pitch

between the tubes, S_T/d , are studied in detail. These parameters were specified as $\Delta T = [5 \text{ K}, 10 \text{ K}]$, $\text{Re}_{L,\text{in}} = [20, 40, 80]$, $d = [12.7 \text{ mm}, 19.05 \text{ mm}, 28.575]$, and $S_T/d = [3, 6, 9]$. The computational domain size before and after the tube are $L_1 = d$ and $L_2 = 5d$, respectively. These upstream and downstream lengths were sufficient to investigate the falling film before and after the tube and satisfy the domain outlet boundary conditions in the liquid and gas phases. A sufficient number of grid cells were allocated in the x and y directions as shown in Table 7.4 to ensure the grid independence based on the grid examination explained in Section 7.2. In the parametric study cases, the liquid inlet mass fraction and pressure are $\xi_{W,\text{in}} = 0.4$ and $P_{L,\text{in}} = 1 \text{ kPa}$, respectively. The equilibrium temperature consistent with the Mittermaier et al. [12] equilibrium condition at the inlet mass fraction and pressure is $T = 44.368^\circ\text{C}$ which leads to a subcooling of $\Delta T_{\text{sub}} = 9.368 \text{ K}$ and 4.368 K for cases with $T_{L,\text{in}} = 35^\circ\text{C}$ and 40°C , respectively. The tube wall temperature is $T_{\text{wall}} = 30^\circ\text{C}$. Water vapour enters the computational domain (gas phase) at a uniform velocity with $\text{Re}_{G,\text{in}} = 20$ and $T_{G,\text{in}} = 20^\circ\text{C}$. It was assumed that the liquid film falling velocity at the entrance of the domain is $U_{L,\text{in}} = 0.23 \text{ m s}^{-1}$. The liquid film thickness at the inlet was calculated by using the liquid film properties at the inlet conditions and the liquid inlet Reynolds number. The Froude numbers for the parametric study cases are presented in Table 7.5. The variable thermophysical properties and the equilibrium relation presented by Mittermaier et al. [12] were applied to the LiBr solution and the interface, respectively. Partial enthalpies of the LiBr solution components were calculated based on the Pátek and Klomfar [56] function to be applied to the liquid energy equation and the variable heat of absorption (Equation (2.36)) at the interface. The gas phase constant properties evaluated at the the inlet conditions are given in Lemmon et al. [57]. The surface tension effect at the interface was neglected in parametric study cases.

In the figures presented in this section, the following values were used to plot dimensionless quantities: $\dot{m}''_{L,\text{in}} = 3.823 \times 10^2 \text{ kg m}^{-2} \text{ s}^{-1}$ and $3.585 \times 10^2 \text{ kg m}^{-2} \text{ s}^{-1}$ in cases with $\Delta T = 5 \text{ K}$ and 10 K , respectively, $U_{L,\text{in}} = 0.23 \text{ m s}^{-1}$, and $U_{G,\text{in}} = 1.35 \text{ m s}^{-1}$.

Table 7.4: Number of nodes in the x and y direction in parametric study cases*.

	$d = 1/2$ [in] (12.7 [mm])			$d = 3/4$ [in] (19.05 [mm])			$d = 1 1/8$ [in] (28.575 [mm])		
	N_x	$N_{y,L}$	$N_{y,G}$	N_x	$N_{y,L}$	$N_{y,G}$	N_x	$N_{y,L}$	$N_{y,G}$
$S_T/d = 3$	590	50	60	800	50	70	940	50	80
$S_T/d = 6$	590	50	90	800	50	110	940	50	130
$S_T/d = 9$	590	50	110	800	50	140	940	50	190

* In cases with $Re_{L,in} = 80$, $N_{y,L}$ is 60.

7.4.1 Effect of changing ΔT and $Re_{L,in}$

To investigate the effect of the liquid-wall temperature difference and the film inlet Reynolds number, the liquid film thickness, the film shape before and after the tube, and the interface parameters variation were studied for the selected tube diameters. The y direction distance between the tubes is $S_T/d = 6$ for the cases presented in this section.

Figure 7.13 shows the liquid film thickness variation around the tube, $d = 12.7$ mm, for cases with $\Delta T = 5$ K and 10 K and $Re_{L,in} = 20, 40$, and 80. δ_θ is the film thickness in the radial direction (normal to the tube surface). According to the definition of δ_θ , $\delta_\theta \rightarrow \infty$ at the top and bottom of the tube where $\theta \rightarrow 0$ and 180, respectively (Figure 7.1). As the liquid film reaches the top of the tube, the film thins over a certain section before thickening rapidly as the film flows over the top of the tube. This increase in the film thickness happens earlier for the film with the smaller $Re_{L,in}$, at $\theta \approx 2^\circ, 3^\circ$, and 5° for $Re_{L,in} = 20, 40$, and 80, respectively. After reaching a maximum value, the film thickness decreases when the liquid film passes $\theta \approx 11^\circ, 25^\circ$, and 45° in the cases with $Re_{L,in} = 20, 40$, and 80, respectively. At $\theta = 90^\circ$, δ_θ for $Re_{L,in} = 80$ is 1.3 and 1.6 times thicker than $Re_{L,in} = 40$ and 20 when $\Delta T = 5$ K and 1.25 and 1.58 times thicker than $Re_{L,in} = 40$ and 20 when $\Delta T = 10$ K. After $\theta = 90^\circ$, the film thickens slightly before reaching the bottom of the tube. The

Table 7.5: Froude number for the parametric study cases.

	$Re_{L,in}$	ΔT [K]	$d = 1/2$ [in] (12.7 [mm])	$d = 3/4$ [in] (19.05 [mm])	$d = 1 1/8$ [in] (28.575 [mm])
$S_T/d = 3$	20	5	66.47	66.47	66.47
		10	66.47	66.47	66.47
	40	5	33.23	33.23	33.23
		10	33.23	33.23	33.23
	80	5	16.62	16.62	16.62
		10	16.62	16.62	16.62
$S_T/d = 6$	20	5	66.47	66.47	66.47
		10	66.47	66.47	66.47
	40	5	33.23	33.23	33.23
		10	33.23	33.23	33.23
	80	5	16.62	16.62	16.62
		10	16.62	16.62	16.62
$S_T/d = 9$	20	5	66.47	66.47	66.47
		10	66.47	66.47	66.47
	40	5	33.23	33.23	33.23
		10	33.23	33.23	33.23
	80	5	16.62	16.62	16.62
		10	16.62	16.62	16.62

film transitions to a falling film at $\theta \approx 170^\circ$ and δ_θ increases at a greater rate and goes to ∞ . The transition to a falling film in $Re_{L,in} = 80$ happens before $Re_{L,in} = 40$ and 20. The cases with $\Delta T = 5$ K and 10 K show similar trends in variation of the film thickness. The film thickness difference between $\Delta T = 5$ K and 10 K is more noticeable between $\theta = 30^\circ$ and 150° where a maximum of 6.3%, 3.2%, and 3% difference is observed for $Re_{L,in} = 80, 40,$ and 20, respectively.

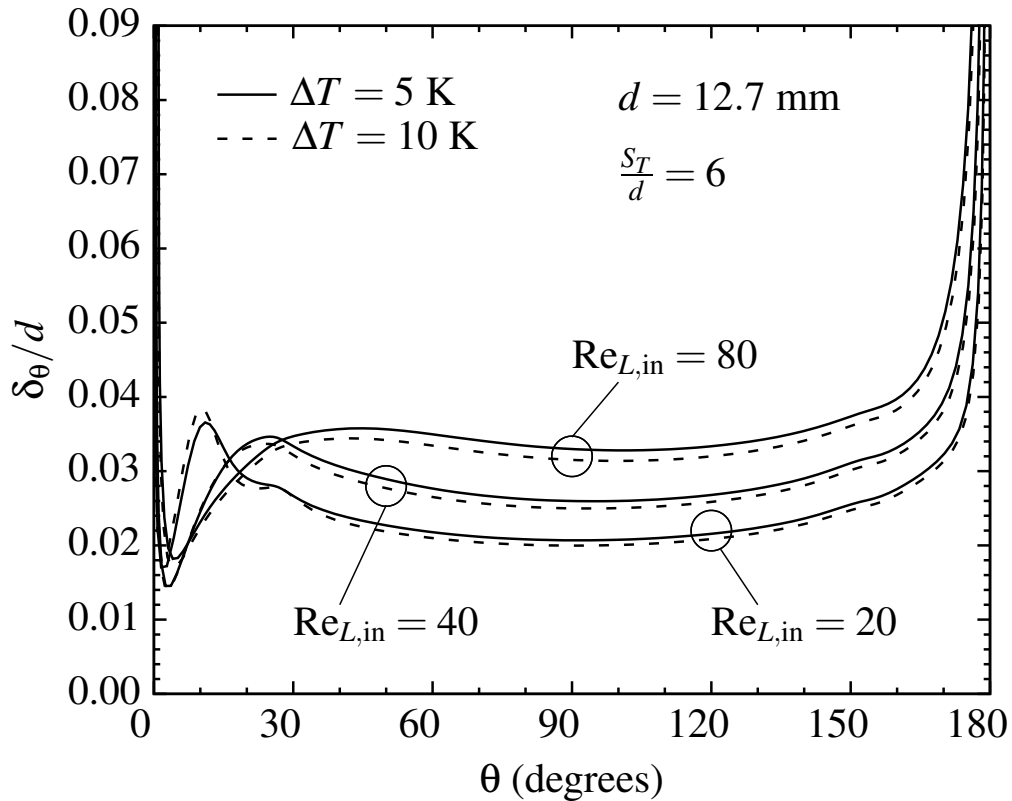


Figure 7.13: Variation of the liquid film thickness around the tube with ΔT for $Re_{L,in} = [20, 40, 80]$, $S_T/d = 6$, and $d = 12.7$ mm.

The liquid film shape at the top and bottom of the tube, $d=12.7$ mm, for cases with $\Delta T = 5$ K and 10 K and $Re_{L,in} = 20, 40,$ and 80 is shown in Figure 7.14. At the tube top stagnation point where the falling liquid film meets the tube surface, the film velocity is very small. The liquid film with the smaller mass flow rate, $Re_{L,in} = 20$, becomes very thin at this point. Coming out of this resting position, the liquid film needs to accelerate. However, the liquid-solid friction

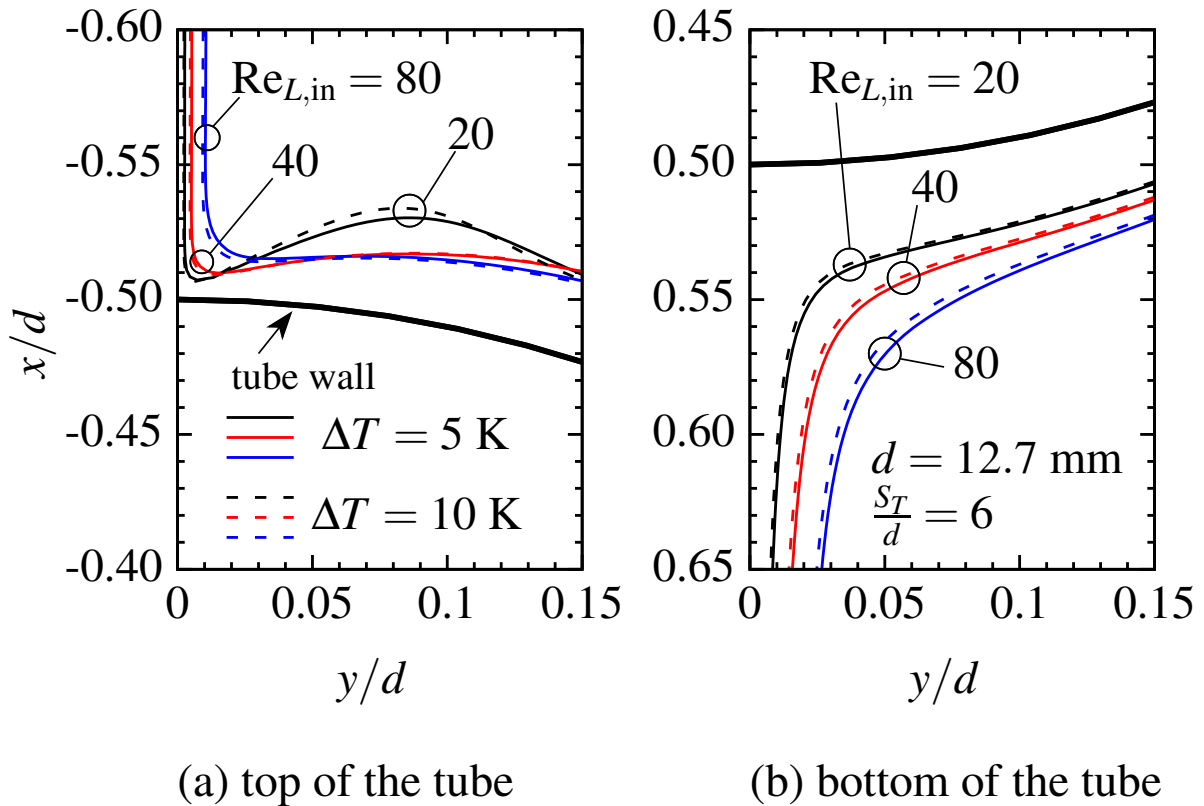


Figure 7.14: Change of the liquid film shape at the top and bottom of the tube with ΔT for $Re_{L,in} = [20, 40, 80]$, $S_T/d = 6$, and $d = 12.7$ mm.

acting on the film holds the flow back and the film starts thickening. This increase in the film thickness is considerably more in $Re_{L,in} = 20$ which experiences more friction force at the wall. The cases with $\Delta T = 5$ K and 10 K exhibit similar shapes at the top of the tube for each Reynolds number. The case with $Re_{L,in} = 20$ and $\Delta T = 10$ K produces a slightly thicker film than $\Delta T = 5$ K at $0.05 \leq y/d \leq 0.1$. At the bottom of the tube, the film with the lower $Re_{L,in}$ stays longer at the tube surface before changing to a falling film. The liquid film thickness in the y direction at the bottom of the tube ($x/d = 0.57$) for $Re_{L,in} = 80$ and $\Delta T = 5$ K is 1.83 and 3.6 times thicker than $Re_{L,in} = 40$ and 20 with the same ΔT , respectively. The film is slightly thinner for $\Delta T = 10$ K compared to $\Delta T = 5$ K at the bottom of the tube. This very small difference is more noticeable for $Re_{L,in} = 80$.

The variation of the interface mass fraction and temperature over the tube, $d = 12.7$ mm, for

cases with $\Delta T = 5$ K and 10 K and $Re_{L,in} = 20, 40,$ and 80 is presented in Figure 7.15 (a) and (b), respectively. The non-dimensional temperature, T^* , is defined as follows:

$$T^* = \frac{T - T_{wall}}{T_{L,in} - T_{wall}} = \frac{T - T_{wall}}{\Delta T} \quad (7.6)$$

As mentioned in Section 7.4, the liquid film enters the domain with subcooling, i.e. $\Delta T_{sub} = 9.368$ K for $\Delta T = 5$ K and $\Delta T_{sub} = 4.368$ K for $\Delta T = 10$ K. Because of subcooling, the solution to the energy balance and equilibrium relation at the interface produces a new equilibrium combination of temperature and mass fraction at the interface, e.g., $T_{intf} = 39.83^\circ\text{C}$ and $\xi_{W,intf} = 0.425$ in the case with $\Delta T = 5$ K and $Re_{L,in} = 20$ and $T_{intf} = 42.23^\circ\text{C}$ and $\xi_{W,intf} = 0.411$ in the case with $\Delta T = 10$ K and $Re_{L,in} = 20$. The subcooling also causes a relatively more initial water absorption at the inlet which facilitates the increase in $\xi_{W,intf}$ at that point. At the top of the tube, at $\theta = 1^\circ$, the cases with $\Delta T = 5$ K (larger subcooling at the inlet) show a larger water mass fraction and smaller temperature (larger T^*) at the interface. At this point, $\xi_{W,intf}$ of $Re_{L,in} = 20$ is noticeably smaller than the two larger Re numbers in both $\Delta T = 5$ K and 10 K. The difference between T_{intf}^* in $Re_{L,in} = 20$ and 80 is considerably larger in $\Delta T = 5$ K than $\Delta T = 10$ K at $\theta = 1^\circ$. When the LiBr solution reaches the bottom of the tube, $\xi_{W,intf}$ is increased by 2.17% and 0.48% for $Re_{L,in} = 20$ and 40 with $\Delta T = 5$ K, respectively and by 4.18% and 1.22% for $Re_{L,in} = 20$ and 40 with $\Delta T = 10$ K, respectively. The increase in $\xi_{W,intf}$ causes a decrease in T_{intf}^* according to equilibrium condition. The interface mass fraction and temperature remains almost constant over the tube for $Re_{L,in} = 80$ with $\Delta T = 5$ K and 10 K.

Figure 7.16 shows the variation of the local Nusselt number and the dimensionless rate of absorption around the tube, $d = 12.7$ mm, for cases with $\Delta T = 5$ K and 10 K and $Re_{L,in} = 20, 40,$ and 80. The local Nusselt number, Nu, is defined as follows:

$$Nu = \frac{\dot{q}''_{wall} d}{k_L (T_{L,in} - T_{wall})} \quad (7.7)$$

The wall heat flux is the highest at the top of the tube and decreases along the circumference of the tube. This trend can be explained by the decrease in the liquid-wall temperature difference

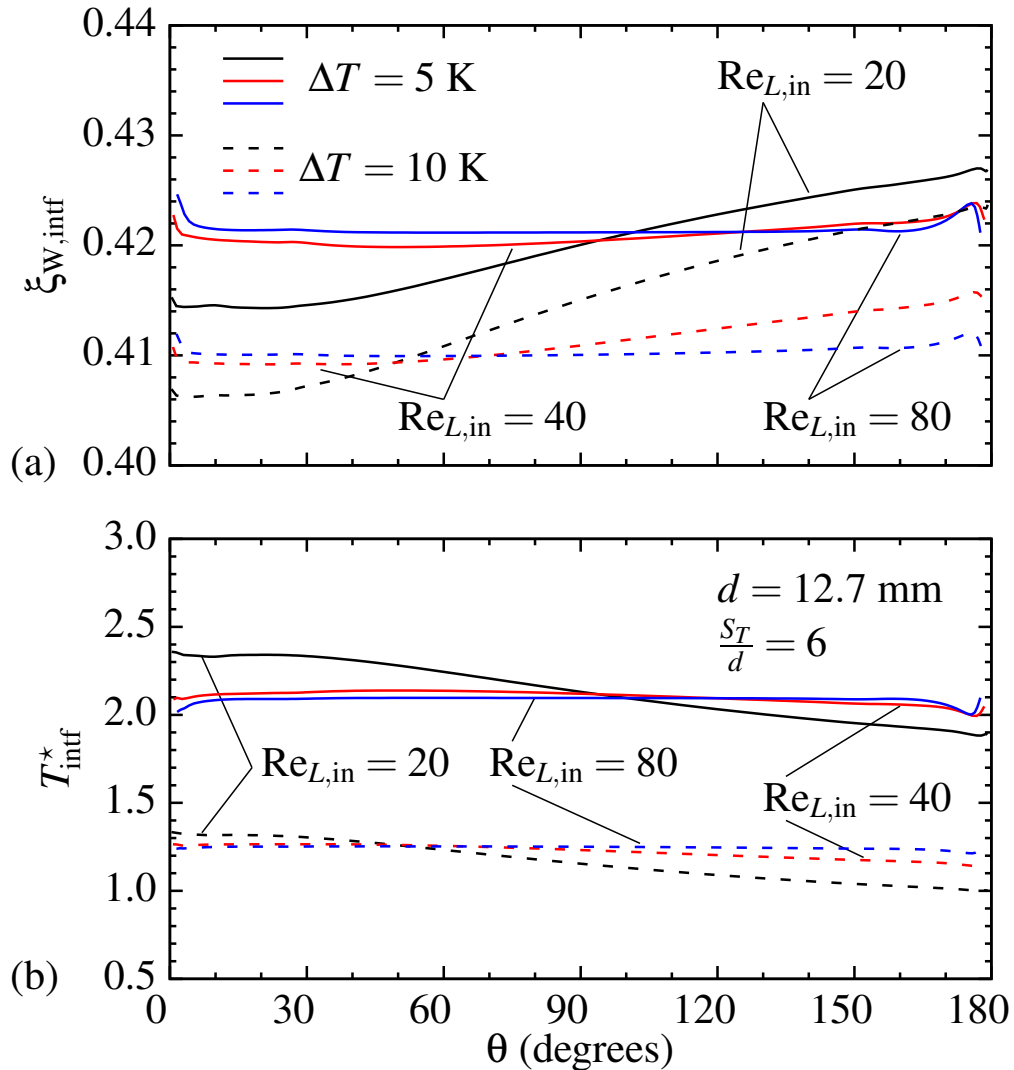


Figure 7.15: Variation around the tube of (a) interface mass fraction and (b) interface dimensionless temperature for $\Delta T = [5 \text{ K}, 10 \text{ K}]$ and $\text{Re}_{L,\text{in}} = [20, 40, 80]$ with $S_T/d = 6$ and $d = 12.7$ mm.

as the liquid film flows over the tube and transfers more energy to the colder wall. In cases with $\text{Re}_{L,\text{in}} = 20$, the Nu number decreases to a minimum at $\theta \approx 12^\circ$ where the liquid film thickness shows a maximum value (see Figure 7.13). Over the range $30^\circ \leq \theta \leq 150^\circ$, Nu decreases slowly. The sudden drop in Nu as θ approaches 180° is due to the rapid thickening of the film at the bottom of the tube as it transitions to a vertical falling film and the increase in the thermal resistance

across the film. The differences between Nusselt numbers at different Reynolds numbers are more noticeable in cases with $\Delta T = 5$ K. Figure 7.16 (b) shows the dimensionless absorption mass flux at the interface. A decrease in the absorption of mass is observed at the top of the tube in all the cases. The liquid films with $\Delta T = 5$ K absorb greater amount of mass at the initial part of the tube compared to the cases with $\Delta T = 10$ K. This trend changes differently for the Re numbers as the liquid film flows over the tube. For $\theta > 30^\circ$, more mass is absorbed by the case with $\Delta T = 10$ K compared to $\Delta T = 5$ K for $Re_{L,in} = 20$. The mass absorption rate in the case with $Re_{L,in} = 40$ and $\Delta T = 10$ K increases rapidly up to $\theta = 120^\circ$ and remains as large as $\Delta T = 5$ K until the flow reaches the bottom of the tube. At $Re_{L,in} = 80$, the absorbed mass in $\Delta T = 5$ K is considerably greater than $\Delta T = 10$ K over the tube circumference. When the film approaches the falling region ($\theta = 170^\circ$), the interface mass flux increases and a thicker film is formed at this region.

Figure 7.17 shows the liquid film thickness variation around the tube, $d = 19.05$ mm, for cases with $\Delta T = 5$ K and 10 K and $Re_{L,in} = 20, 40$, and 80. The radial film thickness is minimum at the top of the tube ($0^\circ \leq \theta \leq 10^\circ$) in all the cases. To flow over the top of the tube, the liquid film thickens to $\delta_\theta/d = 0.027, 0.025$, and 0.026 at $\theta = 8^\circ, 17^\circ$, and 28° in the cases with $Re_{L,in} = 20, 40$, and 80, respectively. After passing the thickening region, the film thickness decreases up to $\theta \approx 90^\circ$ while flowing over the tube. At this point, $\delta_\theta/d = 0.014, 0.017$, and 0.022 in the cases with $\Delta T = 5$ K and $Re_{L,in} = 20, 40$, and 80, respectively. In cases with $\Delta T = 10$ K, the liquid film is slightly thinner in comparison to the corresponding $\Delta T = 5$ K cases at $\theta = 90^\circ$. The liquid film thickens gradually until it starts leaving the tube surface and thickening rapidly. An increase of 57%, 59%, and 45% is observed in the film thickness from $\theta = 90^\circ$ to $\theta = 170^\circ$ in cases with $Re_{L,in} = 20, 40$, and 80, respectively.

The liquid film shape at the top and bottom of the tube, $d = 19.05$ mm, for cases with $\Delta T = 5$ K and 10 K and $Re_{L,in} = 20, 40$, and 80 is shown in Figure 7.18. The falling film of $Re_{L,in} = 20$ forms a smaller concave surface over a narrow range of θ at the top of the tube compared to the higher Reynolds numbers. This small concave changes to a significant convex interface as the film flows over the top of the tube. The liquid film shape in $Re_{L,in} = 40$ is very similar to

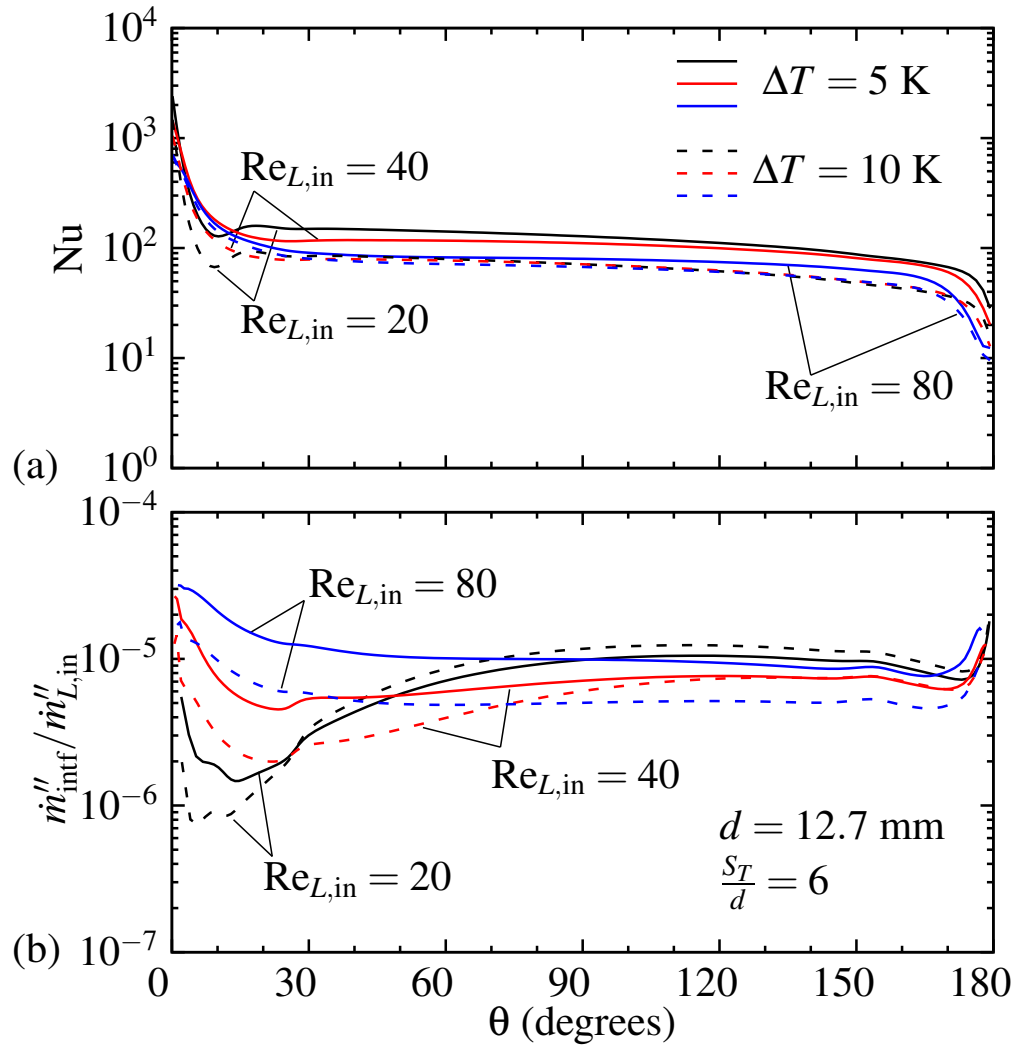


Figure 7.16: Variation around the tube of (a) local Nusselt number and (b) interface dimensionless mass flux for $\Delta T = [5 \text{ K}, 10 \text{ K}]$ and $Re_{L,in} = [20, 40, 80]$ with $S_T/d = 6$ and $d = 12.7$ mm.

$Re_{L,in} = 20$ at $0 \leq y/d \leq 0.01$, however, it thickens slower than $Re_{L,in} = 20$ over the top of the tube. The cases with $Re_{L,in} = 80$ reach the top of the tube at a larger thickness which results in a larger concave surface. The liquid film with $Re_{L,in} = 80$ thickens at a lower rate than $Re_{L,in} = 40$ at $0.05 \leq y/d \leq 0.15$. A slight difference is observed between the $Re_{L,in} = 20$ liquid film shapes in cases with $\Delta T = 5$ K and 10 K. When the liquid film reaches the bottom of the tube, the higher $Re_{L,in}$ leaves the tube surface earlier and forms a thicker falling film below the tube. The liquid

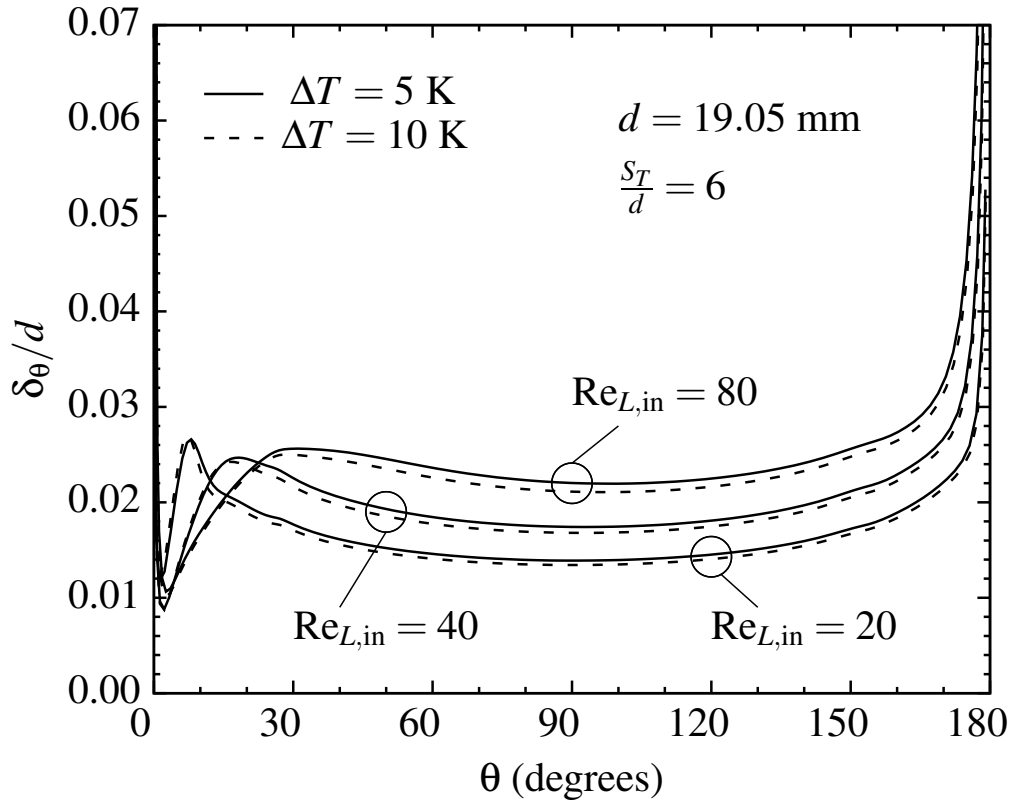
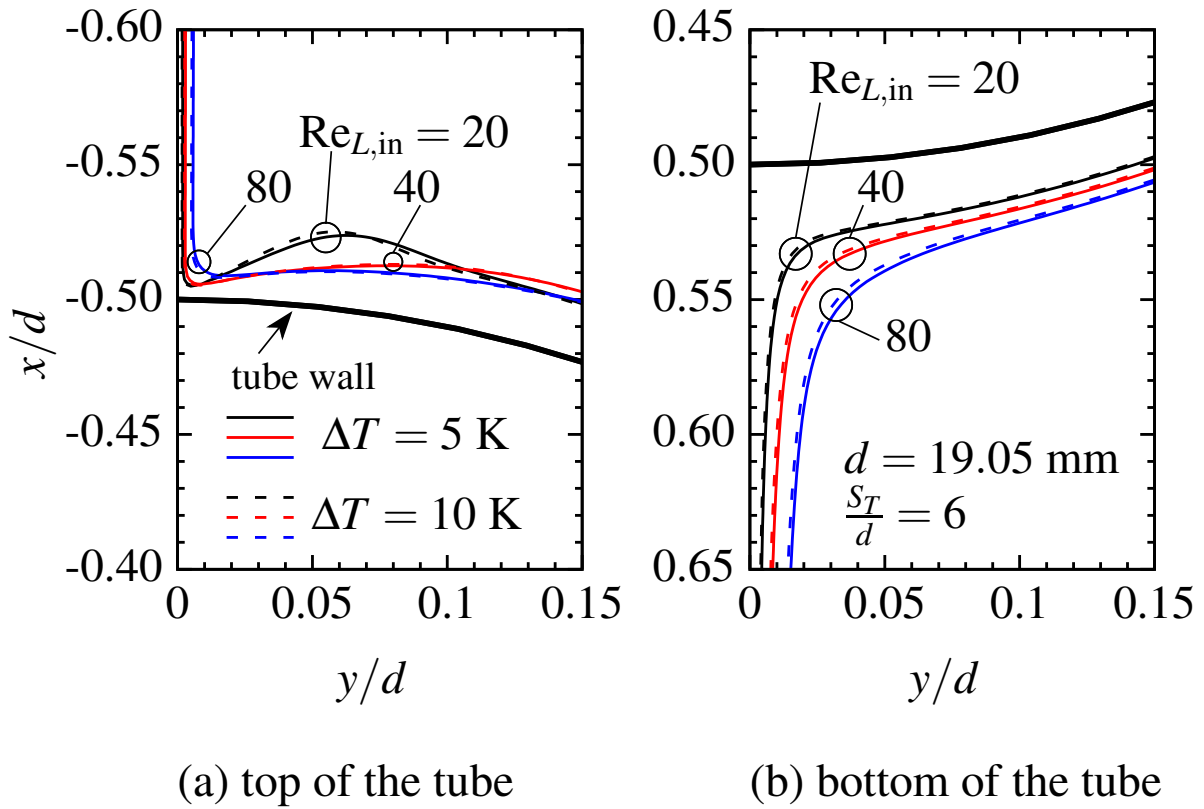


Figure 7.17: Variation of the liquid film thickness around the tube with ΔT for $\text{Re}_{L,\text{in}} = [20, 40, 80]$, $S_T/d = 6$, and $d = 19.05$ mm.

films with $\Delta T = 5$ K are slightly thicker than $\Delta T = 10$ K cases at the bottom of the tube.

The variations of the interface mass fraction and temperature over the tube, $d = 19.05$ mm, for cases with $\Delta T = 5$ K and 10 K and $\text{Re}_{L,\text{in}} = 20, 40$, and 80 are presented in Figure 7.19 (a) and (b), respectively. The liquid film with a smaller Reynolds number reaches the tube surface at a smaller $\xi_{W,\text{intf}}$ in both $\Delta T = 5$ K and 10 K cases. Consequently, according to the equilibrium relation at the interface, these cases have the highest interface temperature in each ΔT group. The change in $\xi_{W,\text{intf}}$ and T_{intf}^* at the top of the tube is more noticeable when $\text{Re}_{L,\text{in}}$ changes from 20 to 40. The interface water mass fraction increases while the liquid film flows over the tube and absorbs water vapour at the interface. The increase in $\xi_{W,\text{intf}}$ occurs more rapidly in $\text{Re}_{L,\text{in}} = 20$ cases. $\xi_{W,\text{intf}}$ of $\text{Re}_{L,\text{in}} = 20$ becomes larger than both $\text{Re}_{L,\text{in}} = 40$ and 80 at $\theta \approx 40^\circ$ and $\theta \approx 82^\circ$ in cases with



(a) top of the tube

(b) bottom of the tube

Figure 7.18: Change of the liquid film shape at the top and bottom of the tube with ΔT for $Re_{L,in} = [20, 40, 80]$, $S_T/d = 6$, and $d = 19.05$ mm.

$\Delta T = 10$ K and 5 K, respectively. At $\theta \approx 68^\circ$ in $\Delta T = 10$ K and $\theta \approx 118^\circ$ in $\Delta T = 5$ K, $\xi_{W,intf}$ of $Re_{L,in} = 40$ becomes larger than $Re_{L,in} = 80$. T_{intf}^* shows an opposite trend at the same θ values as in $\xi_{W,intf}$ figure. There is a slight change in the interface mass fraction and temperature at $Re_{L,in} = 80$ in both $\Delta T = 5$ K and 10 K over the tube.

Figure 7.20 shows the variation of the local Nusselt number and the dimensionless rate of absorption around the tube, $d = 19.05$ mm, for cases with $\Delta T = 5$ K and 10 K and $Re_{L,in} = 20, 40$, and 80. The heat transfer from the liquid film to the wall of the tube is at its maximum value at the top of the tube where the temperature difference between the wall and the film is larger. As the liquid film flows over the tube and becomes colder, the local Nu number decreases. In cases with $Re_{L,in} = 20$, Nu reaches a minimum value at $\theta \approx 8^\circ$ where the film thickens signifi-

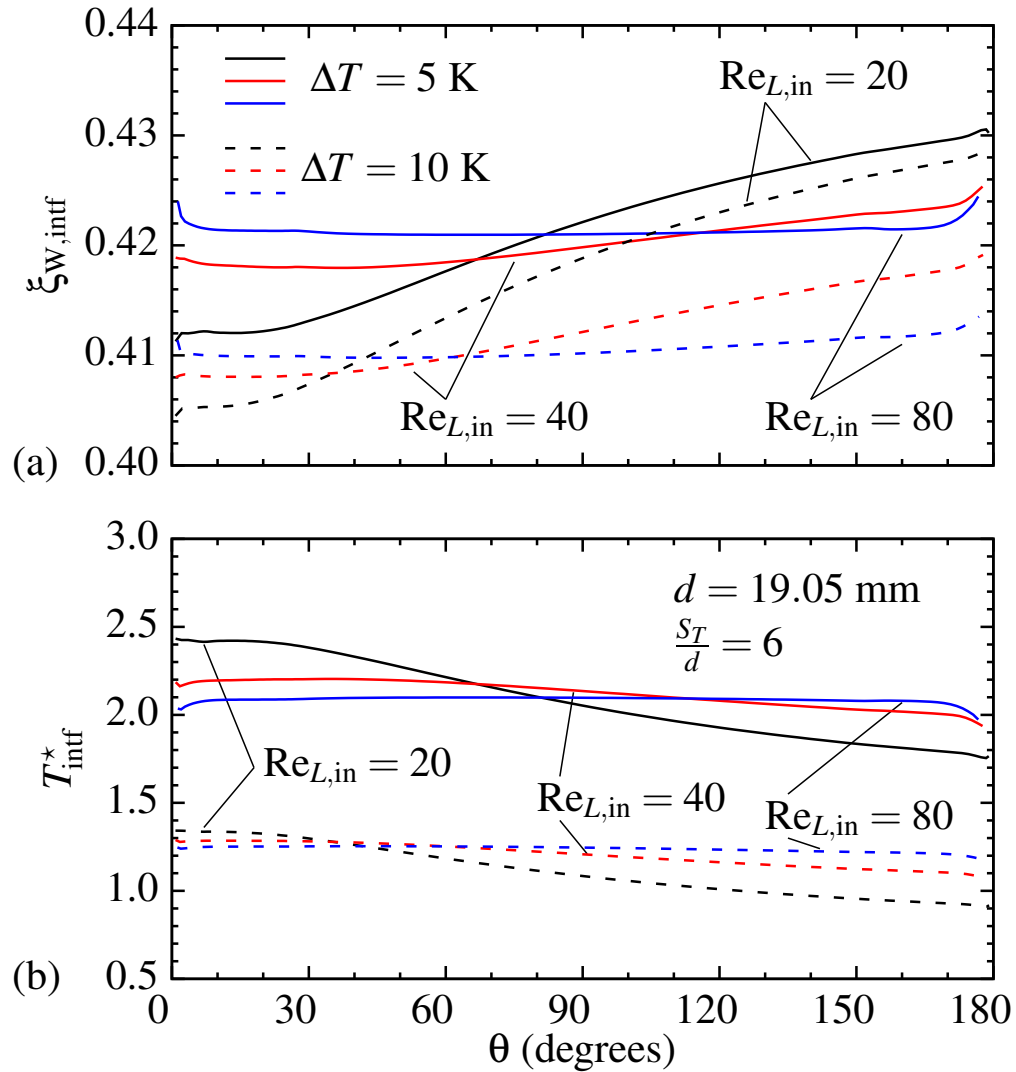


Figure 7.19: Variation around the tube of (a) interface mass fraction and (b) interface dimensionless temperature for $\Delta T = [5 \text{ K}, 10 \text{ K}]$ and $Re_{L, \text{in}} = [20, 40, 80]$ with $S_T/d = 6$ and $d = 19.05 \text{ mm}$.

cantly (see Figure 7.17). Nusselt number is higher over the tube in cases with $\Delta T = 5 \text{ K}$ compared to their counterpart cases with $\Delta T = 10 \text{ K}$. In cases with $\Delta T = 5 \text{ K}$, the lower Reynolds number shows a higher local Nu at $30^\circ < \theta < 180^\circ$, however in cases with $\Delta T = 10 \text{ K}$, the Nu values are only slightly different over that section of the tube. Figure 7.20 (b) shows that the cases with higher $Re_{L, \text{in}}$ absorb more water vapour when they reach the surface of the tube at $0^\circ < \theta < 10^\circ$. At this re-

gion, the interface mass flux is considerably higher in cases with $\Delta T = 5$ K compared to the similar cases with $\Delta T = 10$ K. As the liquid film flows over the tube ($30^\circ < \theta < 150^\circ$), the mass absorption rate in cases with $Re_{L,in} = 20$ and 40 increases gradually. In cases with $Re_{L,in} = 80$, the interface mass flux is increased slightly in $\Delta T = 10$ K and is almost constant in $\Delta T = 5$ K at $60^\circ < \theta < 150^\circ$. The mass absorption rate at the interface in cases with $\Delta T = 10$ K is more than the cases with $\Delta T = 5$ K over the most of the tube circumference (after $\theta \approx 20^\circ$ and 80° in $Re_{L,in} = 20$ and 40 , respectively). The cases with $Re_{L,in} = 80$ show an opposite behaviour. When the liquid film reaches the bottom of the tube, the mass absorption rate decreases over a small section, $160^\circ < \theta < 170^\circ$, and increases as the film leaves the tube surface.

Figure 7.21 shows the liquid film variation around the tube, $d = 28.575$ mm, for cases with $\Delta T = 5$ K and 10 K and $Re_{L,in} = 20, 40$, and 80 . The radial liquid film thickness is very small at the top of the tube where the falling film meets the tube surface ($\theta < 4^\circ$). The thickening of the film occurs at different rates for different mass flow rates at the top of the tube. The film with $Re_{L,in} = 20$ thickens faster to a larger value at $\theta \approx 6^\circ$. At this point, the case with $\Delta T = 5$ K reaches a higher maximum compared to $\Delta T = 10$ K. The primary maximum film thickness in $Re_{L,in} = 40$ and 80 occurs at $\theta \approx 14^\circ$ and 26° , respectively. After passing the initial part of the tube ($\theta \approx 30^\circ$), the film reaches its narrowest thickness at the side of the tube ($\theta \approx 90^\circ$). Over the section of $30^\circ < \theta < 170^\circ$, the cases with higher $Re_{L,in}$ form a thicker film. At each Re number, the liquid film is slightly thicker in case with $\Delta T = 5$ K compared to 10 K. δ_θ/d increases rapidly at the bottom of the tube.

The liquid film shape at the top and bottom of the tube, $d = 28.575$ mm, for cases with $\Delta T = 5$ K and 10 K and $Re_{L,in} = 20, 40$, and 80 is shown in Figure 7.22. At the top stagnation point, the liquid film with $Re_{L,in} = 20$ forms a small concave surface that changes to a bump at the interface when the film begins flowing over the top of the tube. In $Re_{L,in} = 40$ and 80 , the increase in the film thickness occurs very smoothly. At the top of the tube, the liquid films with $Re_{L,in} = 40$ are thicker than cases with $Re_{L,in} = 80$. The liquid film development at the top of the tube for cases with $\Delta T = 5$ K and 10 K are very similar at each Re number. At the bottom of the tube, the larger Re number forms a thicker liquid film. The liquid film thickness is negligibly larger in $\Delta T = 5$ K

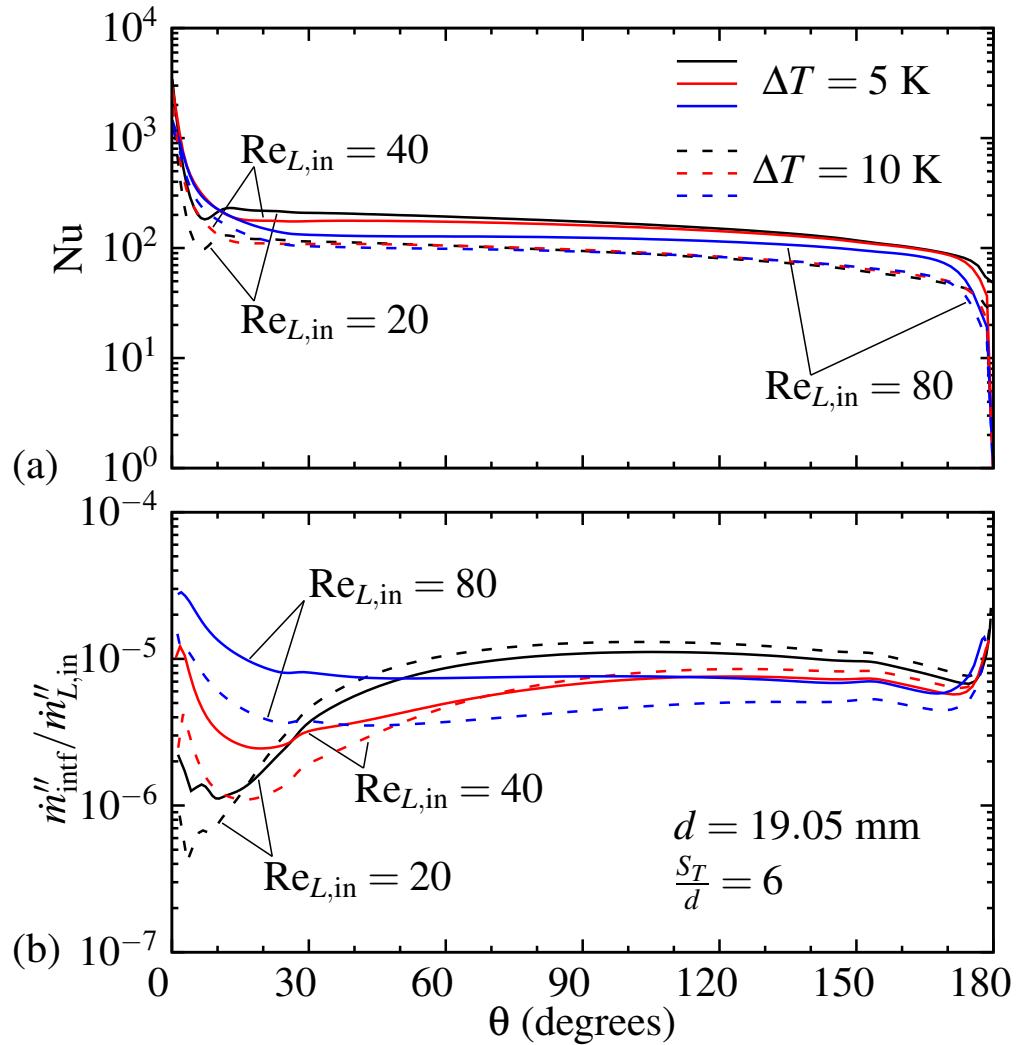


Figure 7.20: Variation around the tube of (a) local Nusselt number and (b) interface dimensionless mass flux for $\Delta T = [5 \text{ K}, 10 \text{ K}]$ and $Re_{L,in} = [20, 40, 80]$ with $S_T/d = 6$ and $d = 19.05$ mm.

cases.

The variation of the interface mass fraction and temperature over the tube, $d = 28.575$ mm, for cases with $\Delta T = 5$ K and 10 K and $Re_{L,in} = 20, 40$, and 80 is presented in Figure 7.23 (a) and (b), respectively. The liquid films with $\Delta T = 5$ K reach the top of the tube at a larger $\xi_{W,intf}$ in comparison to the similar cases with $\Delta T = 10$ K. In each ΔT group of cases, the film with the

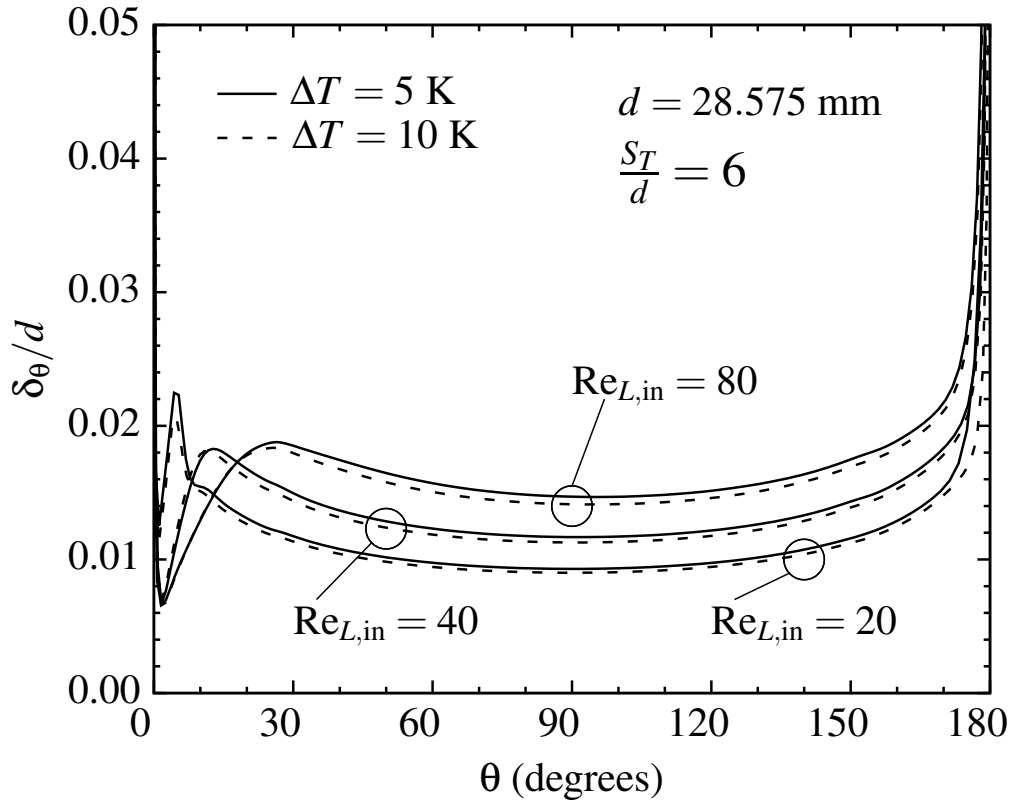


Figure 7.21: Variation of the liquid film thickness around the tube with ΔT for $Re_{L,in} = [20, 40, 80]$, $S_T/d = 6$, and $d = 28.575$ mm.

higher Re number has the larger interface water mass fraction at the top stagnation point of the tube. The absorption of water vapour at the interface results in an increase in $\xi_{W,intf}$ and consequently a decrease in T_{intf}^* because of the equilibrium condition at the interface. The increase in the interface water mass fraction over the tube with $d = 28.575$ mm for $Re_{L,in} = 20$ is 6.34% and 7.42% in cases with $\Delta T = 5$ K and 10 K, respectively. At higher Re numbers the increase in $\xi_{W,intf}$ becomes smaller, i.e., 2.64% and 3.68% for $Re_{L,in} = 40$ and only 0.47% and 1.46% for $Re_{L,in} = 80$ in cases with $\Delta T = 5$ K and 10 K, respectively. The difference in T_{intf}^* between different Reynolds numbers at $\theta = 0^\circ$ is more noticeable in cases with $\Delta T = 5$ K. Similar to $\xi_{W,intf}$, the cases with $Re_{L,in} = 20$ have the largest T_{intf}^* variation over the tube in each ΔT group of cases. T_{intf}^* decreases by 36%, 17.62%, and 5.31% in $\Delta T = 5$ K and by 39.25%, 21.54%, and 8% in $\Delta T = 10$ K over the tube for

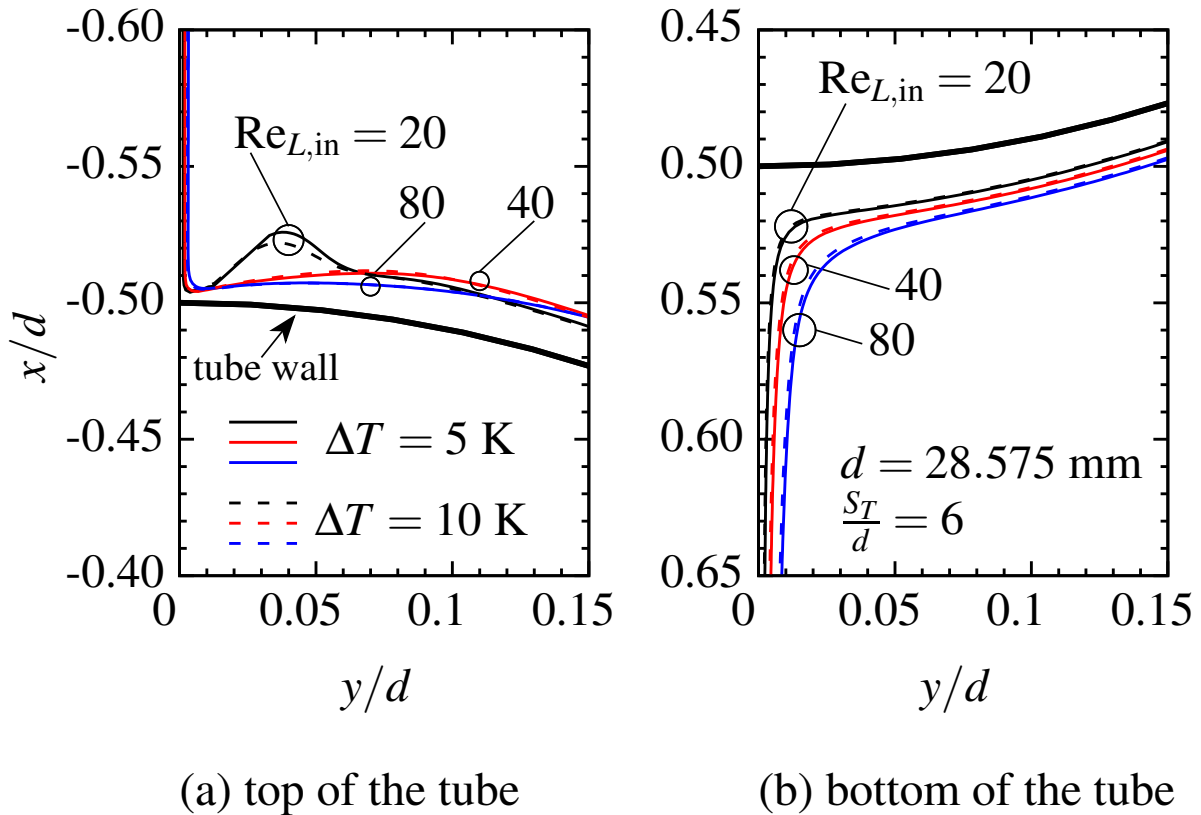


Figure 7.22: Change of the liquid film shape at the top and bottom of the tube with ΔT for $Re_{L,in} = [20, 40, 80]$, $S_T/d = 6$, and $d = 28.575$ mm.

$Re_{L,in} = 20, 40$, and 80 , respectively.

Figure 7.24 shows the variation of the local Nusselt number and the dimensionless rate of absorption around the tube, $d = 28.575$ mm, for cases with $\Delta T = 5$ K and 10 K and $Re_{L,in} = 20, 40$, and 80 . As the temperature difference between the liquid film and the tube wall decreases around the tube, smaller amount of heat is transferred to the tube wall and the local Nu number decreases. At $\theta \approx 5^\circ$, the local Nu number of $Re_{L,in} = 80$ is larger in both ΔT group cases. In $\Delta T = 5$ K cases, Nu of $Re_{L,in} = 80$ becomes smaller than $Re_{L,in} = 20$ and 40 at $\theta \approx 15^\circ$. The local Nu is nearly equal for $Re_{L,in} = 20$ and 40 with $\Delta T = 5$ K at $60^\circ < \theta < 170^\circ$. In $\Delta T = 10$ K cases, Nu of $Re_{L,in} = 80$ becomes slightly smaller than $Re_{L,in} = 20$ and 40 at $\theta \approx 20^\circ$. Over the rest

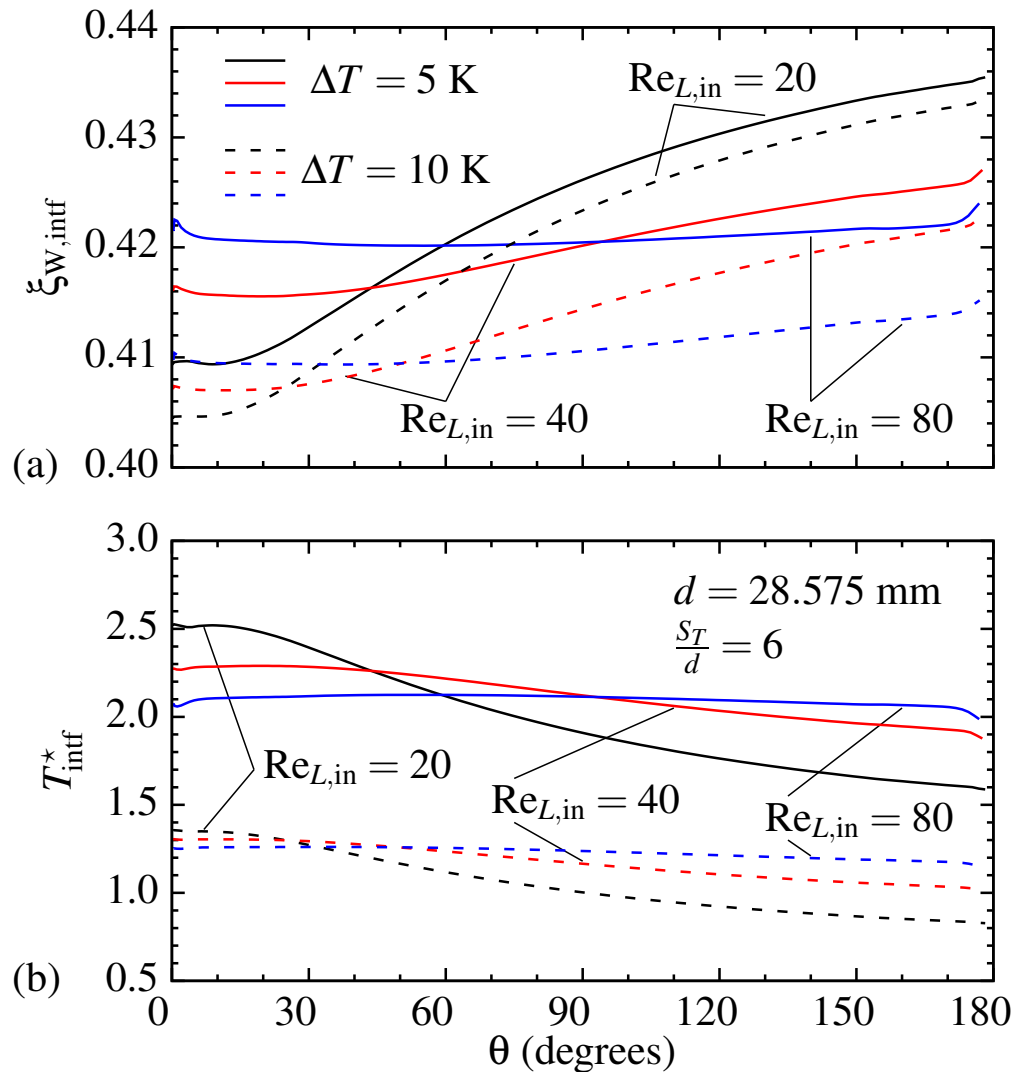


Figure 7.23: Variation around the tube of (a) interface mass fraction and (b) interface dimensionless temperature for $\Delta T = [5 \text{ K}, 10 \text{ K}]$ and $Re_{L, \text{in}} = [20, 40, 80]$ with $S_T/d = 6$ and $d = 28.575$ mm.

of the tube, the difference between Nu numbers of different Reynolds numbers in $\Delta T = 10$ K cases is negligible. At the bottom of the tube where the higher $Re_{L, \text{in}}$ forms a thicker film, Nu decreases rapidly in those cases. Figure 7.24 (b) shows that the absorption of water vapour at the interface increases over tube. This increase is noticeably higher in the cases with $Re_{L, \text{in}} = 20$. The interface mass flux is larger in $\Delta T = 10$ K for $Re_{L, \text{in}} = 20$ and 40 compared to $\Delta T = 5$ K. In cases with

$Re_{L,in} = 80$, however, $\Delta T = 5$ K absorbs more mass at the interface over the tube circumference in comparison to $\Delta T = 10$ K.

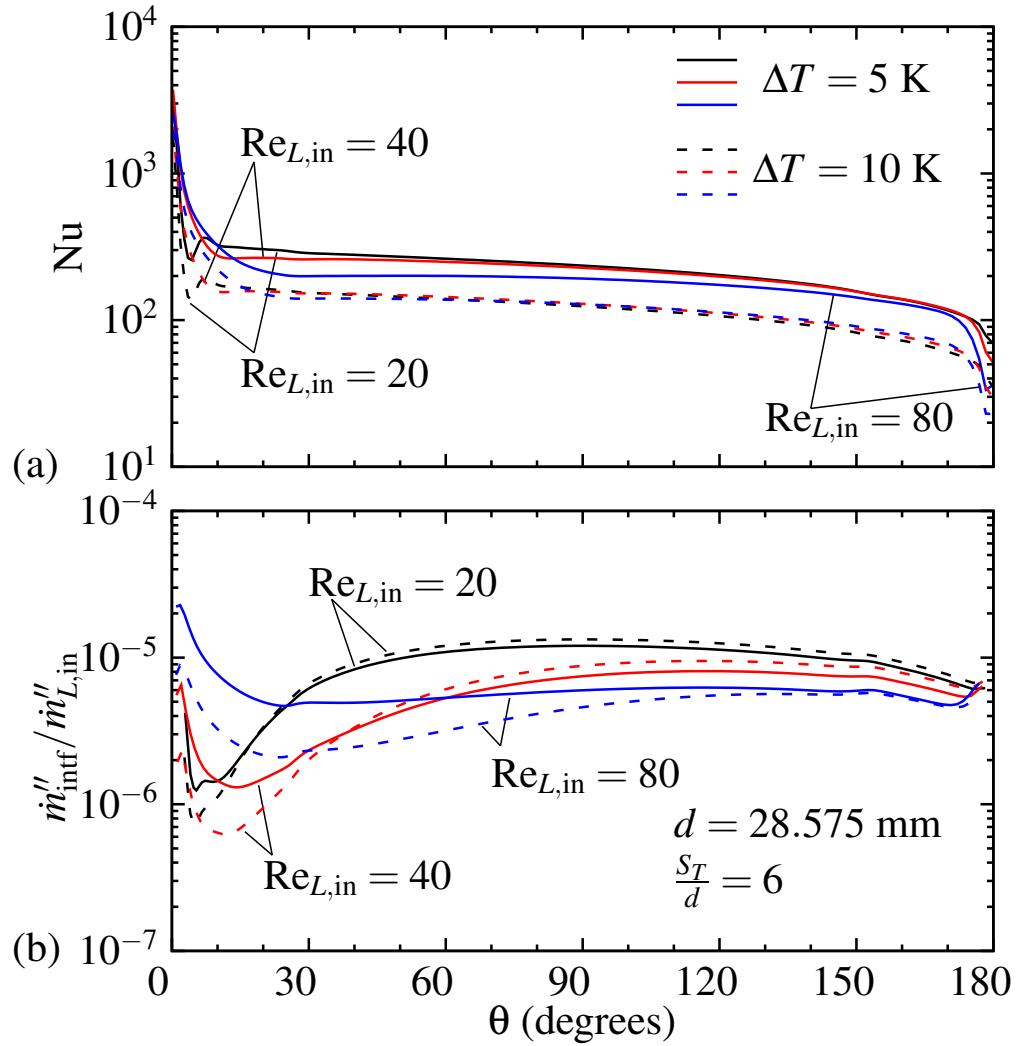


Figure 7.24: Variation around the tube of (a) local Nusselt number and (b) interface dimensionless mass flux for $\Delta T = [5$ K, 10 K] and $Re_{L,in} = [20, 40, 80]$ with $S_T/d = 6$ and $d = 28.575$ mm.

7.4.2 Effect of changing d

Figure 7.25 compares the liquid film thickness over the tubes with $d = 12.7$ mm, 19.05 mm, and 28.575 mm for $Re_{L,in} = 20$ and 80. In these cases, $S_T/d = 6$ and $\Delta T = 10$ K. The liquid film with $Re_{L,in} = 20$ thickens rapidly at the top of the tube. In this section of the tube, the maximum ratio of the film thickness to tube diameter increases with the decrease in d , i.e., in $Re_{L,in} = 20$, δ_θ/d of $d = 12.7$ mm is 1.8 times larger than $d = 28.575$ mm. At each Reynolds number, δ_θ/d is noticeably larger over the smaller tube. In the liquid film with $Re_{L,in} = 80$ at $\theta = 90^\circ$, δ_θ/d for $d = 12.7$ mm is 52.9% and 126.1% larger than $d = 19.05$ mm and 28.575 mm, respectively. At $\theta = 90^\circ$, the δ_θ/d difference between the tubes is smaller in cases with $Re_{L,in} = 20$, i.e., δ_θ/d for $d = 12.7$ mm is 45.5% and 128.6% larger than $d = 19.05$ mm and 28.575 mm, respectively. As seen in the previous section, the liquid film with a higher Reynolds number forms a thicker film over each tube after passing the initial part of the tube. Figure 7.25 shows that the film thickness difference between the low and high Reynolds numbers at $\theta = 90^\circ$ is larger in the tube with the smaller diameter.

The liquid film shape at the top and bottom of the tubes with different diameters, $d = 12.7$ mm, 19.05 mm, and 28.575 mm, for cases with $\Delta T = 10$ K and $Re_{L,in} = 20$ and 80 is shown in Figure 7.26. The liquid film is thicker at the top stagnation point in the falling films with the higher $Re_{L,in}$. In this group of falling films, the thicker falling film is formed at the top of the smaller tube. The small concave surface formed at the initial section of the tube in cases with $Re_{L,in} = 20$, changes to a bump as the liquid film flows further over the top of the tube. This convex surface is larger and formed in a greater distance from the top of the tube as the tube becomes smaller. In the cases with $Re_{L,in} = 80$, the films thicken gradually over the top of the tube. In these cases also the film is thicker over the tube with the smaller diameter. The liquid film thickness at the bottom of the tube increases as the tube becomes smaller and $Re_{L,in}$ increases. The liquid film with $Re_{L,in} = 80$ flowing over $d = 12.7$ mm leaves the tube surface before other films and changes to a thicker falling film below the tube.

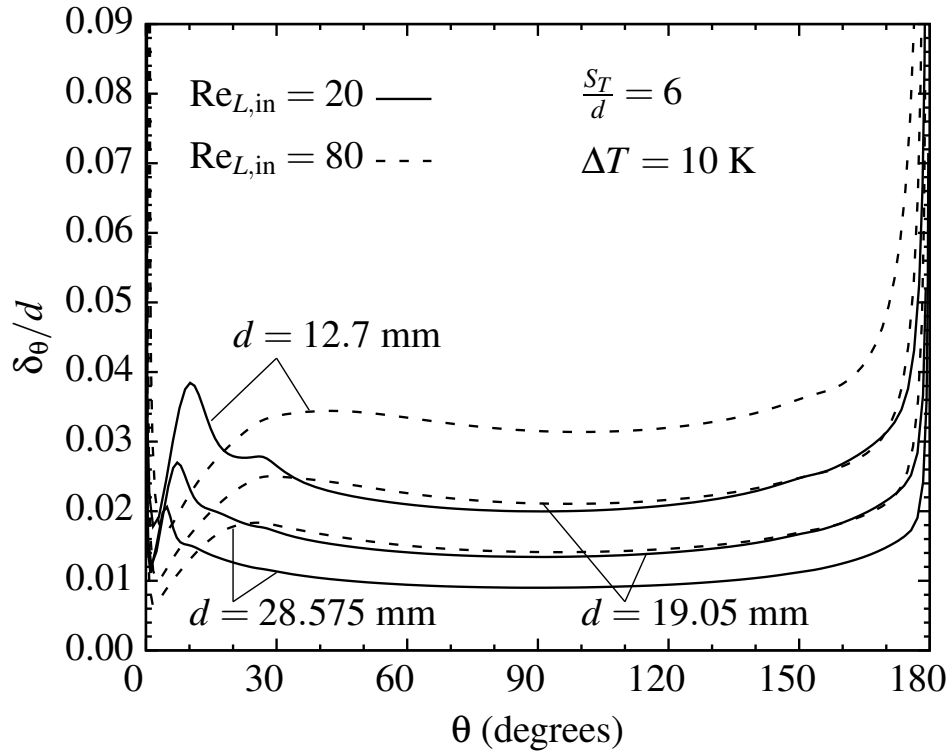


Figure 7.25: Variation of the liquid film thickness around the tube with d for $S_T/d = 6$ and $\Delta T = 10$ K.

The variation of the interface mass fraction and temperature over the tubes with $d = 12.7$ mm, 19.05 mm, and 28.575 mm, for cases with $\Delta T = 10$ K and $Re_{L,in} = 20$ and 80 is presented in Figure 7.27 (a) and (b), respectively. The liquid films with $Re_{L,in} = 20$ reach the top surface of the tube at a lower $\xi_{W,intf}$ compared to $Re_{L,in} = 80$ but the mass fraction increase over the tube is noticeably higher in these cases. The interface water mass fraction is nearly constant over $0^\circ < \theta < 15^\circ$ and $0^\circ < \theta < 60^\circ$ in $Re_{L,in} = 20$ and $Re_{L,in} = 80$, respectively. After passing this section of the tube, the liquid films flowing over the larger tube show a higher $\xi_{W,intf}$ over the rest of the tube circumference. At the bottom of the tube, $\theta \approx 180^\circ$, $\xi_{W,intf}$ in $Re_{L,in} = 20$ is 3.85%, 3.38%, and 2.91% larger than $\xi_{W,intf}$ in $Re_{L,in} = 80$ for $d = 28.575$ mm, 19.05 mm, and 12.7 mm, respectively. At this point, by increasing the tube diameter from 12.7 mm to 28.575 mm, $\xi_{W,intf}$ increases by almost 1.88% and 0.97% for $Re_{L,in} = 20$ and 80, respectively. Figure 7.27 (b) shows

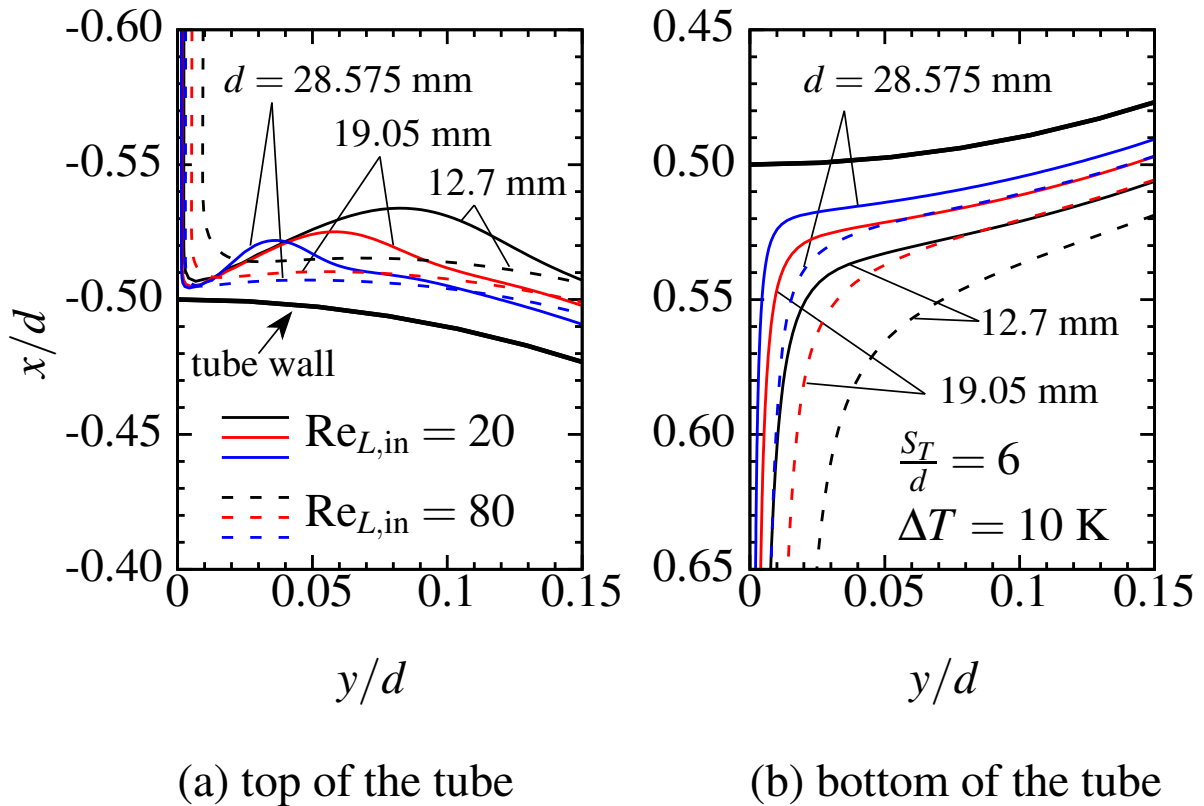


Figure 7.26: Change of the liquid film shape at the top and bottom of the tube with d for $S_T/d = 6$ and $\Delta T = 10$ K.

that the decrease in the interface temperature between the inlet and the tube surface is greater in the cases with the higher Re number. However, the interface temperature decrease in contact with the tube wall occurs faster in the liquid films with $Re_{L,in} = 20$. At $\theta \approx 180^\circ$, following the equilibrium condition at the interface, the film flowing over the larger tube and with the higher $\xi_{W,intf}$ has the smaller T_{intf} in each Re number. Similar to the interface mass fraction, the interface temperature difference at the bottom of the tube is noticeably larger in cases with $Re_{L,in} = 20$.

Figure 7.28 shows the variation of the local Nusselt number and the around the tubes with $d = 12.7$ mm, 19.05 mm, and 28.575 mm, for cases with $\Delta T = 10$ K and $Re_{L,in} = 20$ and 80. The local Nu of the liquid films with $Re_{L,in} = 20$ decreases to a minimum value at the top of the tube. This minimum value is larger and happens earlier in the case with the larger tube diameter because

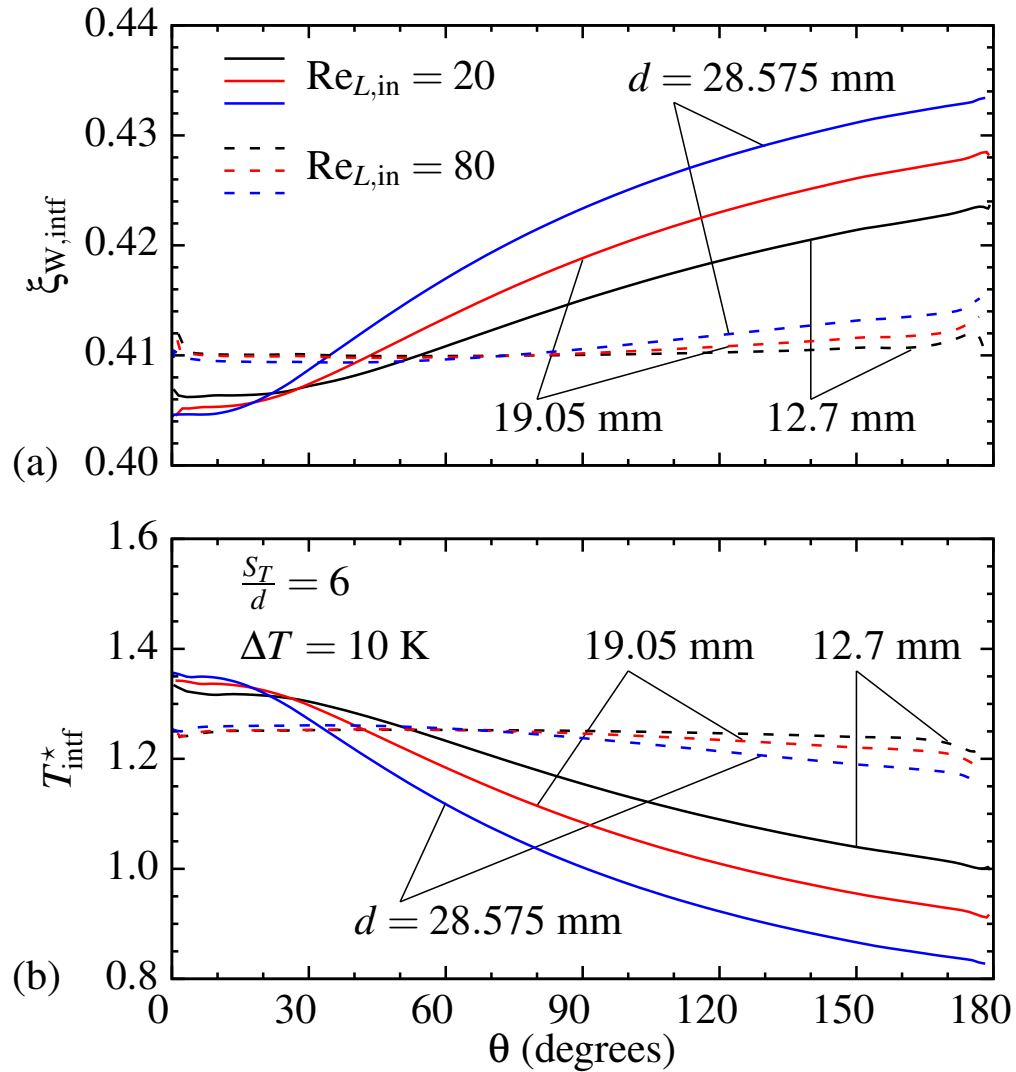


Figure 7.27: Variation around the tube of (a) interface mass fraction and (b) interface dimensionless temperature for $d = [12.7 \text{ mm}, 19.05 \text{ mm}, 28.575 \text{ mm}]$ and $\text{Re}_{L, \text{in}} = [20, 80]$ with $S_T/d = 6$ and $\Delta T = 10$ K.

of the thickness of the film at the top of the tube (Figure 7.26). At this initial section of the tube, the Nusselt number decreases gradually in liquid films with $\text{Re}_{L, \text{in}} = 80$. At $20^\circ < \theta < 170^\circ$, the heat transfer to the tube wall is nearly equal for $\text{Re}_{L, \text{in}} = 20$ and 80 over each tube. It is clear that Nu is larger along the tube surface for the larger tube diameter. When the film reaches the bottom

of the tube, Nu decreases suddenly for the cases with $Re_{L,in} = 80$ in which the film thickens more rapidly as θ approaches 180° . In Figure 7.28 (b), vapour absorption rate is higher in cases with $Re_{L,in} = 80$ at $\theta = 0$. These cases produced a thicker falling liquid film at the top stagnation point in Figure 7.26 (a). While the interface mass flux decrease in $Re_{L,in} = 80$ cases over $0^\circ < \theta < 20^\circ$, the cases with $Re_{L,in} = 20$ show a rapid increase in the interface mass flux over $10^\circ < \theta < 40^\circ$. In $Re_{L,in} = 80$, the film flowing over the smaller tube absorbs more water vapour at the interface before $\theta = 90^\circ$, however, the cases with $Re_{L,in} = 20$ show an opposite behaviour. After $\theta = 90^\circ$, the interface mass flux profiles collapse on each other for the selected tube diameters in each Re number. As the liquid film changes to a vertical falling film at the tube bottom surface, the mass absorption at the interface increases in all the cases.

Figure 7.29 shows the normalized film thickness, δ/d , versus a normalized distance, S/d , that goes along the x axis above and below the tube and along the tube surface. The film thickness is measured normal to the x axis, δ_y , above and below the tube and normal to the tube surface, δ_θ , over the tube. δ_θ is measured at $0.5^\circ < \theta < 177^\circ$. The last point where δ_y is calculated above the tube is the same point where δ_θ is calculated (vertical grey line at $S/d \approx 1$ in Figure 7.29). The same rule was applied to the point below the tube where δ_θ and δ_y are separated using the grey vertical line at $S/d \approx 2.6$. Figure 7.29 (a) and (b) show the falling film thickness for $Re_{L,in} = 40$ and 80 , $\Delta T = 5$ K and 10 K on tube $d = 12.7$ mm and $d = 28.575$ mm, respectively. The falling film above the tube is thicker in $Re_{L,in} = 80$ and $\Delta T = 5$ K cases for both tube diameters. δ_y decreases as the film falls from the inlet to reach the tube surface. At the tube top stagnation point, $\delta_\theta \rightarrow \infty$. Around the tube, δ_θ/d is larger for $Re_{L,in} = 80$ compared to $Re_{L,in} = 40$ in both tubes. The difference in δ_θ/d between $\Delta T = 5$ K and 10 K in each Re number is more noticeable over the smaller tube. After $\theta = 177^\circ$, the film over the tube transitions rapidly to a falling film so δ normal to the tube is no longer a meaningful quantity. In the falling film region the film height decreases rapidly over a short distance due to the gravitational force. For greater values of S/d (farther in the x direction), the film height decreases with a very slow rate towards an equilibrium height. The difference in δ_y/d between similar Reynolds numbers is only noticeable in the films

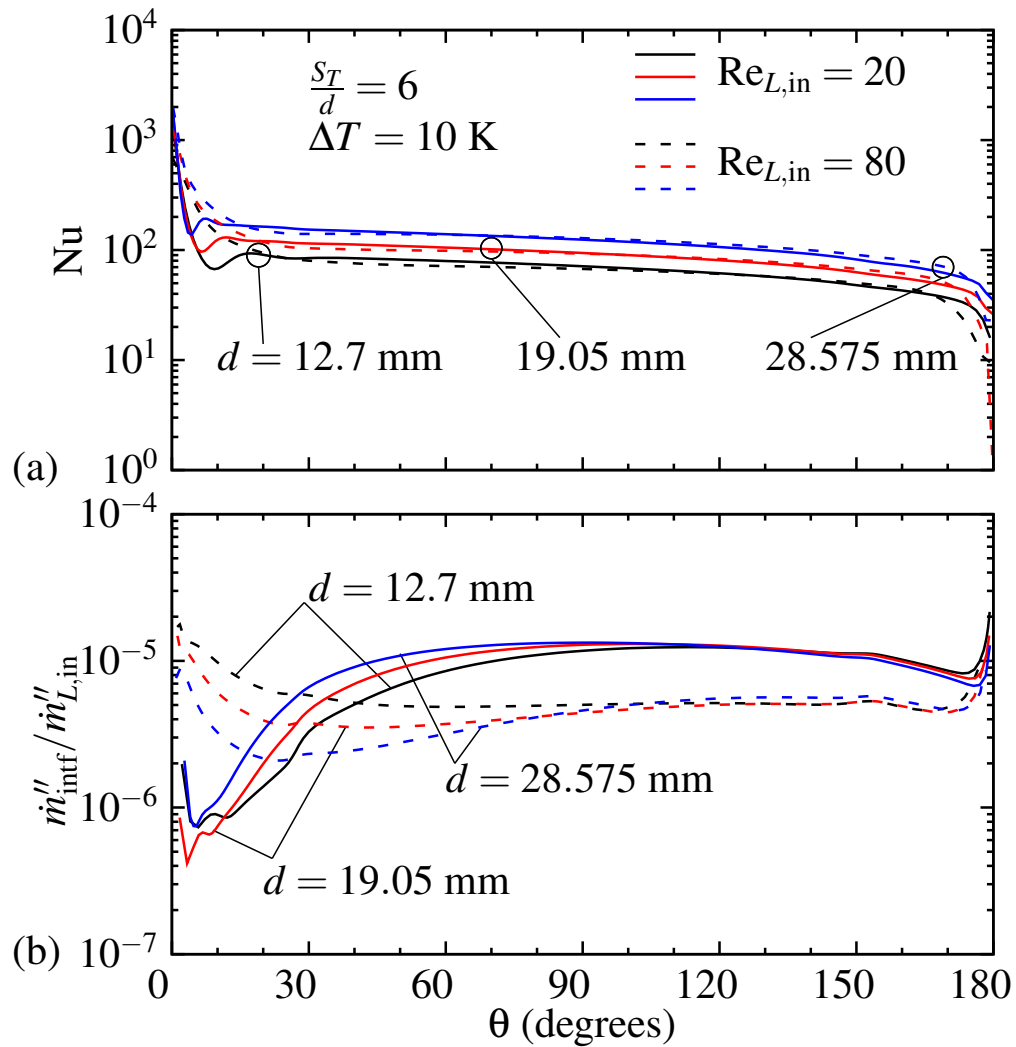


Figure 7.28: Variation around the tube of (a) local Nusselt number and (b) interface dimensionless mass flux for $d = [12.7$ mm, 19.05 mm, 28.575 mm] and $Re_{L,in} = [20, 80]$ with $S_T/d = 6$ and $\Delta T = 10$ K.

with $Re_{L,in} = 80$ and $d = 12.7$ mm.

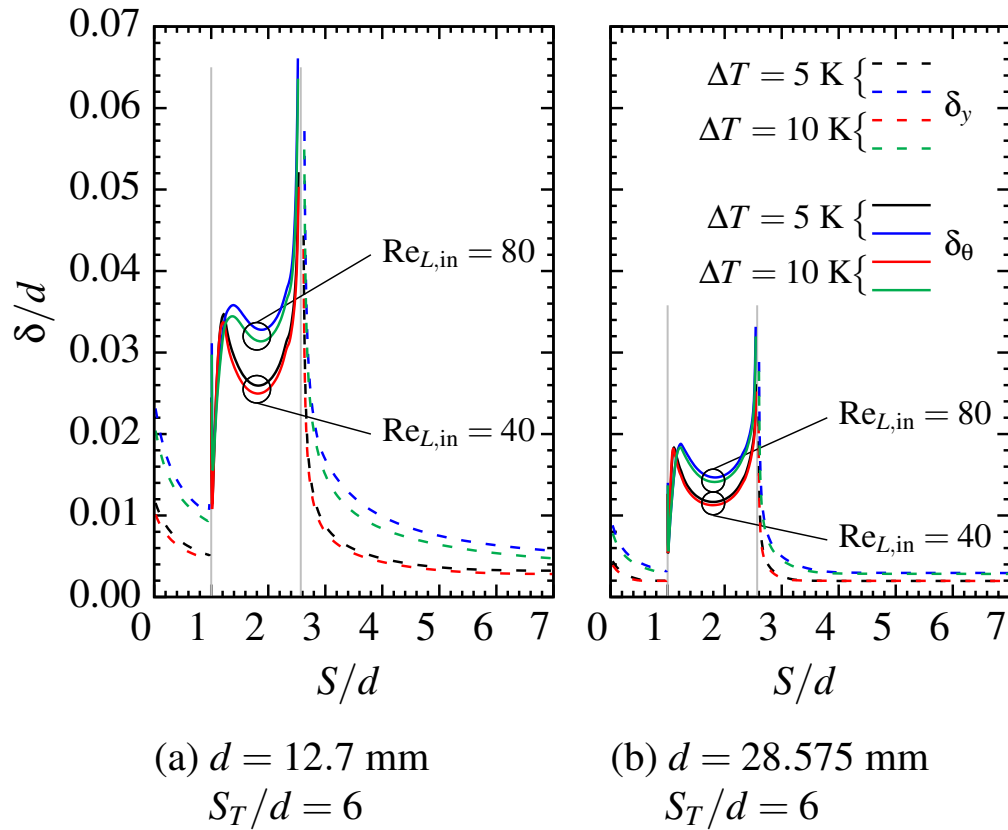


Figure 7.29: Film thickness at the top and bottom of the tube and over the tube for $Re_{L,in} = [40, 80]$ and $\Delta T = [5 \text{ K}, 10 \text{ K}]$ with $S_T/d = 6$ (a) $d = 12.7$ mm and (b) $d = 28.575$ mm.

7.4.3 Effect of changing S_T/d

7.4.3.1 Over-Tube Variations

To investigate the effect of the changing tube spacing in the y direction on the interface parameters and the liquid film and gas phase development over the tube, $S_T/d = 3$ and 9 are applied to cases with $Re_{L,in} = 20$ and $\Delta T = 5 \text{ K}$ and 10 K .

Figure 7.30 shows the liquid film variation around the tubes for cases with $S_T/d = 3$ and 9 , $Re_{L,in} = 20$, and $\Delta T = 5 \text{ K}$ and 10 K . The increase in the liquid film thickness at the upper part of the tube occurs before $\theta = 10^\circ$ in all the cases presented in Figure 7.30. The maximum film

thickness is larger for the cases with $\Delta T = 10$ K and the smallest tube diameter. The results demonstrate that the film thickness over the tube is not impacted by the change in S_T/d . In each tube diameter, the film is slightly thicker in cases with $\Delta T = 5$ K. The film thickness difference between $\Delta T = 5$ K and 10 K becomes smaller as the tube diameter becomes larger.

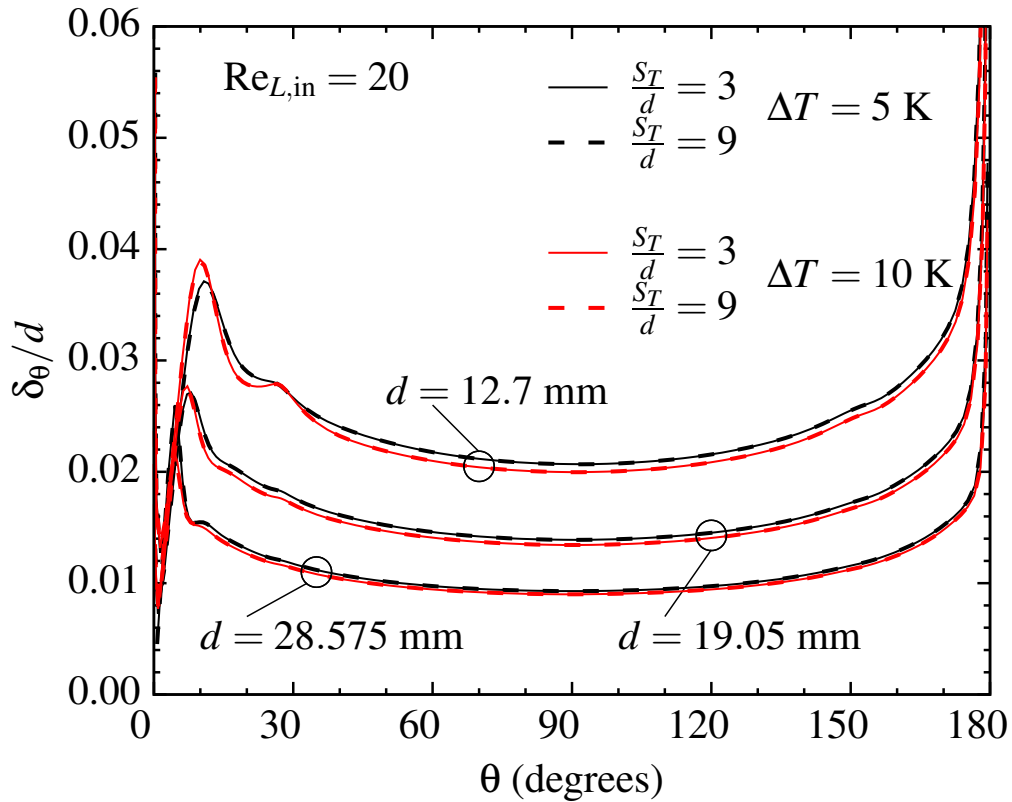


Figure 7.30: Variation of the liquid film thickness around the tube with S_T/d for $Re_{L,in} = 20$ and $\Delta T = [5 \text{ K}, 10 \text{ K}]$.

The liquid film shape at the top and bottom of the tube for cases with $S_T/d = 3$ and 9, $Re_{L,in} = 20$, and $\Delta T = 5$ K and 10 K is shown in Figure 7.31. The liquid film growth over the top of the tube is noticeably larger for the cases with $d = 12.7$ mm. For the larger tube diameters the film sudden thickening and afterwards transition to a uniform thickness occurs at a smaller y/d . As Figure 7.31 (a) demonstrates, the change in S_T/d did not affect the film shape. At the bottom of the tube, the shape of the liquid film is slightly affected by ΔT . For each tube diameter and ΔT ,

$S_T/d = 3$ and 9 form identical films at the lower part of the tube.

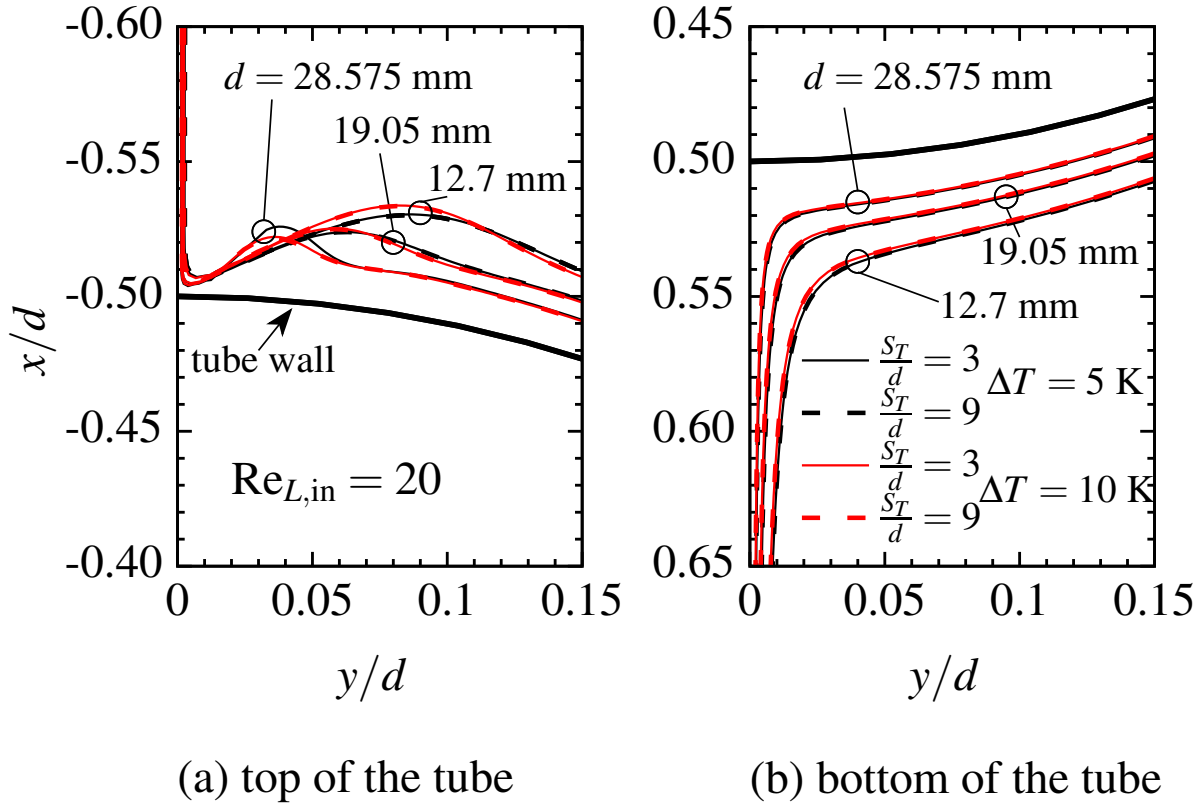


Figure 7.31: Change of the liquid film shape at the top and bottom of the tube with S_T/d for $Re_{L,in} = 20$ and $\Delta T = [5 \text{ K}, 10 \text{ K}]$.

The variation of the interface mass fraction and temperature over the tube for cases with $S_T/d = 3$ and 9 , $Re_{L,in} = 20$, and $\Delta T = 5 \text{ K}$ and 10 K is presented in Figure 7.32 (a) and (b), respectively. The cases with $\Delta T = 10 \text{ K}$ show a more similar values of interface mass fraction and temperature at $\theta = 0^\circ$ in comparison to cases with $\Delta T = 5 \text{ K}$. The liquid films in contact with the larger tube, $d = 28.575 \text{ mm}$, have a greater water mass fraction and a smaller temperature at the interface over $60^\circ < \theta < 180^\circ$. As the liquid film approaches the bottom of the tube, the mass fraction difference between $\Delta T = 5 \text{ K}$ and 10 K decreases for each tube. This difference is larger for $d = 12.7 \text{ mm}$ at $\theta \approx 180^\circ$. Changing S_T/d from 3 to 9 did not have any noticeable impact on the interface mass fraction and temperature.

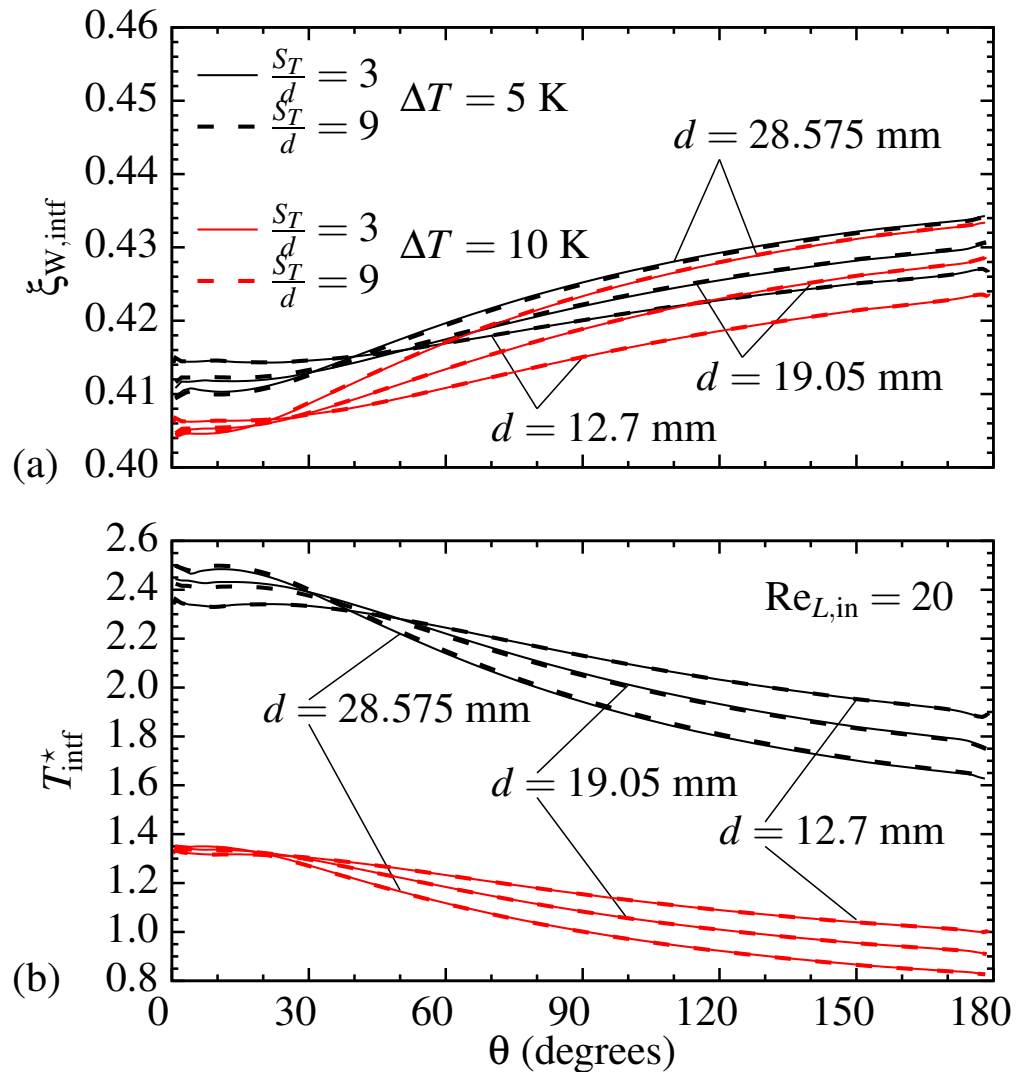


Figure 7.32: Variation around the tube of (a) interface mass fraction and (b) interface dimensionless temperature for $S_T/d = [3, 9]$ and $\Delta T = [5 \text{ K}, 10 \text{ K}]$ with $d = [12.7 \text{ mm}, 19.05 \text{ mm}, 28.575 \text{ mm}]$ and $Re_{L,in} = 20$.

Figure 7.33 shows the variation of the local Nusselt number and the dimensionless rate of absorption around the tube for cases with $S_T/d = 3$ and 9 , $Re_{L,in} = 20$, and $\Delta T = 5 \text{ K}$ and 10 K . The profiles of the decrease in the local Nu over the tube circumference are very similar for cases with $\Delta T = 10 \text{ K}$ and 5 K . In each group, Nu is higher in the case with $d = 28.575 \text{ mm}$. The mass

absorption at the interface occurs at a higher rate for cases with the smaller ΔT at the initial section of the tube. The liquid films show an opposite behaviour after $\theta \approx 20^\circ$. The cases with same ΔT absorb nearly the same amount of mass at the interface between $\theta = 120^\circ$ and 150° . While changing to a falling film at the bottom of the tube, the interface mass flux becomes smaller in cases with the smaller tube diameter. The change in Nu over the tube surface and mass flux at the interface is almost identical for $S_T/d = 3$ and 9 in all the cases presented in Figure 7.33.

For the investigation of the effect of changing S_T/d on the liquid film with $Re_{L,in} = 80$, six cases with similar ΔT and d to cases studied in this section are presented in Appendix H.

7.4.3.2 Transverse Profiles

In this section, the transverse-direction profiles of U , V , and T in the liquid and gas phases and ξ_W in the liquid phase are presented to investigate the effect of S_T/d on the domain variables. The selective axial locations where the field variables are calculated are shown in Figure 7.34.

In Figure 7.35, the dimensionless x -direction velocity profiles in liquid region versus y^\star for $S_T/d = 3$ and 9 are shown at different axial locations. To help in comparing profiles of variables in the liquid at different locations, a local dimensionless y variable, y^\star , is defined as follows:

$$y^\star = \frac{y - y_{min}(x)}{y_{max}(x) - y_{min}(x)} \quad (7.8)$$

where y_{min} and y_{max} are the minimum and maximum value of y in the liquid region at each x/d location. Figure 7.35 shows the U profiles for the cases with $d = 19.05$ mm, $Re_{L,in} = 40$ and $\Delta T = 10$ K. $U_{L,in}$ in these cases is 0.23 m s⁻¹. In the falling film before the tube, at $x/d = -1$, U velocity is uniform and at the high value of $U_L/U_{L,in} = 2.1$. Close to the top of the tube, the velocity decreases across the liquid film especially at the interface. Over the tube at $x/d = -0.35$, $U_L/U_{L,in}$ becomes zero and 0.4 at the tube wall and the interface, respectively. The interface velocity increases when the flow reaches the side of the tube at $x/d = 0$. U velocity profiles at $x/d = 0.35$ ($\theta = 135^\circ$) are on top of $x/d = -0.35$ ($\theta = 45^\circ$) profiles. The velocity profile becomes

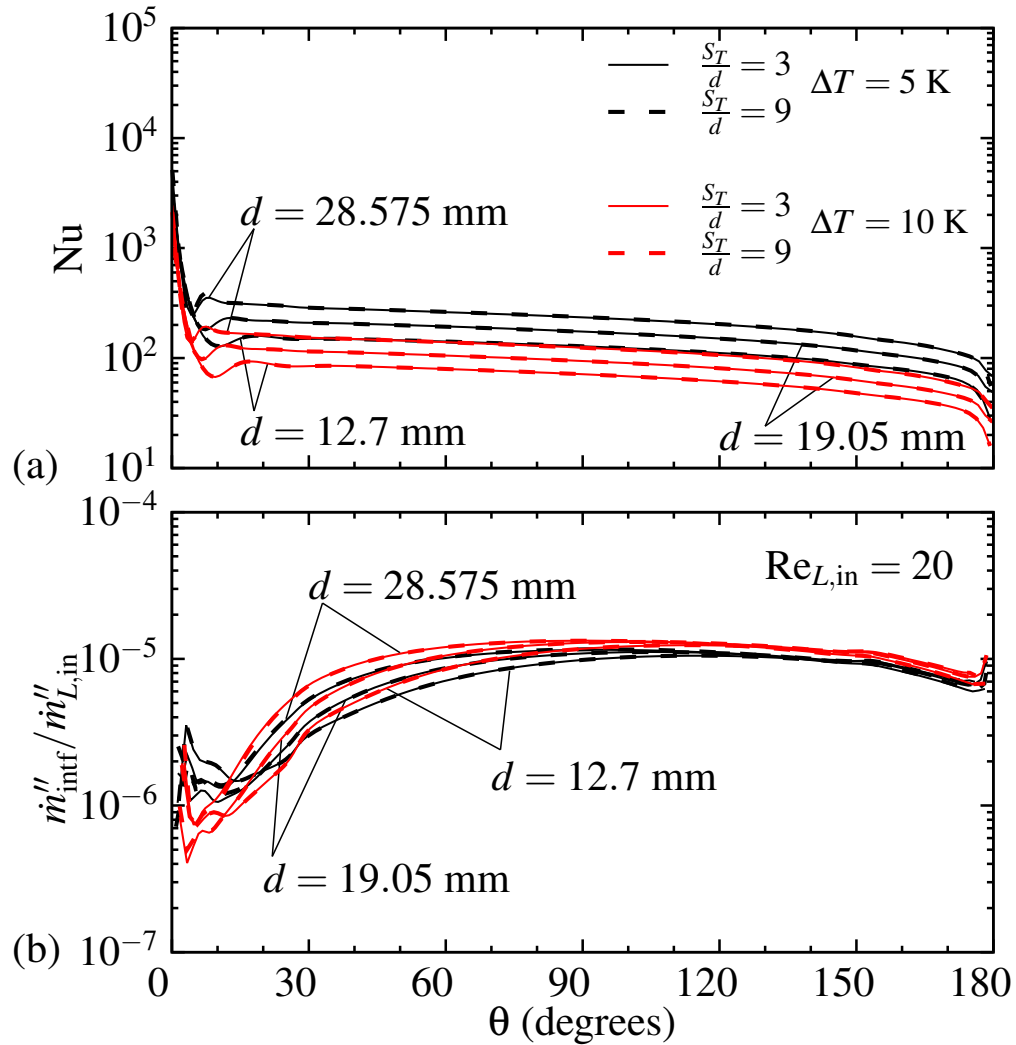


Figure 7.33: Variation around the tube of (a) local Nusselt number and (b) interface dimensionless mass flux for $S_T/d = [3, 9]$ and $\Delta T = [5 \text{ K}, 10 \text{ K}]$ with $d = [12.7 \text{ mm}, 19.05 \text{ mm}, 28.575 \text{ mm}]$ and $Re_{L,\text{in}} = 20$.

nearly uniform below the tube surface ($x/d = 0.55$). Farther along the x direction, the velocity increases as the liquid film falls under the tube. The liquid film U velocity profiles were not affected by the change in S_T/d except at $x/d = 2.5$ where the liquid film was impacted by the flow of water vapour entering the gas region at the outlet of the domain. This will be explained in detail when examining the gas region profiles.

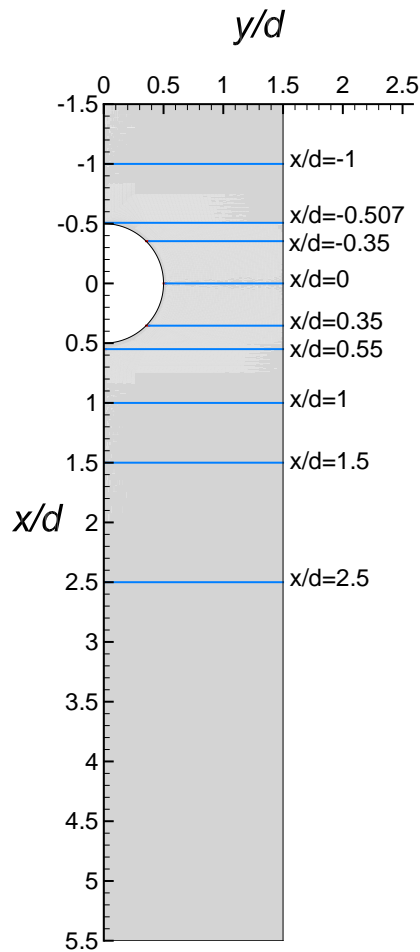


Figure 7.34: x/d locations in the domain ($S_T/d = 3$).

The dimensionless V velocity profiles in the liquid region are given in Figure 7.36 for the case with $d = 19.05$ mm, $Re_{L,in} = 40$ and $\Delta T = 10$ K. V velocity profiles are identical for $S_T/d = 3$ and 9 in Figure 7.36. At $x/d = -1$, $V_L/U_{L,in}$ is nearly zero across the liquid film. The interface V velocity increases when the flow reaches the tube surface $x/d = -0.507$. A decrease in $V_L/U_{L,in}$ is observed as the liquid film flows around the tube ($45^\circ < \theta < 135^\circ$). $V_L/U_{L,in}$ decreases while the liquid film leaves the tube surface at $x/d = 0.55$ and becomes very small when it falls in the x direction below the tube.

In Figure 7.37, the dimensionless temperature profiles in the liquid region are shown at different

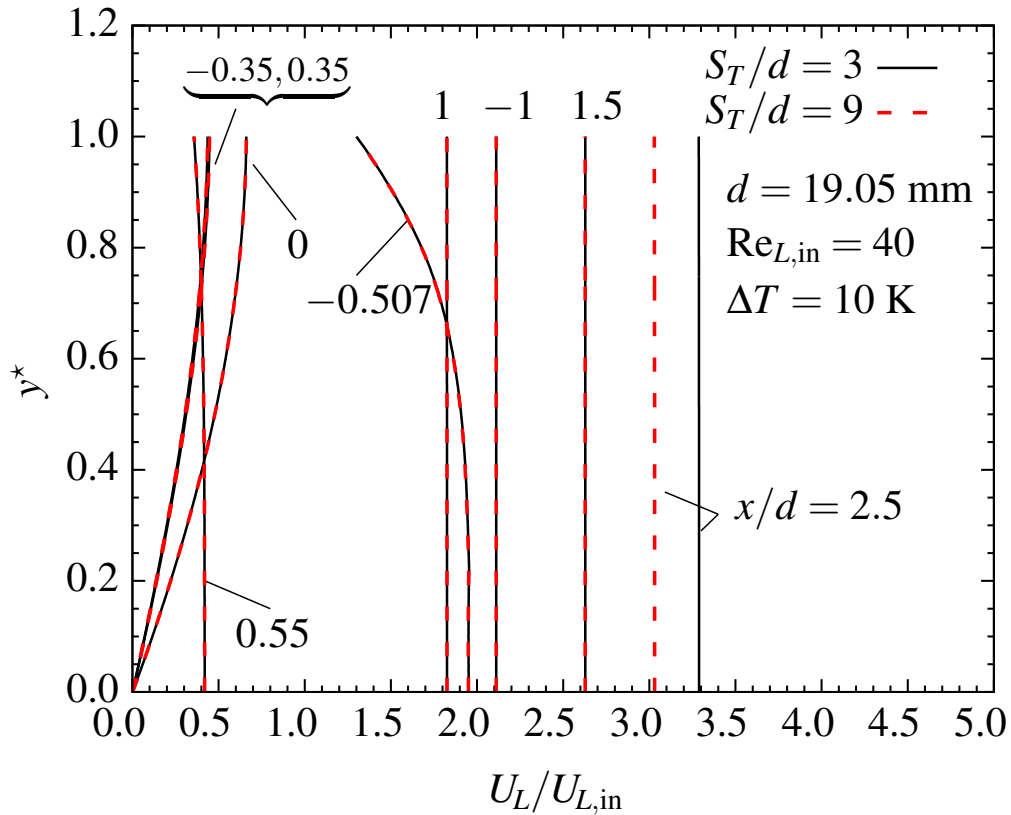


Figure 7.35: U velocity profiles in the liquid film at different axial locations for $S_T/d = [3, 9]$, $d = 19.05$ mm, $Re_{L,in} = 40$ and $\Delta T = 10$ K ($U_{L,in} = 0.23$ m s⁻¹).

axial locations for $S_T/d = 3$ and 9 . For the cases presented in this figure, $T^* = 1.5$ at the inlet of the computational domain. At $x/d = -1$, T^* is decreased to 1.14 and 1.25 at $y^* = 0$ and 1 (the interface), respectively. The temperature increases across the liquid film at the top of the tube, i.e. $x/d = -0.507$ compared to the falling film above the tube. When the film comes in contact with the tube surface, the interface temperature decreases while flowing from $\theta = 45^\circ$ to $\theta = 135^\circ$. Below the tube, T^* increases at $y^* = 0$ and the T^* difference between this point and the interface decreases until the temperature profile becomes uniform at $x/d = 2.5$. The temperature variation across the liquid film was not affected by the change in S_T/d .

Figure 7.38 shows the transverse-direction profiles of water mass fraction in the liquid for cases

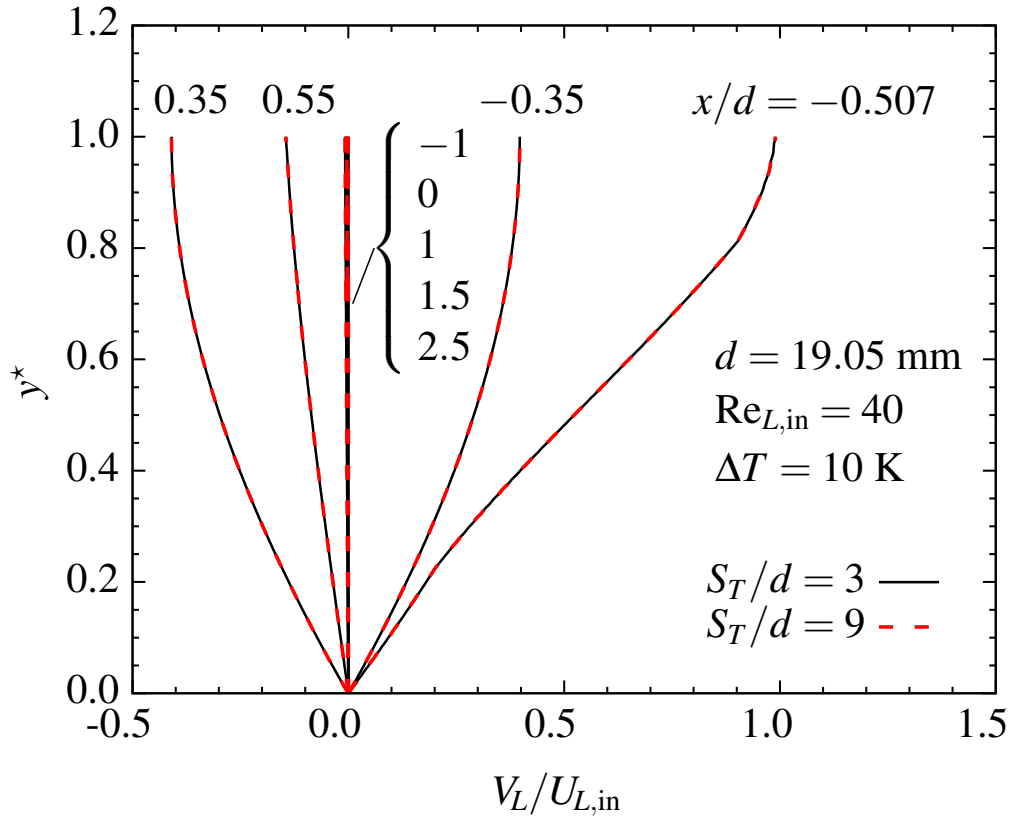


Figure 7.36: V velocity profiles in the liquid film at different axial locations for $S_T/d = [3, 9]$, $d = 19.05 \text{ mm}$, $Re_{L,in} = 40$ and $\Delta T = 10 \text{ K}$ ($U_{L,in} = 0.23 \text{ m s}^{-1}$).

with $S_T/d = 3$ and 9 . At $x/d = -1$, a large portion of the liquid film is at the uniform inlet mass fraction. At this point, ξ_W increases towards the interface because of the mass absorption at the interface. At the top of the tube ($x/d = -0.507$), the gradient of ξ_W becomes more noticeable across the film. Over the most of the tube circumference, $45^\circ < \theta < 135^\circ$, ξ_W does not change from to $y^* = 0$ to $y^* = 0.8$. Over this section of the tube, ξ_W increases close to the interface as more water is diffused into the liquid film. While the liquid film falls below the tube, the diffusion of water towards $y^* = 0$ increases the water mass fraction between $y^* = 0$ and $y^* = 0.8$. The interface water mass fraction decreases after flow passes $x/d = 1$. Increasing the y -direction tube distance from $S_T/d = 3$ to 9 did not change the mass fraction distribution at different axial locations in the domain.

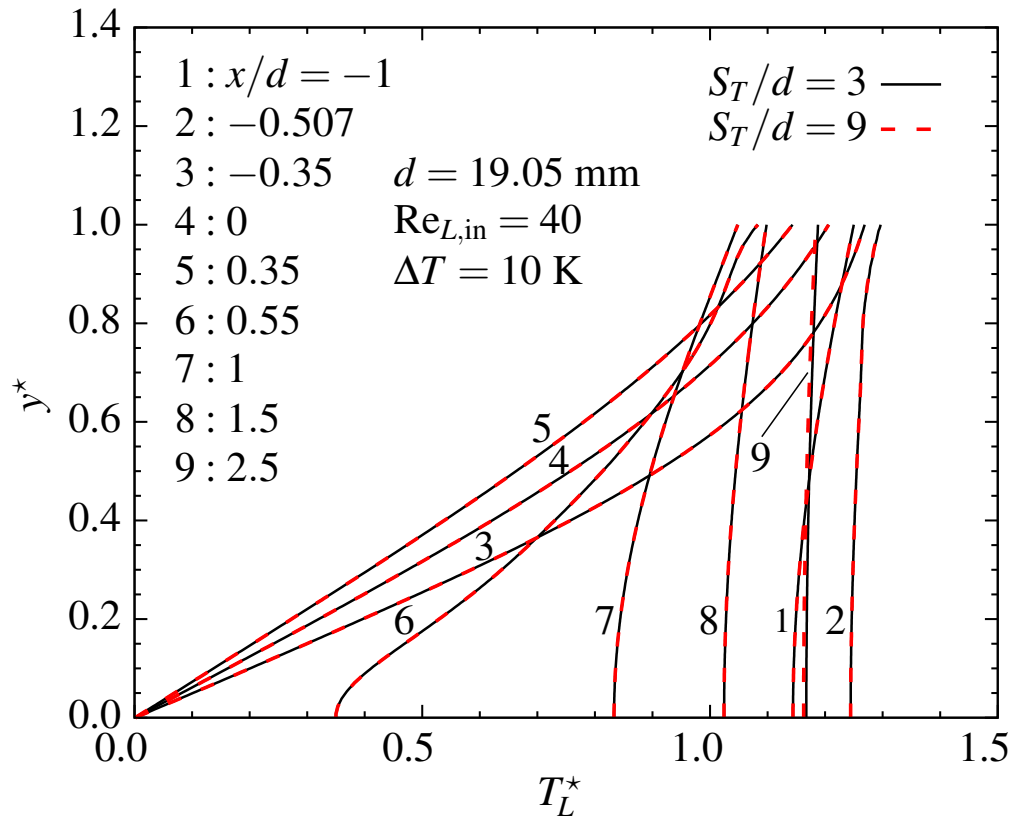


Figure 7.37: Temperature profiles in the liquid film at different axial locations for $S_T/d = [3,9]$, $d = 19.05$ mm, $Re_{L,in} = 40$ and $\Delta T = 10$ K.

Figure 7.39 shows the temperature contour and the flow streamlines in cases with $S_T/d = 3, 6,$ and 9 . The liquid film and the water vapour enter the domain at $T_{L,in} = 45^\circ\text{C}$ and $T_{G,in} = 20^\circ\text{C}$, respectively. The gas phase temperature increases in contact with the liquid film over tube. The flow streamlines and the temperature distributions are very similar before $x/d = 1$ in cases with different S_T/d . In the case with $S_T/d = 3$, the vapour flow at the existing liquid film temperature is pulled in through the outlet of the domain. This occurs because most of the available vapour in the gas phase is absorbed in $S_T/d = 3$ before $x/d = 1$ and the lacking amount of vapour to be absorbed at the interface is provided through the domain outlet. The entrance of the vapour flow with a higher temperature than the gas phase, changes the temperature distribution in $S_T/d = 3$ compared to $S_T/d = 6$ and 9 .

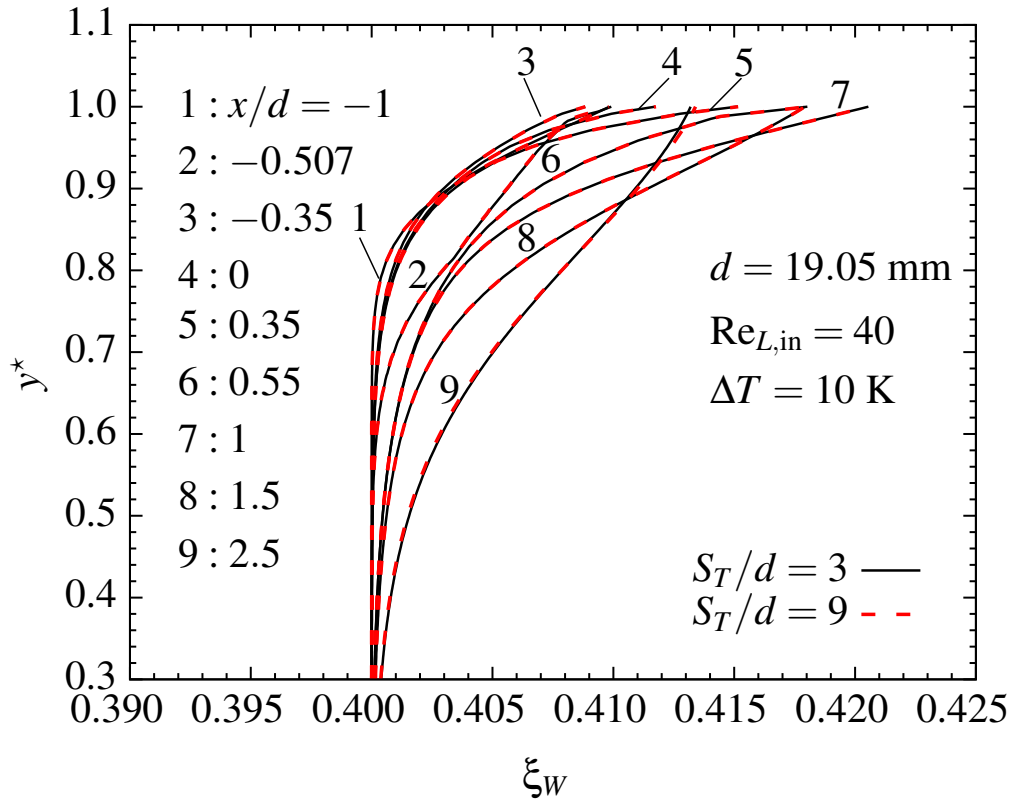


Figure 7.38: Mass fraction profiles in the liquid film at different axial locations for $S_T/d = [3, 9]$, $d = 19.05$ mm, $Re_{L,in} = 40$ and $\Delta T = 10$ K.

Figure 7.40 shows the temperature contours and the flow streamlines in cases with $S_T/d = 6$ to compare the effect of changing $Re_{L,in}$, d , and ΔT . Similar to Figure 7.39 (b), $S_T/d = 6$ provides enough water vapour to be absorbed at the interface for $Re_{L,in} = 20$ and 80 in Figure 7.40 (a) and (b). The gas flow temperature at the top of the tube in $Re_{L,in} = 20$ is more impacted by the liquid film. The increase in the vapour temperature close to the interface is the result of the liquid film rapid growth at the top stagnation point in $Re_{L,in} = 20$. As the liquid film leaves the stagnation point and flows around the tube, it thickens considerably in $Re_{L,in} = 80$ and the thermal boundary layer expands more in to the gas region in the y direction. Below the tube, the film for the $Re_{L,in} = 80$ case leaves the tube surface at a larger thickness compared to the $Re_{L,in} = 20$ case and the thermal boundary layer is thicker. In the falling film under the tube, the acceleration of the flow velocity

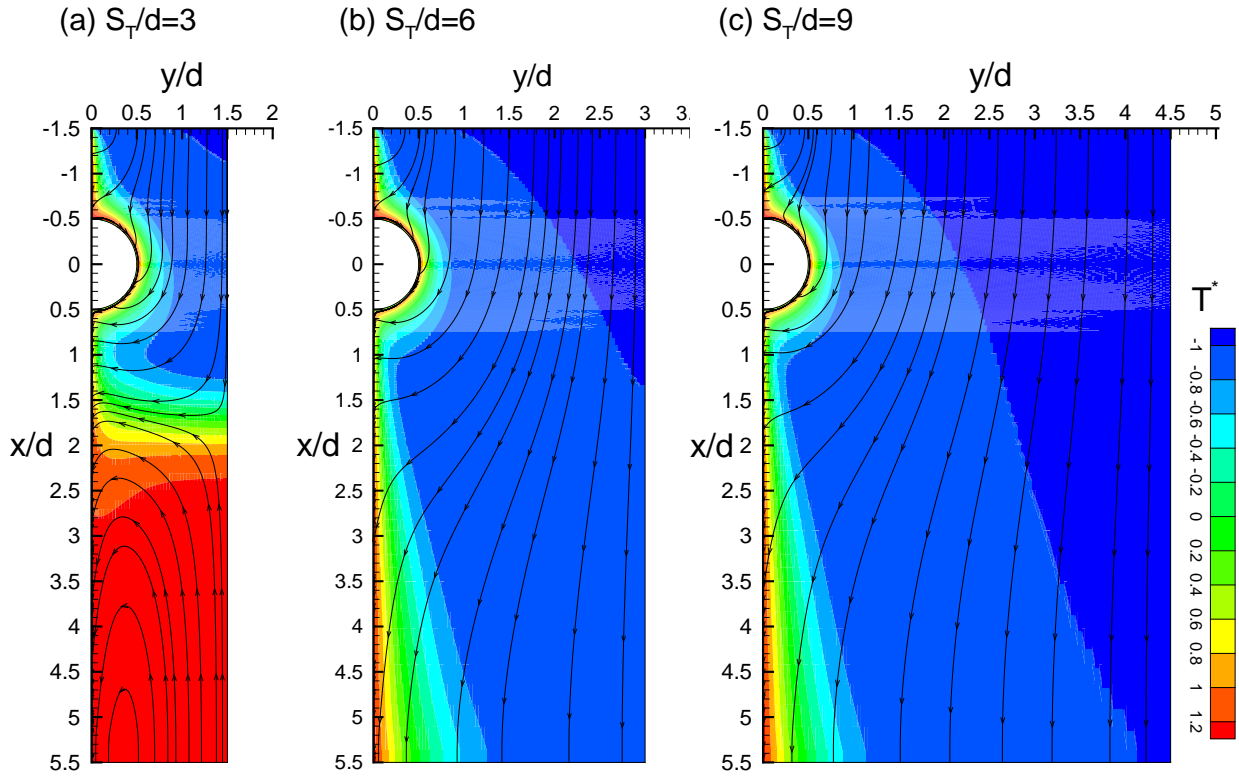


Figure 7.39: Flow streamlines and temperature contours for $d = 19.05$ mm, $\Delta T = 10$ K, and $Re_{L,in} = 40$ (a) $S_T/d = 3$, (b) $S_T/d = 6$, and (c) $S_T/d = 9$.

thins the film and the thermal boundary layer. This acceleration starts closest to the tube in the $Re_{L,in} = 20$ case. While the liquid film approaches the outlet of the domain, the thermal boundary layer grows linearly in the $Re_{L,in} = 20$ case and a larger portion of the gas becomes affected by the release of heat at the interface compared to the $Re_{L,in} = 80$ case. Figures 7.40 (c) and (d) compare the temperature contours and the flow streamlines in cases with $Re_{L,in} = 40$ and $\Delta T = 10$ K for $d = 12.7$ mm and 28.575 mm. The liquid film flowing over the smaller tube forms a thicker film (Figure 7.25 and Figure 7.39 (b)). At $\theta = 90$, $T^* = -0.8$ occurs at $y/d = 1$ and $y/d = 0.8$ for $d = 12.7$ mm and 28.575 mm, respectively. Under the tube at $x/d = 1$, the thermal boundary layer in $d = 12.7$ mm expands to a larger y/d in comparison to $d = 28.575$ mm. At this location the

flow of the case with $d = 28.575$ mm reaches $T^* = -0.8$ at a higher y/d . Figure 7.40 (e) shows the temperature contours and the flow stream lines in the case with $Re_{L,in} = 40$, $d = 19.05$ mm, and $\Delta T = 5$ K. Comparison of this case with Figure 7.39 (b) shows that the temperature of the gas region before the tube in contact with $\Delta T = 5$ K liquid film is not as highly affected. These two cases show a similar temperature distribution over and after the tube up to $x/d = 4$. After that point, the temperature of a larger portion of the gas region is increased in the case with $\Delta T = 5$ K compared to $\Delta T = 10$ K.

In Figure 7.41, the dimensionless U velocity profiles in the gas region are shown for $S_T/d = 3$ and 9 at different axial locations. At the top of the gas region, $\frac{y}{S_T/2} = 1$, the magnitude of $U_G/U_{G,in}$ decreases for $S_T/d = 3$ and 9 as the water vapour flows farther in the x direction. This decrease along x is more notable for $S_T/d = 3$. Between $x/d = -0.35$ and 0.55, the maximum value of $U_G/U_{G,in}$ occurs at $\frac{y}{S_T/2} \approx 0.2$ in $S_T/d = 9$. In this case, the slow falling film below the tube impacts the gas phase more than over the tube and the gas phase velocity becomes smaller at the interface compared to $\frac{y}{S_T/2} = 1$. An opposite trend is observed in $S_T/d = 3$. In this case, the vapour flow entering the domain from the outlet increases the U velocity of the gas flow near the interface relative to the flow at higher $\frac{y}{S_T/2}$.

In Figure 7.42, the dimensionless V velocity profiles in the gas region are shown for $S_T/d = 3$ and 9 at different axial locations. Far from the interface, the water vapour flows in the x direction and $V_G/U_{G,in}$ is zero. In the falling film above the tube, $x/d = -1$, the magnitude of the V velocity increases towards the interface. This increase is more noticeable in $S_T/d = 3$ because of the shorter distance between the interface and the top boundary of the gas phase. When the liquid film passes $\theta = 45^\circ$ at $x/d = -0.35$, V_G becomes positive close to the interface to facilitate absorption of vapour to the liquid film flowing along the tube curvature in both the $S_T/d = 3$ and 9 cases. At the side of the tube, $|V_G|$ increases towards the interface but suddenly becomes very small (almost zero) at the interface. A similar behaviour is observed in both S_T cases as the gas flow reaches the bottom of the tube and moves farther down the domain. The maximum value of $|V_G|$ increases between $x/d = 0.35$ to $x/d = 1$. This maximum value is larger for $S_T/d = 9$ compared to $S_T/d = 3$. V_G

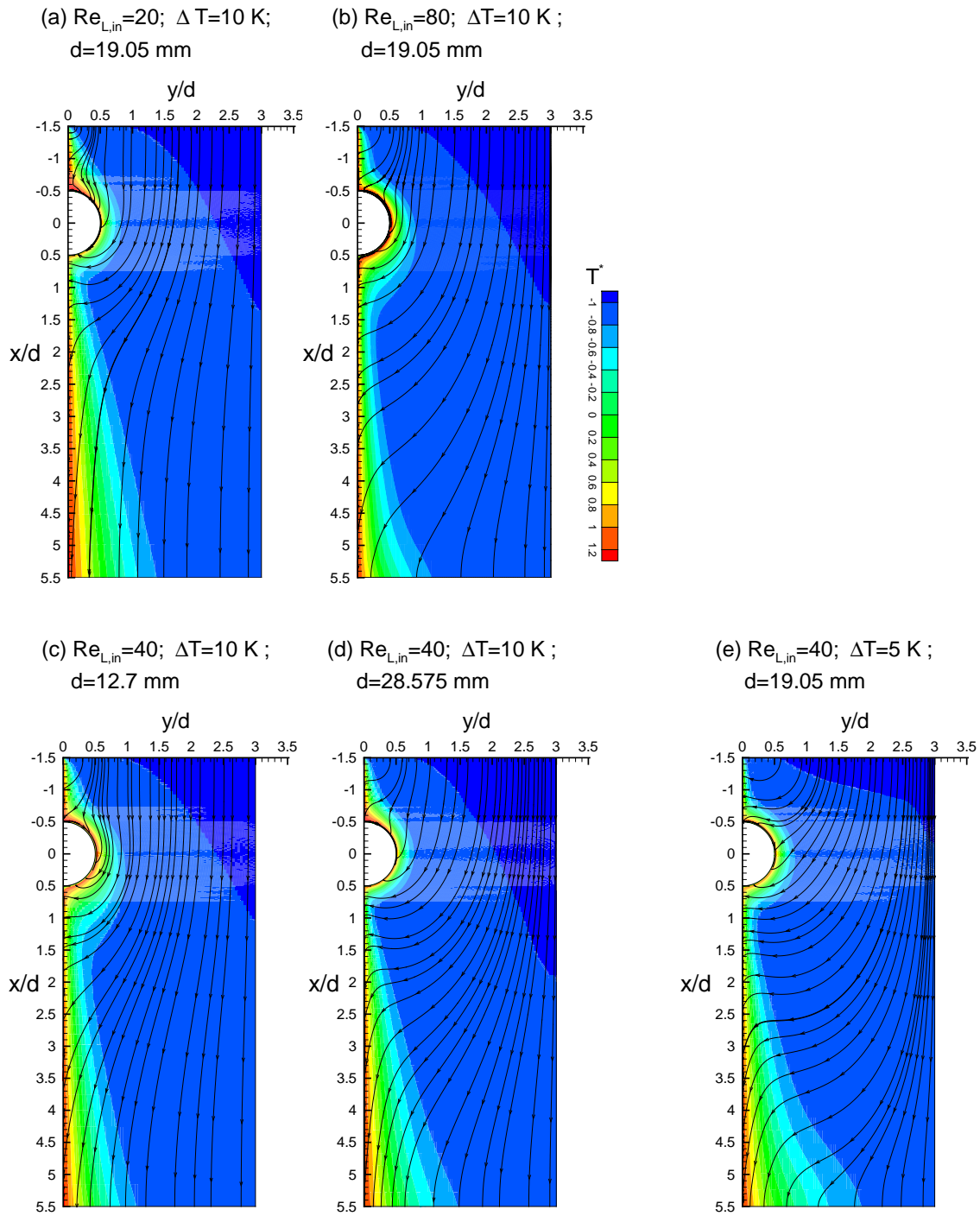


Figure 7.40: Flow streamlines and temperature contours in $S_T/d = 6$ for various combinations of $Re_{L,in}$, ΔT , and d , as indicated in the figure labels.

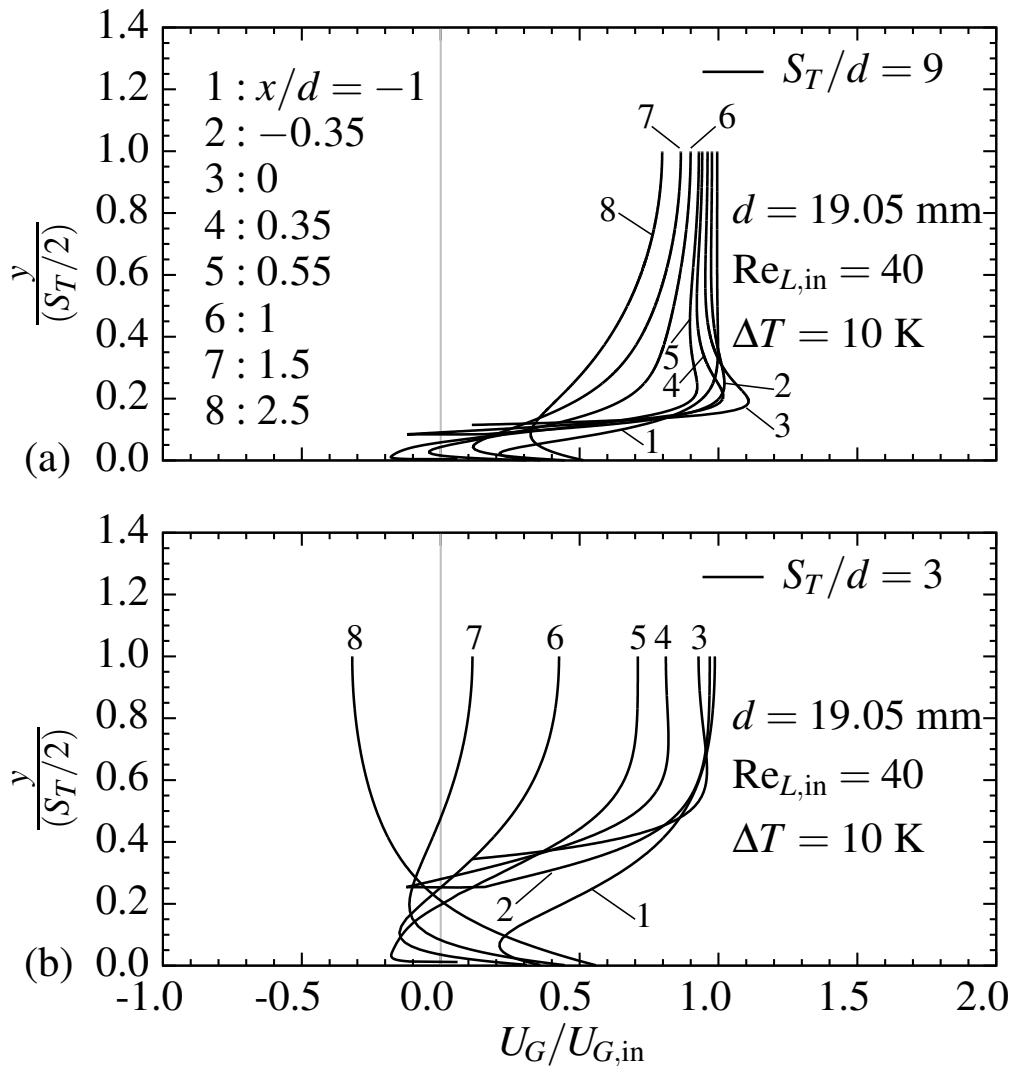


Figure 7.41: U velocity profiles in the gas at different axial locations for $d = 19.05$ mm, $Re_{L,in} = 40$ and $\Delta T = 10$ K (a) $S_T/d = 9$ and (b) $S_T/d = 3$ ($U_{G,in} = 1.35$ m s⁻¹).

decreases across the gas region farther in the x direction in both cases.

In Figure 7.43, the dimensionless temperature profiles in the gas region are shown at different axial locations for $S_T/d = 3$ and 9. The water vapour enters the computational domain at $T^* = -10$. For $S_T/d = 9$, a large portion of the gas phase remains at the initial temperature at all the selected axial locations whereas for $S_T/d = 3$ deviation from the initial temperature happens after $x/d = 1$

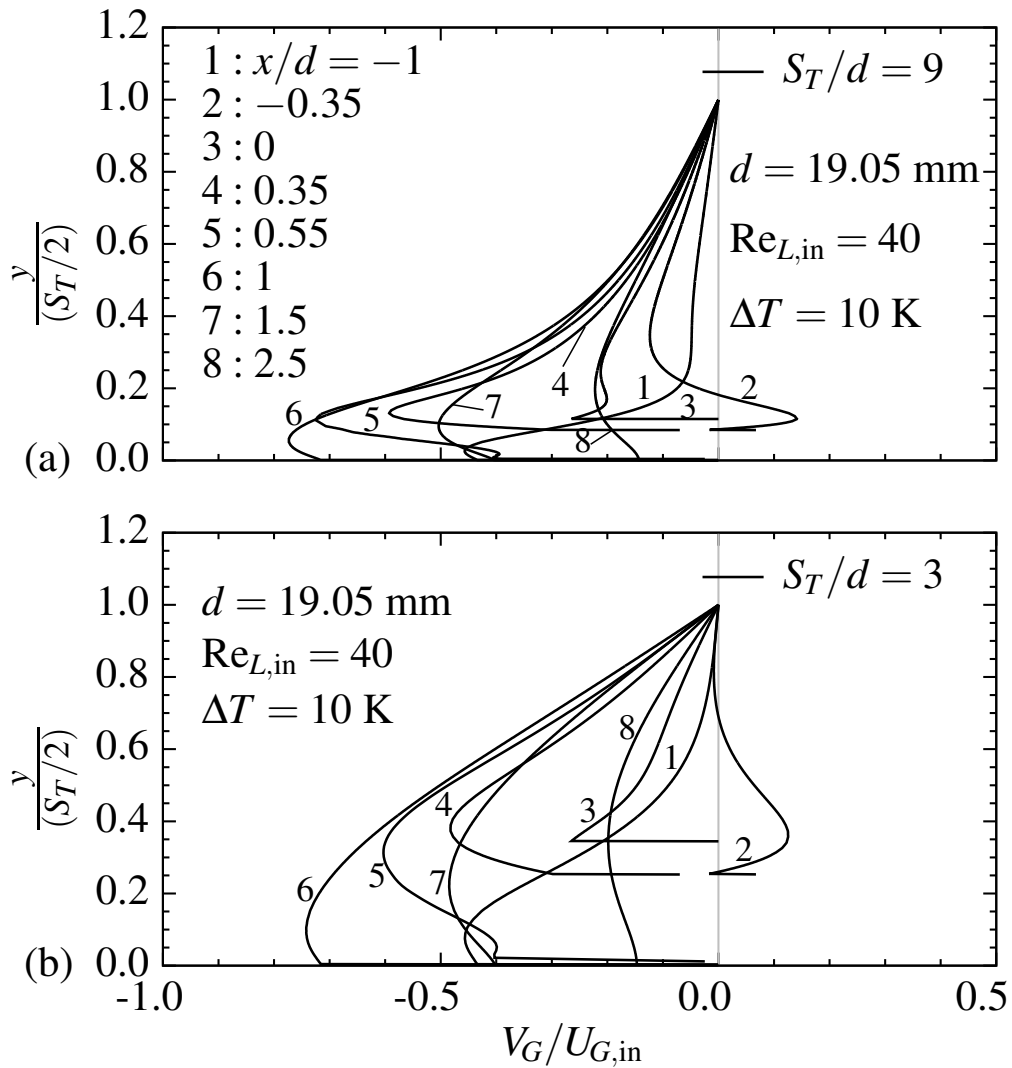


Figure 7.42: V velocity profiles in the gas at different axial locations for $d = 19.05$ mm, $Re_{L,in} = 40$ and $\Delta T = 10$ K (a) $S_T/d = 9$ and (b) $S_T/d = 3$ ($U_{G,in} = 1.35$ m s⁻¹).

at higher y values. The increase in T^* in the case with $S_T/d = 3$ occurs due to the entrance of mass at the outlet of the gas region. The water vapour enters the gas region at a high temperature (the film temperature when exiting the domain) to provide sufficient amount of vapour mass to be absorbed at the interface. As the gas flows in the x direction, the heat conducted from the liquid film to the vapour increases the temperature in nearly 25% and 80% of the gas phase region in

cases with $S_T/d = 9$ and 3, respectively. For $S_T/d = 9$, T^* increases in the x direction at the first half of the tube circumference and then decreases until the flow reaches $x/d = 1.5$. An increase in temperature is also observed between $x/d = 1.5$ and 2.5 in the x direction for $S_T/d = 9$. Over this section, the vapour is at the liquid outlet temperature, $T^* = 1.2$, in the case with $S_T/d = 3$.

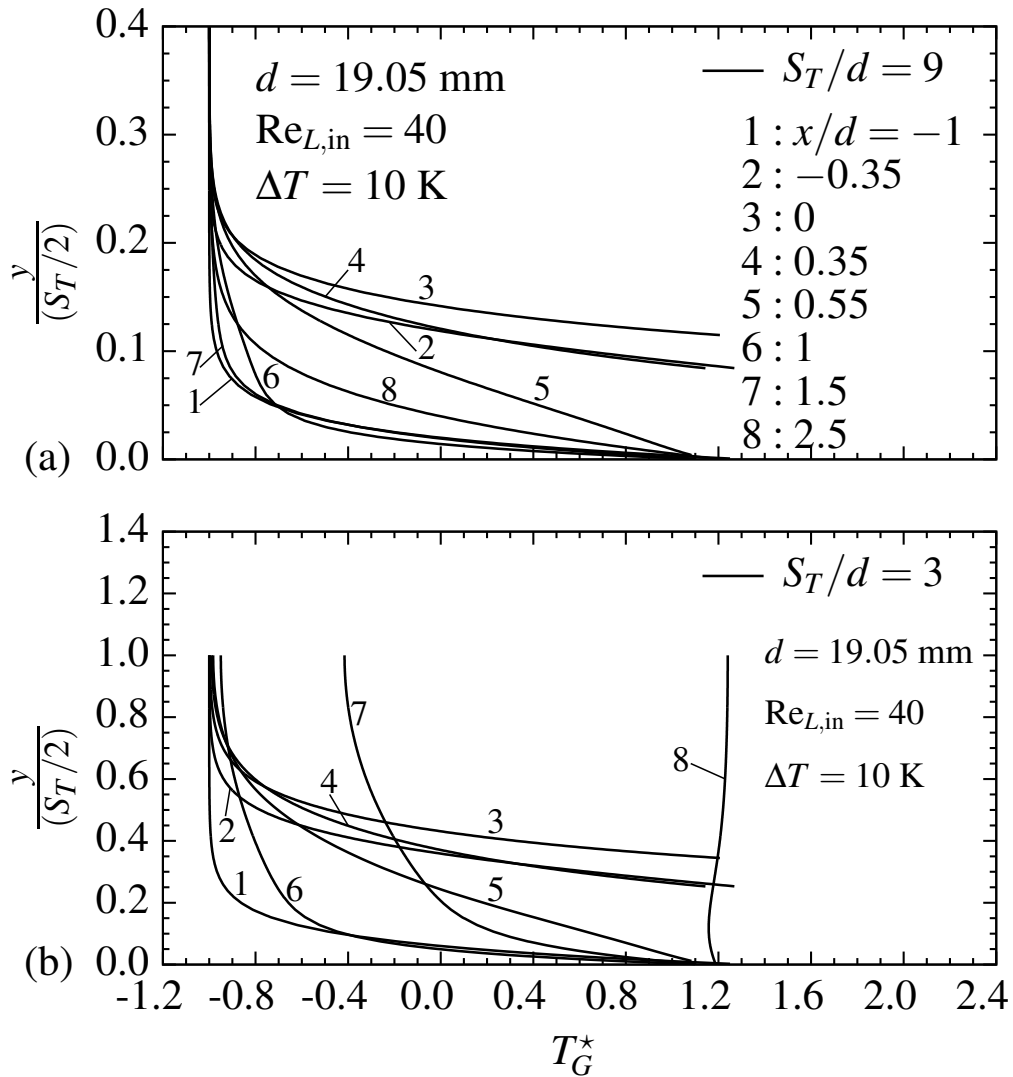


Figure 7.43: Temperature profiles in the gas at different axial locations for $d = 19.05$ mm, $Re_{L,in} = 40$ and $\Delta T = 10$ K (a) $S_T/d = 9$ and (b) $S_T/d = 3$.

For more details on the liquid film and gas phase development over the horizontal tube, the

dimensionless pressure profiles at different axial locations in the liquid and gas regions for $S_T/d = 3$ and 9 are presented in Appendix I.

The percentage of the total amount of mass absorbed over the tube to the liquid film inlet mass flow rate for all the parametric study cases is presented in Table 7.6. In cases with $\Delta T = 5$ K, $\dot{m}_{L,in} = 2.938 \times 10^{-2}$ kg s⁻¹, 5.876×10^{-2} kg s⁻¹, and 1.175×10^{-1} kg s⁻¹ for $Re_{L,in} = 20, 40,$ and $80,$ respectively. In cases with $\Delta T = 10$ K, $\dot{m}_{L,in} = 2.446 \times 10^{-2}$ kg s⁻¹, 4.893×10^{-2} kg s⁻¹, and 9.786×10^{-2} kg s⁻¹ for $Re_{L,in} = 20, 40,$ and $80,$ respectively. The absorbed mass ratio over the tube is very similar in $S_T/d = 3, 6,$ and $9.$ In cases with $Re_{L,in} = 20,$ absorption of mass at the interface increases over all the selected tubes as the inlet-to-wall temperature increases. $Re_{L,in} = 40$ shows a similar behaviour except over the tube with $d = 12.7$ mm. In this case, the increase in ΔT from 5 to 10 causes 10% decrease in total mass absorption. When the $Re_{L,in}$ increases to $80,$ all the cases show a noticeable decrease in the total mass absorbed at the interface. In $Re_{L,in} = 80,$ total absorbed mass ratio to the inlet liquid mass decreases by almost $42\%, 34\%,$ and 17% over $d = 12.7$ mm, 19.05 mm, and 28.575 mm, respectively when ΔT increases.

7.4.4 Computational Time

The system of equations of the coupled two-phase flow problems in this study is ill-conditioned and extremely hard to solve, and therefore requires the use of a computationally expensive direct solver. Table 7.7 shows the computational time for some of the parametric study cases to perform $10,000$ iterations. The compute times in Table 7.7 are serial calculation times. The parallelization of the elliptic model was tried using the PETSc software libraries. However, no significant improvement in the calculations times was observed. Therefore, serial calculation method was used to obtain the numerical results of the elliptic model.

Table 7.6: Total amount of the mass absorbed over the tube $\left(\frac{\dot{m}_{\text{inf,tot}}}{\dot{m}_{L,\text{in}}}\right)_{5 \leq \theta \leq 175} \times 100\%$ for the parametric study cases.

	$\text{Re}_{L,\text{in}}$	ΔT [K]	$d = 1/2$ [in] (12.7 [mm])	$d = 3/4$ [in] (19.05 [mm])	$d = 1 1/8$ [in] (28.575 [mm])
$S_T/d = 3$	20	5	1.943×10^{-3}	3.104×10^{-3}	4.922×10^{-3}
		10	2.541×10^{-3}	4.105×10^{-3}	6.442×10^{-3}
	40	5	8.647×10^{-4}	1.099×10^{-3}	1.619×10^{-3}
		10	7.799×10^{-4}	1.257×10^{-3}	2.100×10^{-3}
	80	5	6.965×10^{-4}	7.428×10^{-4}	8.169×10^{-4}
		10	3.999×10^{-4}	4.893×10^{-4}	6.762×10^{-4}
$S_T/d = 6$	20	5	1.941×10^{-3}	3.105×10^{-3}	5.206×10^{-3}
		10	2.543×10^{-3}	4.106×10^{-3}	6.440×10^{-3}
	40	5	8.657×10^{-4}	1.103×10^{-3}	1.643×10^{-3}
		10	7.803×10^{-4}	1.258×10^{-3}	2.101×10^{-3}
	80	5	6.999×10^{-4}	7.478×10^{-4}	8.202×10^{-4}
		10	4.019×10^{-4}	4.895×10^{-4}	6.756×10^{-4}
$S_T/d = 9$	20	5	1.944×10^{-3}	3.105×10^{-3}	4.979×10^{-3}
		10	2.542×10^{-3}	4.102×10^{-3}	6.421×10^{-3}
	40	5	8.658×10^{-4}	1.103×10^{-3}	1.636×10^{-3}
		10	7.804×10^{-4}	1.258×10^{-3}	2.101×10^{-3}
	80	5	7.000×10^{-4}	7.478×10^{-4}	8.225×10^{-4}
		10	4.001×10^{-4}	4.896×10^{-4}	6.749×10^{-4}

Table 7.7: Elliptic model compute times in horizontal tube cases.

	$d = 1/2$ [in] (12.7 [mm])		$d = 3/4$ [in] (19.05 [mm])		$d = 1 1/8$ [in] (28.575 [mm])	
	Grid $N_x \times N_y$	Compute time/10k [h]	Grid $N_x \times N_y$	Compute time/10k [h]	Grid $N_x \times N_y$	Compute time/10k [h]
$S_T/d = 3$	590×120	74	800×130	95	940×140	143
$S_T/d = 6$	590×150	121	800×170	202	940×190	312
$S_T/d = 9$	590×170	143	800×200	263	940×250	382

Chapter 8

Summary, Conclusions, and Recommendations for Future Work

8.1 Summary

In recent decades, growing concern toward environmental issues and energy needs provided the opportunity to improve the development and application of absorption refrigeration systems. These systems can run on low-grade energy such as solar energy, waste hot water, or a process excess steam. Using these energy sources reduces CO₂ emissions related to traditional vapour-compression cooling systems. Falling film absorbers are commonly used in absorption refrigeration systems and have a critical role in the efficiency and the cost of the cycle. In these absorbers, a liquid film of absorbent falling down over a surface is in contact with the absorbate vapour. The main objective of the present work was to enable a deeper understanding of the coupled heat, mass, and momentum transfer in the absorption process by a detailed simulation of the two-phase flow that will lead to a suitable numerical model. Such a model would permit refinements needed to optimize refrigeration system performance.

Previous numerical studies on LiBr falling film absorption can be categorized by the type of governing partial differential equations being solved: parabolic or elliptic. Many researchers used the parabolic approach to solve a set of simplified governing equations by applying a marching scheme to the single-phase flow of LiBr solution with a constant film thickness. As mentioned in the literature review, to the best knowledge of the author the implementation of an elliptic approach to study the two-phase falling film absorption in vertical channels and over horizontal tubes is limited to few numerical articles. In some of those studies, the film thickness variation and energy transfer due to mass diffusion were neglected and the impermeability of LiBr into the gas phase was not assured.

In the present study, first a laminar parabolic two-phase numerical method was applied to model the absorption of water vapour into a liquid film of LiBr-water solution flowing inside a vertical parallel plate channel. Compared to previous single-phase models, this two-phase model provided the opportunity of exploring the effect of gas flow on the transfer of heat, mass, and momentum at the interface. This approach was potentially a more accurate overall model that included the gas phase flow completely. Compared to previous two-phase models, this model had a variable film thickness. A mesh adaption to changing film thickness was facilitated by a coordinate transformation. The liquid-gas interface location was matched exactly with the mesh at every axial location in the solution. The appropriate interaction between the flows of the liquid and gas was assured by fundamental balances of energy, mass and shear force at the interface. A complete set of two-dimensional parabolic governing equations was solved using a marching scheme and a robust fully coupled solution approach. Detailed results were compared with the literature to demonstrate the validity of the this approach. The temperature, mass fraction and velocity profiles were presented for the single phase application of the model. The numerical model was then applied to the two-phase problem of simultaneous heat and mass transfer between the liquid and vapour phases. The effect of the liquid phase inlet Reynolds number, mass fraction, and cold wall temperature on the absorption process was examined. New results were presented to investigate the gas phase effect on mass absorption and liquid film thickness development. The examination of the absorber operating parameters effect showed that:

- The parabolic model predictions for the interfacial heat and mass fluxes, temperature and mass fraction in a vertical channels were in a good agreement with the previous works. However, for developing and fully developed liquid films with higher inlet Reynolds number, the parabolic model results were in qualitative agreement with the single-phase falling film models in the literature.
- The vapour mass absorption increases at the interface when a liquid film richer in LiBr is in contact with the water vapour.

- At a specific inlet mass fraction and Reynolds number, a decrease in the wall temperature increases the total amount of absorbed mass during absorption and thickens the film along the channel.
- At a specific inlet mass fraction and wall temperature, the mass and energy diffusion across the liquid film occurs faster in a slower moving liquid film and the interface temperature and mass fraction approach the end of absorption state in a shorter distance from the entrance of the channel.
- New results demonstrated that the axial development of the liquid film thickness is highly affected by the interfacial shear caused by the gas phase. A higher Reynolds number in the gas phase thins the liquid film and reduces the distance to reach the end of absorption conditions.

Next, an Eulerian approach was used to solve an implicitly coupled co-located elliptic two-dimensional set of governing equations on a structured non-orthogonal grid in a vertical channel. Mass, momentum, and energy conservation equations were solved for both liquid and gas phases. The comprehensive form of the energy conservation equation including the partial massive enthalpies and mass diffusion terms, and water mass fraction conservation equation were solved in the liquid phase. The pressure field was calculated implicitly for the entire domain. An adaptive-grid Eulerian method was used to track the interface precisely so that a grid line always coincides with the liquid-vapour interface. At each time step, the solution variables were first obtained on a fixed mesh. Then the new interface location was computed followed by a regeneration of the grid. This scheme was iterated over many time steps until the convergence to the desired solution was achieved. The fundamental balances of energy, mass, shear and normal forces were applied at the interface and the variation of thermophysical and transport properties was included. Detailed comparisons of the this work with Habib and Wood [18] and the parabolic model (developed previously) were conducted to demonstrate the validity of this model and also differentiate the characteristics of two-phase elliptic and parabolic approaches. The effect of changing the LiBr

solution mass diffusion coefficient, the interface heat of absorption, and the mass fraction condition were studied in those comparisons. Those results can be a useful benchmark for future detailed two-phase analysis of absorption. New results were also presented to investigate the pressure change effect on the interface heat and mass transfer and the liquid film development along the channel. The following results were obtained for the falling film in a vertical channel using the elliptic model:

- Excellent agreement was found between the elliptic model and the parabolic model results up to the axial point where insufficient vapour mass ceased the advancement of the parabolic model.
- Good agreement was obtained for the case study in which the liquid diffusion coefficient and the interface heat of absorption and impermeability condition were changed to reproduce the case in Habib and Wood [18]. A decrease in the total amount of LiBr was observed at the end of the channel when the interface mass fraction condition of Habib and Wood [18] was applied.
- The interface LiBr mass fraction, temperature, and mass and heat flux increased when the liquid diffusion coefficient and the heat of absorption were calculated based on well-established functions and applied to the case of Habib and Wood [18].
- Implementation of impermeability of LiBr to the gas phase at the interface increased the absorption of mass at the interface and the liquid film thickness in the case of Habib and Wood [18].
- When the pressure was increased from $P = 1$ kPa to $P = 2$ kPa with an increase in the liquid inlet temperature, the interface mass and heat transfer increased to noticeably higher values compared to the other case. It was observed that the larger temperature difference between the liquid inlet and the isothermal wall increases the total amount of mass absorbed at the interface and thickens the film along the channel.

- When the absorber inlet pressure was increased while keeping the inlet mass fraction and inlet liquid-wall temperature difference unchanged, a similar decrease in the interface LiBr mass fraction and temperature was observed between the lower and higher pressure absorbers. Higher heat and mass transfer to the liquid film was obtained in the higher pressure case.

To the best knowledge of the author, there are no experimental data to compare the results of the LiBr absorption simulation in a vertical parallel-plate channel. Therefore, the next step in this research was to apply the elliptic model to a falling film over a horizontal tube. The difficulty of numerical modelling of two-phase flow over a tube geometry added to the challenge of numerical modelling of the absorption phenomena. The elliptic model was validated against single-phase parabolic and elliptic numerical models and experimental data in the literature. The liquid energy equation and properties and the interface and tube wall conditions were modified if required to match the cases from the open literature. Finally, a parametric study was conducted using different tube diameters with different tube-to-tube spacing. The effects of changes in the liquid film inlet Reynolds number and the liquid-wall temperature on the absorption of water vapour into the liquid film over a horizontal tube were also investigated. The liquid film thickness, liquid film shape, interface temperature and mass fraction, local Nusselt number, and the interface mass flux variations over the tube were presented. The U -velocity, V -velocity, and temperature profiles in the liquid and gas regions and the mass fraction profiles in the liquid region were presented and discussed in detail. The following results were obtained for the flow over a horizontal tube:

- The elliptic model successfully predicted the shape of the liquid film, i.e. the falling film thickness above the tube, around the tube, and in the falling film region below the tube.
- The numerical results showed that an increase in the absorber pressure increases the liquid film outlet temperature below the tube. It was also shown that the liquid film outlet temperature increases almost linearly with the liquid inlet temperature at a constant pressure.

- The parametric study cases showed that liquid film thickness increases around the tube when the liquid film inlet Reynolds number increases. The liquid film shape at the top of the tube is highly affected by the liquid film inlet Reynolds number. The liquid film with a higher Reynolds number, thickens more under the tube and leaves the tube surface at a larger circumferential distance from the bottom stagnation point.
- The elliptic model predicted that the interface temperature and mass fraction variation over the horizontal tube is more significant at a higher liquid film inlet Reynolds number.
- A slight decrease in the liquid film thickness was observed when the liquid-tube wall temperature difference was increased. A smaller liquid-wall temperature difference produced higher water mass fraction from the top to the bottom of the tube.
- The local Nusselt number and the interface mass flux variations between different liquid Reynolds numbers are more noticeable when the liquid-wall temperature difference is smaller.
- Increasing the tube diameter decreased the liquid film thickness around the tube. For a smaller tube, at a smaller Reynolds number the film forms a larger bump at the top of the tube, whereas, at a higher Reynolds number the falling film is thicker below the tube.
- The liquid interface parameters were not affected by changing the transverse-direction distance between the tubes by a factor of three.

8.2 Conclusion

The two-phase fully-coupled parabolic and elliptic numerical models were successfully applied to simulate LiBr liquid film absorption in a vertical parallel-plate channel. The elliptic model also successfully computed the liquid and gas flow characteristics around a horizontal tube. The

following conclusions are drawn based on the performance and the capability of the parabolic and elliptic models:

1. A detailed parabolic model of falling film absorption in a vertical channel performs well in predicting absorption mass flow rate and film thickness for laminar film and vapour conditions.
2. The parabolic model applied to the falling film in a vertical channel is limited to situations where there is sufficient inlet mass flow of vapour to match the absorption rate.
3. The elliptic model performs very well but is computationally more expensive. Applying elliptic set of equations couples the interface position to all other unknowns and makes the numerical simulation more challenging. An improved solver for the equation set is needed.
4. The elliptic model predicts well the falling film absorption over a horizontal tube for laminar film and vapour flow conditions. The interface location at the top and bottom section of the tube is highly affected by the pressure gradient in the liquid film. Special treatment is required to maintain the numerical solution stable at these areas.
5. Explicit computation of the liquid film curvature and surface tension makes the elliptic model unstable. It is therefore concluded that implicit coupling of the curvature to the pressure and velocity variations at the interface and the interface location would be required to overcome this difficulty.

8.3 Recommendation for Future Works

To improve the capability and performance of the elliptic numerical model and to examine its potential the following future work is recommended:

1. Include the surface tension in the interface force balance

The surface tension coefficient and the interface curvature play an important role in forming the shape of the liquid film at the tube upper and lower stagnation points especially when the Reynolds number is low. The efforts made in this research to include the surface tension did not lead to a stable algorithm. A stable solution could be obtained by developing a robust, coupled calculation of the surface tension.

2. Apply effective iterative solvers to improve the model efficiency

The system of equations in the elliptic two-phase model is ill-conditioned because of the strong coupling of the solution variables at the interface. Not all the iterative solvers are capable of solving such a system. The direct solvers used in this work solved this type of equation system but it was not computationally cost-effective. To benefit from the advantages of both type of solvers, one could solve the system of equations in the gas and liquid regions by iterative solvers and then apply the direct solver to the interface equations. A suitable method of information transfer between the liquid and gas phases would be required to assure the interaction between phases.

3. Couple the interface movement and location into the field variable set of equations

A faster convergence in the elliptic numerical solution in complex geometries, e.g. flow over a tube, could be achieved if the location of the interface were implicitly coupled to the two-phase governing equations.

4. Investigate the effect of a non-absorbable gas on LiBr absorption

The presence of a non-absorbable gas, e.g. air, in the gas region could highly affect the mass absorption, temperature, and mass fraction variation at the liquid-gas interface. Consideration of the presence of non-absorbable gas in the LiBr falling film absorption would allow the extension of the numerical solution to mixtures with volatile absorbent, e.g. ammonia-water with and without air in the gas phase.

5. Apply the elliptic numerical model to simulate the absorption of a volatile absorbent

In the case of absorption of a volatile absorbent, e.g. ammonia, the liquid and gas regions are both binary mixtures. In this case, an extra conservation of mass equation is required to calculate the absorbent mass fraction in the gas region. The presence of a non-absorbable gas could change the gas phase to a ternary system and adds to the complexity of the heat and mass transfer in absorption phenomena. This would lead to development of a general model that can be applied to different fluid combinations.

6. Add turbulence models to the liquid and gas phase equations

Applying a turbulence model to the liquid and gas regions would provide the possibility of modelling the flows with higher Reynolds number and investigation of the falling film characteristics in a wider range of mass flow rates.

References

- [1] L. A. McNeely, Thermodynamic properties of aqueous solutions of lithium bromide, *ASHARE, Trans.* **85** (1977), 413–434.
- [2] T. Uemura and S. Hasaba, Studies on the lithium bromide-water absorption refrigerating machine, Tech. Rep. 6 (1964).
- [3] D. A. Siebe, Evaluation of air-conditioning systems utilizing liquid absorbents regenerated by solar energy, Ph.D. thesis, Arizona State University, Tempe, Arizona (1986).
- [4] K. E. Herold, R. Radermacher and S. A. Klein, *Absorption Chillers and Heat Pumps*, 1st ed., CRC Press (1996).
- [5] J. D. Killion and S. Garimella, A critical review of models of coupled heat and mass transfer in falling-film absorption, *International Journal of Refrigeration* **24**(8) (Dec. 2001), 755–797.
- [6] V. E. Nakoryakov and N. I. Grigor'eva, Combined heat and mass transfer during absorption in drops and films, *Journal of engineering physics* **32**(2) (1977), 243–247.
- [7] N. I. Grigor'eva and V. E. Nakoryakov, Exact solution of combined heat and mass transfer problems during film absorption, *Journal of engineering physics* **33**(5) (1977), 1349–53.
- [8] G. Grossman, Simultaneous heat and mass transfer in film absorption under laminar flow, *International Journal of Heat and Mass Transfer* **26**(3) (Mar. 1983), 357–371.
- [9] A. T. Conlisk and J. Mao, Nonisothermal absorption on a horizontal cylindrical tube –1. The film flow, *Chemical Engineering Science* **51**(8) (Apr. 1996), 1275–1285.
- [10] J. W. Andberg and G. C. Vliet, Nonisothermal absorption of gases into falling liquid films, in *ASME-JSME*, Vol. 2, pp. 423–431, Honolulu, HI, USA (1983).
- [11] N. Kawae, T. Shigechi, K. Kanemaru and T. Yamada, Water vapor evaporation into laminar film flow of a lithium bromide-water solution (influence of variable properties and inlet film

References

- thickness on absorption mass transfer rate), *Heat Transfer Japanese Research* **18** (1989), 58–70.
- [12] M. Mittermaier, P. Schulze and F. Ziegler, A numerical model for combined heat and mass transfer in a laminar liquid falling film with simplified hydrodynamics, *International Journal of Heat and Mass Transfer* **70** (Mar. 2014), 990–1002.
- [13] M. Mittermaier and F. Ziegler, Theoretical evaluation of absorption and desorption processes under typical conditions for chillers and heat transformers, *International Journal of Refrigeration* **59** (Nov. 2015), 91–101.
- [14] M. Mittermaier and F. Ziegler, Impact of a developing velocity profile on heat and mass transfer in absorbing laminar falling films, *Chemie Ingenieur Technik* **88**(1-2) (Feb. 2016), 139–146.
- [15] M. Mittermaier and F. Ziegler, The impact of viscosity on the combined heat, mass and momentum transfer in laminar liquid falling films, *Heat and Mass Transfer* **54**(4) (2018), 1199–1215.
- [16] L. Zhang, Y. Wang, Y. Fu, L. Xing and L. Jin, Numerical simulation of H₂O/LiBr falling film absorption process, *Energy Procedia* **75** (Aug. 2015), 3119–3126.
- [17] S. Armou, R. Mir, Y. El hammami, S. El hamdani and K. Zine-Dine, Numerical study of simultaneous heat and mass transfer in absorption of vapor in laminar liquid film, *International Journal of Enhanced Research in Science, Technolog & Engineering* **5**(4) (2016), 36–46.
- [18] H. M. Habib and B. D. Wood, Simultaneous heat and mass transfer for a falling film absorber – the two phase flow problem, in *ASME*, Miami, Florida, USA (1990).
- [19] H. M. Habib and B. D. Wood, Simultaneous heat and mass transfer in film absorption with the presence of non-absorbable gases, *Journal of Heat Transfer* **123**(5) (Dec. 2000), 984–989.

References

- [20] W. Chen and G. C. Vliet, Effect of an inert gas on heat and mass transfer in a vertical channel with falling films, *Journal of Solar Energy Engineering* **119**(1) (Feb. 1997), 24–30.
- [21] J. W. Andberg, Absorption of vapors into liquid films flowing over cooled horizontal tubes, PhD Thesis, Texas, Austin (1986).
- [22] J. W. Andberg and G. C. Vliet, A simplified model absorption of vapors into liquid films flowing over cooled horizontal tubes, *ASHRAE Transaction* **93**(Part 2) (1987), 2454–2466.
- [23] S. K. Choudhury, D. Hisajima, T. Ohuchi, A. Nishiguchi, T. Fukushima and S. Sakaguchi, Absorption of vapors into liquid films flowing over cooled horizontal tubes, *ASHRAE Transaction Research* **99**(Part 2) (1993), 81–89.
- [24] J. K. Min and D. H. Choi, Analysis of the absorption process on a horizontal tube using Navier-Stokes equations with surface-tension effects, *International Journal of Heat and Mass Transfer* **42** (Dec. 1999), 4567–4578.
- [25] V. M. Soto Francés and J. M. Pinazo Ojer, Validation of a model for the absorption process of H₂O(vap) by a LiBr(aq) in a horizontal tube bundle, using a multi-factorial analysis, *International Journal of Heat and Mass Transfer* **46**(17) (Aug. 2003), 3299–3312.
- [26] J. D. Killion and S. Garimella, Simulation of pendant droplets and falling films in horizontal tube absorbers, *Journal of Heat Transfer* **126**(6) (Dec. 2004), 1003–1013.
- [27] F. Babadi and B. Farhanieh, Characteristics of heat and mass transfer in vapor absorption of falling film flow on a horizontal tube, *International communications in heat and mass transfer* **32**(9) (2005), 1253–1265.
- [28] V. D. Papaefthimiou, D. C. Karampinos and E. D. Rogdakis, A detailed analysis of water-vapour absorption in LiBr–H₂O solution on a cooled horizontal tube, *Applied Thermal Engineering* **26**(17) (Dec. 2006), 2095–2102.

References

- [29] S. S. Seol and S. Y. Lee, Experimental study of film flow and heat/mass transfer in LiBr–H₂O solution flowing over a cooled horizontal tube, *International Communications in Heat and Mass Transfer* **32**(3) (Feb. 2005), 445–453.
- [30] I. Kyung, K. E. Herold and Y. T. Kang, Model for absorption of water vapor into aqueous LiBr flowing over a horizontal smooth tube, *International Journal of Refrigeration* **30**(4) (Jun. 2007), 591–600.
- [31] M. J. Kirby and P. Perez-Blanco, A design model for horizontal tube water/lithium bromide absorbers, in: *Heat Pump and Refrigeration Systems Design, Analysis and Applications*, ASME AES-32 (1994), 1–10.
- [32] I. Kyung, K. E. Herold and Y. T. Kang, Experimental verification of H₂O/LiBr absorber bundle performance with smooth horizontal tubes, *International Journal of Refrigeration* **30**(4) (Jun. 2007), 582–590.
- [33] I.-S. Kyung and K. E. Herold, Performance of horizontal smooth tube absorber with and without 2-ethyl-hexanol, *Journal of Heat Transfer* **124**(1) (Jun. 2001), 177–183.
- [34] V. D. Papaefthimiou, I. P. Koronaki, D. C. Karampinos and E. D. Rogdakis, A novel approach for modelling LiBr–H₂O falling film absorption on cooled horizontal bundle of tubes, *International Journal of Refrigeration* **35**(4) (Jun. 2012), 1115–1122.
- [35] T. Nomura, N. Nishimura, S. Wei, S. Yamaguchi and R. Kawakami, Heat and mass transfer mechanism in the absorber of water/LiBr conventional absorption refrigerator: experimental examination by visualized model, Vol. 31, pp. 203–208, The Advanced Energy System Division, ASME, New Orleans, Louisiana (1993).
- [36] G. Ji, J. Wu, Y. Chen and G. Ji, Asymmetric distribution of falling film solution flowing on hydrophilic horizontal round tube, *International Journal of Refrigeration* **78** (Jun. 2017), 83–92.

References

- [37] F. Cosenza and G. C. Vliet, Absorption in falling water/LiBr films on horizontal tubes, *ASHRAE Transaction* **96**(Part 1) (1990), 693–701.
- [38] L. Hoffmann, I. Greiter, A. Wagner, V. Weiss and G. Alefeld, Experimental investigation of heat transfer in a horizontal tube falling film absorber with aqueous solutions of LiBr with and without surfactants, *International Journal of Refrigeration* **19**(5) (Jun. 1996), 331–341.
- [39] V. M. Soto Francés and J. M. Pinazo Ojer, Experimental study about heat and mass transfer during absorption of water by an aqueous lithium bromide solution, in *ASME-ZSITS International Thermal Science Seminar*, ASME, Bled, Slovenia (2000).
- [40] K. Kwon and S. Jeong, Effect of vapor flow on the falling-film heat and mass transfer of the ammonia/water absorber, *International Journal of Refrigeration* **27**(8) (Dec. 2004), 955–964.
- [41] S. Lee, L. K. Bohra, S. Garimella and A. K. Nagavarapu, Measurement of absorption rates in horizontal-tube falling-film ammonia-water absorbers, *International Journal of Refrigeration* **35**(3) (May 2012), 613–632.
- [42] A. K. Nagavarapu and S. Garimella, Falling-film absorption around microchannel tube banks, *Journal of Heat Transfer* **135**(12) (Dec. 2013), 122001 (1–10).
- [43] ASHRAE, *ASHRAE Handbook of Fundamentals*, chap. Thermophysical Properties of Refrigerants, p. 30.73, American Society of Heating, Refrigerating and Air-Conditioning Engineers, Atlanta, GA, U.S.A. (2017).
- [44] E. A. Saleh and S. J. Ormiston, A sharp-interface elliptic numerical model of laminar two-phase gas-liquid downward flow in a vertical parallel plate channel, *The Canadian Journal of Chemical Engineering* **95**(3) (Mar. 2017), 568–577.
- [45] J. W. Andberg, Non-isothermal absorption of gases into falling liquid films, M.Sc. thesis, Texas, Austin (1982).

References

- [46] J. D. Killion and S. Garimella, A review of experimental investigations of absorption of water vapor in liquid films falling over horizontal tubes, *HVAC&R Research* **9**(2) (Apr. 2003), 111–136.
- [47] E. C. Siow, Numerical solution of a two-phase model for laminar film condensation of vapour-gas mixtures in channels, M.Sc. thesis, University of Manitoba, Department of Mechanical and Industrial Engineering (July 2001).
- [48] Y. Q. Wang, L. A. Penner and S. J. Ormiston, Analysis of laminar forced convection of air for crossflow in banks of staggered tubes, *Numerical Heat Transfer, Part A: Applications* **38**(8) (2000), 819–845.
- [49] S. V. Patankar, *Numerical Heat Transfer and Fluid Flow*, Hemisphere, Washington DC (1980).
- [50] A. Behie, D. Collins and P. Forsyth Jr., Fully coupled multiblock wells in oil simulation, *Society of Petroleum Engineers Journal* (1985), 535–542.
- [51] C. M. Rhie and W. L. Chow, Numerical study of the turbulent flow past an airfoil with trailing edge separation, *AIAA Journal* **21**(11) (1983), 1525–1532.
- [52] G. D. Raithby and G. E. Schneider, *Elliptic systems: Finite-difference method II*, *Handbook of Numerical Heat Transfer*, edited by W. J. Minkowycz, E. M. Sparrow, G. E. Schneider and R. H. Pletcher, John Wiley & Sons (1988).
- [53] J. Van Doormaal and C. Raithby, Enhancements of the simple method for predicting incompressible fluid flows, *Numerical Heat Transfer* **7** (1984), 147–163.
- [54] X. S. L and J. W. Demmel, Superlu-dist: A scalable distributed-memory sparse direct solver for unsymmetric linear systems, *ACM Trans. Math. Softw.* **29**(2) (June 2003), 110–140.

References

- [55] G. A. Florides, S. A. Kalogirou, S. A. Tassou and L. C. Wrobel, Design and construction of a LiBr–water absorption machine, *Energy Conversion and Management* **44**(15) (Sep. 2003), 2483–2508.
- [56] J. Pátek and J. Klomfar, A computationally effective formulation of the thermodynamic properties of LiBr–H₂O solutions from 273 to 500K over full composition range, *International Journal of Refrigeration* **29**(4) (Jun. 2006), 566–578.
- [57] E. W. Lemmon, M. L. Huber and M. O. McLinden, NIST Standard Reference Database 23: Reference Fluid Thermodynamic and Transport Properties-REFPROP, Version 9.1, National Institute of Standards and Technology (2013).
- [58] R. Abbasi Havestini and S. J. Ormiston, Fully coupled two-phase numerical model for falling film absorption in a vertical parallel plate channel, *International Journal of Refrigeration* **95** (Nov. 2018), 108–121.
- [59] T. Kashiwagi, Heat and mass diffusion in the absorption of water vapor by aqueous solution of lithium bromide, *Transactions of the Japanese Association of Refrigeration* **1** (1984), 89–98.
- [60] Z. Yuan and K. E. Herold, Thermodynamic properties of aqueous lithium bromide using a multiproperty free energy correlation, *HVAC&R Research* **11**(3) (Jul. 2005), 377–393.
- [61] R. E. Balzhiser, M. R. Samuels and J. D. Eliassen, *Chemical Engineering Thermodynamics: The Study of Energy, Entropy, and Equilibrium*, Prentice-Hall, Inc., New Jersey (1972).
- [62] J. M. Smith, H. C. Van Ness, M. M. Abbott and M. T. Swihart, *Introduction to Chemical Engineering Thermodynamics*, eighth ed., McGraw-Hill Education, New York (2018).
- [63] R. B. Bird, W. E. Stewart and E. N. Lightfoot, *Transport Phenomena*, 2nd ed., John Wiley and Sons, Inc., New York (2002).

Appendix A

Equilibrium Conditions

A.1 Equilibrium Condition by McNeely [1]

In Equation (A.1) the temperature and pressure are in °C and kPa, respectively. The mass fraction between 0 and 1 is represented as a value between 0 and 100; for example, 0.45 is represented as 45.

$$T = \left[\frac{-2E_0}{D_0 + [D_0^2 - 4E_0(C_0 - \log P)]^{0.5}} - 273.15 \right] \left[\sum_{i=0}^3 A_i \xi_{\text{LiBr}}^i \right] + \left[\sum_{i=0}^3 B_i \xi_{\text{LiBr}}^i \right]$$

$5^\circ\text{C} < T < 175^\circ\text{C}$

$45 < \xi_{\text{LiBr}} < 70$ (percentage)

(A.1)

i	A_i	B_i	C_i	D_i	E_i
0	-2.00755	124.937	7.05	-1603.54	-104095.5
1	0.16976	-7.71649			
2	-3.133362×10^{-3}	0.152286			
3	1.97668×10^{-5}	-7.9509×10^{-4}			

Note that D_0 has been changed from the incorrect value of -1596.49 that appeared in [43].

A.2 Equilibrium Condition by Uemura and Hasaba [2]

In Equation (A.2) the temperature and pressure are in K and kPa, respectively. The mass fraction is a value between 0 and 100.

$$T = \frac{-B + \sqrt{B^2 - 4(A - \log P)C}}{2(A - \log P)}$$

$$A = \sum_{i=0}^2 A_i \xi_{\text{LiBr}}^i \quad B = \sum_{i=0}^2 B_i \xi_{\text{LiBr}}^i \quad C = \sum_{i=0}^2 C_i \xi_{\text{LiBr}}^i \quad (\text{A.2})$$

$$293.15 \text{ K} < T < 433.15 \text{ K}$$

$$22.8 < \xi_{\text{LiBr}} < 64.5 \quad (\text{percentage})$$

i	A_i	B_i	C_i
0	3.1934	1.0575×10^3	-6.0135×10^5
1	1.3292×10^{-1}	-9.4632×10^1	1.9734×10^4
2	-1.4278×10^{-3}	0.9816	-2.3701×10^2

A.3 Equilibrium Condition by Siebe [3]

In Equation (A.3) the temperature and pressure are in K and kPa, respectively. The mass fraction is a value between 0 and 100.

$$T = \frac{-B + \sqrt{B^2 - 4(A - \log P)C}}{2(A - \log P)}$$

$$A = \sum_{i=0}^3 A_i \xi_{\text{LiBr}}^i \quad B = \sum_{i=0}^3 B_i \xi_{\text{LiBr}}^i \quad C = \sum_{i=0}^3 C_i \xi_{\text{LiBr}}^i \quad (\text{A.3})$$

$$278.15 \text{ K} < T < 453.15 \text{ K}$$

$$45 < \xi_{\text{LiBr}} < 70 \quad (\text{percentage})$$

i	A_i	B_i	C_i
0	7.21801125	-1.7357634×10^3	-7.9200099×10^4
1	-5.338194×10^{-2}	4.114777×10^1	-7.9495427×10^3
2	3.02272×10^{-3}	-2.34992885	4.5392005×10^2
3	$-4.0777142 \times 10^{-5}$	3.011991×10^{-2}	-6.04903641

A.4 Equilibrium Condition by Mittermaier et al. [12]

The equilibrium condition from Mittermaier et al. [12] was written as:

$$\begin{aligned} \frac{-1}{T} = & a_0 + a_1 \xi_{\text{LiBr}} + a_2 \ln P + a_3 \xi_{\text{LiBr}} \ln P + a_4 \xi_{\text{LiBr}}^2 + a_5 (\ln P)^2 + a_6 \xi_{\text{LiBr}}^2 \ln P + a_7 \xi_{\text{LiBr}} (\ln P)^2 \\ & + a_8 \xi_{\text{LiBr}}^2 (\ln P)^2 + a_9 \xi_{\text{LiBr}}^3 + a_{10} (\ln P)^3 + a_{11} \xi_{\text{LiBr}}^3 \ln P + a_{12} \xi_{\text{LiBr}}^3 (\ln P)^2 + a_{13} \xi_{\text{LiBr}} (\ln P)^3 \\ & + a_{14} \xi_{\text{LiBr}}^2 (\ln P)^3 + a_{15} \xi_{\text{LiBr}}^3 (\ln P)^3 \end{aligned} \quad (\text{A.4})$$

In Equation (A.4), the temperature and pressure are in K and Pa, respectively. The mass fraction is between 0 and 1. Note that the coefficient a_6 is changed to -0.000495401 from the incorrect value that appeared in [12]. The range of applicability of Equation (A.4) was not stated by Mittermaier et al. [12].

i	a_i	i	a_i
0	-4.708580×10^{-3}	8	$+1.104770 \times 10^{-4}$
1	-1.276757×10^{-3}	9	$+4.915398 \times 10^{-3}$
2	$+1.455970 \times 10^{-4}$	10	-7.21234×10^{-8}
3	$+4.282610 \times 10^{-4}$	11	-5.81210×10^{-4}
4	$+9.485260 \times 10^{-4}$	12	-2.23738×10^{-5}
5	$+3.475010 \times 10^{-6}$	13	$+2.39788 \times 10^{-6}$
6	-4.954010×10^{-4}	14	-6.64049×10^{-6}
7	-5.444720×10^{-5}	15	$+4.26683 \times 10^{-6}$

Appendix B

Mixture Energy Equation

The enthalpy of a multicomponent solution (if there is no chemical reaction between the components) is a function of pressure, temperature, and mass fraction of the components. In general, for a multicomponent system like a solution, the change in enthalpy (which is related to energy transport) must include pressure, temperature, and mass fraction effects.

$$h = h(P, T, \xi_1, \xi_2, \dots, \xi_i, \dots) \quad (\text{B.1})$$

where ξ_i is the mass fraction of component i in the solution.

The total differential of h is then:

$$dh = \left(\frac{\partial h}{\partial P} \right)_{T, \xi} dP + \left(\frac{\partial h}{\partial T} \right)_{P, \xi} dT + \sum_{i=1}^n \left(\frac{\partial h}{\partial \xi_i} \right)_{P, T, \xi_j} d\xi_i \quad (\text{B.2})$$

The partial massive enthalpy \bar{h}_i of species i is defined as:

$$\bar{h}_i = \left(\frac{\partial h}{\partial \xi_i} \right)_{P, T, \xi_j} \quad (\text{B.3})$$

Equation (B.3), sometimes called a *response function*, is a *measure* of the response of total enthalpy to the addition of an infinitesimal amount of species i to a finite amount of solution at constant P and T . Therefore, $\bar{h}_i d\xi_i$ represents the change in enthalpy of the solution brought about by adding an increment of component i , $d\xi_i$, to the solution while holding the pressure, temperature, and all the other components mass fraction constant. \bar{h}_i is a function of pressure, temperature, and the composition of the solution.

Equations (B.2) and (B.3) may express the solution enthalpy on a unit-mass basis:

$$d(mh) = \left(\frac{\partial(mh)}{\partial P} \right)_{T, m} dP + \left(\frac{\partial(mh)}{\partial T} \right)_{P, m} dT + \sum_{i=1}^n \left(\frac{\partial(mh)}{\partial m_i} \right)_{P, T, m_j} dm_i \quad (\text{B.4})$$

$$\bar{h}_i = \left(\frac{\partial(mh)}{\partial m_i} \right)_{P,T,m_j} \quad (\text{B.5})$$

Because the first two partial derivatives on the right-hand side of Equation (B.4) are evaluated at constant m and because the partial derivative of the last term is given by Equation (B.5), Equation (B.4) can have a simpler form:

$$d(mh) = m \left(\frac{\partial h}{\partial P} \right)_{T,\xi} dP + m \left(\frac{\partial h}{\partial T} \right)_{P,\xi} dT + \sum_{i=1}^n \bar{h}_i dm_i \quad (\text{B.6})$$

Because $m_i = \xi_i m$,

$$dm_i = \xi_i dm + m d\xi_i \quad (\text{B.7})$$

Moreover,

$$d(mh) = mdh + hdm \quad (\text{B.8})$$

If dm_i and $d(mh)$ are replaced in Equation (B.6) and terms are collected for m and dm :

$$\left[dh - \left(\frac{\partial h}{\partial P} \right)_{T,\xi} dP - \left(\frac{\partial h}{\partial T} \right)_{P,\xi} dT - \sum_{i=1}^n \bar{h}_i d\xi_i \right] m + \left[h - \sum_{i=1}^n \xi_i \bar{h}_i \right] dm = 0 \quad (\text{B.9})$$

m and dm are independent and arbitrary. The only way that the left-hand side of Equation (B.9) can, in general, be zero is for each bracket to be zero. Making the first bracket zero will give the change in solution enthalpy based on the mass fraction (Equations (B.2) and (B.3)):

$$dh = \left(\frac{\partial h}{\partial P} \right)_{T,\xi} dP + \left(\frac{\partial h}{\partial T} \right)_{P,\xi} dT + \sum_{i=1}^n \bar{h}_i d\xi_i \quad (\text{B.10})$$

Making the second bracket zero yields to:

$$h = \sum_{i=1}^n \xi_i \bar{h}_i \quad (\text{B.11})$$

Equation (B.11), known as *summability relation*, allows the calculation of mixture enthalpy from partial enthalpies. Partial enthalpies of species could be evaluated using the intercept rule, to be

explained later, on a mixture enthalpy diagram. These diagrams are usually based on experimental data.

For a binary solution the summability relation becomes:

$$h = \xi_1 \bar{h}_1 + \xi_2 \bar{h}_2 \quad (\text{B.12})$$

and

$$dh = \xi_1 d\bar{h}_1 + \bar{h}_1 d\xi_1 + \xi_2 d\bar{h}_2 + \bar{h}_2 d\xi_2 \quad (\text{B.13})$$

Combining this equation with Equation (B.10) for a binary mixture yields to:

$$\left(\frac{\partial h}{\partial P}\right)_{T,\xi} dP + \left(\frac{\partial h}{\partial T}\right)_{P,\xi} dT - \xi_1 d\bar{h}_1 - \xi_2 d\bar{h}_2 = 0 \quad (\text{B.14})$$

For any enthalpy change at constant P and T :

$$\xi_1 d\bar{h}_1 + \xi_2 d\bar{h}_2 = 0 \quad (\text{B.15})$$

This result is known as Gibbs-Duhem equation. dh in Equation (B.13) at constant pressure and temperature becomes:

$$dh = \bar{h}_1 d\xi_1 + \bar{h}_2 d\xi_2 \quad (\text{B.16})$$

The last term in Equation (B.10) can be replaced by Equation (B.16) for a binary mixture:

$$dh = \left(\frac{\partial h}{\partial P}\right)_{T,\xi} dP + \left(\frac{\partial h}{\partial T}\right)_{P,\xi} dT + \bar{h}_1 d\xi_1 + \bar{h}_2 d\xi_2 \quad (\text{B.17})$$

Because $\xi_1 + \xi_2 = 1$ and $d\xi_1 = -d\xi_2$:

$$dh = \left(\frac{\partial h}{\partial P}\right)_{T,\xi} dP + \left(\frac{\partial h}{\partial T}\right)_{P,\xi} dT + (\bar{h}_1 - \bar{h}_2) d\xi_1 \quad (\text{B.18})$$

On a mass fraction-enthalpy diagram for a binary mixture, the partial enthalpies are calculated directly from an expression for the solution enthalpy as a function of composition at constant P and T :

$$\frac{dh}{d\xi_1} = \bar{h}_1 - \bar{h}_2 \quad (\text{B.19})$$

Equation (B.12) can be written as:

$$h = \xi_1 (\bar{h}_1 - \bar{h}_2) + \bar{h}_2 \quad \text{and} \quad h = \bar{h}_1 - (1 - \xi_1) (\bar{h}_1 - \bar{h}_2) \quad (\text{B.20})$$

Combination of these equations and Equation (B.19) become:

$$\bar{h}_1 = h + (1 - \xi_1) \frac{dh}{d\xi_1} \quad \text{and} \quad \bar{h}_2 = h - \xi_1 \frac{dh}{d\xi_1} \quad (\text{B.21})$$

Thus, the intercepts tangent to the enthalpy digram of a solution (right-hand sides in Equation (B.21)) give the value of partial enthalpies.

The change in the enthalpy of a binary mixture at constant pressure with no chemical reaction becomes:

$$dh = C_p dT + (\bar{h}_1 - \bar{h}_2) d\xi_1 \quad (\text{B.22})$$

where

$$C_p = \left(\frac{\partial h}{\partial T} \right)_{P, \xi} \quad (\text{B.23})$$

The relationship of the mixture specific heat, C_p , to the specific heats of the components can be found by applying the definition in Equation (B.23) to summability rule, Equation (B.12):

$$C_p = \xi_1 \left(\frac{\partial h_1}{\partial T} \right)_{P, \xi_1} + (1 - \xi_1) \left(\frac{\partial h_2}{\partial T} \right)_{P, \xi_1} = \xi_1 \bar{C}_{p1} + (1 - \xi_1) \bar{C}_{p2} \quad (\text{B.24})$$

where \bar{C}_{p1} and \bar{C}_{p2} are partial massive specific heats of the two mixture components.

The energy equation based on the partial enthalpies for a steady state system of a binary mixture is:

$$\frac{\partial}{\partial x} (\rho_1 U_1 \bar{h}_1 + \rho_2 U_2 \bar{h}_2) + \frac{\partial}{\partial y} (\rho_1 V_1 \bar{h}_1 + \rho_2 V_2 \bar{h}_2) = \frac{\partial}{\partial x} \left(k \frac{\partial T}{\partial x} \right) + \frac{\partial}{\partial y} \left(k \frac{\partial T}{\partial y} \right) \quad (\text{B.25})$$

The mass flux of each species in a multicomponent system is composed of two parts, the diffusion flux and the advection flux:

$$\rho_i U_i = j_i + \rho_i U \quad (\text{B.26})$$

Where U_i and V_i are the velocity of component i in the x and y directions and j_i is the mass flux of component i relative to the mass average velocity U . According to Fick's law, component i diffuses in the decreasing direction of its own mass fraction:

$$j_i = -\rho D^{AB} \frac{\partial \xi_i}{\partial x} \quad (\text{B.27})$$

Substitution of Equations (B.26) and (B.27) in Equation (B.25) for species 1 and 2 in the x and y directions yields to:

$$\begin{aligned} & \frac{\partial}{\partial x} \left(-\rho D^{AB} \frac{\partial \xi_1}{\partial x} \bar{h}_1 + \rho_1 U \bar{h}_1 - \rho D^{AB} \frac{\partial \xi_2}{\partial x} \bar{h}_2 + \rho_2 U \bar{h}_2 \right) + \\ & \frac{\partial}{\partial y} \left(-\rho D^{AB} \frac{\partial \xi_1}{\partial y} \bar{h}_1 + \rho_1 V \bar{h}_1 - \rho D^{AB} \frac{\partial \xi_2}{\partial y} \bar{h}_2 + \rho_2 V \bar{h}_2 \right) + \\ & = \frac{\partial}{\partial x} \left(k \frac{\partial T}{\partial x} \right) + \frac{\partial}{\partial y} \left(k \frac{\partial T}{\partial y} \right) \end{aligned} \quad (\text{B.28})$$

Substituting Equation (B.12) and $\xi_i = \frac{\rho_i}{\rho}$ in Equation (B.28) and moving mass diffusion terms to the right-hand side results in the following energy equation for a binary mixture:

$$\begin{aligned} & \frac{\partial}{\partial x} (\rho U h) + \frac{\partial}{\partial y} (\rho V h) = \frac{\partial}{\partial x} \left(k \frac{\partial T}{\partial x} \right) + \frac{\partial}{\partial y} \left(k \frac{\partial T}{\partial y} \right) + \\ & \frac{\partial}{\partial x} \left(\rho D^{AB} \frac{\partial \xi_1}{\partial x} (\bar{h}_1 - \bar{h}_2) \right) + \frac{\partial}{\partial y} \left(\rho D^{AB} \frac{\partial \xi_1}{\partial y} (\bar{h}_1 - \bar{h}_2) \right) \end{aligned} \quad (\text{B.29})$$

If the enthalpy of the mixture in Equation (B.29) is substituted by Equation (B.22), the result will be the energy equation based on temperature and partial enthalpy used by Mittermaier and Ziegler [13]:

$$\begin{aligned} & \frac{\partial}{\partial x} \left[\rho U (C_p T + \xi_1 (\bar{h}_1 - \bar{h}_2)) \right] + \frac{\partial}{\partial y} \left[\rho V (C_p T + \xi_1 (\bar{h}_1 - \bar{h}_2)) \right] = \\ & \frac{\partial}{\partial x} \left(k \frac{\partial T}{\partial x} \right) + \frac{\partial}{\partial y} \left(k \frac{\partial T}{\partial y} \right) + \frac{\partial}{\partial x} \left(\rho D^{AB} \frac{\partial \xi_1}{\partial x} (\bar{h}_1 - \bar{h}_2) \right) + \frac{\partial}{\partial y} \left(\rho D^{AB} \frac{\partial \xi_1}{\partial y} (\bar{h}_1 - \bar{h}_2) \right) \end{aligned} \quad (\text{B.30})$$

Appendix B. Mixture Energy Equation

For more information on mixture energy equation and properties please refer to Balzhiser et al. [61], Smith et al. [62], Herold et al. [4], and Bird et al. [63].

Appendix C

Parabolic Model Coefficients in Algebraic Equations

C.1 Coefficients of Liquid Mass Fraction Equation

The coefficients of the liquid mass fraction algebraic linear equation, Equation (4.33), are as following:

$$A_{L,S}^{\xi,J} = -\xi W_s^o \quad (C.1)$$

$$A_{L,S}^{\xi,\xi} = -J_{L_S}^o \left(0.5 + \alpha_{L_S}^{\xi}\right) - \frac{\rho_{L_S} D_{L_S}^{AB} \beta_{L_S}^{\xi} \Delta \chi}{\delta_P^o (\eta_P - \eta_S)} \quad (C.2)$$

$$A_{L,P}^{\xi,U} = 2\rho_{L_e} \Delta \eta \xi W_P^o \delta_P^o - \delta_w \rho_{L_e} \Delta \eta \xi W_P^o \quad (C.3)$$

$$A_{L,P}^{\xi,J} = \xi W_n^o \quad (C.4)$$

$$\begin{aligned} A_{L,P}^{\xi,\xi} &= 2\rho_{L_e} \Delta \eta U_{L_P}^o \delta_P^o - \delta_w \rho_{L_e} \Delta \eta U_{L_P}^o + J_{L_P}^o \left(0.5 + \alpha_{L_n}^{\xi}\right) \\ &\quad - J_{L_S}^o \left(0.5 - \alpha_{L_S}^{\xi}\right) + \frac{\rho_{L_n} D_{L_n}^{AB} \beta_{L_n}^{\xi} \Delta \chi}{\delta_P^o (\eta_N - \eta_P)} + \frac{\rho_{L_S} D_{L_S}^{AB} \beta_{L_S}^{\xi} \Delta \chi}{\delta_P^o (\eta_P - \eta_S)} \end{aligned} \quad (C.5)$$

$$A_{L,N}^{\xi,\xi} = J_{L_P}^o \left(0.5 - \alpha_{L_n}^{\xi}\right) - \frac{\rho_{L_n} D_{L_n}^{AB} \beta_{L_n}^{\xi} \Delta \chi}{\delta_P^o (\eta_N - \eta_P)} \quad (C.6)$$

$$A_{L,P}^{\xi,\delta} = 2\rho_{L_e} \Delta \eta \xi W_P^o U_{L_P}^o + \frac{\rho_{L_n} D_{L_n}^{AB} \Delta \chi}{(\delta_P^o)^2} \left. \frac{\partial \xi_1}{\partial \eta} \right|_n^o - \frac{\rho_{L_S} D_{L_S}^{AB} \Delta \chi}{(\delta_P^o)^2} \left. \frac{\partial \xi_W}{\partial \eta} \right|_s^o \quad (C.7)$$

$$\begin{aligned} B_{L,P}^{\xi} &= 4\rho_{L_e} \Delta \eta \delta_P^o \xi W_P^o U_{L_P}^o - \delta_w \rho_{L_e} \Delta \eta \xi W_P^o U_{L_P}^o + \delta_w \rho_{L_w} U_{L_w} \xi W_W \Delta \eta \\ &\quad + J_{L_N}^o \xi W_n^o - J_{L_S}^o \xi W_s^o + \frac{\rho_{L_n} D_{L_n}^{AB} \Delta \chi}{\delta_P^o} \left. \frac{\partial \xi_W}{\partial \eta} \right|_n^o - \frac{\rho_{L_S} D_{L_S}^{AB} \Delta \chi}{\delta_P^o} \left. \frac{\partial \xi_W}{\partial \eta} \right|_s^o \end{aligned} \quad (C.8)$$

C.2 Coefficients of Interfacial Boundary Condition Equations

C.2.1 Velocity Continuity

The coefficients of Equation (4.37) are:

$$A_{\text{intf},S}^{U,U} = -\frac{\mu_{LP}}{\delta_P^o(\eta_P - \eta_S)} \quad (\text{C.9})$$

$$A_{\text{intf},P}^{U,U} = \frac{\mu_{LP}}{\delta_P^o(\eta_P - \eta_S)} + \frac{\mu_{GP}}{(H - \delta_P^o)(\eta_N - \eta_P)} \quad (\text{C.10})$$

$$A_{\text{intf},N}^{U,U} = -\frac{\mu_{GP}}{(H - \delta_P^o)(\eta_N - \eta_P)} \quad (\text{C.11})$$

$$A_{\text{intf},P}^{U,\delta} = -\frac{\mu_{LP}(U_{GP}^o - U_{LS}^o)}{(\delta_P^o)^2(\eta_P - \eta_S)} - \frac{\mu_{GP}(U_{GN}^o - U_{GP}^o)}{(H - \delta_P^o)^2(\eta_N - \eta_P)} \quad (\text{C.12})$$

$$B_{\text{intf},P}^U = -\frac{\mu_{LP}(U_{GP}^o - U_{LS}^o)}{\delta_P^o(\eta_P - \eta_S)} - \frac{\delta_P^o \mu_{GP}(U_{GN}^o - U_{GP}^o)}{(H - \delta_P^o)^2(\eta_N - \eta_P)} \quad (\text{C.13})$$

C.2.2 Mass Continuity

The coefficients of Equation (4.38) are:

$$A_{\text{intf},S}^{J,J} = -1 \quad (\text{C.14})$$

$$A_{\text{intf},P}^{J,J} = 1 \quad (\text{C.15})$$

$$B_{\text{intf},P}^J = 0 \quad (\text{C.16})$$

C.2.3 Temperature Continuity

The coefficients of Equation (4.39) are:

$$A_{\text{intf},P}^{T,T} = 1 \quad (\text{C.17})$$

$$A_{\text{intf},P}^{T,\xi} = -\frac{\partial T_{\text{Eq}}}{\partial \xi_W} \quad (\text{C.18})$$

$$A_{\text{intf},P}^{T,P} = -\frac{\partial T_{\text{Eq}}}{\partial P_{\text{Eq}}} \frac{\Delta\chi}{2} \quad (\text{C.19})$$

$$B_{\text{intf},P}^T = T_{\text{Eq}}^o - \frac{\partial T_{\text{Eq}}^o}{\partial \xi_{WP}} \xi_{WP}^o - \frac{\partial T_{\text{Eq}}^o}{\partial P_{\text{Eq}}} P_{\text{Eq}}^o + \frac{\partial T_{\text{Eq}}^o}{\partial P_{\text{Eq}}} P_W \quad (\text{C.20})$$

C.2.4 LiBr Impermeability

The coefficients of Equation (4.40) are:

$$A_{\text{intf},S}^{\xi,\xi} = \frac{\rho_{LP} D_{LP}^{AB} \Delta\chi}{\delta_P^o (\eta_P - \eta_S)} \quad (\text{C.21})$$

$$A_{\text{intf},P}^{\xi,J} = \xi_{WP}^o - 1 \quad (\text{C.22})$$

$$A_{\text{intf},P}^{\xi,\xi} = J_{LP}^o - \frac{\rho_{LP} D_{LP}^{AB} \Delta\chi}{\delta_P^o (\eta_P - \eta_S)} \quad (\text{C.23})$$

$$A_{\text{intf},P}^{\xi,\delta} = \frac{\rho_{LP} D_{LP}^{AB} \Delta\chi (\xi_{WP}^o - \xi_{WS}^o)}{(\delta_P^o)^2 (\eta_P - \eta_S)} \quad (\text{C.24})$$

$$B_{\text{intf},P}^{\xi} = J_{LP}^o \xi_{WP}^o + \frac{\rho_{LP} D_{LP}^{AB} \Delta\chi (\xi_{WP}^o - \xi_{WS}^o)}{\delta_P^o (\eta_P - \eta_S)} \quad (\text{C.25})$$

C.2.5 Energy Continuity

The coefficients of Equation (4.41) are:

$$A_{\text{intf},S}^{\delta,T} = \frac{k_{LP} \Delta\chi}{\delta_P^o (\eta_P - \eta_S)} \quad (\text{C.26})$$

$$A_{\text{intf},P}^{\delta,J} = H_a \quad (\text{C.27})$$

$$A_{\text{intf},P}^{\delta,T} = \frac{k_{LP} \Delta\chi}{\delta_P^o (\eta_P - \eta_S)} + \frac{k_{GP} \Delta\chi}{(H - \delta_P^o) (\eta_N - \eta_P)} \quad (\text{C.28})$$

$$A_{\text{intf},N}^{\delta,T} = -\frac{k_{GP}\Delta\chi}{(H - \delta_P^o)(\eta_N - \eta_P)} \quad (\text{C.29})$$

$$A_{\text{intf},P}^{\delta,\delta} = -\frac{k_{LP}\Delta\chi(T_{GP}^o - T_{LS}^o)}{(\delta_P^o)^2(\eta_P - \eta_S)} - \frac{k_{GP}\Delta\chi(T_{GN}^o - T_{GP}^o)}{(H - \delta_P^o)^2(\eta_N - \eta_P)} \quad (\text{C.30})$$

$$B_{\text{intf},P}^{\delta} = -\frac{k_{LP}\Delta\chi(T_{GP}^o - T_{LS}^o)}{\delta_P^o(\eta_P - \eta_S)} - \frac{\delta_P^o k_{GP}\Delta\chi(T_{GN}^o - T_{GP}^o)}{(H - \delta_P^o)^2(\eta_N - \eta_P)} \quad (\text{C.31})$$

C.2.6 Overall Mass Balance

The coefficients of Equation (4.42) are:

$$A_{L,jL}^{P,U} = (2\delta_P^o - \delta_w)\rho_{L,jL}\Delta\eta_{jL} \quad (\text{C.32})$$

$$A_{G,jG}^{P,U} = (H - 2\delta_P^o + \delta_w)\rho_{G,jG}\Delta\eta_{jG} \quad (\text{C.33})$$

$$A_P^{P,\delta} = \sum_{jL=1}^{N_{y,L}-1} 2\rho_{L,jL}U_{L,jL}^o\Delta\eta_{jL} - \sum_{jG=1}^{N_{y,G}} 2\rho_{G,jG}U_{G,jG}^o\Delta\eta_{jG} \quad (\text{C.34})$$

$$B_P^P = \sum_{jL=1}^{N_{y,L}-1} 2\delta_P^o\rho_{L,jL}U_{L,jL}^o\Delta\eta_{jL} - \sum_{jG=1}^{N_{y,G}} 2\delta_P^o\rho_{G,jG}U_{G,jG}^o\Delta\eta_{jG} + \dot{m}'_{L,\text{in}} + \dot{m}'_{G,\text{in}} \quad (\text{C.35})$$

Appendix D

Bordered Block Matrix Entries in Parabolic Model

The block matrices in Equation (4.43) are as follows:

For $jL = 1, 2, \dots, N_{y,L} - 1$:

$$\mathbf{A}_{L,P}^{jl} = \begin{bmatrix} A_{L,P}^{U,U} & A_{L,P}^{U,J} & 0 & 0 \\ A_{L,P}^{J,U} & A_{L,P}^{J,J} & 0 & 0 \\ A_{L,P}^{T,U} & A_{L,P}^{T,J} & A_{L,P}^{T,T} & A_{L,P}^{T,\xi} \\ A_{L,P}^{\xi,U} & A_{L,P}^{\xi,J} & 0 & A_{L,P}^{\xi,\xi} \end{bmatrix}_{jL} \quad (\text{D.1})$$

$$\mathbf{A}_{L,N}^{jl} = \begin{bmatrix} A_{L,N}^{U,U} & 0 & 0 & 0 \\ 0 & 0 & 0 & 0 \\ 0 & 0 & A_{L,N}^{T,T} & A_{L,N}^{T,\xi} \\ 0 & 0 & 0 & A_{L,N}^{\xi,\xi} \end{bmatrix}_{jL} \quad (\text{D.2})$$

$$\mathbf{A}_{L,S}^{jl} = \begin{bmatrix} A_{L,S}^{U,U} & A_{L,S}^{U,J} & 0 & 0 \\ 0 & A_{L,S}^{J,J} & 0 & 0 \\ 0 & A_{L,S}^{T,J} & A_{L,S}^{T,T} & A_{L,S}^{T,\xi} \\ 0 & A_{L,S}^{\xi,J} & 0 & A_{L,S}^{\xi,\xi} \end{bmatrix}_{jL} \quad (\text{D.3})$$

For the interface:

$$\mathbf{A}_{I,P} = \begin{bmatrix} A_{I,P}^{U,U} & 0 & 0 & 0 \\ 0 & A_{I,P}^{J,J} & 0 & 0 \\ 0 & 0 & A_{I,P}^{T,T} & A_{I,P}^{T,\xi} \\ 0 & A_{I,P}^{\xi,J} & 0 & A_{I,P}^{\xi,\xi} \end{bmatrix} \quad (\text{D.4})$$

$$\mathbf{A}_{I,N} = \begin{bmatrix} A_{I,N}^{U,U} & 0 & 0 & 0 \\ 0 & 0 & 0 & 0 \\ 0 & 0 & 0 & 0 \\ 0 & 0 & 0 & 0 \end{bmatrix} \quad (\text{D.5})$$

$$\mathbf{A}_{I,S} = \begin{bmatrix} A_{I,S}^{U,U} & 0 & 0 & 0 \\ 0 & A_{I,S}^{J,J} & 0 & 0 \\ 0 & 0 & 0 & 0 \\ 0 & 0 & 0 & A_{I,S}^{\xi,\xi} \end{bmatrix} \quad (\text{D.6})$$

For $jG = 2, \dots, N_{y,G}$:

$$\mathbf{A}_{G,P} = \begin{bmatrix} A_{G,P}^{U,U} & A_{G,P}^{U,J} & 0 & 0 \\ A_{G,P}^{J,U} & A_{G,P}^{J,J} & 0 & 0 \\ A_{G,P}^{T,U} & A_{G,P}^{T,J} & A_{G,P}^{T,T} & 0 \\ 0 & 0 & 0 & 1 \end{bmatrix}_{jG} \quad (\text{D.7})$$

$$\mathbf{A}_{G,N} = \begin{bmatrix} A_{G,N}^{U,U} & 0 & 0 & 0 \\ 0 & 0 & 0 & 0 \\ 0 & 0 & A_{G,N}^{T,T} & 0 \\ 0 & 0 & 0 & 0 \end{bmatrix}_{jG} \quad (\text{D.8})$$

$$\mathbf{A}_{G,S} = \begin{bmatrix} A_{G,S}^{U,U} & A_{G,S}^{U,J} & 0 & 0 \\ 0 & A_{G,S}^{J,J} & 0 & 0 \\ 0 & A_{G,S}^{T,J} & A_{G,S}^{T,T} & 0 \\ 0 & 0 & 0 & 0 \end{bmatrix}_{jG} \quad (\text{D.9})$$

$$\mathbf{E}_1 = \begin{bmatrix} (0000)_1 & (0000)_2 & \cdots & (00A_{I,S}^{\delta,T}0) & (0A_{I,P}^{\delta,J}A_{I,P}^{\delta,T}0) & (00A_{I,N}^{\delta,T}0) & \cdots & (0000)_{N_{y,G}} \\ (A_L^{P,U}000)_1 & (A_L^{P,U}000)_2 & \cdots & (A_L^{P,U}000)_{N_{y,L}-1} & (A_G^{P,U}000)_1 & (A_G^{P,U}000)_2 & \cdots & (A_G^{P,U}000)_{N_{y,G}} \end{bmatrix} \quad (\text{D.10})$$

$$\mathbf{E}_2 = \begin{bmatrix}
 (A_{L,P}^{U,\delta} \ A_{L,P}^{J,\delta} \ A_{L,P}^{T,\delta} \ A_{L,P}^{\xi,\delta})_1 & (A_{L,P}^{U,P} \ 0 \ 0 \ 0)_1 \\
 (A_{L,P}^{U,\delta} \ A_{L,P}^{J,\delta} \ A_{L,P}^{T,\delta} \ A_{L,P}^{\xi,\delta})_2 & (A_{L,P}^{U,P} \ 0 \ 0 \ 0)_2 \\
 \vdots & \vdots \\
 (A_{L,P}^{U,\delta} \ A_{L,P}^{J,\delta} \ A_{L,P}^{T,\delta} \ A_{L,P}^{\xi,\delta})_{jL} & (A_{L,P}^{U,P} \ 0 \ 0 \ 0)_{jL} \\
 \vdots & \vdots \\
 (A_{L,P}^{U,\delta} \ A_{L,P}^{J,\delta} \ A_{L,P}^{T,\delta} \ A_{L,P}^{\xi,\delta})_{N_y,L-1} & (A_{L,P}^{U,P} \ 0 \ 0 \ 0)_{N_y,L-1} \\
 (A_{I,P}^{U,\delta} \ 0 \ 0 \ A_{I,P}^{\xi,\delta}) & (0 \ 0 \ A_{I,P}^{T,P} \ 0) \\
 (A_{G,P}^{U,\delta} \ A_{G,P}^{J,\delta} \ A_{G,P}^{T,\delta} \ 0)_2 & (A_{G,P}^{U,P} \ 0 \ 0 \ 0)_2 \\
 \vdots & \vdots \\
 (A_{G,P}^{U,\delta} \ A_{G,P}^{J,\delta} \ A_{G,P}^{T,\delta} \ 0)_{jG} & (A_{G,P}^{U,P} \ 0 \ 0 \ 0)_{jG} \\
 \vdots & \vdots \\
 (A_{G,P}^{U,\delta} \ A_{G,P}^{J,\delta} \ A_{G,P}^{T,\delta} \ 0)_{N_y,G} & (A_{G,P}^{U,P} \ 0 \ 0 \ 0)_{N_y,G}
 \end{bmatrix} \quad (\text{D.11})$$

$$\mathbf{E}_3 = \begin{bmatrix}
 A_{I,P}^{\delta,\delta} & 0 \\
 A_P^{P,\delta} & 0
 \end{bmatrix} \quad (\text{D.12})$$

$$\mathbf{B}_1 = \begin{bmatrix}
 (B_{L,P}^U \ B_{L,P}^J \ B_{L,P}^T \ B_{L,P}^\xi)_1 \\
 (B_{L,P}^U \ B_{L,P}^J \ B_{L,P}^T \ B_{L,P}^\xi)_2 \\
 \vdots \\
 (B_{L,P}^U \ B_{L,P}^J \ B_{L,P}^T \ B_{L,P}^\xi)_{jL} \\
 \vdots \\
 (B_{L,P}^U \ B_{L,P}^J \ B_{L,P}^T \ B_{L,P}^\xi)_{N_y,L-1} \\
 (B_{I,P}^U \ B_{I,P}^J \ B_{I,P}^T \ B_{I,P}^\xi) \\
 (B_{G,P}^U \ B_{G,P}^J \ B_{G,P}^T \ 0)_2 \\
 \vdots \\
 (B_{G,P}^U \ B_{G,P}^J \ B_{G,P}^T \ 0)_{jG} \\
 \vdots \\
 (B_{G,P}^U \ B_{G,P}^J \ B_{G,P}^T \ 0)_{N_y,G}
 \end{bmatrix} \quad (\text{D.13})$$

$$\mathbf{B}_2 = \begin{bmatrix} B_{I,P}^\delta \\ B_P^P \end{bmatrix} \quad (\text{D.14})$$

$$\mathbf{X}_1 = \begin{bmatrix} (U_L \ J_L \ T_L \ \xi_W)_1 \\ (U_L \ J_L \ T_L \ \xi_W)_2 \\ \vdots \\ (U_L \ J_L \ T_L \ \xi_W)_{jL} \\ \vdots \\ (U_L \ J_L \ T_L \ \xi_W)_{N_{y,L}-1} \\ (U_G \ J_G \ T_G \ \xi_{\text{dummy}})_1 \\ (U_G \ J_G \ T_G \ \xi_{\text{dummy}})_2 \\ \vdots \\ (U_G \ J_G \ T_G \ \xi_{\text{dummy}})_{jG} \\ \vdots \\ (U_G \ J_G \ T_G \ \xi_{\text{dummy}})_{N_{y,G}} \end{bmatrix} \quad (\text{D.15})$$

$$\mathbf{X}_2 = \begin{bmatrix} \delta \\ \frac{dP}{d\chi} \end{bmatrix} \quad (\text{D.16})$$

Appendix E

Elliptic Model Coefficients in Interface Algebraic Equations

E.1 Normal Force Balance

The coefficients of Equation (4.181) are:

$$a_{iL,P}^{c,P} = 1 \quad (\text{E.1})$$

$$a_{iL,N}^{c,P} = -1 \quad (\text{E.2})$$

$$a_{iL,P}^{c,u} = -2 \mu_{iL,P} (n_{xn}^2 A_{x2} + n_{xn} n_{yn} A_{y2})_{iL,S} \quad (\text{E.3})$$

$$a_{iL,E}^{c,u} = -2 \mu_{iL,P} (n_{xn}^2 A_{x3} + n_{xn} n_{yn} A_{y3})_{iL,S} \quad (\text{E.4})$$

$$a_{iL,W}^{c,u} = -2 \mu_{iL,P} (n_{xn}^2 A_{x4} + n_{xn} n_{yn} A_{y4})_{iL,S} \quad (\text{E.5})$$

$$a_{iL,S}^{c,u} = -2 \mu_{iL,P} (n_{xn}^2 A_{x1} + n_{xn} n_{yn} A_{y1})_{iL,S} \quad (\text{E.6})$$

$$a_{iL,P}^{c,v} = -2 \mu_{iL,P} (n_{xn} n_{yn} A_{x2} + n_{yn}^2 A_{y2})_{iL,S} \quad (\text{E.7})$$

$$a_{iL,E}^{c,v} = -2 \mu_{iL,P} (n_{xn} n_{yn} A_{x3} + n_{yn}^2 A_{y3})_{iL,S} \quad (\text{E.8})$$

$$a_{iL,W}^{c,v} = -2 \mu_{iL,P} (n_{xn} n_{yn} A_{x4} + n_{yn}^2 A_{y4})_{iL,S} \quad (\text{E.9})$$

$$a_{iL,S}^{c,v} = -2 \mu_{iL,P} (n_{xn} n_{yn} A_{x1} + n_{yn}^2 A_{y1})_{iL,S} \quad (\text{E.10})$$

$$a_{iL,N}^{c,u} = 2 \mu_{iG,P} (n_{xs}^2 B_{x2} + n_{xs} n_{ys} B_{y2})_{iG,N} \quad (\text{E.11})$$

$$a_{iL,NE}^{c,u} = 2 \mu_{iG,P} (n_{xs}^2 B_{x3} + n_{xs} n_{ys} B_{y3})_{iG,N} \quad (\text{E.12})$$

$$a_{iL,NW}^{c,u} = 2 \mu_{iG,P} (n_{xs}^2 B_{x4} + n_{xs} n_{ys} B_{y4})_{iG,N} \quad (\text{E.13})$$

$$a_{iL,N}^{c,v} = 2 \mu_{iG,P} (n_{xs} n_{ys} B_{x2} + n_{ys}^2 B_{y2})_{iG,N} \quad (\text{E.14})$$

$$a_{iL,NE}^{c,v} = 2 \mu_{iG,P} (n_{xs} n_{ys} B_{x3} + n_{ys}^2 B_{y3})_{iG,N} \quad (\text{E.15})$$

$$a_{iL,NW}^{c,v} = 2 \mu_{iG,P} (n_{xs} n_{ys} B_{x4} + n_{ys}^2 B_{y4})_{iG,N} \quad (\text{E.16})$$

$$b_{iL,P}^c = -\sigma K - 2\mu_{iG,P} \left(n_{xs}^2 B_{x1} + n_{xs} n_{ys} B_{y1} \right)_{iG,N} U_{iG,N} - 2\mu_{iG,P} \left(n_{xs} n_{ys} B_{x1} + n_{ys}^2 B_{y1} \right)_{iG,N} V_{iG,N} \quad (\text{E.17})$$

E.2 Zero Pressure Gradient

The coefficients of Equation (4.183) are:

$$a_{iG,P}^{c,p} = \left(B_{x2} n_{xs} + B_{y2} n_{ys} \right)_{iG,N} \quad (\text{E.18})$$

$$a_{iG,N}^{c,p} = \left(B_{x1} n_{xs} + B_{y1} n_{ys} \right)_{iG,N} \quad (\text{E.19})$$

$$a_{iG,W}^{c,p} = \left(B_{x4} n_{xs} + B_{y4} n_{ys} \right)_{iG,N} \quad (\text{E.20})$$

$$a_{iG,E}^{c,p} = \left(B_{x3} n_{xs} + B_{y3} n_{ys} \right)_{iG,N} \quad (\text{E.21})$$

E.3 Tangential Force Balance

The coefficients of Equation (4.187) are:

$$a_{iG,P}^{u,u} = -\mu_{iG,P} \left(2n_{xs}s_{xs}B_{x2} + (n_{ys}s_{xs} + n_{xs}s_{ys})B_{y2} \right)_{iG,N} \quad (\text{E.22})$$

$$a_{iG,E}^{u,u} = -\mu_{iG,P} \left(2n_{xs}s_{xs}B_{x3} + (n_{ys}s_{xs} + n_{xs}s_{ys})B_{y3} \right)_{iG,N} \quad (\text{E.23})$$

$$a_{iG,W}^{u,u} = -\mu_{iG,P} \left(2n_{xs}s_{xs}B_{x4} + (n_{ys}s_{xs} + n_{xs}s_{ys})B_{y4} \right)_{iG,N} \quad (\text{E.24})$$

$$a_{iG,N}^{u,u} = -\mu_{iG,P} \left(2n_{xs}s_{xs}B_{x1} + (n_{ys}s_{xs} + n_{xs}s_{ys})B_{y1} \right)_{iG,N} \quad (\text{E.25})$$

$$a_{iG,P}^{u,v} = -\mu_{iG,P} \left(2n_{ys}s_{ys}B_{y2} + (n_{ys}s_{xs} + n_{xs}s_{ys})B_{x2} \right)_{iG,N} \quad (\text{E.26})$$

$$a_{iG,E}^{u,v} = -\mu_{iG,P} \left(2n_{ys}s_{ys}B_{y3} + (n_{ys}s_{xs} + n_{xs}s_{ys})B_{x3} \right)_{iG,N} \quad (\text{E.27})$$

$$a_{iG,W}^{u,v} = -\mu_{iG,P} \left(2n_{ys}s_{ys}B_{y4} + (n_{ys}s_{xs} + n_{xs}s_{ys})B_{x4} \right)_{iG,N} \quad (\text{E.28})$$

$$a_{iG,N}^{u,v} = -\mu_{iG,P} \left(2n_{ys}s_{ys}B_{y1} + (n_{ys}s_{xs} + n_{xs}s_{ys})B_{x1} \right)_{iG,N} \quad (\text{E.29})$$

$$a_{iG,S}^{u,u} = \mu_{iL,P} \left(2n_{xn}s_{xn}A_{x2} + (n_{yn}s_{xn} + n_{xn}s_{yn})A_{y2} \right)_{iL,S} \quad (\text{E.30})$$

$$a_{iG,SE}^{u,u} = \mu_{iL,P} \left(2n_{xn}s_{xn}A_{x3} + (n_{yn}s_{xn} + n_{xn}s_{yn})A_{y3} \right)_{iL,S} \quad (\text{E.31})$$

$$a_{iG,SW}^{u,u} = \mu_{iL,P} \left(2n_{xn}s_{xn}A_{x4} + (n_{yn}s_{xn} + n_{xn}s_{yn})A_{y4} \right)_{iL,S} \quad (\text{E.32})$$

$$a_{iG,S}^{u,v} = \mu_{iL,P} \left(2n_{yn}s_{yn}A_{y2} + (n_{yn}s_{xn} + n_{xn}s_{yn})A_{x2} \right)_{iL,S} \quad (\text{E.33})$$

$$a_{iG,SE}^{u,v} = \mu_{iL,P} \left(2n_{yn}s_{yn}A_{y3} + (n_{yn}s_{xn} + n_{xn}s_{yn})A_{x3} \right)_{iL,S} \quad (\text{E.34})$$

$$a_{iG,SW}^{u,v} = \mu_{iL,P} \left(2n_{yn}s_{yn}A_{y4} + (n_{yn}s_{xn} + n_{xn}s_{yn})A_{x4} \right)_{iL,S} \quad (\text{E.35})$$

$$b_{iG,P}^u = \frac{\partial \sigma}{\partial s} \Big|_{L,\text{intf}} - \mu_{iL,P} \left(2n_{xn}s_{xn}A_{x1} + (n_{yn}s_{xn} + n_{xn}s_{yn})A_{y1} \right)_{iL,S} U_{iL,S} - \mu_{iL,P} \left(2n_{yn}s_{yn}A_{y1} + (n_{yn}s_{xn} + n_{xn}s_{yn})A_{x1} \right)_{iL,S} V_{iL,S} \quad (\text{E.36})$$

E.4 Tangential Velocity Equality

The coefficients of Equation (4.189) are:

$$a_{iL,P}^{u,u} = s_{xn}|_{iL,S} \quad (\text{E.37})$$

$$a_{iL,N}^{u,u} = -s_{xs}|_{iG,N} \quad (\text{E.38})$$

$$a_{iL,P}^{u,v} = s_{yn}|_{iL,S} \quad (\text{E.39})$$

$$a_{iL,N}^{u,v} = -s_{ys}|_{iG,N} \quad (\text{E.40})$$

E.5 Continuity of Mass at the Interface

The coefficients of Equation (4.191) are:

$$a_{iG,P}^{v,u} = (\rho A)_{iG,P}(n_{xs})_{iG,N} \quad (\text{E.41})$$

$$a_{iG,S}^{v,u} = -(\rho A)_{iL,P}(n_{xn})_{iL,S} \quad (\text{E.42})$$

$$a_{iG,P}^{v,v} = (\rho A)_{iG,P}(n_{ys})_{iG,N} \quad (\text{E.43})$$

$$a_{iG,S}^{v,v} = -(\rho A)_{iL,P}(n_{yn})_{iL,S} \quad (\text{E.44})$$

E.6 Continuity of Energy at the Interface

The coefficients of Equation (4.193) are:

$$a_{iL,P}^{v,u} = (\rho A)_{iL,P} (n_{xn})_{iL,S} \quad (\text{E.45})$$

$$a_{iL,P}^{v,v} = (\rho A)_{iL,P} (n_{yn})_{iL,S} \quad (\text{E.46})$$

$$a_{iL,P}^{v,t} = \frac{kA}{H_a} \Big|_{iL,P} (A_{x2} n_{xn} + A_{y2} n_{yn})_{iL,S} \quad (\text{E.47})$$

$$a_{iL,E}^{v,t} = \frac{kA}{H_a} \Big|_{iL,P} (A_{x3} n_{xn} + A_{y3} n_{yn})_{iL,S} \quad (\text{E.48})$$

$$a_{iL,W}^{v,t} = \frac{kA}{H_a} \Big|_{iL,P} (A_{x4} n_{xn} + A_{y4} n_{yn})_{iL,S} \quad (\text{E.49})$$

$$a_{iL,S}^{v,t} = \frac{kA}{H_a} \Big|_{iL,P} (A_{x1} n_{xn} + A_{y1} n_{yn})_{iL,S} \quad (\text{E.50})$$

$$a_{iL,N}^{v,t} = -\frac{kA}{H_a} \Big|_{iG,P} (B_{x2} n_{xs} + B_{y2} n_{ys})_{iG,N} \quad (\text{E.51})$$

$$a_{iL,NE}^{v,t} = -\frac{kA}{H_a} \Big|_{iG,P} (B_{x3} n_{xs} + B_{y3} n_{ys})_{iG,N} \quad (\text{E.52})$$

$$a_{iL,NW}^{v,t} = -\frac{kA}{H_a} \Big|_{iG,P} (B_{x4} n_{xs} + B_{y4} n_{ys})_{iG,N} \quad (\text{E.53})$$

$$b_{iL,P}^v = \frac{kA}{H_a} \Big|_{iG,P} (B_{x1} n_{xs} + B_{y1} n_{ys})_{iG,N} T_{iG,N} \quad (\text{E.54})$$

E.7 Equilibrium Condition at the Interface

The coefficients of Equation (4.195) are:

$$a_{iL,P}^{t,t} = 1 \quad (\text{E.55})$$

$$a_{iL,P}^{t,\xi} = -\frac{\partial T_{\text{Eq}}}{\partial \xi_W} \quad (\text{E.56})$$

$$a_{iL,P}^{t,P} = -\frac{\partial T_{\text{Eq}}}{\partial P_{iL}} \quad (\text{E.57})$$

$$b_{iL,P}^t = T_{iL,P}^o - \frac{\partial T_{\text{Eq}}}{\partial \xi_W} \xi_W^o - \frac{\partial T_{\text{Eq}}}{\partial P_{iL}} P_{iL}^o \quad (\text{E.58})$$

E.8 Temperature Equality at the Interface

The coefficients of Equation (4.196) are:

$$a_{iG,P}^{t,t} = 1 \quad (\text{E.59})$$

$$a_{iG,S}^{t,t} = -1 \quad (\text{E.60})$$

E.9 Impermeability of LiBr

The coefficients of Equation (4.198) are:

$$\begin{aligned} a_{iL,P}^{\xi,\xi} = & -(\rho AD^{AB})_{iL,P} (n_{xn} A_{x2} + n_{yn} A_{y2})_{iL,S} \\ & + (\rho AU^o)_{iL,P} n_{xn}|_{iL,S} + (\rho AV^o)_{iL,P} n_{yn}|_{iL,S} \end{aligned} \quad (\text{E.61})$$

$$a_{iL,E}^{\xi,\xi} = -(\rho AD^{AB})_{iL,P} (n_{xn} A_{x3} + n_{yn} A_{y3})_{iL,S} \quad (\text{E.62})$$

$$a_{iL,W}^{\xi,\xi} = -(\rho AD^{AB})_{iL,P} (n_{xn} A_{x4} + n_{yn} A_{y4})_{iL,S} \quad (\text{E.63})$$

$$a_{iL,S}^{\xi,\xi} = -(\rho AD^{AB})_{iL,P} (n_{xn} A_{x1} + n_{yn} A_{y1})_{iL,S} \quad (\text{E.64})$$

$$a_{iL,P}^{\xi,u} = (\rho A)_{iL,P} n_{xn}|_{iL,S} (\xi_W^o - 1)_{iL,P} \quad (\text{E.65})$$

$$a_{iL,P}^{\xi,v} = (\rho A)_{iL,P} n_{yn}|_{iL,S} (\xi_W^o - 1)_{iL,P} \quad (\text{E.66})$$

$$b_{iL,P}^{\xi} = (\rho AU^o \xi_W^o)_{iL,P} n_{xn}|_{iL,S} + (\rho AV^o \xi_W^o)_{iL,P} n_{yn}|_{iL,S} \quad (\text{E.67})$$

Appendix F

LiBr-Water Solution Thermophysical Properties by Mittermaier and Ziegler [12]

In the following equations, the temperature is in K and the mass fraction is between 0 and 1. The range of applicability of Equations (F.1) to (F.6) was not stated by Mittermaier et al. [12].

F.1 LiBr-Water Solution Density ρ_L

$$\rho_L = a_0 + a_1 \xi_{\text{LiBr}} + a_2 T_L + a_3 \xi_{\text{LiBr}} T_L + a_4 \xi_{\text{LiBr}}^2 + a_5 T_L^2 + a_6 \xi_{\text{LiBr}}^2 T_L + a_7 \xi_{\text{LiBr}} T_L^2 + a_8 \xi_{\text{LiBr}}^2 T_L^2 + a_9 \xi_{\text{LiBr}}^3 + a_{10} T_L^3 + a_{11} \xi_{\text{LiBr}}^3 T_L + a_{12} \xi_{\text{LiBr}}^3 T_L^2 + a_{13} \xi_{\text{LiBr}} T_L^3 + a_{14} \xi_{\text{LiBr}}^2 T_L^3 + a_{15} \xi_{\text{LiBr}}^3 T_L^3 + a_{16} \xi_{\text{LiBr}}^4 \quad (\text{F.1})$$

i	a_i	i	a_i
0	$-1.58792071 \times 10^{+2}$	9	$+8.62525194 \times 10^{+4}$
1	$+1.850267064 \times 10^{+4}$	10	$+2.04622 \times 10^{-5}$
2	$+9.79173601$	11	$-7.942826466 \times 10^{+2}$
3	$-1.586456762 \times 10^{+2}$	12	$+2.390046288$
4	$-7.384671379 \times 10^{+4}$	13	-4.53566×10^{-4}
5	$-2.5910389 \times 10^{-2}$	14	$+2.046451 \times 10^{-3}$
6	$+6.792667079 \times 10^{+2}$	15	-2.39635×10^{-3}
7	$4.65762844 \times 10^{-1}$	16	$+2.093332625 \times 10^{+3}$
8	-2.043875777		

F.2 LiBr-Water Solution Kinematic viscosity ν_L

$$\begin{aligned} \nu_L = \exp \left[a_0 + a_1 T_L + a_2 \xi_{\text{LiBr}} + a_3 T_L \xi_{\text{LiBr}} + a_4 T_L^2 + a_5 \xi_{\text{LiBr}}^2 + a_6 T_L^2 \xi_{\text{LiBr}} + a_7 T_L \xi_{\text{LiBr}}^2 \right. \\ \left. + a_8 T_L^2 \xi_{\text{LiBr}}^2 + a_9 \ln T_L + a_{10} (\ln T_L)^2 + a_{11} (\ln T_L)^3 + a_{12} \ln(1 + \xi_{\text{LiBr}}) + a_{13} (\ln(1 + \xi_{\text{LiBr}}))^2 \right. \\ \left. + a_{14} (\ln(1 + \xi_{\text{LiBr}}))^3 + a_{15} \ln T_L \ln(1 + \xi_{\text{LiBr}}) \right] \times 10^{-6} \quad (\text{F.2}) \end{aligned}$$

i	a_i	i	a_i
0	$-7.712238243 \times 10^{+2}$	8	-1.03042×10^{-4}
1	$+1.313986647$	9	$+2.831165871 \times 10^{+2}$
2	$+6.661751115 \times 10^{+3}$	10	-5.806649869
3	$-1.76584923 \times 10^{-1}$	11	-5.412275708
4	-4.9714×10^{-4}	12	$-6.824256192 \times 10^{+3}$
5	$-3.272586134 \times 10^{+2}$	13	$-2.993737847 \times 10^{+3}$
6	$+1.36026 \times 10^{-4}$	14	$-8.167742305 \times 10^{+2}$
7	$+6.9697926 \times 10^{-2}$	15	$+3.58541012 \times 10^{+1}$

F.3 LiBr-Water Solution specific Heat $C_{p,L}$

$$\begin{aligned} C_{p,L} = a_0 + a_1 \xi_{\text{LiBr}} + a_2 T_L + a_3 \xi_{\text{LiBr}} T_L + a_4 \xi_{\text{LiBr}}^2 + a_5 T_L^2 + a_6 \xi_{\text{LiBr}}^2 T_L + a_7 \xi_{\text{LiBr}} T_L^2 + a_8 \xi_{\text{LiBr}}^2 T_L^2 \\ + a_9 \xi_{\text{LiBr}}^3 + a_{10} T_L^3 + a_{11} \xi_{\text{LiBr}}^3 T_L + a_{12} \xi_{\text{LiBr}}^3 T_L^2 + a_{13} \xi_{\text{LiBr}} T_L^3 + a_{14} \xi_{\text{LiBr}}^2 T_L^3 + a_{15} \xi_{\text{LiBr}}^3 T_L^3 \quad (\text{F.3}) \end{aligned}$$

In Equation (F.3) the coefficient a_9 is changed to $+2.885672066 \times 10^{+4}$ from the incorrect value that appeared in Mittermaier et al. [12].

i	a_i	i	a_i
0	$+6.462731914 \times 10^{+3}$	8	$+1.688020 \times 10^{-1}$
1	$-6.815825241 \times 10^{+4}$	9	$+2.885672066 \times 10^{+4}$
2	$-1.7426854 \times 10^{+1}$	10	-2.95603×10^{-5}
3	$+5.20285681 \times 10^{+2}$	11	$-1.9710322 \times 10^{+2}$
4	$+5.800384892 \times 10^{+3}$	12	$+4.74334 \times 10^{-1}$
5	$+4.1611 \times 10^{-2}$	13	$+1.25375 \times 10^{-3}$
6	$-5.5755167 \times 10^{+1}$	14	-1.81967×10^{-4}
7	-1.4047670	15	-3.38265×10^{-4}

F.4 LiBr-Water Solution Thermal Conductivity k_L

$$\begin{aligned}
 k_L = a_0 + a_1 T_L + a_2 T_L^2 + a_3 T_L^3 + a_4 \xi_{\text{LiBr}} + a_5 \xi_{\text{LiBr}}^2 + a_6 \xi_{\text{LiBr}}^3 + a_7 T_L \xi_{\text{LiBr}} + a_8 T_L^2 \xi_{\text{LiBr}} \\
 + a_9 T_L \xi_{\text{LiBr}}^2 + a_{10} T_L^2 \xi_{\text{LiBr}}^2
 \end{aligned} \tag{F.4}$$

i	a_i	i	a_i
0	-3.289756188	6	$+1.9951162 \times 10^{-1}$
1	$+3.15131868 \times 10^{-2}$	7	$-2.3665808 \times 10^{-3}$
2	$-8.5591584 \times 10^{-5}$	8	$+2.8033128 \times 10^{-6}$
3	$+7.95845188 \times 10^{-8}$	9	$-3.88631292 \times 10^{-3}$
4	$+1.9623046 \times 10^{-1}$	10	$+5.74312181 \times 10^{-6}$
5	$+4.3183769 \times 10^{-1}$		

F.5 LiBr-Water Solution Binary Diffusion Coefficient D_L^{AB}

The LiBr-water solution diffusion coefficient at $T_L = 25^\circ\text{C} = 298.15\text{ K}$ was given as:

$$D_L^{AB}(298.15\text{ K}) = (1.3528 + 0.19881b - 0.036382b^2 + 0.0020299b^3 - 0.000039375b^4) \times 10^{-9} \quad (\text{F.5})$$

where $b = \frac{\xi_{\text{LiBr}}}{M\xi_{\text{W}}}$ and $M = 86.845 \times 10^{-3}\text{ kg mol}^{-1}$.

$$D_L^{AB} = D_L^{AB}(298.15\text{ K}) \frac{T_L}{298.15} \frac{\mu_L(298.15\text{ K}, \xi_{\text{LiBr}})}{\mu_L(T_L, \xi_{\text{LiBr}})} \quad (\text{F.6})$$

Appendix G

Heat of Absorption by Papaefthimiou et al. [28]

In the following equations, the heat of absorption is in kJ kg^{-1} and the mass fraction between 0 and 1 is represented as a value between 0 and 100; for example, 0.45 is represented as 45.

$$H_a = a_0 + a_1 \xi_{\text{LiBr}} + a_2 \xi_{\text{LiBr}}^2 + a_3 \xi_{\text{LiBr}}^3$$
$$20 \text{ }^\circ\text{C} < T < 180 \text{ }^\circ\text{C} \quad (\text{G.1})$$
$$40 < \xi_{\text{LiBr}} < 70 \text{ (percentage)}$$

T_L [°C]	a_0	a_1	a_2	a_3
20	6.79645601×10^3	-2.59628371×10^2	4.93366230	$-2.82873784 \times 10^{-2}$
60	7.62306284×10^3	-3.18402318×10^2	6.21048626	$-3.75609876 \times 10^{-2}$
80	7.53365154×10^3	-3.15333677×10^2	6.15836244	$-3.73261100 \times 10^{-2}$
100	7.03119843×10^3	-2.88290721×10^2	5.64531982	$-3.41429544 \times 10^{-2}$
120	6.39744301×10^3	-2.54066296×10^2	5.00335057	$-3.01924962 \times 10^{-2}$
140	6.03279793×10^3	-2.35152700×10^2	4.64239505	$-2.79121610 \times 10^{-2}$
160	5.68371644×10^3	-2.18342057×10^2	4.33746473	$-2.60467306 \times 10^{-2}$
180	5.36693989×10^3	-2.03428526×10^2	4.06645498	$-2.43752669 \times 10^{-2}$

Note: the isothermal line for the heat of absorption at $T_L = 40^\circ\text{C}$ was not presented by Papaefthimiou et al. [28].

Appendix H

The Effect of Changing S_T/d on the Falling Liquid Film with $Re_{L,in} = 80$ Over a Horizontal Tube

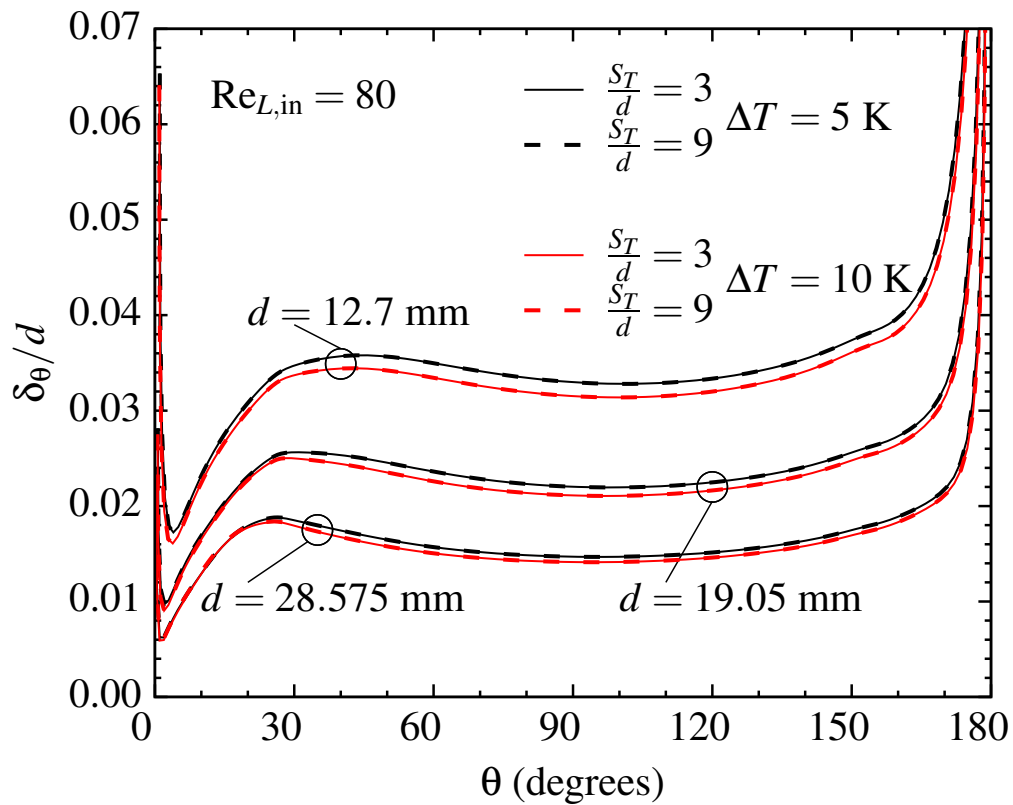


Figure H.1: Variation of the liquid film thickness around the tube with S_T/d for $Re_{L,in} = 80$ and $\Delta T = [5 \text{ K}, 10 \text{ K}]$.

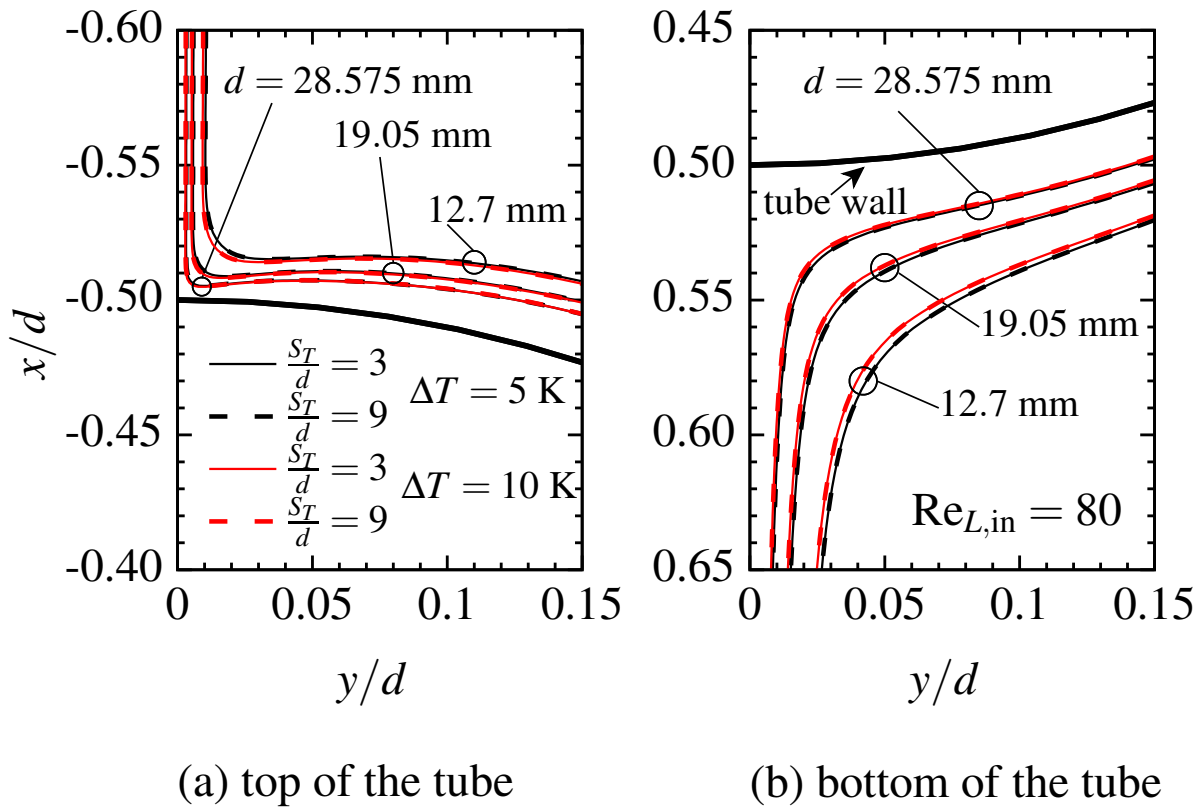


Figure H.2: Change of the liquid film shape at the top and bottom of the tube with S_T/d for $Re_{L,in} = 80$ and $\Delta T = [5 \text{ K}, 10 \text{ K}]$.

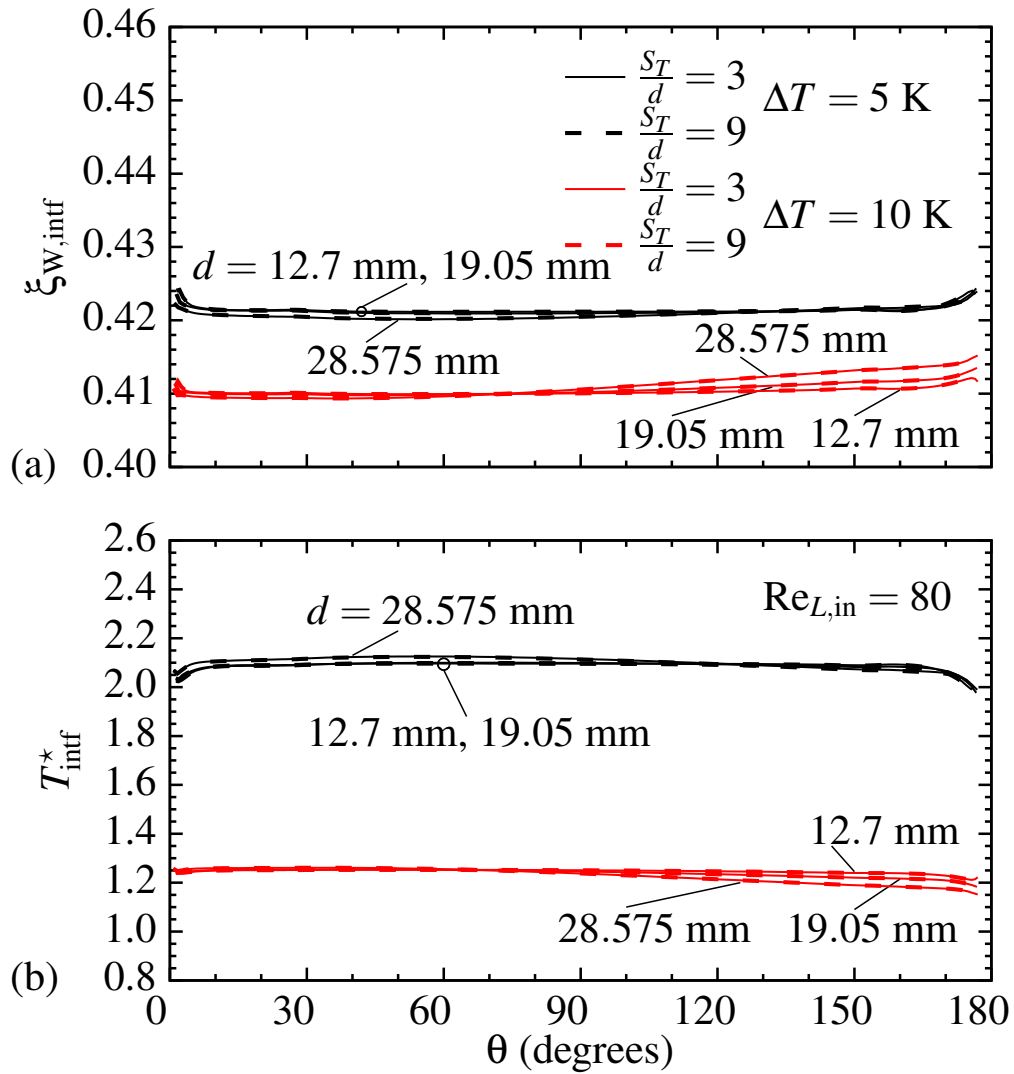


Figure H.3: Variation around the tube of (a) interface mass fraction and (b) interface dimensionless temperature for $S_T/d = [3,9]$ and $\Delta T = [5 \text{ K}, 10 \text{ K}]$ with $d = [12.7 \text{ mm}, 19.05 \text{ mm}, 28.575 \text{ mm}]$ and $Re_{L,in} = 80$.

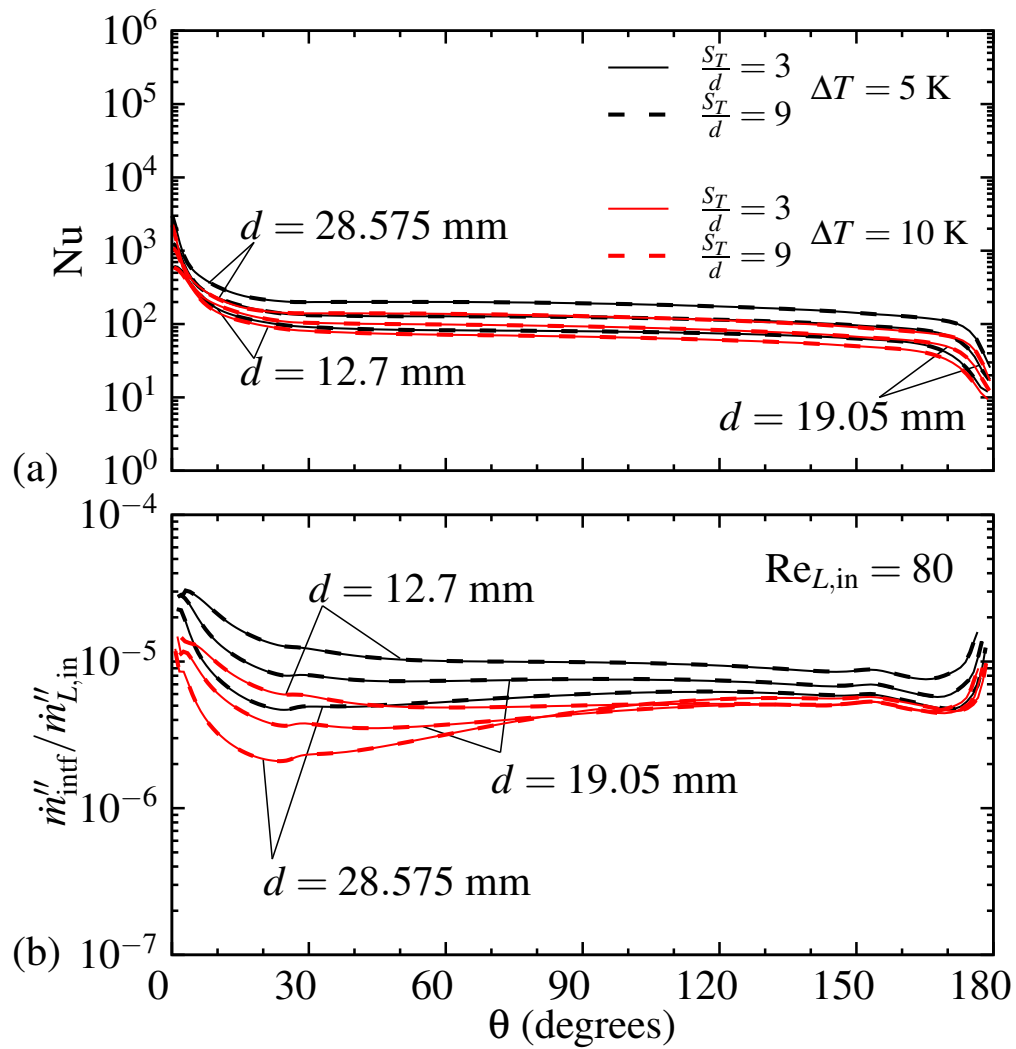


Figure H.4: Variation around the tube of (a) local Nusselt number and (b) interface dimensionless mass flux for $S_T/d = [3,9]$ and $\Delta T = [5 \text{ K}, 10 \text{ K}]$ with $d = [12.7 \text{ mm}, 19.05 \text{ mm}, 28.575 \text{ mm}]$ and $Re_{L,in} = 80$.

Appendix I

The Liquid and Gas Pressure Profiles for $S_T/d = 3$ and 9 Over a Horizontal Tube

In Figure I.1, $P_L^* = \frac{2(P_L - P_{\text{intf.in}})}{\rho_{L,\text{in}} U_{L,\text{in}}^2}$.

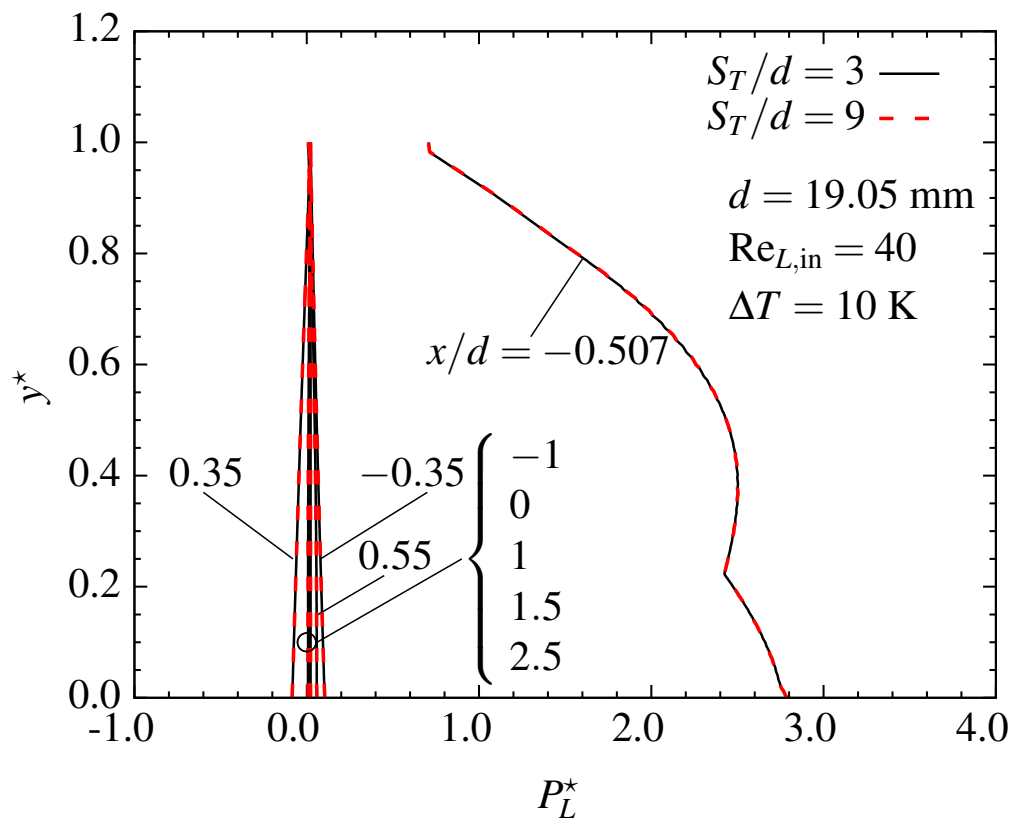


Figure I.1: Pressure profiles in the liquid at different axial locations for $d = 19.05$ mm, $\text{Re}_{L,\text{in}} = 40$ and $\Delta T = 10$ K (a) $S_T/d = 9$ and (b) $S_T/d = 3$.

In Figure I.2, $P_G^* = \frac{2(P_G - P_{\text{intf.in}})}{\rho_{G,\text{in}} U_{G,\text{in}}^2}$.

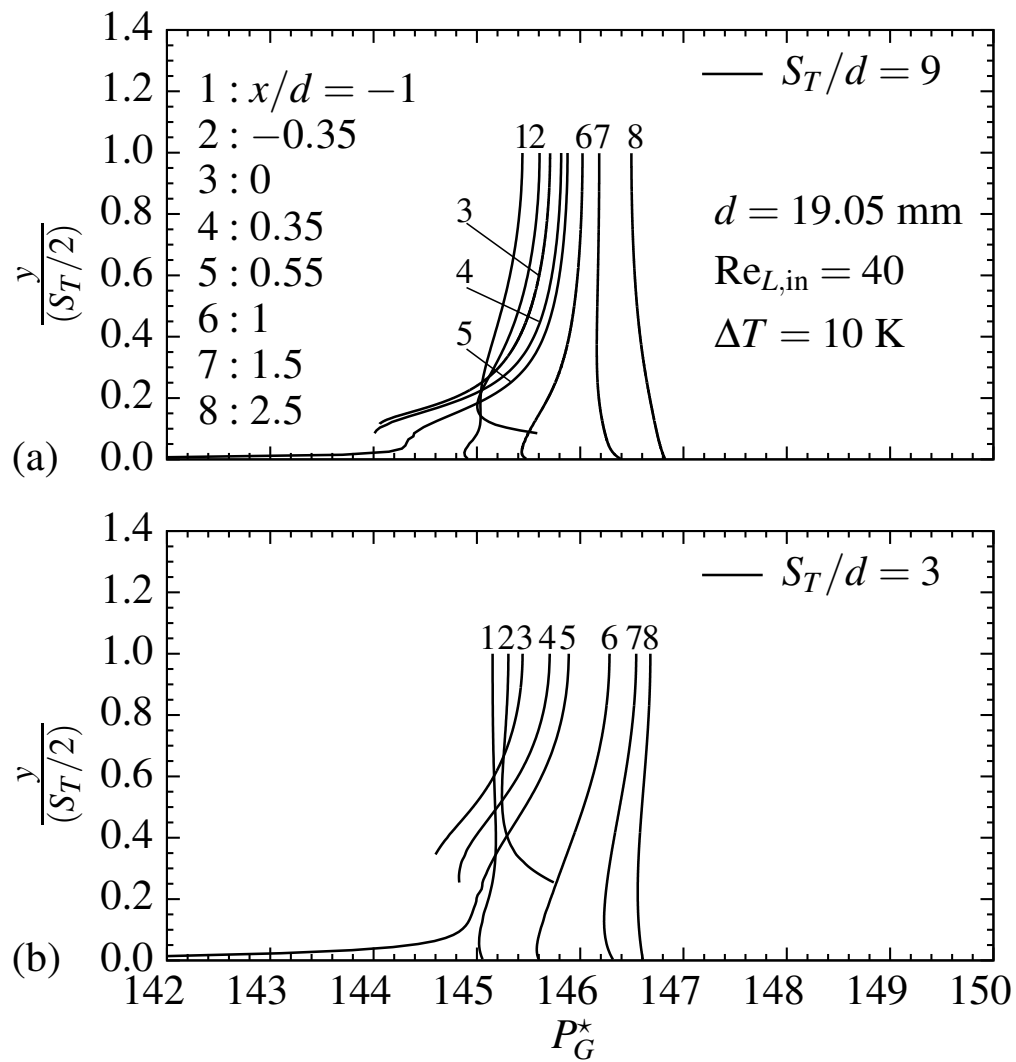


Figure I.2: Pressure profiles in the gas at different axial locations for $d = 19.05$ mm, $Re_{L,in} = 40$ and $\Delta T = 10$ K (a) $S_T/d = 9$ and (b) $S_T/d = 3$.